Optimization of sustainable mix design for alkali-activated materials using machine learning methods

By

Yukun KONG

A thesis submitted in partial fulfilment of the requirements for the degree of Doctor of Philosophy in Engineering

Professor Kiyofumi Kurumisawa

Supervisor

English Engineering Education Program (e3)

Laboratory of Eco-Materials and Resources

Division of Sustainable Resources Engineering

Graduate School of Engineering

Hokkaido University

Sapporo, Japan

June 2024

Abstract

The rapid increase in greenhouse gas emissions, primarily due to human activities, has become a significant environmental concern in the 21st century. According to measurements conducted at NOAA's Mauna Loa Atmospheric Baseline Observatory, atmospheric carbon dioxide (CO_2) levels have been steadily rising, reaching a peak monthly average of 420 parts per million (ppm) in May 2021, with an annual increase of 1.85 ppm. The manufacturing of ordinary Portland cement (OPC) contributes significantly to these emissions, accounting for approximately 6%–8% of total anthropogenic CO_2 emissions worldwide. Thus, there is a pressing need for alternative technologies aimed at reducing CO_2 emissions from this industry. Alkali-activated material (AAM) is a promising replacement to ordinary Portland cement (OPC), which is generally produced by low carbon-footprint supplementary cementitious materials (SCMs) mixed with alkali solution. The superior performance of AAM in strength to OPC is strongly dependent on the dense pore structures which is closely related to the mix design. However, the current commercial application of AAMs is still hindered due to three major problems. First, existing prediction models for the fresh and hardened properties of AAMs are often based on narrow sets of experimental data, leading to a lack of generality and convenience. Second, while forward analysis models predict properties based on mix design parameters, there is a growing need for inverse analysis to determine the "best" mix design that satisfies specific construction requirements. However, there is a lack of methods that can predict all mix design parameters based

on desired properties. Third, achieving a balance between high performance and sustainability remains a challenge in optimizing mix designs for AAMs. Mix designs need to be carefully considered to achieve desired properties while minimizing environmental impacts. For fulfilling this research gap, the presented research incorporates three main areas involving the material design of AAM that are (i) Identifying the key factors of mix design and constructing mathematical models for predicting the workability, compressive strength and drying shrinkage of AAM; (ii) Inverse analysis for determining the mix design of AAMs; and (iii) Life cycle assessment of the optimized AAM mixtures considering the key factors. Overall, the above research systematically investigated the AAM and provided a practical guidance for the mix design of AAM. It is believed that an optimized mix design of AAM with high performance and sustainability can be drawn out.

Chapter 1 sets the stage by providing the research background, articulating the problems addressed across the three main research areas investigated in this thesis, and outlining the primary objectives and contributions of this study.

Chapter 2 offers an extensive literature review covering alkali-activated materials (AAMs), the impact of mix design on both fresh and hardened properties, the utilization of machine learning technology, and the environmental implications associated with AAMs.

In the next three chapters, forward predictive models for fresh and hardened properties of AAMs are given using three machine learning methods, i.e., artificial neural network (ANN), LightGBM (LGBM) and XGBoost (XGB). **Chapter 3** gives a prediction model for workability of AAMs based on 402 individual mixtures collected from 26 existing papers. For constructing the prediction model for AAMs, a typical workflow including data collection, data processing, data analysis and modelling is used. This workflow is as well adopted for constructing the models for predicting compressive strength and drying shrinkage. Eight key factors influencing the workability performance of AAMs are recognized, including the activity moduli and specific surface area of precursors (SSA), Silicate modulus (Ms) of the alkali activator, NaOH concentration, Liquid to binder ratio (L/B ratio), Geopolymer paste content (GPC), and aggregate ratio. The qualitative results show that workability increases with the Ms and GPC but decreases with the NaOH concentration and aggregate content. In the proposed models, the above eight factors are set as input data, while the flowability results are set as output data. Three machine learning-based models demonstrate notable robustness and accuracy in forecasting the workability of AAMs, achieving coefficient of determination (R^2) values of 0.81, 0.96 and 0.95 for ANN, LGBM and XGB, respectively. Feature importance analysis points out the high importance of Ms on the flowability of AAMs.

Chapter 4 offers the prediction model for 28-day compressive strength of AAMs utilizing a total of 301 AAM mixture from 23 previous papers. Eight key factors are

considered for data analysis and modelling, including the activity moduli and SSA of precursors, Ms, NaOH concentration, L/B ratio, GPC, and aggregate ratio. The data analysis results reveal that higher activity of precursor, Ms and NaOH concentration may favor the strength development of AAMs, while L/B ratio and GPC usually hinder the strength development. In this machine learning-based model, the abovementioned key factors were inserted as the input data and the compressive strength is set as the output data. ANN, LGBM and XGB models all achieve significantly high R^2 values of 0.85, 0.96 and 0.97, respectively, in which XGB display the highest performance. Feature importance results show the dominant effect of coarse aggregate content on the compressive strength development of AAMs.

Chapter 5 presents machine learning-based models developed for predicting the drying shrinkage of AAMs. For constructing this model, the database is built using 438 individual AAM mixes extracted from 43 previous papers. Different from the previous two chapters, there are eleven key factors considered for model construction, i.e., the activity moduli and SSA of precursors, GPC, L/B ratio, NaOH concentration, Ms, fine and coarse aggregate content ratio, curing temperature, relative humidity (RH) and Volume/Surface ratio (V/S). Qualitative analysis revealed that the resistance to drying shrinkage in AAMs typically increases with higher concentrations of NaOH, aggregate ratios, curing temperature, RH, and V/S ratios. Conversely, it declined with increasing GPC, L/B ratio, and Ms. The prediction performance of these three models shows high accuracy and robustness, accompanied with high generality covering a wide range of

AAMs. The ANN, LGBM and XGB models demonstrate effective performance in predicting the ultimate drying shrinkage, achieving notably high R^2 values of 0.94, 0.99 and 0.99, respectively. Additionally, the results of feature importance analysis reveals the great importance of GPC on the ultimate drying shrinkage of AAMs.

Chapter 6 provides the inverse analysis method used to predict the optimal mix design of AAMs based on target properties. This inverse model is consisted with data generation, property prediction, and mix design filtration. The data generation is achieved by Gaussian mixture model based on the pre-collected database. Data distribution results on satisfied mix designs show a good agreement with the existing AAM mixes with the similar property. Afterwards, mechanical properties of the inversely predicted AAM mixes are estimated by the XGB algorithm due to its highest performance in predicting fresh and hardened properties. Meantime, the life-cycle assessment are conducted to evaluate five environmental impact categories, i.e., Global warming, Ozone depletion, Acidification, Eutrophication, and Ecotoxicity, using CML 2002 approach. Life-cycle assessment results display unneglectable environmental burdens of alkali activator on human toxicity. Therefore, an optimization of AAM mix design is conducted by the addition of coarse aggregate according to the previously constructed database. Such optimization can simultaneously lower the environmental impacts and remain the desired properties. Combining mechanical properties and environmental impacts, a workflow for decision-makers to determine the needed AAM mixes is given.

Finally, **Chapter 7** serves as the conclusion, summarizing the key findings of the thesis. It also delves into discussions concerning the challenges and potential of utilizing machine learning techniques in civil engineering. Additionally, it proposes potential directions for future research endeavors.

Keywords: Alkali-activated materials; Strength; Workability; Drying shrinkage; Machine learning; Life-cycle assessment.

Authorship Attribution Statement

This thesis contains material from 5 papers published in the following peer-reviewed journals in which the author was the first and/or corresponding author.

Chapter 2 is published as (1) Y.K. Kong, K. Kurumisawa, Fresh properties and characteristic testing methods for alkali-activated materials: A review, J. Build. Eng. 75 (2023) 106830. https://doi.org/10.1016/j.jobe.2023.106830; (2) Y.K. Kong, M. Kato, K. Kurumisawa, Recent advances in x-ray computed tomography for alkali-activated materials: A review, J. Adv. Concr. Technol. 21 (2023) 573-595. https://doi.org/10.3151/jact.21.573.

Chapter 3 is published as (1) Y.K. Kong, K. Kurumisawa, Application of machine learning in predicting workability for alkali-activated materials, Case Stud. Constr. Mater. 18 (2023) e02173. https://doi.org/10.1016/j.cscm.2023.e02173.

Chapter 4 is published as (1) S.H. Chu, Y.K. Kong, Mathematical model for strength of alkali-activated materials, J. Build. Eng. 44 (2021) 103189. https://doi.org/10.1016/j.jobe.2021.103189.

Chapter 5 is published as (1) Y.K. Kong, K. Kurumisawa, Prediction of the drying shrinkage of alkali-activated materials using artificial neural networks, Case Stud. Constr. Mater. 17 (2022) e01166. https://doi.org/10.1016/j.cscm.2022.e01166.

Table of contents

List of Tables

List of Figures

Chapter 1: Introduction

1.1. General background

Climate change caused by rapidly increasing amounts of greenhouse gas emissions has been one of the biggest environmental problems in the 21st century [1-3]. According to the atmospheric carbon dioxide (CO_2) measurement results conducted by NOAA's Mauna Loa Atmospheric Baseline Observatory [4], the current CO_2 levels in the air kept rising at a high annual rate of 1.85 ppm and peaked for 2021 in May at a monthly average of 420 ppm. The ordinary Portland cement (OPC) manufacturing industry accounts for approximately 6%–8% of the total CO_2 anthropogenic emissions on earth [5]. Therefore, alternative technologies to reduce CO_2 emissions are required. In this sense, cementless alkali-activated materials (AAMs), characterized by energy-saving and waste-recycling properties, have attracted the interest of researchers in the field of civil engineering to achieve sustainability in concrete production [6-9].

AAMs, produced using 100% industrial by-products or other minerals and alkali activators, can vastly mitigate the environmental impacts associated with concrete production [10, 11]. Interest on AAMs keeps increasing in the past decades. Jiang et al. [12] reported that compared to OPC production, AAM production could lower greenhouse gas emissions by 73%, energy demand by 43%, and water usage by 25% because of the repurposing of steel industry by-products. Although preparation of alkali activation for AAMs may cause pollution [13-15], the total environmental impacts of

producing AAMs are still lower than producing conventional OPC-based concrete with the similar strength [16]. In general, commonly used industrial wastes with pozzolanic activity are referred to as supplementary cementitious materials (SCMs), which are normally extracted from pig iron and alloy, or combustion of coal and clay, such as ground granulated blast-furnace slag (GGBFS), silica fume (SF), metakaolin, and fly ash (FA) [7]. In the presence of different alkali solutions, the pozzolanic reaction of SCMs results in the formation of amorphous alkali-alumina-silicate-hydrate (N-A-S-H) gels and/or calcium-alumina-silicate-hydrate (C-A-S-H) gels in AAMs [17]. These two gels can coexist in the same binder, although N-A-S-H is only stable when the environmental pH is lower than 12; otherwise, the presence of Ca degrades N-A-S-H in favor of C-A-S-H formation [18]. According to the existing literature, AAMs exhibit comparable mechanical properties to those of PC-based mixtures. However, limited knowledge is available on their long-term durability in terms of shrinkage performance [17], carbonation resistance [19], chloride induced corrosion of rebar [20] and potential alkali-aggregate reactions [21], hindering the broader application of AAMs in practical construction work.

Material design plays a role of importance in macroscopical and microscopical performance of cementitious materials. Significant research carried has been devoted to exploring the influence of mix design on the physical properties and microstructures of AAMs. Apart from the conventional measurement on workability and strength, drying shrinkage, one of the most problematic issues for AAMs, was always researched. Therefore, several researchers have put forward various prediction model on properties

of AAMs. However, these models were still far from satisfactory, which was discussed later. The long-term durability performance is closely related to the multiscale microstructural characteristics and pore networks of mixtures. Although the forward analysis, namely from the mix design to predicting the properties of AAMs, is always mentioned and researched, decision-makers favor more on the “best” mix design, which needs an inverse analysis. Herein, the inverse analysis is determination of mix design based on the required mechanical properties in the real construction work. However, there is still a scarcity of such mix design prediction model. Moreover, environmental burden from production of AAMs is directly determined by its mix design. SCMs, recycled from the industrial waste, exhibit lower environmental impacts compared to OPC though, high content of alkali activator inevitably results in resource use and environmental damage. Considering the potential environmental impacts brought by production of alkali activators, several researchers conducted life-cycle assessment (LCA) analysis on various AAM mixtures.

1.2. Statement of problems and objectives

1.2.1. Prediction model on properties of AAMs based on the mix design

For any construction and building materials, workability and compressive strength are always concerned. Workability is critical to the in-situ construction work and viability of any building material. Loss in workability is detrimental to mixing machine and concrete quality. Compressive strength is of necessity for concrete structures,

directly determining the load capacity of the whole building. Previous studies recommended to adjust the mix design like precursor type and alkaline activator solution content to improve the fresh and hardened properties of AAM [22]. Admittedly, workability and strength models have been by previous studies and building codes. Several researchers tried to build the workability prediction model for AAM-based composite materials. Kuang et al. [23] used backpropagation neural network to construct the slump and compressive strength of composite geopolymers. Zhang et al. [24] utilized the inverse analysis to build the correlation model between the rheological parameters and flow parameters for nano-SiO_2 and PVA fiber reinforced alkali-activated composites. Nazar et al. [25] constructed a machine learning-based gene expression model for estimation of strength, rheology, and impact of raw materials of alkali-activated mortar using their own experimental data. Likewise, Gomaa et al. [26] used machine learning technique to predict the slump flow and compressive strength of alkali-activated concrete based on their own results. However, these models were generally built based on their own experimental data, lacking generality.

Regarding the strength models in previous studies, most of the related studies only presented experimental results without modeling, and these limited studies on modeling often presented a model based on their own test results and exhibited less generality. More importantly, the strength models given in previous studies generally do not agree with each other. Regarding the strength models in building codes, ACI 318 [27] and AS3600 codes [28] give the square root functions of compressive strength and flexural strength. However, it is also reported that these two models may underestimate the

compressive strength of geopolymer [29]. Well-established strength models for AAM are still lacking.

Another practical construction concerning property is drying shrinkage performance. The drying shrinkage of AAM, which occurs because of water evaporation under the effect of an unsaturated environment, is significantly influenced by the raw materials of the precursor, types and dosages of alkali activator, aggregate content, chemical admixtures, and curing conditions composing of temperature and relative humidity (RH) [30-32]. However, because of the complexity of the effects of the aforementioned factors, the existing prediction models for shrinkage are far from satisfactory. These models can be classified into two types: shrinkage models constructed as a function of mechanical properties rather than the mixture design and curing conditions such as Eurocode 2 [33] and Model Code 2010 [34], and shrinkage models established based on their own data obtained from self-designed experiments that cannot be used as a general model for various types of AAMs [35-37]. For the standard shrinkage model (e.g., Eurocode 2 and ACI-209), certain physical properties of AAMs, such as 28-day compressive strength or slump value, are needed for further prediction of drying shrinkage, requiring for a specimen preparation to acquire these parameters. Otherwise, these models cannot be used for prediction. From all indications, there is a desperate need for a shrinkage model that can be applicable under different situations using only mixture design and curing conditions as input for the system. Another thing should be mentioned that when designing AAM mixes, the concerned properties are not only limited to the workability, compressive strength and drying

shrinkage. Other durability properties as well are significant for AAMs such as carbonation performance, resistance to sulfate attack. There are two major reasons for not considering these properties in this dissertation. First, these durability properties may vary among different structures' applications. We put the view sight on the most important properties of AAMs. Second, durability properties in general increase with the higher compressive strength.

From the above, it could be seen that the current prediction models for fresh and hardened properties of AAMs, albeit advanced, are still faced with several problems. First, most researchers established their models based on their own experimental data, resulting in the narrow application of the model to a particular type of AAM, lacking the generality. Second, some researchers used other mechanical properties rather than the mix design factors as the input data to predict the workability, strength and shrinkage results, which still needs the rigorous specimen preparation to acquire these parameters. Existing models suffer from limitations such as narrow applicability, reliance on specific experimental data, and insufficient training datasets. Moreover, a systematical review on the mix design key factors is also needed. In this sense, there is still an absence of a prediction model with high generality and robustness for the workability of AAMs based on the mix design key factors.

1.2.2. Performance-based prediction for AAM mix design

As abovementioned, numerous researchers put their focus on construction of prediction models for different properties of AAMs. These models predicted the

mechanical properties of AAMs without conducting any trial experiments, which can save material and labor costs. Such researches provided a forward analysis that is using the mix design parameters to predict the properties. However, in the real construction work, decision-makers and engineers prefer more on the determination of “best” mix design. Herein, the “best” mix design refers to the one that can satisfy the required construction needs, e.g., specific strength or maximum drying shrinkage. In this sense, an inverse analysis, namely using the desired mechanical properties to predict the mix design, is strongly needed. The traditional forward analysis that can be expressed as the following equation:

$$Y = f(x) \tag{1.1}$$

where Y indicates the predicted properties (e.g., workability, strength, drying shrinkage, etc.); x indicates the various input data (e.g., liquid-to-binder ratio, aggregate content, etc.).

On the other hand, the inverse analysis can be expressed as the following equation:

$$X(x_1, x_2, x_3\ldots) = f(Y) \tag{1.2}$$

where X indicates the various mix design parameters including x_1, x_2, x_3 and etc.

Different from the forward analysis using multi-variables to predict one property (Eq. 1.1), inverse analysis (Eq. 1.2) uses only one or two desired properties to predict a

series of mix design properties. Obviously, such prediction is extremely difficult to be achieved by manual calculation. Meanwhile, machine learning techniques make it possible to apply analytical methods to search for the optimum mixture. Admittedly, the inverse analysis for optimizing the concrete mixtures has been put forward by some researchers. Yeh [38] pioneered in constructing a novel Computer-Aided Design (CAD) tool for undertaking the mix design of cement-based concrete. Huang et al. [39] adopted a support vector regression and firefly algorithm based multi-objective optimization model to optimize the mixture design of steel-fiber reinforced concrete. Ke and Duan [40] used Gaussian process emulator (GP emulator) to design the high performance concrete with the target strength based on the Bayesian theory. As it can be seen, computer-aided optimization technology is quite mature for cement-based mixtures, especially within the machine learning-introduced era. Nevertheless, the intelligent optimization for mix design of AAMs is still limited. Huo et al. [41] tried to use the pre-built XGBoost model to reversely predict and optimize the mix proportions of calcium-based geopolymer. The specific idea they used is to take the target compressive strength as one of the input variables, select an original input feature (i.e., $n(SiO_2)/n(CaO)$) as the output variable, train the model, and then predict this value under different scenarios (i.e., different target strengths, Na_2O contents and $n(H_2O)/n(Na_2O)$). Likewise, Sun et al. [42] developed their random forest machine learning algorithm to first predict the fresh and hardened properties of alkali-activated concrete, including compressive strength, slump values, yield stress and plastic viscosity. Then, an inverse application of this algorithm was used to optimize the silicate modulus of alkali activator with the

lowest environmental burden. Albeit advanced, the major drawback of these two methods is that the output was limited with only one mix design parameter rather than optimizing all input variables. Thus, there is an urgent need on the inverse analysis for predicting all mix design parameters of AAMs.

1.2.3. Life cycle assessment (LCA) of AAMs

Low carbon footprint cement and concrete is pursued worldwide in recent decades, aiming at decreasing the environmental impacts of OPC production [1-3]. It is reported that OPC production annually emits 2 billion tons of CO_2, corresponding to 8-10% of anthropogenic emissions in the world [2]. Hence, AAMs are recommended to be alternative cementitious materials by virtue of its high performance and recycling of industrial wastes [43]. The precursors used in AAMs normally are GGBFS, SF, FA and metakaolin [44], which were extensively studied by different research workers since 20^{th} century [45]. The presence of SCMs provides the possibility to 100% replace OPC in the concrete, which can result in reduction of greenhouse gas emissions by 73% [12]. However, these industrial by-products are faced with the limited global generation problem [16]. Compared to the world production of OPC (3-4 billion tons per year), the generation of GGBFS (170-250 Mt per year) and FA (500-700 Mt per year) is much lower [46-48]. Because of the fast urbanization, there is an increasing demand in construction material. It is estimated that global OPC demand will be increased by 216% from now to 2030, while GGBFS and FA generation may only increase by 15% [49]. However, for achieving the comparable performance to OPC-based mixtures, AAMs

always require for a high geopolymer paste content, leading to a high material cost and low dimensional stability [31]. Thus, it is of necessity to optimize the mix design to lower the usage of precursors.

Another major drawback of AAMs is attributed to the presence of alkali activator. In general, SCMs could be manufactured without the clinkerization process, which is opposed to the OPC production [16]. Nevertheless, the presence of high concentration alkali activator in AAMs still causes an unneglectable environmental impact, especially in Global warming potential (GWP), besides accounting for the most expensive part in the material cost [50]. For instance, sodium silicate production causes heavy effects on environmental impacts. Habert et al. [14] reported that GWP score of sodium silicate solution (37%) production was 117.8 kg CO_2 eq., while that of FA production was only 2.14 kg CO_2 eq. when compared to a 100% OPC concrete with the same strength. Another commonly used alkali activator in AAM is sodium hydroxide, normally in pellet form. The source of sodium hydroxide largely influences the overall impacts. Salas et al. [51] compared the average European energy mix and Ecuadorian energy mix and concluded that the former one performed worse because of the higher shares of thermoelectricity. On the other hand, it was also discovered that several key factors of AAM design may influence the usage of alkali activator, consisting of Si/Al ratio of precursors, type and concentration of alkali solution, and provenance of components. Si/Al ratio of precursors, for example, was suggested to be around 2.00 to reach sufficient mechanical properties [52]. Therefore, a suitable Si/Al ratio of precursors could minimize the amount of sodium silicate in AAMs. Environmental implications

of AAMs production cannot be simply defined as low carbon footprint before a detailed LCA analysis is made. However, the current LCA on AAMs normally focused more on one certain mix design compared to the OPC-based mixtures. There exists limited research reporting scenario analysis on how altering key factors of mix design affects the environmental impacts of AAMs. Herein, it should be noted that the mix design is changed although, the mechanical properties should be maintained or even improved. For example, increasing L/B ratio may reduce the strength of AAMs, while adjusting reactivity of precursors to be 2.00 may increase the strength of AAMs. Meantime, the environmental burden brought by different mix design should be clearly identified. Achieving a balance among high performance, low cost and sustainability is of significance for the wider application of AAMs.

1.2.4. Research significance

Conclusively, there are three major research challenges lying on the study of AAMs with the regard to mix design optimization. First, key factors of mix design for AAMs should be identified. These key factors macroscopically govern the properties of AAMs. Then, a robust prediction model with high generality for the properties of AAMs should be constructed based on the key factors of mix design. A practical and easily-handling guideline for mix design of AAMs could be drawn out. Second, for widening the commercial applications of AAMs, an inverse analysis for predicting the mix design with the target fresh and hardened properties was conducted by using machine learning technology. The third area focused on the assessment of the environmental impacts of

AAMs production. Combining the previous two parts, LCA could provide suggestions on how to optimize AAM mix design being more sustainable. For filling the above research gap, a summary of the structure of this study is displayed in Fig. 1.1.

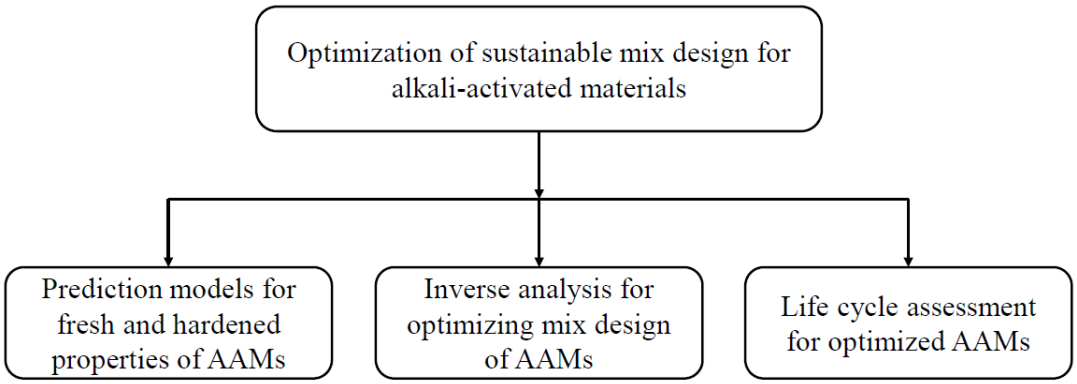

Fig. 1.1. Structure of the research project presented in this report

1.3. Goals and novelty of the research

According to the previous parts, this study focused on three major research tasks that have not been detailed investigated or even untouched. The first research task was summarizing key factors of mix design and constructing practical and easily-handling prediction model for the properties of AAMs. The key factors of material design were only related to the amount and/or property of each component in the AAMs regardless of mix design method or other operator-dependent stuff. To better understand how these key factors influenced the AAMs, abundant data extracted from the existing literature were collected and processed. Different properties, specifically workability, compressive strength and drying shrinkage in this study, were dominant by different key material design factors which were clearly distinguished. For slump flow and 28-

day compressive strength of AAMs, eight dominant key parameters were determined that were reactivity of precursors (i.e., activity moduli and specific surface area), sodium hydroxide concentration, silicate modulus ratio, liquid-to-binder ratio, geopolymer paste content, and fine and coarse aggregate content. For ultimate drying shrinkage of AAMs, considering the shrinkage mechanism behind it, curing conditions should also be listed in the key factors. Therefore, apart from the abovementioned eight dominant key factors, curing temperature, relative humidity and specimen size were also considered as the input variables. To construct robust models with high generality and accuracy, the models for predicting the workability, strength and drying shrinkage were constructed based on the abundant data from the literature. Due to the different mechanisms behind various properties and difficulties on data processing, different mathematical model construction methods were used. For each property, three different machine learning algorithms were adopted and compared, including artificial neural networks, XGBoost and LightGBM. The objectives of the first research task were:

1. Collecting appropriate data from the existing papers and processing these data into the same units for high consistency, in which the mass of each component was converted into volumetric ratio.
2. Identifying the influence of key factors in mix design on slump flow, 28-day compressive strength and ultimate drying shrinkage of AAMs.
3. Modelling the slump flow, strength and drying shrinkage of AAMs based on the acquired data using machine learning algorithms.

4. Giving practical guidelines on AAM mix design with high performance and sustainability based on the data analysis and prediction model.

The second research task was involved with the inverse analysis for intelligent determination of AAM mix design. The main idea is to firstly construct a forward prediction model, and then calculate the properties of AAMs based on the generated abundant data. Thus, a huge dataset on AAM mix design accompanied with various mechanical properties was formed. This dataset can work as a quick index for decision-makers to determine the needed AAM mixes with the required properties without any trial-and-error experiment. Prior to the inverse analysis, the collected data on different AAM mixtures were reused for generation of new mixes. Two data generation methods were compared, including Gaussian mixture method and Random generation method. Therefore, this part involved the following research objectives:

1. Generation of new mix design data using Gaussian mixture model (GMM). GMM could ensure the generated mixes lying in the range consistent with the collected data.
2. Calculation of workability, strength and drying shrinkage results for new mix designs by using the pre-constructed model.
3. Proving the accuracy of the proposed mix design by producing the same AAM mixture and measuring its mechanical properties.

The last research area focused on the environmental impacts of the production of the predicted AAM mixtures. The goal of this part was to evaluate the environmental impacts of the predicted AAM production compared to that of the conventional OPC-based and AAM-based mixtures. This study resulted in the evaluation of the relevant environmental burdens involved within the manufacture of the predicted AAM from the raw material preparation to the final product packaging. The CML (Center of environmental science of Leiden University) 2002 approach was used in this study, which is one of the most commonly used LCA methods. The key environmental impact categories were investigated and identified, including Global warming (GWP), Ozone depletion (ODP), Acidification (AP), Eutrophication (EP), and Ecotoxicity (ETP). Meantime, a sensitivity analysis was conducted based on the various scenarios of changing the mix design key factors raised in the previous parts. Through sensitivity analysis, the influence of each key factor on the total environmental impacts of AAM production could be identified. Therefore, the objectives of this part were listed below:

1. Assessment of the environmental burdens of the optimized AAM production.
2. Evaluation and comparison of the environmental impact categories (i.e., GWP, ODP, AP, EP and ETP) of the conventional OPC-based, normal AAM and optimized AAM mixtures with the similar mechanical properties.
3. Utilization of a sensitivity analysis for different scenarios by varying mix design key factors for identifying the effects of key factors on the total environmental impacts.

1.4. Layout of the dissertation

Based on the aforementioned research significance and study objectives, this dissertation includes 7 chapters in total. The detailed information of each chapter was given as follows:

Chapter 1 introduces the research background, presents the statement of the problems on the three research topics studied in this thesis, and provides the main goals and novelty of this research.

Chapter 2 gives a detailed literature review on the AAMs, influence of the mix design on the fresh and hardened properties, machine learning technology, and environmental impacts of the AAMs.

Chapter 3 presents a prediction model for the workability of AAMs, based on data from 402 individual mixtures sourced from 26 existing papers. The model construction follows a typical workflow encompassing data collection, processing, analysis, and modeling. Three typical machine learning algorithms are chosen, i.e., artificial neural networks, LightGBM and XGBoost. This approach is also applied to develop models for predicting compressive strength and drying shrinkage of AAMs.

Chapter 4 offers three machine learning-based prediction models for the 28-day compressive strength of AAMs, utilizing data from 301 AAM mixtures collected from 23 previous papers.

Chapter 5 introduces machine learning-based models designed to predict the drying shrinkage of AAMs. The model construction involves building a database comprising 438 individual AAM mixes extracted from 43 previous papers.

Chapter 6 outlines an inverse analysis method for predicting the optimal mix design of AAMs based on target properties. It includes data generation using a Gaussian mixture model from the pre-collected database, property prediction with the XGBoost algorithm, and life-cycle assessment (LCA) to evaluate environmental impacts across five categories. By integrating mechanical properties and environmental impacts, a decision-making workflow is provided for selecting the required AAM mixes.

Chapter 7 is the conclusion part for the whole thesis.

Chapter 2: Literature review

2.1. Importance of studying key factors in AAM mix design

Compared to traditional cement-based mix design, AAM-based mixtures are much more complicated due to the totally different components. Table 2.1 lists out the raw material components used in OPC and AAM concrete. It can be seen that apart from the aggregate and admixture content, the components of precursors and liquid part are different. For traditional cement concrete, only cement is used as the precursor which is generally standardized. Thus, it is quite convenient to manufacture the property-required concrete with the given cement. In contrast, AAM-based concrete adopts SCMs as the precursors, covering a wide range of various types, e.g., GGBFS, FA, etc. The hydration product of AAM is varied a lot with different types of AAMs. Regarding the liquid part, traditional cement concrete only needs water to mix, while AAM concrete needs not only water for mixing but also the alkali activator to activate due to the low reactivity of SCMs. Based on that, we can see that four main key factors in general are enough for determining a conventional cement-based mix, including water-to-cement ratio, cement paste content, fine aggregate content and coarse aggregate content. However, for AAM-based mixes, the key factors should cover type and dosage of precursor (i.e., activity moduli and specific surface area) and alkali activator (i.e., alkali concentration and silicate modulus). The detailed key factors were introduced in the latter chapters.

Table 2.1. Comparison of raw material components

Types	Precursor	Liquid		Aggregate	Admixture
OPC concrete	Cement	Water		Sand and Gravel	SP, AE, etc.
AAM concrete	SCMs	NaOH or KOH	Na_2SiO_3 or K_2SiO_3	Sand and Gravel	SP, AE, etc.

Note: SP = Superplasticizer; AE = Air entraining agent.

2.2. Influence of mix design on the fresh and hardened properties of AAMs

Physical properties including workability, mechanical performance and durability are dominant by the material design of AAM which directly affects the microstructure [53]. The mix design can be concluded into several key factors. Specifically, these key factors in this study referred to properties of precursors, alkali concentrations, silicate modulus (Ms), geopolymer paste content (GPC), aggregate content, liquid-to-binder (L/B) ratio and curing conditions (i.e., curing temperature, relative humidity, and mold size). These factors have been studied by several researchers with regard to their effects on the physical properties of AAMs.

2.2.1. Precursors

The type and amount of precursors directly influence the properties of AAMs. GGBFS, being the by-product from the extraction of pig iron in blast furnaces, has been the most widely utilized slags in AAMs [18, 54, 55]. Common alkali-activated slag (AAS) pastes displays a higher workability than OPC paste [56]. FA is a giga-scale material owing to the over one billion tons of by-products of coal combustion annually [57]. Due to the relatively lower pozzolanic reactivity of FA, higher content of FA could retard the initial and final setting but impair the strength gaining of AAM [58]. SF, obtained from the silicon metal and ferro-silicon alloy industries, demonstrates a fairly high pozzolanic reactivity because of its high SiO_2 content and large fineness [59]. Metakaolin (MK) is acquired from the burned kaolinite-rich materials with high reactivity and water demand [7, 60]. Lastly, natural pozzolan, derived from the volcanic rocks, is not widely considered as precursors in the past but possesses a good potential [61]. Additionally, the physical properties of particles (e.g., specific surface area) demonstrate a significant effect on the workability of AAM, which determines the water demand of the mixes. Ling et al. [62] studied the effect of SiO_2/Na_2O mole module, solute concentration of alkali activator and liquid to fly ash mass ratio on the heat of geopolymer reaction, setting time, and compressive strength of fly ash geopolymer. Hadi et al. [63] investigated different values of GGBFS contents ranging from 0% to 40% with a constant alkaline solution to binder ratio on the basis of compressive strength, setting time and workability.

2.2.2. Alkali activator

Alkali activation technique of AAMs is the major difference compared to other construction materials. Various alkali activators contribute to the different pozzolanic reaction of SCMs resulting in the different pH environment and formation of hydration products. Silicate modulus (*Ms* = SiO_2/Na_2O) and NaOH concentration of the activators are the two key factors affecting the fresh and hardened properties of AAMs [64]. Jafari Nadoushan and Ramezanianpour [65] provided a comprehensive research on the effect of alkaline solution type and concentration, modulus of Na_2SiO_3, and Na_2SiO_3-to-alkaline solution ratio on the flowability of alkali-activated slag/NP-based pastes. An optimum Ms and Na_2SiO_3-to-alkaline solution ratio of 2.33 and 0.4 respectively was determined for AAS-based paste with high workability and improved compressive strength. Pacheco-Torgal et al. [66] found that the workability of alkali-activated metakaolin (AAMK) decreased with the increasing NaOH concentration. Hu et al. [67] optimized the type and dosage of precursor and alkali activator and the curing temperature to establish early strength prediction model for unary and binary geopolymers. Luan et al. [68] focused on the NaOH concentration (by molarity) and sodium silicate to sodium hydroxide ratio. In view of the foregoing statement, properties of alkali activators in terms of Ms and NaOH concentration are two important factors governing the workability of AAMs.

2.2.3. Liquid-to-binder ratio

L/B ratio is always mentioned in the mix design for cementitious materials. It is well-known that varying L/B ratio directly influenced the workability, mechanical

properties, durability, microstructures and characteristic pore networks of AAMs [69-74]. The influence of L/B ratio on the fresh and hardened properties of AAM mixtures is quite similar to those of OPC-based mixtures. Alonso et al. [56] researched the workability and rheology of AAS and AAFA mortars with different L/B ratio. The workability of both these two AAM mortars increased with the L/B ratio. Tuyan et al. [73] focused on the influence of water-to-solid ratio on the AAS grouts efflux time and reported that this ratio is the major contribution to the efflux time. Ling et al. [62] observed that the initial setting time of AAFA increased with higher amount of L/B ratio when the SiO_2/Na_2O module of geopolymer was lower than 1.5.

2.2.4. Geopolymer paste content and aggregates

Last but not least, geopolymer paste content and aggregate phase play significant roles in mix design of AAMs, which were always underestimated or even ignored. Conventionally, many researchers put their focus only on the AAM paste part leading to manufacture of AAM mixtures without the addition of fine and/or coarse aggregates [73]. In this sense, an extremely high geopolymer paste content was occurred, implying a considerable material cost, low dimensional stability and a high environment burden [31, 75, 76]. Chu and Kong [31] pioneered in summarizing the effect of geopolymer paste volume on the 28-day compressive strength of AAM pastes, mortars and concretes utilizing the experimental data extracted from the literature, in which a pronounced decreasing trend of strength with the geopolymer paste content was revealed. Following that, Kong and Kurumisawa [32] summarized the effect of

geopolymer paste content on the ultimate drying shrinkage of AAM and observed larger drying shrinkage strains with higher paste volume. The systematical investigation of varying aggregate content in AAM related research is still in scarce yet, although it governs the wet packing density of the whole matrix. A consensus was reached that lower geopolymer paste content, in other words, higher aggregate volumetric ratio contributed to a lower workability, which had certain adverse effect on the pumpability of AAM concrete and was detrimental to the mixing machine [75, 77]. Overall, the aggregate content is by no means negligible to the fresh and hardened properties of AAMs.

2.2.5. Curing conditions

Curing conditions are of vitality to construction materials. Herein, the curing conditions refers to curing temperature, relative humidity and curing mold size. Temperature plays a critical role in the hydration process of the alkali-activated binder. When cured at elevated temperatures, the inner hydration product of C-S-H in slag-based AAMs changes the volume of fine porosity in the matrix and the water content within the gel [78]. Heating treatment can increase the early age compressive strength and accelerate the strength development rate, but may hinder later age strength. Bakharev et al. [78] stated that heating curing could also improve the shrinkage resistance owing to the lower water content in the C-S-H formation. Thus, heating curing at an appropriate temperature is recommended for AAM, which could improve the volumetric stability and reduce the total porosity.

The effect of relative humidity (RH) mainly lies in the drying shrinkage performance of cement- and AAM-based mixtures. Normally, at relatively low RH environment (40~50%), high drying shrinkage tends to occur due to the surface tension of the pore solution in the pores. According to the capillary pressure theory, this surface tension is generated in the meniscus formed by the water evaporation leading to the volume reduction [79]. However, as the RH further decreases lower than 40%, the driving force of drying shrinkage changes, which cannot be explained by capillary pressure theory. First, the capillary meniscus destabilizes at approximately 40% RH corresponding to a Kelvin radius of around 1 nm, and triggers a significant alteration in the shrinkage mechanism. Second, a marked shift in the slope of shrinkage concerning moisture loss occurs at roughly 40% RH, and a reversible shrinkage after adequate rewetting time could be found below 40% RH [80]. Meantime, Ye and Radlińska [17] revealed the mechanism of drying shrinkage for alkali-activated slag and attributed the larger shrinkage in alkali-activated slag to the structural incorporation of alkali cations in C-A-S-H, leading to the reduction of the stacking regularity of C-A-S-H layers and easier potential of C-A-S-H collapse and redistribution upon drying. Therefore, the mechanism behind the drying shrinkage of AAMs is much more complicated than cement-based materials.

Lastly, specimen size is an easily-neglected key factor that influences the strength development and drying shrinkage. When assessing the macroscopic characteristics of a random heterogeneous material, it is essential for the specimen size to be sufficiently large to statistically represent the property of interest. Note that the specimen size is

normally considered as the volume-to-surface ratio of specimens that is also named as effective drying thickness. Ohama and Kan [81] investigated the effects of specimen size on strength and drying shrinkage of polymer-modified concrete. They found that compressive strength increased with a reduction of specimen size, while drying shrinkage decreased with an increase of specimen size [81]. Ba et al.'s experimental results indicated that the effects of specimen size and shape on water loss were in line with those on drying shrinkage [82]. Furthermore, the effects of specimen size and shape on the water loss were considered in an established model of averaged RH across the effective drying thickness [82]. Thus, the specimen size and shape are of significance to the mechanical properties of cementitious materials.

2.3. Advanced machine learning algorithm

Early concrete research has adhered to three scientific paradigms: empiricism, theory, and computation [83]. Specifically, trail-and-error experiments (empiricism) provided abundant first-hand experimental data on the properties of cement- or AAM-based concrete for improving the material design [83]; development of microstructural models for hydration process advanced the understanding of microstructure-property relationships, marked as the second paradigm (theory) [84]; the third paradigm, namely, computation, was thrived due to the utilization of density-function theory and classical molecular dynamics [85]. Admittedly, the previous three paradigms of concrete science have set milestones, providing valuable contributions to the development of

construction material research. However, these three paradigms are still faced with several issues, consisting of the iterative trial-and-error cycles, substantial domain expertise required, and extremely high labor and computational costs. Machine learning, born as the fourth paradigm, has been prevalent in civil engineering in recent years because of its high feasibility in analyzing big data acquired for difficult practical problems [86-88]. By leveraging the existing datasets through data-driven models, machine learning has the capability to autonomously learn implicit patterns and extract valuable insights, all while accommodating the intricate nature of concrete mixtures and their associated properties [89]. Modern machine learning techniques, such as artificial neural networks (ANN), extreme gradient boosting (XGBoost), and light gradient boosting machine (LightGBM), are deemed effective tools for developing prediction models. Some researchers have adopted machine learning technology to predict various properties of cementitious materials. Alabdullah et al. [90] used LightGBM and XGBoost to predict the rapid chloride penetration resistance of MK-based concretes. Hilloulin and Tran [91] predicted the autogenous shrinkage of high-performance and ultra-high-performance concrete using K-nearest neighbors, random forest, gradient boosting, and XGBoost. Nguyen et al. [92] constructed deep neural and deep residual networks to calculate the compressive strength of an FA geopolymer concrete using mix design factors. In the proposed research, Backpropagation neural network (BPNN) was chosen to be used for construction of prediction model of various properties of AAMs.

2.3.1. Overview of BPNN

Backpropagation Neural Networks, abbreviated as BPNN, is a commonly used machine learning method to construct prediction models via the cooperation of interconnected but simple elements [93, 94]. Fig. 2.1 displayed a typical architecture of BPNN [32]. BPNN structure can be regarded as a multi-linear perceptron made up by an activation function, a weight matrix, bias vectors, an input vector and an output vector. The weighted input vector and bias are applied to the neighboring neurons, and the weighted sum function calculates the net input. The weighted input vector is applied to the neuron accompanied by a bias *b*, and the weighted sum function computes the net input applied to the neuron using Eq. 2.1 as follows [95]:

$$s_j = \sum_{i=1}^{n} w_{ij} x_i + b \tag{2.1}$$

where s_j is the weighted sum of the *jth* neuron, w_{ij} represents the weight matrix, x_i is the input vector, and *n* represents the number of neurons.

Subsequently, the activation function processes the weighted sums of the inputs and converts them into neuron outputs. In this study, the tangent-sigmoid activation function (Eq. 2.2) was used for the hidden layers, whereas a linear function was used for the output layer [93]:

$$v_j = \frac{2}{1+e^{-2s_j}} - 1 \tag{2.2}$$

Tangent-sigmoid functions generally show a return value (here, v_j) in the range from -1 to 1; however, if needed, the outputs of the tangent-sigmoid function can be adjusted to the range from 0 to 1 [93].

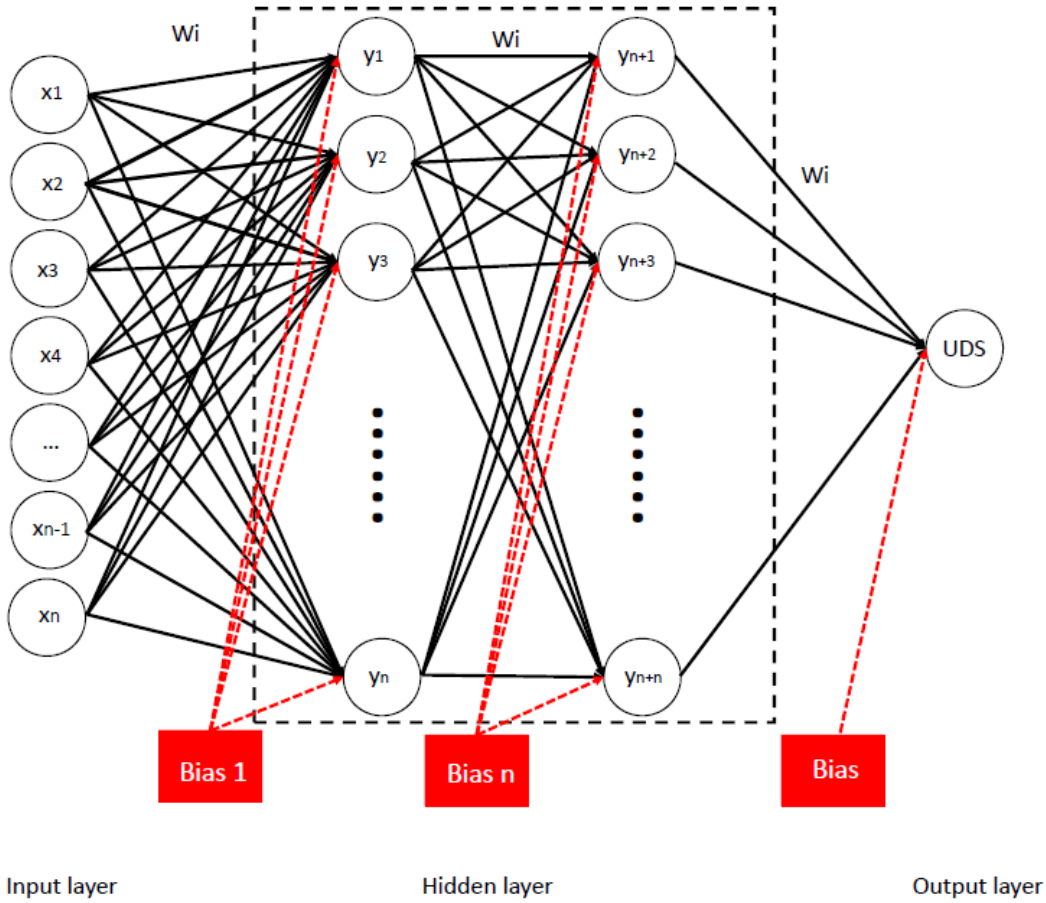

Fig. 2.1. Typical architecture of BPNN

The backpropagation (BP) algorithm works as a gradient descent technique to reduce the error between the actual outputs of neural networks and the real values of response during the training pattern [96-98]. The network error is passed backwards from the output layer to the input layer, meantime, the weights are re-adjusted based on learning strategies to decrease the error to an acceptable level [99]. In this BP phase,

the error between the output and the desired output values is calculated based on the generalized delta rule, and the weights between neurons are re-adjusted based on the Eq. 2.3 as follows [96]:

$$w_{ji}^{n+1} = w_{ji}^{n} + \alpha\delta_j o_j + \beta w_{ji}^{n} \quad (2.3)$$

where δ_j is the error signal at *jth* neuron which is calculated based on the partial derivate of the error function in the output and other layers, o_j is the output of *jth* neuron, α and β are learning rate parameter and momentum factor, respectively, and n is the number of iteration.

As the iterative process converged, the training process is finished. The weights are collected from the trained network and used in the recall phase [96].

2.3.2. Overview of XGBoost

EXtreme Gradient Boosting (XGBoost) is a recently developed machine learning algorithm that became widespread in the civil engineering [90]. This technique is constructed based on the "boosting" idea, combining the weak learners' prediction with additive training approaches to make a strong learner. XGBoost aims at preventing over-fitting but also optimize the computational resources by simplifying the objective functions. Such optimization can combine predictive and regularization terms, but maintain an acceptable computational speed. Furthermore, parallel calculations are executed for the functions as well in XGBoost during the training phase [93, 94].

The mechanisms behind the additive learning process are introduced here. For fixing the limits of a weak learner, the first learner is applied to the whole input database, and then the second model is applied to the residuals. Such fitting process is repeated for several times until the stopping criterion is satisfied. The final model for prediction is acquired by the sum of the prediction of each learner. The determining equations for the generic function of predicting phase is shown below. Fig. 2.2 depicts the typical structure of XGBoost.

$$f_i^p = \sum_{k=1}^{l} f_k(x_i) = f_i^{p-1} + f_i(x_i) \tag{2.4}$$

where $f_k(x_i)$ is the learner at the *pth* phase, f_i^p and f_i^{p-1} are the prediction at the *pth* and (p-1)*th* phase, and x_i represents the input variables.

An analytical formula is generated by XGBoost to evaluate the "goodness" of the prediction model for avoiding over-fitting issues, shown as Eq. 2.5.

$$Obj^p = \sum_{k=1}^{l} l(\overline{y}_i, y_i) + \sum_{k=1}^{p} \sigma(f_i) \tag{2.5}$$

where l represents the loss function between the prediction $\overline{y}_i$ and the target y_i, n denotes the number of observations, σ represents the regularization term that can be calculated as the following function:

$$\sigma(f) = \gamma T + \frac{1}{2}\lambda\|\omega\|^2 \quad (2.6)$$

where ω denotes the vector scores in leaves, γ represents the minimum loss and λ represents the regularization parameters.

Such scalable end-to-end tree boosting system is able to solve practical construction problems by using a fewer resources compared to the existing systems.

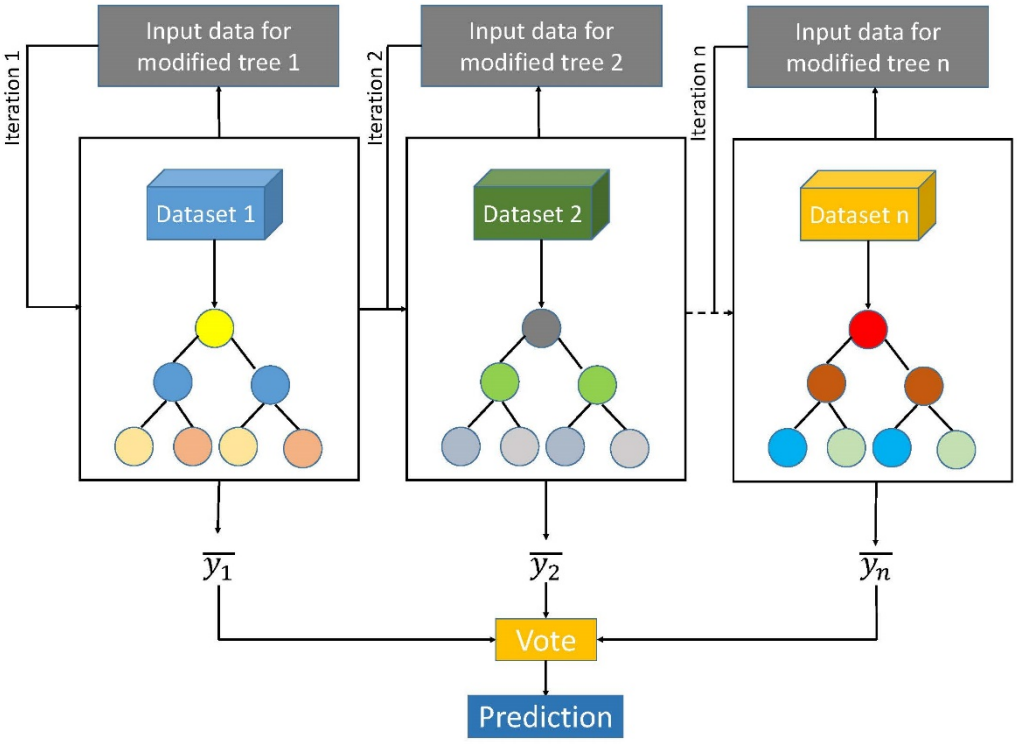

Fig. 2.2. Typical architecture of XGBoost

2.3.3. Overview of LightGBM

Light Gradient Boosting Machine, known as its acronym of LightGBM, is a powerful machine learning technology developed by Microsoft Research. This algorithm is built based on a decision-tree technique for solving regression,

classification and other machine learning-related issues [90]. LightGBM improves the computational efficiency to solve the prediction problem for big dataset more effectively. Traditional gradient boosting decision tree (GBDT) method adopted a presorting approach to precisely select and split indicators. However, such method requires time and memory. Compared to the above GBDT method, LightGBM uses a histogram-based algorithm and trees leaf-wise growth strategy to improve the training speed and decrease memory usage.

The histogram-based algorithm firstly discretizes the successive floating points into small bins. Afterwards, these bins are utilized to build the histogram with certain width. When the data is examined for the first time, the required statistics, herein referred to the sum of gradients and number of samples in one bin, are accumulated in the histogram. Such method can significantly save the computational storage and reduce the memory consumption. Fig. 2.3 illustrates the structure of histogram-based decision tree. The level-wise and leaf-wise growth strategies are displayed in Fig. 2.4. From the level-wise growth (Fig. 2.4a), it can be seen that on the same layer, the leaves are split at the same time. It is advantageous to optimize with plenty threads and maintain model complexity under control [90]. Additionally, the leaves on the same level have different information gain though, these leaves are handled extensively. The information acquisition indicates the projected decrease in entropy as the result of nodes separation based on attributes, which can be determined by the following equations [93, 94]:

$$\text{Gain}(S, A) \equiv \text{Entropy}(S) - \sum_{v \in \text{Values}(A)} \frac{|S_v|}{s} \text{Entropy}(S_v) \quad (2.7)$$

$$\text{Entropy}(S) \equiv \sum_{i=1}^{c} -p_i log_2 p_i \quad (2.8)$$

where Values(*A*) represents the set of all possible values for attribute *A*, S_v represents the subset of *S* for which attribute *A* has value *v*, pi indicates the proportion of *S* (*ith* class), and *c* is the number of classes.

Leaf-wise growth strategy solves the potential problems in extra memory consumption brought by searching and splitting the leaves with low information gain. Leaf-wise growth strategy only separate the leaf with the largest information acquisition on the same layer. However, using this strategy may lead to trees with high depth, or so called over-fitting, therefore, a maximum depth limitation is adopted within this process [90]. Fig. 2.4b displays the structure of leaf-wise growth strategy.

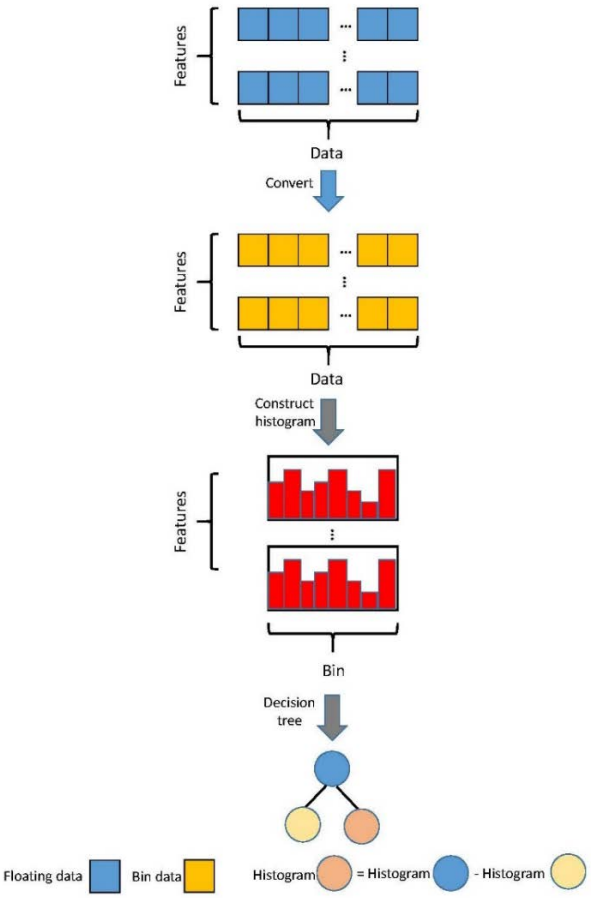

Fig. 2.3. Histogram-based decision tree.

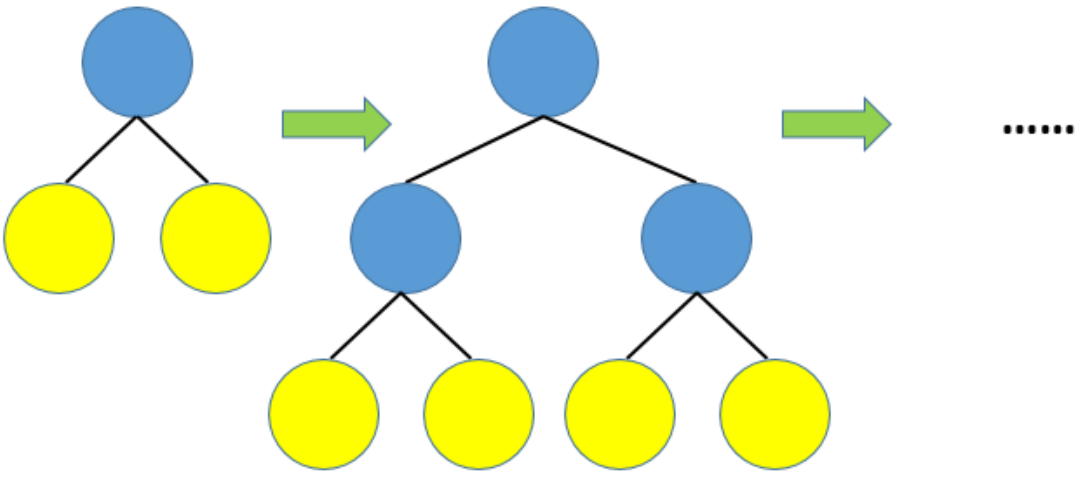

(a)

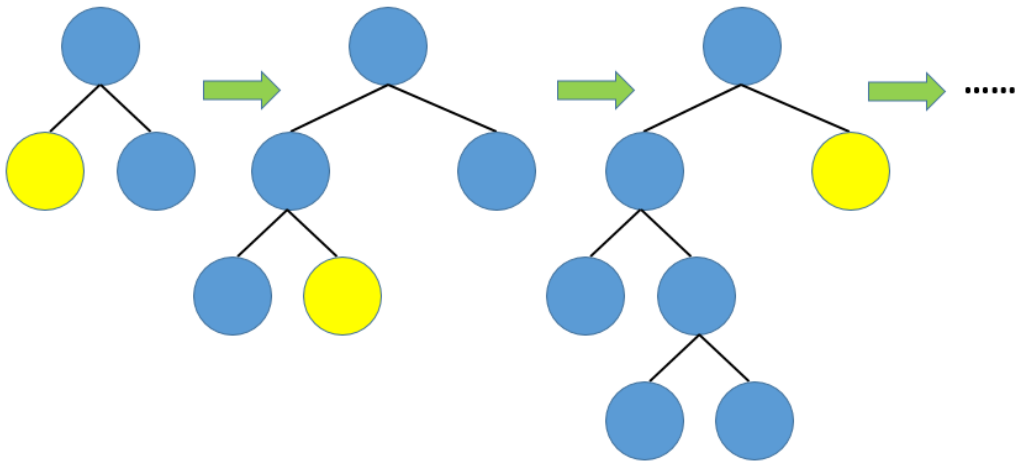

(b)

Fig. 2.4. Construction of decision tree for (a) level-wise growth strategy; and (b) leaf-wise growth strategy.

2.4. Life cycle assessment

Life cycle assessment (LCA) is one of the most common methods for evaluating the environmental impacts of new technologies from cradle to grave, in other words, from production to demolition [100, 101]. This methodology is based on the international standards of series ISO 14040 [102]. LCA could effectively assess the material efficiency of a system, point out the main pollution and present guidelines for improvement [103]. The production of AAM, especially the alkali activator, is involved with the consumption of high content of raw materials, energy and heat. AAM production becomes identical because of its unique alkali activation technology. Recycling the industrial waste and preparation of alkali activator result in a much more complex manufacturing process compared to the production of traditional cement-

based mixture. Utilization of industrial waste reduces the environmental burden brought by production of cement though, the main burden associated with the production of alkali activator cannot be neglected [51].

Robayo-Salazar et al. [16] conducted a comparative LCA for an alkali-activated binary concrete made with granulated blast furnace slag and natural volcanic pozzolan, focusing on the GWP (Global Warming Potential) and GTP (Global Temperature Change Potential). The experimental results showed that in comparison to a “normal strength” OPC-based concrete, alkali-activated binary concrete demonstrated a 44.7% lower GWP. Salas et al. [51] calculated the environmental impacts of geopolymer-based concrete, compared to a conventional concrete mix. They found that the production of sodium hydroxide was the most relevant process in all life cycle impact categories. Specifically, two major differences resulted in the different environmental burdens that were the source of sodium hydroxide (Ecuadorian vs. average European), and the type of sodium chloride used as raw material (obtained through seawater evaporation in Ecuador vs. solution and rock mining in Europe). At last, they suggested that an eco-friendlier geopolymer concrete should be manufactured under two conditions: sodium hydroxide is manufactured using locally sourced solar salt, and the electricity mix aligns with the anticipated energy composition for Ecuador in 2018. Matheu et al. [104] compared the environmental impacts of alkali-activated mortar and traditional OPC-based mortar, and reported that AAM had approximately 25% of the hydraulic mortar impact. Jiang et al. [12] evaluated the cradle-to-gate environmental impacts in terms of greenhouse gas emissions, energy use, water use, and potential environmental toxicity

of conventional, glass powder, and alkali-activated slag concrete and mortar with similar 28-day compressive strength of 35 MPa. The result showed that alkali-activated concrete demonstrated the lowest environmental impacts with 73% lower greenhouse gas emission, 43% less energy, and 25% less water, compared to the conventional concrete. However, a 72% higher ecotoxicity effect for alkali-activated slag concrete was reported due to the existence of alkali activator. The adverse effects of alkali activator hindering the sustainability of AAMs was also found by other researchers. Batuecas et al. [105] investigated the carbon footprint and water use of alkali-activated and hybrid slag and fly ash mortars. The carbon footprint of alkali-activated slag was 406.02 kg CO_2/m^3, while that of hybrid slag cement mortars and hybrid fly ash cement mortars were 253.26 kg CO_2/m^3 and 253.27 kg CO_2/m^3, respectively. This was caused by the high pollution water-glass adopted in AAM system, in which NaOH caused additional water use of 28.29 m^3/m^3 and carbon footprint of 23.74 kg CO_2/m^3, and Na_2SiO_3 caused additional water use of 28.41 m^3/m^3 and carbon footprint of 65.78 kg CO_2/m^3. Patrisia et al. [106] studied the LCA of alkali-activated concretes under marine exposure. Their report points out that alkaline activators and transportation of raw materials dominated the main environmental impact contributors to concrete production. Specifically, Na_2SiO_3 manufacture and transport contributed up to 44% and 35% to global warming potential, respectively, while up to 25% and 40% in the case of alkali activated slag. Such experimental results further indicated that the adoption of alkali activator may result in an even worse environmental impact.

Chapter 3: Machine learning-based model for predicting workability of AAMs

In this chapter, machine learning-based algorithm was used to construct the predictive model for workability of AAMs. There were 402 individual AAM mixtures obtained from 26 existing papers used for data analysis and modelling [58, 60, 61, 65, 66, 69-72, 111, 112, 123-137]. The chemical compositions of raw materials used in these researches were listed in Table 3.1.

3.1. Data collection and processing

Lacking generality is the major drawback lying in the existing models for predicting the fresh and hardened properties of AAMs. In fact, the abundant valuable results on the workability, compressive strength and drying shrinkage of AAM in the literature remain unutilized. Hence, using the existing data obtained from the literature, qualitative and quantitative analyses are recommended. The workflow of building the prediction model can be concluded as: (1) data collection, (2) data processing, (3) data analysis, and (4) model construction. The typical procedure was shown in Fig. 3.1. This workflow was as well used for constructing prediction models for strength and drying shrinkage, which would not be mentioned again in the following two chapters.

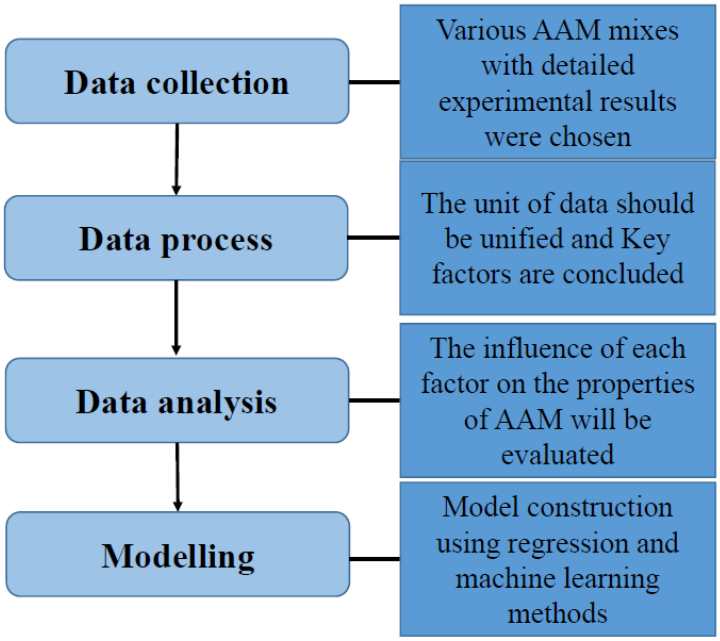

Fig. 3.1. Typical procedure for construction of prediction model

3.1.1. Data collection

First, a bibliometric search on the AAM paste, mortar and concrete was carried out to collect appropriate data in a wide horizon without biases. To minimize error brought by the individual experiments including different geopolymer paste and different testing items, a great number of papers were carefully reviewed and only the papers providing full information on the mixture design of each AAM component, detailed experimental procedure and mechanical results (i.e., flowability, strength, and shrinkage) were adopted. Moreover, to guarantee a high consistency, the type of alkaline activator was narrowed to the mix solution of sodium silicate and sodium hydroxide. It should be noted that due to the different prediction models, the data collection and key factor selection in the latter part were varied with different properties. Specifically, in flowability prediction model, curing conditions have no effect on the workability of

AAMs, while in strength and drying shrinkage prediction models, curing conditions significantly influence the results. Meantime, the experimental results on compressive strength mainly focused on the standard curing environmental (23 ± 3℃, RH = 99~%), while temperature and RH are the two highly-studied factors for drying shrinkage. In strict accordance with these requirements, a total of twenty-six papers for flowability (no curing conditions), twenty-three papers for compressive strength (similar curing conditions), and forty-three papers for drying shrinkage (different curing conditions) were identified and utilized for further analysis.

3.1.2. Data processing

Prior to processing the dataset, some assumptions should be made in advance. Considering the following data processing, specific density and specific surface area of raw materials were needed. However, some researches may not provide the density or specific gravity of each component, therefore, the assumed specific gravity and specific surface area of the studied component was listed in Tables 3.2 and 3.3 [31, 32]. For high consistency, all mixtures were converted into mass-based mix proportions. The unit of each composition will be unified as the mass ratio (no unit). The key factors included reactivity of precursors, sodium hydroxide concentration, silicate modulus, geopolymer paste content, liquid-to-binder ratio, fine aggregate content, coarse aggregate content, and curing conditions. As aforementioned, different properties determined different key factor selections. Table 3.4 listed out the summary of key factors selection for prediction models of flowability. For representing the reactivity of precursors, activity moduli and

specific surface area were chosen. The activity moduli of the binder herein refer to the calculated values based on the chemical compositions and mass content of the SCMs, shown as the following two equations:

$$\text{For GGBFS: Reactivity} = (CaO + MgO + Al_2O_3)/SiO_2 \quad (3.1)$$

$$\text{For non-GGBFS: Reactivity} = SiO_2/Al_2O_3 \quad (3.2)$$

where CaO, MgO, Al_2O_3 and SiO_2 refer to the chemical composition proportion (%) multiplying mass content (kg) [107].

Eq. 3.1 is always used for evaluating the reactivity or hydration modulus of GGBFS, which can assess the balance between fluxing agents (CaO and MgO) and pozzolanic/reactive components (SiO_2 and Al_2O_3) in GGBFS [108]. For other type of SCMs, alumina and silica are two fundamental components. The SiO_2/Al_2O_3 ratio indicates the relative abundance of these two elements, determining setting time and strength development of geopolymer systems [109]. The collected chemical compositions of raw materials used in different researchers were respectively listed in relevant chapters. Because of multiple experimental results in one research, several papers were re-used in different chapters. It should be noted that the reactivity of raw materials is not only affected by the chemical compositions. Other parameters can also have some impact on the reactivity though, these parameters may have difficult acquisition (e.g., molecular structure) or be less significant (e.g., size particle). Although empirical, it provides a rapid index for researchers to estimate the binder

reactivity. Specific surface area (SSA) is the best factor to simultaneously represent these physical properties of precursors, which is directly related to adsorption, heterogeneous catalysis, and reactions on surfaces [110]. The calculation of specific surface area of the binders was based on the specific surface area and mass proportion of each type precursor. Note that the calculated specific surface area of binary/trinary binder may not be equal to the exact value, but could provide a quick index for estimation. Geopolymer paste content (GPC) referred to summed mass ratio of precursor and alkali activator. Liquid-to-binder (L/B) ratio was the value of alkali activator content divided by binder content. The properties of alkali activator were concluded into the sodium hydroxide concentration and silicate modulus (Ms = SiO_2/Na_2O). Aggregate is always underestimated or even neglected in the manufacturing of AAMs. Such natural rigid restraint could remarkably enhance the volume-stability of matrix. For distinguishing the paste, mortar and concrete, the aggregate content were separated into fine aggregate and coarse aggregate contents.

Besides the data processing on the input data, a major challenge lied in the selection and expression of workability, compressive strength and drying shrinkage results. This challenge is mainly caused by two reasons. First, there is no universal testing standard, which is varied in different countries. Second, even for the same properties, there exist different testing items (i.e., workability can be evaluated by flowability, slump, slump-flow, etc.). Therefore, it is of necessity to determine a unified result expression for each property of AAMs. Unlike compressive strength or shrinkage results having their own units (MPa and με) and uniform testing standards, workability can be reflected by

various testing results such as slump flow, flowability, flow consistency and etc., which made a difficulty for the data searching and analyzing. Moreover, another problem was brought by the different measurement methods for workability, mainly due to the testing molds and AAM types. Furthermore, the testing operation can be differed by the mixture types, in which the paste samples normally are not needed for tampering by jolting flow table, while mortar and concrete samples are tampered for 15~25 times to make them flow. The experimental workability results have different expressions including the exact average diameter of patty (unit: mm), the increase ratio of patty compared to the mold (unit: %), and relative slump (calculated by $(d/d_0)^2$-1 where d is the average of the measured diameter of patty, and d_0 is the bottom diameter of mold, no unit) [66, 111, 112]. To overcome these problems, some prerequisites should be made here for high consistency. First, the flowability, or called spread flow diameter, was chosen to be used for workability evaluation; Second, only the initial and ceased flow was chosen regardless of tampering or not; Third, all flowability results were expressed as the diameter increment ratio compared to the bottom diameter of mold calculated by following equation.

$$\text{Flowability} = \frac{d-d_0}{d_0} \times 100\% \quad (3.3)$$

According to the abovementioned method, the processed mix design key factors and the flowability results were listed in Supplementary Table 1.

Table 3.1. Chemical compositions of raw materials (Ref. [58, 60, 61, 65, 66, 69-72, 111, 112, 123-137]).

Reference	Precursor type	SiO_2	CaO	Al_2O_3	Fe_2O_3	SO_3	K_2O	MgO	Na_2O	LOI
Yang et al., 2009	GGBFS	34.7	44.6	13.8	0.11	0.95	0.48	4.38	-	0.24
	FA F	57.7	4.7	28.6	5.08	0.68	0.57	0.67	0.37	0.1
Yang et al., 2009	GGBFS 1	34.7	44.6	13.8	0.11	0.95	0.48	4.38	-	0.24
	GGBFS 2	33.8	45.6	12.9	0.03	0.69	0.42	4.7	-	0.36
	GGBFS 3	33.1	46.3	13.6	0.11	1.1	0.57	3.86	-	0.34
	FA F	57.7	4.7	28.6	5.08	0.68	0.57	0.67	0.37	0.1
Pacheco-Torgal et al., 2011	MK	50.75	-	43.48	2.45	-	-	0.11	0.04	-
Jang et al., 2014	GGBFS	21	56.1	17	0.62	0.77	0.6	0	-	-
	FA F	46	2.6	33	10.5	-	4.8	-	-	-
Nath & Sarker, 2014	GGBFS	32.46	43.1	14.3	0.61	4.58	0.33	3.94	0.24	-
	FA F	50	1.79	28.25	13.5	0.38	0.46	0.89	0.32	0.64
Nematollahi & Sanjayan, 2014	FA F	48.8	6.2	27	10.2	0.22	0.85	1.4	0.37	1.7
Gao et al., 2015	GGBFS	34.4	37.4	13.3	0.47	1.23	0.47	9.89	0.34	1.65
	FA F	54.6	4.44	24.4	7.2	0.46	1.75	1.43	0.73	2.8
Gao et al., 2015	GGBFS	34.44	37.42	13.31	0.47	1.23	0.47	9.89	0.34	1.65
	FA F	54.62	4.44	24.42	7.21	0.46	1.75	1.43	0.73	2.8

Jafari Nadoushan & Ramezanianpour, 2016	GGBFS	37.21	36.75	11.56	1.01	0.97	0.7	8.52	0.61	0.02
Gao et al., 2016	GGBFS	34.44	37.42	13.31	0.47	1.23	0.47	9.89	0.34	1.65
	FA F	54.62	4.44	24.42	7.21	0.46	1.75	1.43	0.73	2.8
Nedeljković et al., 2018	GGBFS	35.5	39.8	13.5	0.64	-	0.53	8	0.4	-1.3
	FA F	56.8	4.8	23.8	7.2	-	1.6	1.5	0.8	1.2
Fang et al., 2018	GGBFS	36.77	37.6	13.56	0.41	1.82	0.55	7.45	0.25	-
	FA F	53.24	3.65	26.42	1.65	0.56	2.57	9.55	0.76	-
Najimi et al., 2018	GGBFS	31	43.64	11.5	0.8	4.85	0.84	4.7	-	-
	NP	71	2.3	7.9	0.7	0.1	4.3	-	3.2	-
Ramezanianpour & Moeini, 2018	GGBFS	37.21	36.75	11.56	1.01	0.97	0.7	8.52	0.61	0.02
	SF	88.5	1.5	1.4	2.1	-	0.75	2	-	3
Ibrahim et al., 2018	NP	40.48	11.83	12.9	17.62	-	1.67	8.33	3.6	1.6
Yousefi Oderji et al., 2019	GGBFS	35.4	41.9	12.4	0.424	-	0.261	5.91	0.275	-
	FA F	49.4	6.84	22.5	4.89	-	1.26	0.955	0.575	-
	GGBFS	35.9	39.8	10.08	0.51	2.601	0.369	10.75	0.335	-

Alanazi et al., 2019	FA F	56.52	8.53	22.75	4.56	0.4	1.16	2.64	0.69	0.35
	SF	94.49	0.5	0.07	0.1	0.11	0.54	0.62	0.09	3.21
	MK	55.01	0.14	40.94	0.55	0	0.6	0.34	0.09	1.54
Alrefaei et al., 2019	GGBFS	18.9	66.9	6.43	0.74	1.97	0.67	1.41	-	0.25
	FA F	44.4	6.67	32.6	6.49	2.27	1.81	1.86	-	3.76
Song et al., 2020	GGBFS	26.22	39.23	15.01	0.4	2.27	0.47	11.69	0.43	1.42
	FA C	39.57	18.45	25.49	5	2.57	1.36	2.23	0.59	2.23
Shah et al., 2020	GGBFS	35.4	41.9	12.4	0.424	1.74	0.261	5.91	0.275	-
	FA F	49.4	6.84	22.5	4.89	1.44	1.26	0.955	0.575	-
Shah et al., 2020	GGBFS	35.4	41.9	12.4	0.424	1.74	0.261	5.91	0.275	-
	FA F	49.4	6.84	22.5	4.89	1.44	1.26	0.955	0.575	-
Alrefaei et al., 2021	GGBFS	31.5	39.2	16.3	0.24	2.5	0.4	8.8	-	-0.6
	FA F	47.8	6.2	33.3	6	1.1	1.1	1.8	-	5.6
Paul, 2022	GGBFS	38.19	35.34	12.42	1.92	-	0.28	8.67	0.9	1.02
	FA F	58.43	-	34.52	34.52	0.25	-	0.63	1.28	0.86
Deng et al., 2022	GGBFS	35.1	38.23	14.01	6.49	-	0.07	5.66	0.1	0.49
	FA F	61.54	5.2	26.98	0.42	-	0.15	2.35	0.2	2.88
Dheyaaldin et al., 2022	GGBFS	28.17	47.75	8.6	0.42	1.45	0.29	3.89	0.02	0.2
	FA F	48.43	15.48	17.15	11.96	0.82	0.41	1.35	0.0019	1.47
	GGBFS	34.48	42.43	11.48	-	2.17	0.66	7.08	0.56	-

Tekle & Holschemacher, 2022	FA F	49.79	4.34	26.71	8.57	1.49	3.36	2.47	1.28	-
	SF	93.81	0.3	0.48	1.49	0.2	0.77	0.46	0.42	-
	MK	53.6	2.9	29.2	0.4	0.1	1.8	0.4	9.7	-

Note: LOI = Loss of ignition.

Table 3.2. Specific densities of materials

Material*	GGBFS	FA C	FA F	SF	MK	NP	NS	NA	SS	SH	Water	SP	Limestone	WGP	Fine agg.	Coarse agg.	Basalt fiber	PP fiber	PVA fiber	Steel fiber
Assumed specific density	2.89	2.52	2.52	2.20	2.60	2.33	2.40	3.90	1.39	1.43	1.00	1.07	2.71	2.42	2.48	2.60	2.80	0.91	1.30	7.80

Note*: GGBFS = ground granulated blast-furnace slag; FA C = fly ash class C; FA F = fly ash class F; SF = silica fume; MK = metakaolin; NP = natural pozzolan; NS = nano-silica; NA = nano-alumina; SS = Na_2SiO_3; SH = NaOH; SP = superplasticizer; WGP = waste glass powder; agg. = aggregate.

Table 3.3. Specific surface area of precursors

Material	GGBFS	FA C	FA F	SF	MK	NP
Assumed specific surface area/m^2/kg	425	420	420	20000	2140	442

Table 3.4. Key factor selections for prediction models

Properties	Activity moduli	Specific surface area	Geopolymer paste content	Liquid-to-binder ratio	NaOH concentration	Silicate modulus	Fine agg. content	Coarse agg. content	Temperature	RH	V/S ratio
Flowability	√	√	√	√	√	√	√	√	×	×	×

Note: √ represents that this factor was selected as the key factor; × represents that this factor was not considered; and Unified represents that this factor was considered though, it has been controlled as the similar value. This notation was the same for the following chapters.

3.2. Data analysis and discussions

To evaluate the effects of key factors on the workability of AAM mixtures, the experimental flowability results were plotted against each key factor. Moreover, according to UNE-EN 1015-6: 1999, a spread flow diameter smaller than 140 mm is deemed as a dry consistency; diameter of 140 mm to 200 mm is deemed as plastic consistency and diameter larger than 200 mm is deemed as fluid consistency [56]. When converted into the increment ratio, these boundaries were < 40%, 40~100% and > 100%, which were also plotted in the figures to provide consistency information on each mix design.

3.2.1. Effect of activity moduli of precursor on workability

Figs. 3.2 (a) and (b) show the effect of activity moduli of precursor on the workability of AAM mixtures. Due to the wide range of activity moduli of precursors, a supplementary figure amplifying the range between 0 to 20 was depicted in Fig. 3.2 (b). Generally, no clear trend between the workability and the moduli activity could be observed in Fig. 3.2 (a), while in Fig. 3.2 (b), a slightly decreasing trend on workability with higher reactivity of binder could be found. It can be directly seen that the reactivity of precursors were varied a lot from 0.58 to approximately 140, assigned to the different types of raw materials. Basically, GGBFS and FA were selected as the precursors with the activity moduli lower than 4. The highest flowability results of 314% were obtained by Nedeljković et al. [70]. They investigated the influence of slag content on the alkali-

activated GGBFS/FA (AAS-FA) paste and reported a significant reduction in slump-flow and setting time but an increase in compressive strength for GGBFS-rich pastes. Jang et al. [71] manufactured the AAS-FA mixtures and also found a decreasing workability but increasing strength with slag content. Ramezanianpour and Moeini [129] reported a decreasing mean workability value from 116.3% to 77.5% when activity moduli increased from 1.45 to 12.22. Gao et al. [126] found that workability value decreased from 220% to 67% when moduli increased from the 1.90 to 10.34. The reduction in the workability of AAMs with higher content of slag may be contributed to the rough surface texture and rapid reaction due to the high CaO content of GGBFS [60]. In comparison to GGBFS, FA demonstrated a much lower reactivity which may extend the setting time but impair the mechanical properties.

Apart from the GGBFS and FA, some researchers added high pozzolanic reactivity materials like SF and nano-silica in the binders. Alanazi et al. [60] mixed SF in the AAFA mixtures and reported a decreasing flow value with higher content of SF. Dheyaaldin et al. [136] produced the fiber-reinforced alkali-activated mortar with the addition of nano-silica, which reduced the flow rate of AAS mortar and had the fairly low average flow value of 73.3%. Similarly, [129], [61] and [126] introduced the nano-silica into the blends, and most of these experimental results located in the plastic consistency zone, revealing a harmful effect of nano-silica, which was caused by the high surface area and smaller particle sizes of SF and nano-silica. However, it should be noted that Tekle and Holschemacher [137] also added certain amount of SF in the alkali-activated concrete but acquired a quite high flowability with the average value of

169%. It may be because that the filler effect of SF improved the wet packing density of AAM mixtures and reduced the required water lubricating the solid-water mixture [138, 139].

3.2.2. Effect of specific surface area on workability

Fig. 3.3 displays the effect of specific surface area of the binder system on workability. A pronounced decreasing trend between specific surface area and flowability could be seen. GGBFS-FA binder system had a specific surface area of approximately 500 m^2/kg. With the introduction of MK, SF and nano-particles, the specific surface area of the binder system increased. When the specific surface area is larger than 2000 m^2/kg, almost all data points located in the plastic and dry consistency zone. In this area, the exact data amount in the fluid, plastic and dry zones took account for 27%, 43% and 30%, respectively. Yang and Song [123] used three types of GGBFS with the specific surface area of 420.4, 615.0, and 816.7 m^2/kg to produce AAS mortar and found a flow loss with higher amount of 816.7 m^2/kg GGBFS. The data from Ramezanianpour and Moeini [129] showed that the flowability values decreased with higher amount of SF and nano-silica. Pacheco-Torgal et al. [66] obtained a fairly low mean flow values of 19.5% for AAMK mixtures with a relatively high specific surface area. The effect of specific surface area on the workability of AAM could be attributed to its water demand. It is composed of a water layer around the particles and the extra water to be filled into the intergranular voids of the powder system. Compared to the sand and aggregates, powders by far accounts for the biggest part of the total specific

surface area, indicating that powders have the strongest influence on the total water demand of a mix [140]. Therefore, the higher specific surface area of the binder, the higher water demand is needed for reaching the satisfied workability. Particularly, nano-silica with extremely high SiO_2 content and enormous specific surface area exhibits enhanced pozzolanic reactivity [141].

3.2.3. Effect of alkali activator on workability

Ms and NaOH concentration are the two parameters for adjusting alkali activator. The effect of these two key factors on the workability of AAMs were respectively reflected in Figs. 3.4 and 3.5. From Fig. 3.5, a non-pronounced increasing tendency on workability with Ms could be found. Jafari Nadoushan and Ramezanianpour [65] researched the influence of type and concentration of activators on the performance of alkali-activated natural pozzolan-GGBFS (AAS-NP) mixtures and found that when Ms increased from 0.00 to 0.79, the flowability increased from 40% to 140%. Meantime, comparing the individual results from Pacheco-Torgal et al. [66] and Alanazi et al. [60], the average flowability increased from 19.5% to 112.6% when Ms increased from 0.28 to 0.61. Additionally, the highest workability was obtained at a fairly high Ms value of 1.45 [70]. However, it should be noted that there were some odd points showing a quite low workability with high Ms. For instance, according to Paul's experimental results, all fresh geopolymer mortar samples displayed plastic consistency [135]. Although Alrefaei et al. (2019) reported a quite high flow value of 200% at Ms of 2.94, a remarkable reduction in flowability could be observed with higher Ms value. The

mechanism behind it was attributed to the soluble Si in Na_2SiO_3 solution promoting the dissolution of precursors, e.g., slag, and the generation of hydrates, resulting in the tendency that workability first increased then decreased with Ms [142]. The dissolution effect was brought by the soluble Si in activator and weakened the passivation adsorption layer of Ca, Mg and Al on the surface of slag [142].

Fig. 3.5 displays the effect of NaOH concentration on the workability performance of AAMs. Apparently, the influence of NaOH concentration could be separated by the boundary of 4 M, within which the workability results varied a lot and beyond which the pronounced decreasing trend could be investigated. The highest workability value (314.2%) was obtained by Nedeljković et al. [70] at the concentration of 4 M. When the concentration was low, the lowest flow results of 0% were obtained by Yang et al. [124] at the concentrations of 0, 0.67, and 1.50 M. Also, this research team conducted workability evaluation for AAS mortars with NaOH concentration of 1 M and got a relatively flow value demonstrating plastic consistency with low average flow value of 74% [123]. Although a quite satisfied workability of 200% could be achieved at low concentration, when take a close look into these data, it could be found that Alrefaei et al. (2021) [69] mixed the AAM mixes with the addition of SP compensating the workability loss. When the concentration was above 4 M, the decreasing trend could be clearly observed from the figure. The average workability values are 118.58%, 107.87% and 20.54% at the sodium hydroxide concentration of 4, 10 and 16 M, respectively. The appropriate NaOH concentration would promote the hydroxide ion concentration and accelerate the dissolution of raw materials, especially for the case

that only NaOH solution was used as activator, which may increase the flowability [143]. However, when the concentration was above a certain boundary, the reduction in workability would be caused by the low water contents in high concentration solution that was not sufficient to wet the particles [144].

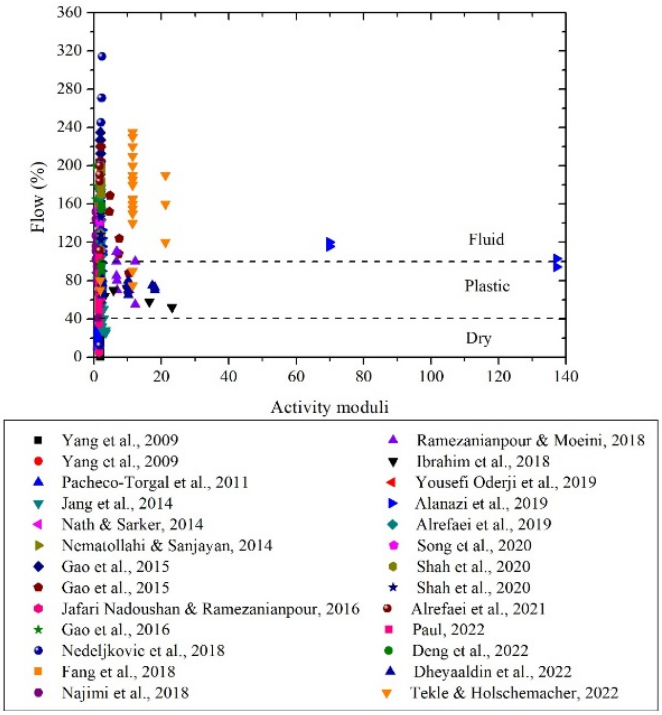

(a)

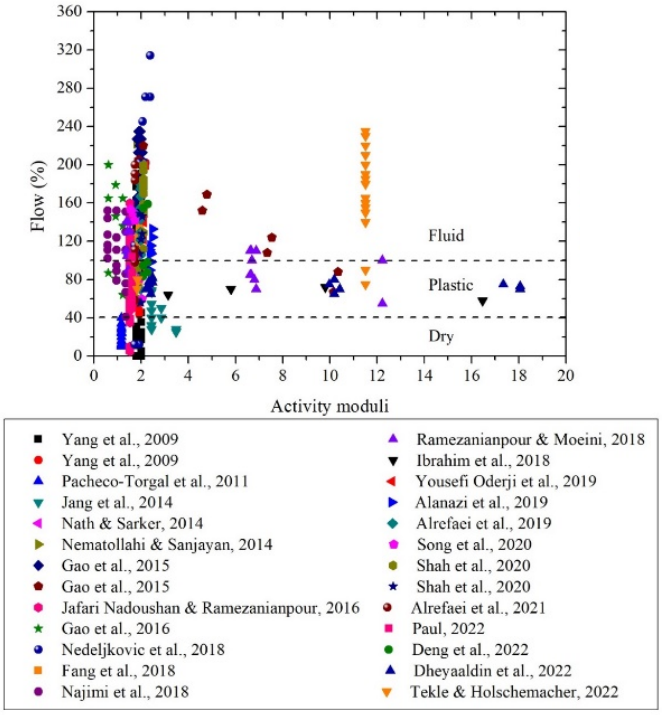

(b)

Fig. 3.2. Effect of reactivity of precursor (a) ranging from 0 to 140; and (b) ranging from 0 to 20 on workability

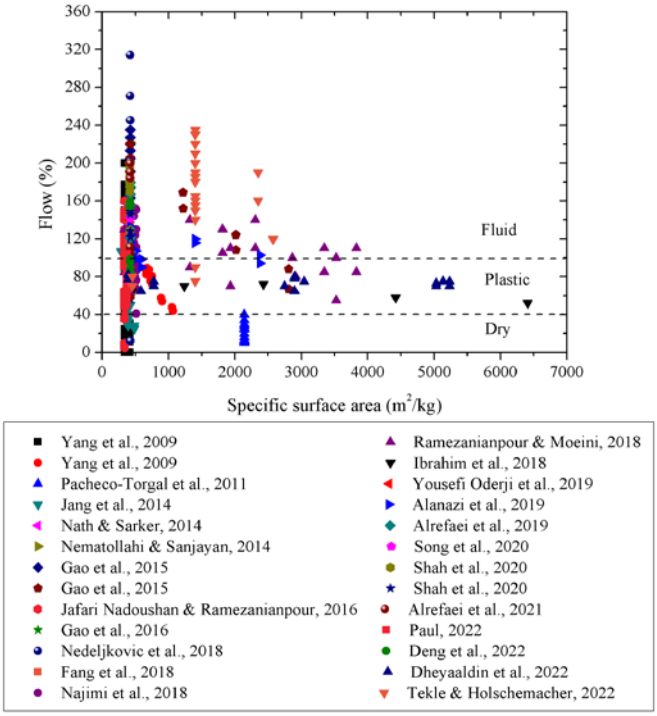

Fig. 3.3. Effect of specific surface area of precursor on workability

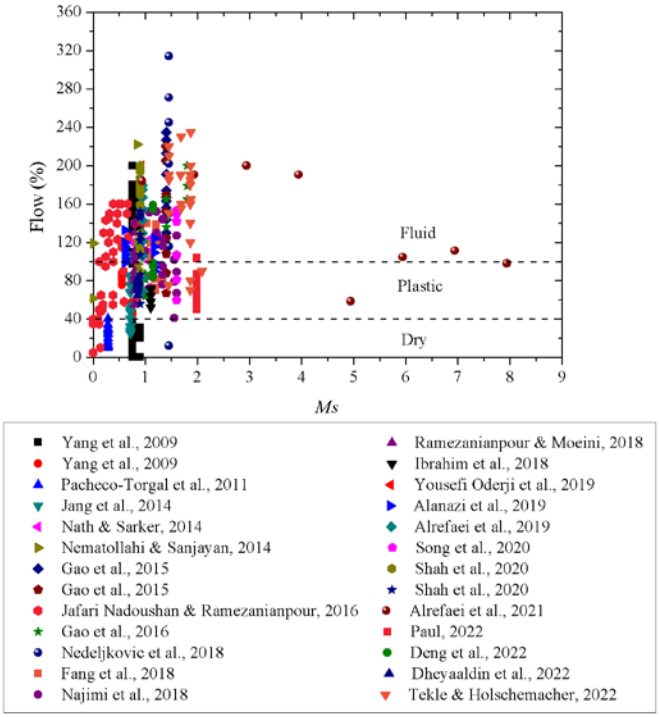

Fig. 3.4. Effect of Ms on workability

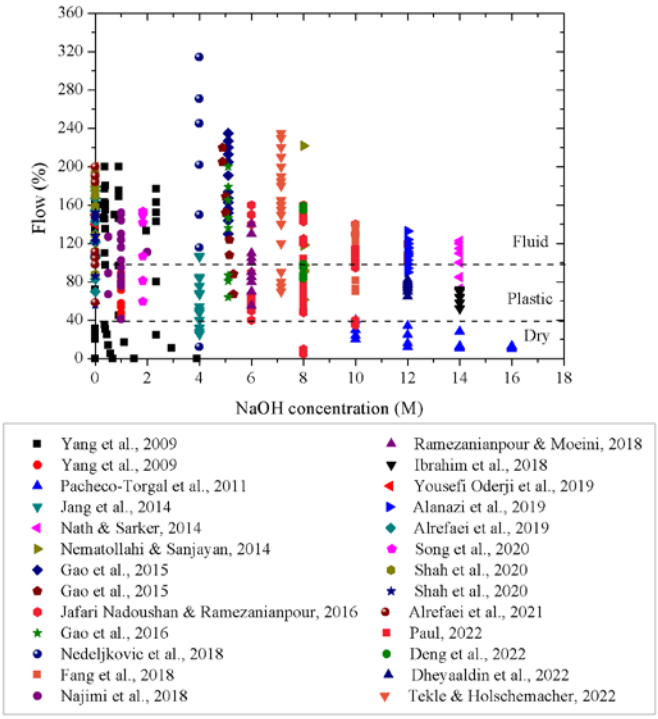

Fig. 3.5. Effect of NaOH concentration on workability

3.2.4. Effect of liquid-to-binder ratio on workability

Fig. 3.6 illustrates the effect of L/B ratio on workability of AAM mixtures. It should be noted that the liquid here refers to all liquid content including alkaline solutions, and water content in SP and nano materials. A clear trend between L/B ratio and flowability was hardly found, which may be assigned to the synergetic effects brought by the liquid content and binder system. Nevertheless, some regulations still could be seen from these data points. First, an increasing trend for workability with L/B ratio has been identified by Yang et al. [124], Gao et al. [58], Ramezanianpour and Moeini [129], and Tekle and Holschemacher [137]. Moreover, the flow results of [70] decreased from 271% to 12% when L/B ratio increased though, the workability was largely improved when liquid-to-binder mass ratio increased from 0.4 to 0.5. Higher L/B ratio could provide more water content for lubricating the solid particles resulting in the higher workability, which was consistent with the OPC-based materials. On the other hand, due to the complicated compositions in liquid part, some experimental results display a decreasing trend. For example, [123] got a decreasing flow values from 87.5% to 57.5% when L/B ratio increased. Therefore, the potential synergetic effects of other key factors may be taken into consideration as well.

3.2.5. Effect of geopolymer paste content and aggregate content on workability

Fig. 3.7 demonstrates the effect of GPC on the flow values of AAM mixtures. Note that GPC is deemed as the paste part of AAM mixtures though, it was not directly

calculated by 1 minus aggregate ratio due to the possible existence of inter-particle fillers and fibers. From the figure, an obvious increasing tendency could be observed. A rapid increasing workability with GPC was reported by Yang et al. [124] (flow values increased from 30% to 200% with GPC increasing) and Fang et al. [127] (flow values increased from 69.7% to 138.7% with GPC increasing). Similarly, the flow results of Tekle and Holschemacher [137] revealed a steady growing trend of flowability from the lowest value to the highest value with higher GPC. There are three major functions for geopolymer paste that are (i) filling the voids between aggregate particles; (ii) forming paste films coating the aggregate to lubricate the particles; and (iii) pushing the coarse aggregate particles apart for reduction of particle interlocking [75]. From the above, it could be known that in order to achieve a required flowability, certain amount of GPC is needed. But, it should also be mentioned that the absence of aggregate in AAM mix is not recommended since the dimensional stability is spoiled and high environmental impacts are generated due to the production of alkali activators [31, 32, 75, 138]. Interestingly, Gao et al.'s experimental results showed a significant decline in workability with GPC [58]. Such reduction may be attributed to the inter fillers that was limestone used in their mix design. These fillers helped fill in the voids between solid particles so as to reduce the excess paste on forming paste filming coating the aggregates improving the wet packing density and workability [75].

Fig. 3.8 shows a totally opposite effect of aggregate volumetric ratio on workability in comparison to the GPC. As aforementioned, higher aggregate content caused higher viscosity, hindered dispersion, more voids to be filled in, and more solid particles

needed wet, which directly resulted in the workability loss [75]. Specifically, Yang et al. [124] reported a decreasing workability value decreased from 200% to 0% with increasing aggregate ratio from 0 to 0.70. Thus, an optimum mix design to balance the workability and volume stability is of significance. It should be noted that although this part discussed the effect of aggregate on the workability of AAMs, the input key factor for aggregate was separated into fine and coarse aggregates in the latter model construction for distinguishing paste, mortar and concrete. This analysis and discussion was same for the Chapters 5 and 6.

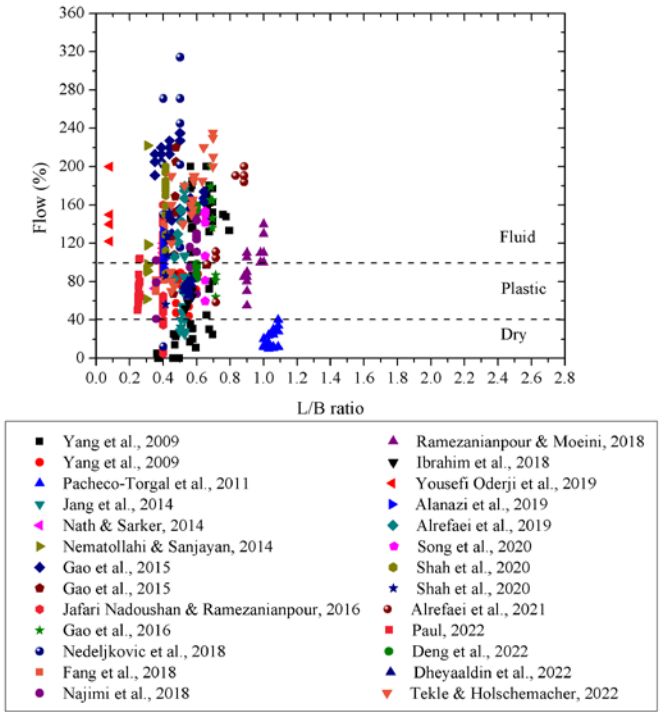

Fig. 3.6. Effect of L/B ratio on workability

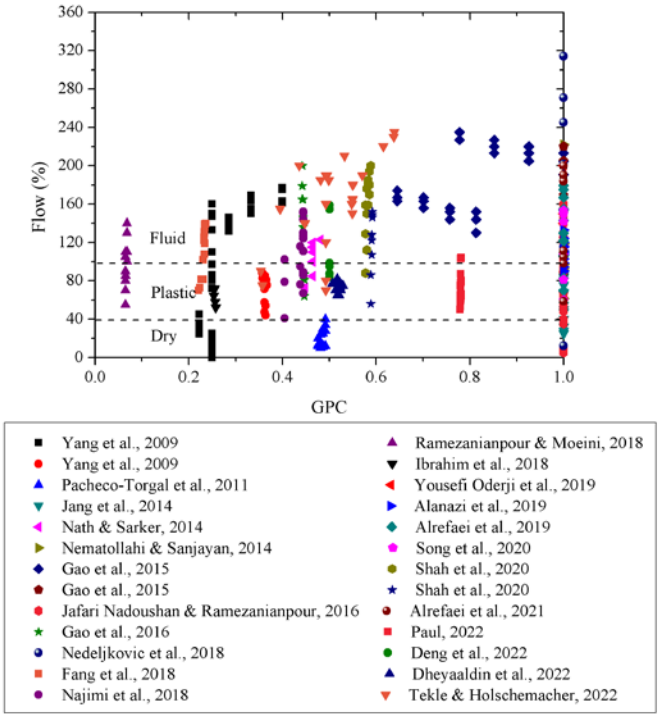

Fig. 3.7. Effect of GPC on workability

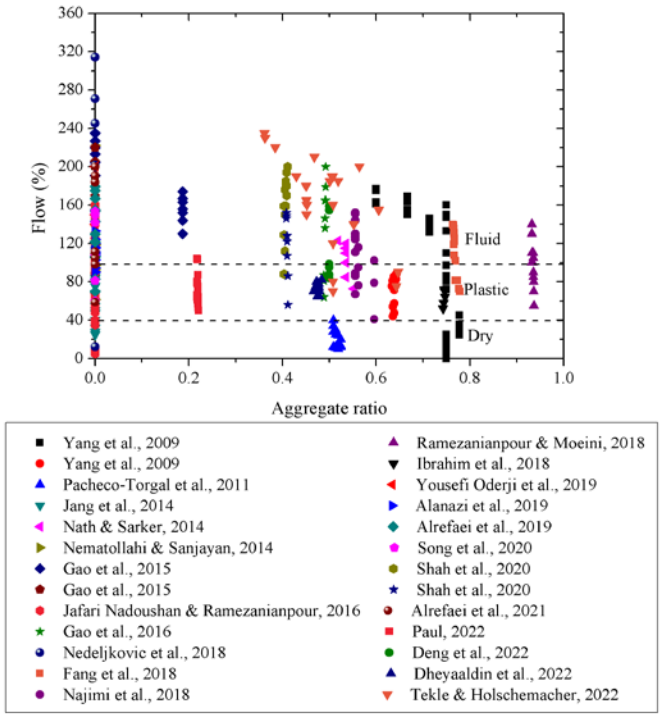

Fig. 3.8. Effect of aggregate content on workability

3.3. Machine learning modelling and discussions

The influence of each individual key factor governing the flowability of AAM mixtures has been qualitatively discussed in the previous section. Further quantitative studies should be conducted by constructing a prediction model for workability to guide and optimize the mix design of various AAMs. In this sense, an ANN model using a BPNN was proposed. The obtained 403 AAM mixtures from literature were all used for the BPNN model construction. The aforementioned key factors of AAM were set as input data that could be easily obtained in predicting workability performance.

3.3.1. BPNN architecture

In this study, the MATLAB R2021b program was used for network construction and training. The general introduction and basic information on the BPNN are illustrated in the previous section. The proposed BPNN architecture developed in this study is shown in Fig. 3.9. Data normalization was conducted prior to training. The input and output data were normalized from 0 to 1 to eliminate over-fitting of the trained network shown as Eq. 3.4 [35].

$$X_{normal} = \frac{X - X_{min}}{X_{max} - X_{min}} \quad (3.4)$$

where X_{normal} indicates the normalized parameter, X indicates the actual parameter, X_{max} represents the maximum value of the scaling range, and X_{min} represents the minimum value of the scaling range.

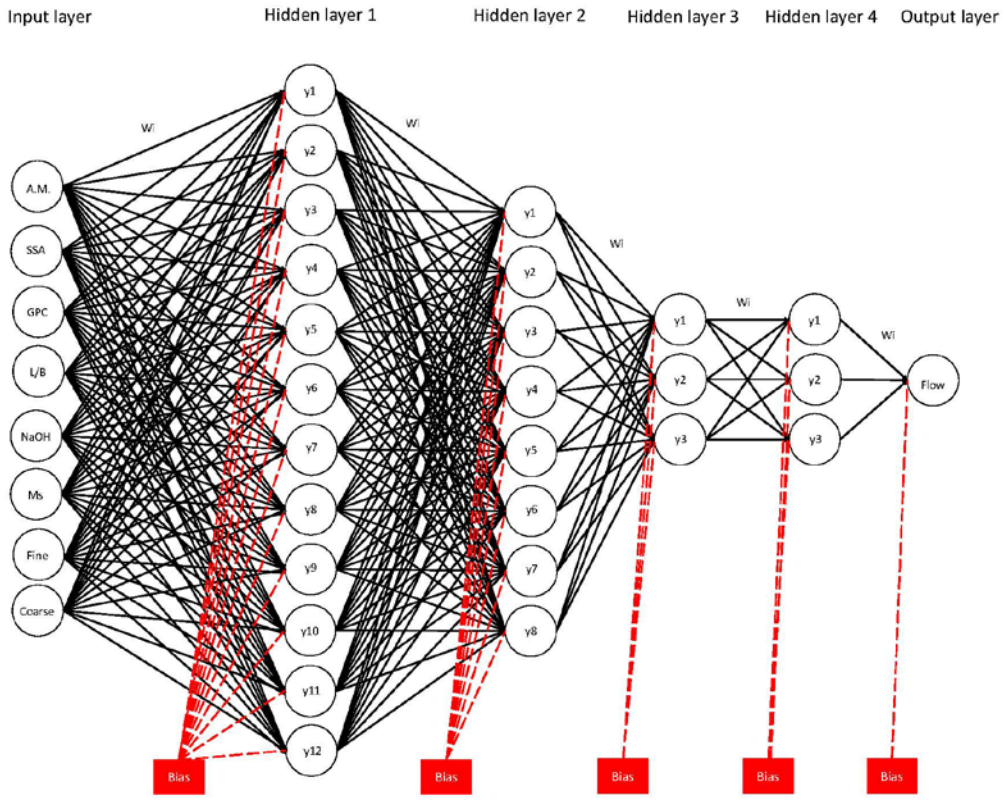

Fig. 3.9. Structure of the proposed BPNN model for workability.

The entire network consisted of one input layer, four hidden layers, and one output layer. The input and output layers have been introduced, previously. To determine the number of neurons in the hidden layers, it was empirically suggested to set more neurons in the first hidden layer and set fewer neurons in the following hidden layers than in the input layer. However, too many neurons in the layer is computational-consuming. Therefore, twelve neurons in the first hidden layer, eight neurons in the second layer, three neurons in the third layer and three neurons in the fourth layer was

quite good for this condition. In addition, different BPNN models with various hidden layer designs were constructed and trained to select the optimum one by comparing the performance indicators, including the mean absolute error (MAE), root mean squared error (RMSE), and R^2 statistics. MAE measures the errors between predictions and the obtained experimental results, RMSE evaluates the accuracy, and R^2 statistics investigate the data fitting between the predicted and obtained experimental results. These three indicators were calculated using following equations:

$$\mathrm{MAE} = \frac{1}{n}\sum_{i=1}^{n}\left|O_{i\ test} - O_{i\ pre}\right| \tag{3.5}$$

$$\mathrm{RMSE} = \sqrt{\frac{\sum_{i=1}^{n}(O_{i\ test}-O_{i\ pre})^2}{n}} \tag{3.6}$$

$$R^2 = 1 - \frac{\sum_{i=1}^{n}(O_{i\ test}-O_{i\ pre})^2}{\sum_{i=1}^{n}(O_{i\ pre})^2} \tag{3.7}$$

where Oi test indicates the target value, Oi pre indicates the model's output value, and n is the total number of observations.

The BPNN architecture was determined based on this process, and actually, it was quite a time-consuming task. After several trails, the properties of the determined BPNN model with the best performance are listed in Table 3.5. For simplification, this model construction method and performance evaluation in the following chapters were the same as the ones in this chapter, which was not mentioned again.

Table 3.5. Properties of BPNN model for workability

Details	Selection

Network architecture	Backpropagation network
Number of input layer	1
Number of hidden layer	4
Number of output layer	1
Number of neurons in input layer	8
Number of neurons in hidden layer 1	12
Number of neurons in hidden layer 2	8
Number of neurons in hidden layer 3	3
Number of neurons in hidden layer 4	3
Number of neurons in output layer	1
Activation function	Tan-sig
Learning rate	0.00001
Moment rate	0.95
Training algorithm	Trained (gradient descent with momentum)

3.3.2. LightGBM architecture

The hyperparameter setting is of essence to the final model performance. For LightGBM (LGBM), there are four major hyperparameters influencing the model performance, including number of trees (n_estimators), shrinkage coefficient of each tree (learning_rate), maximum depth of a tree (max_depth), and number of leaves for each tree (num_leaves) [84]. Empirically, it is recommended to use a relatively large max-bin, small learning rate with large iteration numbers, and large leaves numbers for

regression model construction. Moreover, due to the leaf-wise algorithm of LGBM, when adjusting the complexity of the tree, we used the number of leaves rather than the maximum depth, and an empirical equation between these two parameters is num_leaves = $2^{(max\_depth)}$. However, in the exact model, number of leaves should be smaller than the value of $2^{(max\_depth)}$ to avoid over-fitting. Accordingly, the hyperparameters of the proposed LGBM model was listed in Table 3.6.

Table 3.6. Parameters of the proposed LGBM regression model

Hyperparameter	Selection
boosting_type	GBDT
objective	Regression
learning_rate	0.06
max_depth	4
n_estimators	783
num_leaves	14
min_child_samples	8

3.3.3. XGBoost architecture

As an effective algorithm combining gradient boosting machine and cause based decision tree, XGBoost is able to enhance the tree boosting approach for processing nearly all data types quickly and accurately [36]. By virtue of this ability, XGBoost is often used for building predicting models when regression and classification are

conducted for the database. Regarding the architecture building procedure, XGBoost is quite similar to the LGBM due to the same tree-based gradient boosting frameworks. However, there still are some differences between these two algorithms, which has been illustrated in the previous chapter. The hyperparameter tuning was quite a time-consuming task, which was similar to the LGBM. Finally, the structure of the best performance XGBoost-based model was provided in Table 3.7.

Table 3.7. Parameters of the proposed XGBoost regression model

Hyperparameter	Selection
boosting_type	GBDT
objective	Regression
learning_rate	0.17
max_depth	7
n_estimators	100
subsample	0.8
Colsample_bytree	0.8
min_child_weight	5

3.4. Model performance evaluation

The performance of the proposed BPNN, LGBM and XGBoost models is shown with the best-fitting line and relatively high R^2 values of 0.81, 0.96 and 0.95 in Fig.

3.10. This accuracy of the proposed BPNN model was not as high as that of other existing models [26, 41] though, it should be noted that the proposed BPNN model covered a much larger range of AAM types. Moreover, past models were always established based on their own experimental data, eliminating the errors brought by raw material type, manual operation and etc. The data points obtained from independent test results by independent researchers were generally close to the dashed line of $y = x$, indicating the high accuracy of the workability model. Notably, no data were deliberately abandoned in this model. Clearly, LGBM and XGBoost models demonstrated much higher performance than ANN model. The potential reasons behind this phenomenon may be assigned to two aspects. First, both LightGBM and XGBoost are capable of capturing complex nonlinear relationships between input features and the target variable. They construct decision trees iteratively, allowing them to learn intricate patterns and interactions within the data more effectively compared to traditional ANN models. Second, LightGBM and XGBoost models are highly flexible and can capture complex relationships between features and the target variable through ensemble learning. They can combine the predictions of multiple weak learners (decision trees) to form a strong predictive model. This ensemble approach often results in higher modeling capacity compared to traditional ANN models.

Meantime, a multi-linear regression (MLR) model was also constructed for comparison. We chose it for comparison since it is another widely mathematical method for prediction. MLR and BPNN models are the same type of prediction model based on

establishing a relationship between one dependent value and more than one independent variable. The general form of MLR model was shown as the following equation:

$$y = \alpha_0 + \alpha_1 x_1 + \alpha_2 x_2 + \ldots + \alpha_n x_n + \beta \quad (3.8)$$

where y represents the dependent value, α_0 is the intercept, α_1 to α_n represent the coefficients of the independent variables x_1 to x_n, and β is the error associated with the prediction function. Here, the independent variables were associated with the key factors, same as the ones used in BPNN model, and the dependent value was the predicted mechanical properties (i.e., workability, compressive strength and drying shrinkage). In this sense, the MLR model for prediction of flowability was expressed in Eq. 3.9.

Flowability (%) = 0.47Activity moduli - 0.0028SSA - 511.71GPC + 16.64L/B - 3.35NaOH + 11.39Ms - 548.35Fine agg. - 490.74Coarse agg. + 626.45 (3.9)

in which activity moduli, SSA, GPC and Ms are same as the abbreviations used in the previous sections, L/B represents the liquid-to-binder ratio, NaOH represent the sodium hydroxide concentration, and Fine agg. and Coarse agg. are the fine aggregate content and coarse aggregate content ($Mass_{Fine\ \&\ Coarse\ aggregate}/Mass_{Total}$). From the equation, some coefficients reflect the same trend as the analysis in the previous sections. Obviously, higher SSA of raw materials, and content of aggregate were detrimental to

the workability of AAMs. The prediction performance of MLR model was also depicted in Fig. 3.10. Compared to the BPNN model, MLR model showed much lower prediction performance. Specifically, data points of MLR model was more discrete than those of BPNN model, and most data were far away from the equality line. Additionally, the statistical results for evaluating the accuracy of models also proved the higher accuracy of the tree-based algorithm. The comparison results were listed in Table 3.8.

Table 3.8. Prediction performance comparison

Model	R^2	MAE	RMSE
BPNN model	0.81	16.98	25.09
LGBM model	0.96	5.64	11.20
XGBoost model	0.95	7.38	12.33
MLR model	0.22	41.11	50.59

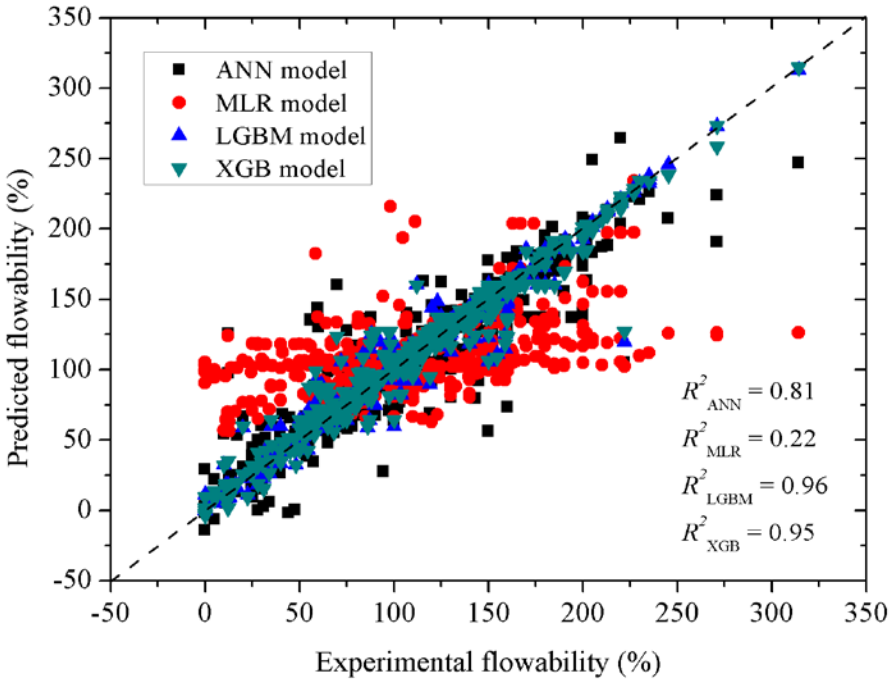

Fig. 3.10. Prediction performance of the BPNN, LGBM, XGBoost and MLR models.

3.5. Feature importance analysis

Based on the results in Section 3.4, the LGBM model with the highest prediction performance were chosen for the feature importance analysis. Feature importance, evaluated by importance score, is used in machine learning to understand which features have the most influence on the model's predictions. The importance score can be easily acquired from the algorithm. In general, the higher importance score of a certain input variable, the higher the importance of this factor in the prediction model. For more clear comparison, all feature importance score were normalized and plotted in Fig. 3.11a. It can be seen that silicate modulus displayed the highest importance score in flowability prediction, making up to over 25% of the total importance score. It can

be explained that silicate modulus directly affected the dissolution effect of precursors. Meantime, L/B ratio and activity moduli of precursors also showed relatively high scores, revealing that the workability of AAMs was mainly dependent on the geopolymer paste part.

Another importance analysis was conducted based on the MLR analysis, which was represented by absolute t values plotted in Fig. 3.11b. The t-value for each coefficient represents the ratio of the estimated coefficient to its standard error. A larger absolute t-value indicates that the coefficient is significantly different from zero, implying greater importance of the corresponding predictor variable. It can be seen that different from the machine learning-based feature importance analysis, MLR-based variable importance analysis results showed that fine aggregate content took the highest importance on the workability development of AAMs. Ranking behind fine aggregate content is GPC. Nevertheless, the influence of Ms on the MLR model for flowability also cannot be neglected, showing a fairly high importance score over 3. Such different results may be explained by these reasons. Firstly, the regression methods were totally different between machine learning and MLR that MLR can only assume the linear relationship, while machine learning can capture the non-linear relationship. Secondly, for the workability measurement aggregate content also left the unneglectable effect on it, reflecting in the previous discussion. Moreover, the fact of GPC being the second most important factor in MLR regression model further proved that workability of AAMs basically was determined by binder part.

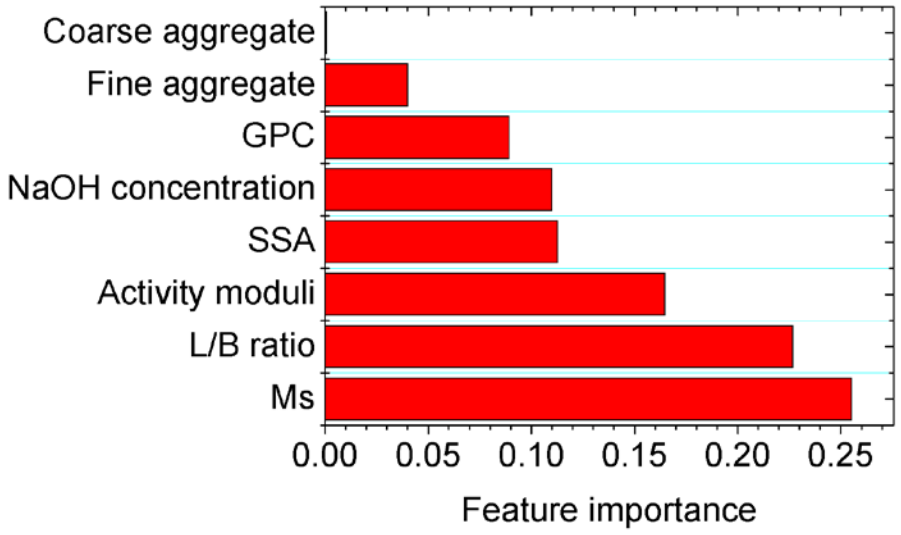

(a)

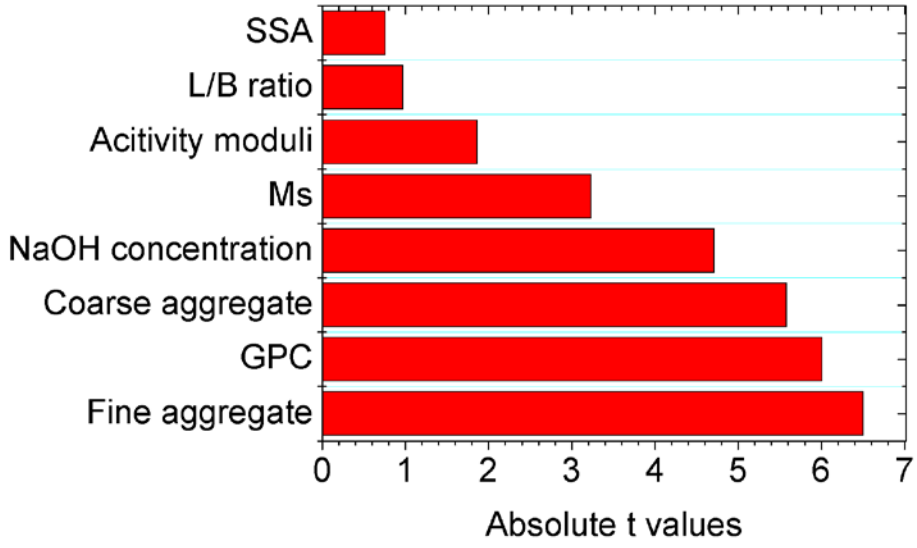

(b)

Fig. 3.11. Feature importance analysis results based on (a) Machine learning algorithm; and (b) MLR regression.

3.6. A summary of key conclusions in this chapter

In this study, the workability of AAMs in terms of flowability was qualitatively and quantitatively evaluated utilizing a total of 402 individual AAM mixtures obtained from 26 existing papers. Eight key factors governing the workability performance of AAMs were identified, i.e., activity moduli and specific surface area of precursors, Ms of the alkali activator, NaOH concentration, L/B ratio, GPC, and aggregate ratio. Moreover, based on the correlation analysis of each key factor, a BPNN regression model for predicting the flowability of AAMs was constructed.

Correlation analysis of the influence of each key factor on the workability of AAMs revealed that the workability normally increased with Ms (when lower than 2.00) and GPC, while decreased with reactivity of precursors, NaOH concentration of activator, and aggregate volumetric ratio. The influence of L/B ratio was quite ambiguous, which may be caused by the synergetic effects of other key factors.

Mathematical analysis was conducted by using machine learning technology to predict the flowability value of AAMs based on BPNN, LGBM and XGBoost regression method. In the proposed model, the key factors were set as the input data, and the flowability results were set as the output data. Among these three algorithms, LightGBM algorithm displayed the best performance, showing a high robustness and accuracy in predicting the workability of AAMs with R^2 value of 0.96, MAE of 5.64, and RMSE of 11.20. Feature importance analysis pointed out that silicate modulus left the highest importance on the prediction model. The importance of activity moduli should also be considered for flowability. However, for MLR-based feature importance analysis, fine aggregate took the domain effect on the workability prediction. Such

difference may be caused by different regression mechanisms in different models. Honestly, the simultaneous pursuit of low cost, high sustainability, and high performance poses a significant challenge for researchers and engineers in civil engineering. This study addresses this issue by collecting and analyzing valuable data from literature, resulting in the establishment of a machine learning model. Consequently, the study aims to advance and bridge the gap between scientific knowledge and practical development of AAMs, aiming to facilitate more efficient and widespread applications of AAM in the field.

Chapter 4: Machine learning-based model for predicting compressive strength of AAMs

4.1. Data analysis and discussions

In this chapter, machine learning-based algorithm was used to construct the predictive model for 28-day compressive strength of AAMs. There were 301 individual mix designs collected from 23 papers used for data analysis and modelling [35, 53, 62, 68, 125, 145-162]. The chemical compositions of precursors used in these researches were listed in Table 4.1.

Compressive strength expression is relatively simpler compared to workability and drying shrinkage results, since it has the widely-accepted and quite similar testing standards. However, due to the difference in curing molds, specimen size effect may be brought to the strength results. Hence, the major difficulty for expressing the strength results is the conversion of various strength results tested by different molds into the ones tested by the same mold. The selected key factors were listed in Table 4.2. For evaluating the hardened properties of AAM, the most-commonly used 28-day compressive strength results measured by the cylinder specimens were chosen, whilst the 28-day flexural strength was tabulated in the last column as a reference. To facilitate comparison, the compressive strength results were consistently converted to cylindrical strength results at constant conversion coefficients of 0.75 for cube strength and 0.97

for ∅150×300 mm cylinder strength [113]. Therefore, the collected and processed experimental data were listed in Supplementary Table 2.

Table 4.1. Chemical compositions of raw materials (Ref. [35, 53, 62, 68, 125, 145-162]).

Ref.	Precursor type	SiO_2	CaO	Al_2O_3	Fe_2O_3	SO_3	K_2O	MgO	Na_2O	LOI
Duran Atiş et al., 2009	GGBFS	36.70	32.61	14.21	0.98	0.99	0.76	10.12	0.42	NA
Chi and Huang, 2012	GGBFS	34.58	40.67	13.69	0.44	0.56	0.64	7.05	0.48	1.13
Aydın, 2013	GGBFS	40.20	35.90	11.66	1.68	0.90	1.47	5.88	0.30	0.88
	FA F	51.31	6.09	23.92	6.50	1.72	3.21	2.63	0.43	2.40
	SF	74.90	2.20	1.15	1.31	0.18	2.26	9.57	2.43	5.70
Aydın and Baradan, 2014	GGBFS	40.20	35.90	11.66	1.68	0.90	1.47	5.88	0.30	0.88
Nath&Sarker, 2014	GGBFS	32.46	43.1	14.3	0.61	4.58	0.33	3.94	0.24	-
	FA F	50	1.79	28.25	13.5	0.38	0.46	0.89	0.32	0.64
Chi, 2015	FA F	56.48	2.82	20.34	6.61	0.25	0.80	0.93	0.33	2.76
Okoye et al., 2016	FA F	50.7	2.38	28.8	8.8	0.3	2.4	1.39	0.84	3.79
	SF	93.67	0.31	0.83	1.3	0.16	1.1	0.84	0.4	2.1
Hadi et al., 2017	GGBFS	32.4	40.7	14.96	0.83	2.74	0.29	5.99	0.42	-
Guo & Pan, 2018	Steel slag	21.9	37.4	9.78	14.9	0.61	0.29	10.3	0.2	2.27
	FA C	40.7	9.46	22.4	5.34	2.17	0.69	0.85	0.45	2.27
Ling et al., 2019	FA C	30.7	28.8	16	6.8	3.47	0.27	6.74	2.97	0.49
Hu et al., 2019	FA F	65.9	1.59	24	2.87	-	1.44	0.42	0.49	1.53
	GGBFS	36	42.6	13.8	0.3	0.56	42.6	5.8	0.21	-1
Sedaghatdoost et al., 2019	GGBFS	32.21	43.13	6.8	-	3.54	1.81	7.32	1	-

Moradikhou et al., 2020	MK	54	-	31.7	4.89	-	4.05	-	2.32	1.41
Mermerdaş et al., 2020	FA F	55.89	11.25	17.54	6.7	0.65	2.09	1.86	0.9	-
Luan et al., 2020	FA F	62.83	6.37	16.71	7.38	-	-	0.64	1.05	-
Shariati et al., 2021	GGBFS	36.15	39	9.3	0.03	2.22	0.6	8.9	0.8	1.01
Shahmansouri et al., 2021	GGBFS	35.85	37.71	13.39	1.06	2.52	0.58	9.1	0.48	0.12
	SF	93	0.3	1.7	1.2	-	1.1	1	0.6	3.5
Albidah et al., 2021	MK	50.995	1.287	42.631	2.114	0.439	0.337	0.127	0.284	-
Adesanya et al., 2021	GGBFS	32.30	38.50	9.50	1.23	4.00	0.50	10.20	0.50	-1.30
	FA C	33.40	42.60	10.10	5.50	1.90	1.20	2.00	0.80	2.90
Xu et al., 2021	GGBFS	26.50	43.70	18.20	1.00	2.70	0.80	4.90	-	-
Wang et al., 2021	GGBFS	36.77	37.60	13.56	0.41	1.82	0.55	7.45	0.25	0.80
	FA F	49.80	4.65	25.08	11.67	1.35	3.30	1.67	0.66	0.58
Sadeghian ert al., 2022	GGBFS	36.50	38.50	11.00	1.00	0.30	0.80	7.80	0.65	0.50
	SF	85.00	1.50	1.00	2.00	-	-	1.50	-	3.50
Ou et al., 2022	GGBFS	33.81	38.81	14.78	0.36	2.49	0.44	7.09	0.26	1.40
	FA F	52.64	1.32	34.11	3.25	0.33	1.38	0.50	0.03	3.25
	SF	94.90	0.56	0.49	1.07	-	-	0.70	-	1.61

Note: LOI = Loss of ignition.

Table 4.2. Key factor selections for prediction models

Properties	Activity moduli	Specific surface area	Geopolymer paste content	Liquid-to-binder ratio	NaOH concentration	Silicate modulus	Fine agg. content	Coarse agg. content	Temperature	RH	V/S ratio
Strength	√	√	√	√	√	√	√	√	Unified	Unified	Unified

Note: √ represents that this factor was selected as the key factor; × represents that this factor was not considered; and Unified represents that this factor was considered though, it has been controlled as the similar value.

4.2. Data analysis and discussions

4.2.1. Effect of activity moduli on strength

Fig. 4.1 presents the effect of activity moduli of raw materials on strength development of AAMs. Generally, an increasing trend between activity moduli and strength could be seen, especially when activity moduli was over 8. Except the experimental results by Sadeghian et al. [156], all the strength results were higher than 35 MPa. Shahmansouri et al. [153] reported an improvement of strength for AAS concrete with the addition of silica fume. Ou et al. [157] reported a relatively high strength over 60 MPa for alkali-activated slag concrete mixed with 5% and 10% of silica fume. Meantime, lowering the activity moduli by adding FA resulted in the reduction of strength. However, it could be seen that a significant decreasing trend was identified in the experiment of Sadeghian et al. [156]. Note that there were two different curing conditions for samples which were water curing and plastic bag curing. When separately observed, the higher strength results were reported when added with silica fume as well. The increasing activity moduli could dramatically decrease the internal porosity and increase the compactness of the mixture matrix. However, there exists a limit for the highly reactive materials improving compressive strength, beyond which the setting time and workability of mixtures were decreased leading to reduction in strength.

4.2.2. Effect of specific surface area on strength

The effect of SSA on 28-day compressive strength of AAMs was showed in Fig. 4.2. Normally, the data points located in the range of SSA around 450 m^2/kg that represented the commonly used GGBFS. A significantly increasing trend could be found in the experimental results reported by Shahmansouri et al. [153], which was caused by the addition of silica fume. Another raw material with high SSA is MK. Albidah et al. [53] developed MK-based geopolymer concrete activated by the mix solution of NaOH and Na_2SiO_3. They obtained several relatively high strength results (e.g., 56.3 MPa, 57.5 MPa). On the other hand, Moradikhou et al. acquired much lower strength of fiber-reinforced MK-based geopolymer concrete. It should be noted that the raw materials with high SSA requires for higher water demand. Therefore, a reduction of workability always happened resulting in the lower compactness and larger porosity of mixtures, which inhibits the strength development of AAMs.

4.2.3. Effect of alkali activator on strength

Figs. 4.3 and 4.4 illustrate the effect of alkali activator, namely, Ms and NaOH concentration, on compressive strength of AAMs. It can be clearly seen that there is an increasing trend between Ms and strength development. This phenomenon is in line with the most existing literature [62, 68, 151]. Higher Ms generally represented a higher content of SiO_2 in system which can promote the C/N-(A)-S-H gel production. From Fig. 4.4, a roughly positive relation between the compressive strength and NaOH concentration can be observed. For instance, Luan et al. [68] reported such a positive relation between strength and NaOH concentration and achieved the highest strength

(69.6 MPa) when the concentration reached 15.5 M. Ling et al. [62] obtained compressive strength of 3.0-7.5 MPa for AAM paste without the presence of NaOH. However, the positive tendency between the strength and the NaOH concentration was observed that the mean values of compressive strength were 7.5, 11.7 and 12.4 MPa at the concentrations of 6, 8 and 10 M respectively [151]. On the other hand, the strength results vary a lot among different studies at the sodium hydroxide concentration of 12 M and 14 M, which are dependent on other factors that have not been taken into consideration. However, an even higher molarity of solution (>14 M) may accelerate the polymerization reaction, resulting in the formation of immature structure and hindering the formation of compact amorphous microstructure [163-165].

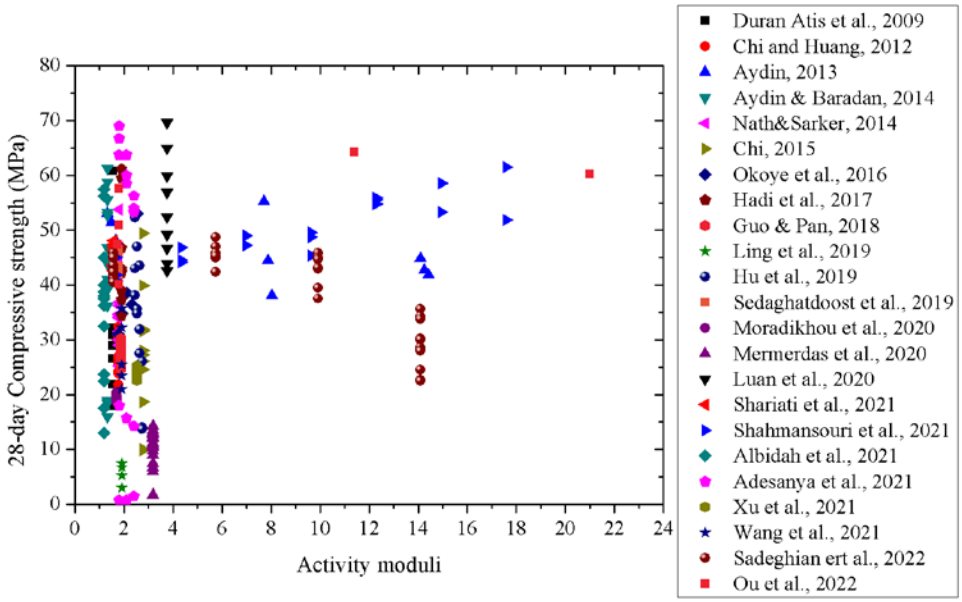

Fig. 4.1. Effect of activity moduli on strength

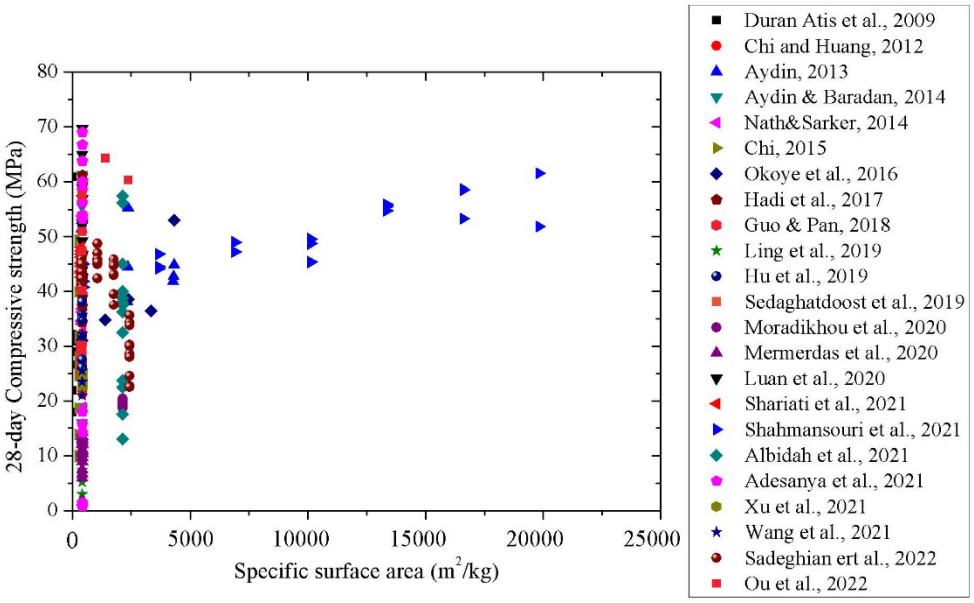

Fig. 4.2. Effect of SSA on strength

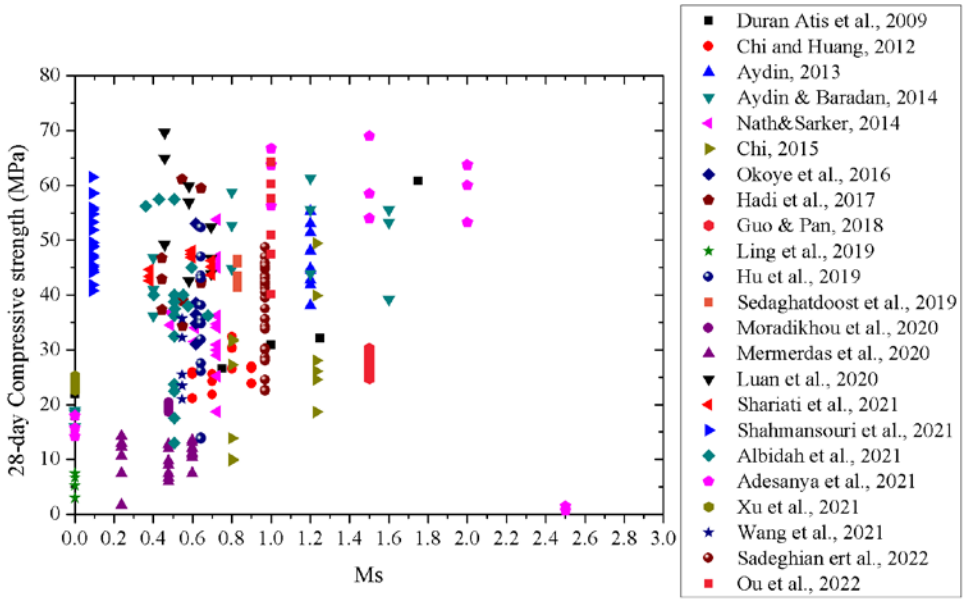

Fig. 4.3. Effect of Ms on strength

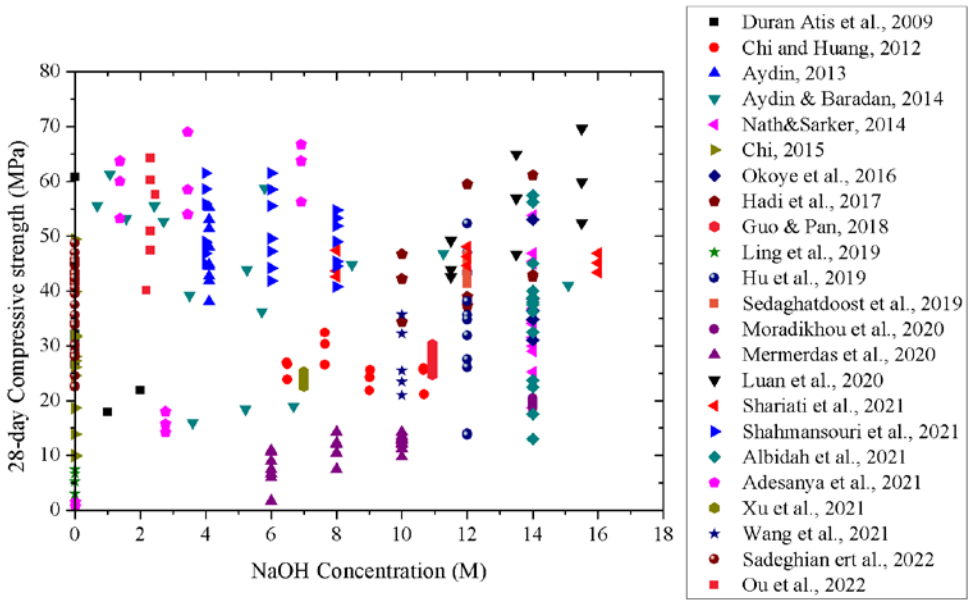

Fig. 4.4. Effect of NaOH concentration on strength

4.2.4. Effect of liquid-to-binder ratio on strength

Fig. 4.5 illustrates the effect of L/B ratio on the 28-day compressive strength of AAM mixtures. No clear trend between the strength and L/B ratio could be observed. The highest compressive strength (69.6 MPa) occurred to the relatively low L/B ratio (0.40) for all the observed mixtures. A close observation revealed certain relation between the strength and the L/B ratio. For instance, Mermerdas et al. [151] and Shahmansouri et al. [153] demonstrated a sharp decrease of strength when the L/B ratio was increased. In addition, Luan et al. [68] reported a negative trend between compressive strength and L/B ratio when the NaOH concentration was constant. Albidah et al. [53] reported a slightly increasing trend of strength with the increasing L/B ratio, while a rapid decreasing trend of strength was reported when the L/B ratio was higher than 1.0. It can be referred from the previous works that no consensus has

been reached on the effect of L/B ratio on the compressive strength and one finding may even be contradictory with the other. This phenomenon, caused by the more complicated liquid with the incorporation of alkali for preparing AAM than the pure water for preparing ordinary mortar/concrete, needs further investigation considering the attributes of the alkaline solution. Among the various attributes, the NaOH concentration, in conjunction with the L/B ratio, would inevitably exert significant effects on the properties of AAM.

4.2.5. Effect of geopolymer paste content and aggregate content on strength

Figs. 4.6 and 4.7 respectively illustrate the effects of GPC and aggregate phase on the compressive strength of AAMs. Obviously, the effects of these two key factors on mechanical property were inverse to each other. From the figure, a non-pronounced decreasing trend of the strength with the increasing GPC is observed. Interestingly, it is worth to note that the mixtures containing a lower GPC would generally yield a higher strength. For instance, Shahmansouri et al. [153] and Luan et al. [68] reported a relatively high strength (~50 MPa) at a relatively low GPC (~0.30), while Ling et al. [62] reported a strength as low as 5.6 MP at GPC of 1.00. However, this is not always true considering a broader range of test results [151, 152], indicating that some other key factors shall be taken into account when analyzing the effect of GPC. Although Mermerdas et al. [151] incorporated aggregate into geopolymer, the aggregates consisted of both fine aggregate and light-weight aggregate instead of normal aggregate, leading to a lower strength. Likewise, Hu et al. [148] and Sedaghatdoost et al. [149]

adopted recycled aggregate partially or totally to replace coarse aggregate, giving a slight reduction in strength at an increased GPC. Hence, the various types of aggregates can also influence the strength of geopolymer mixture. Above all, the effect of GPV on the properties of AAM mixtures is also dependent on the other key factors. In other words, a unified model shall be constructed to quantitatively delineate the possible combined effects among all the key factors.

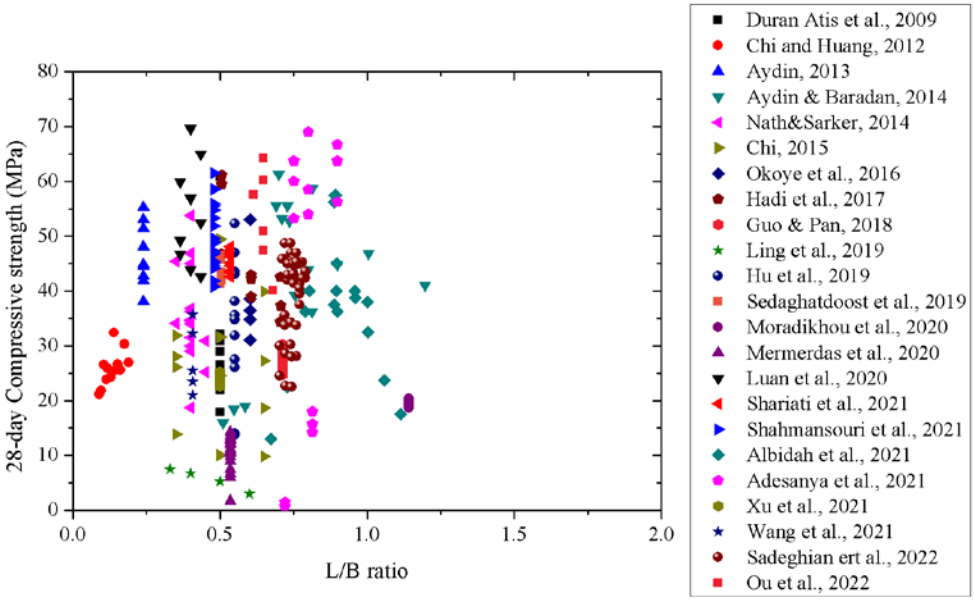

Fig. 4.5. Effect of L/B ratio on strength

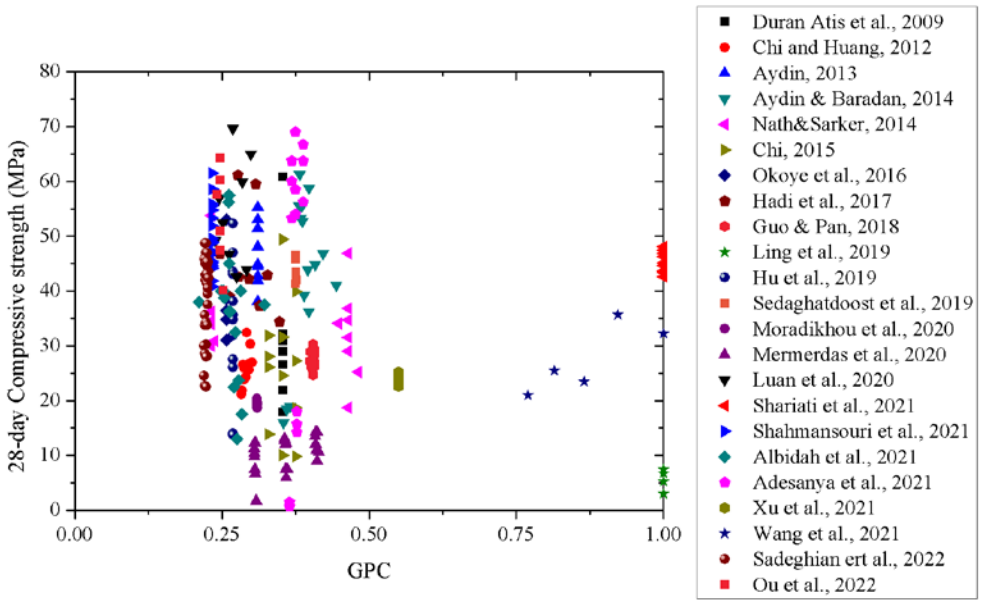

Fig. 4.6. Effect of GPC on strength

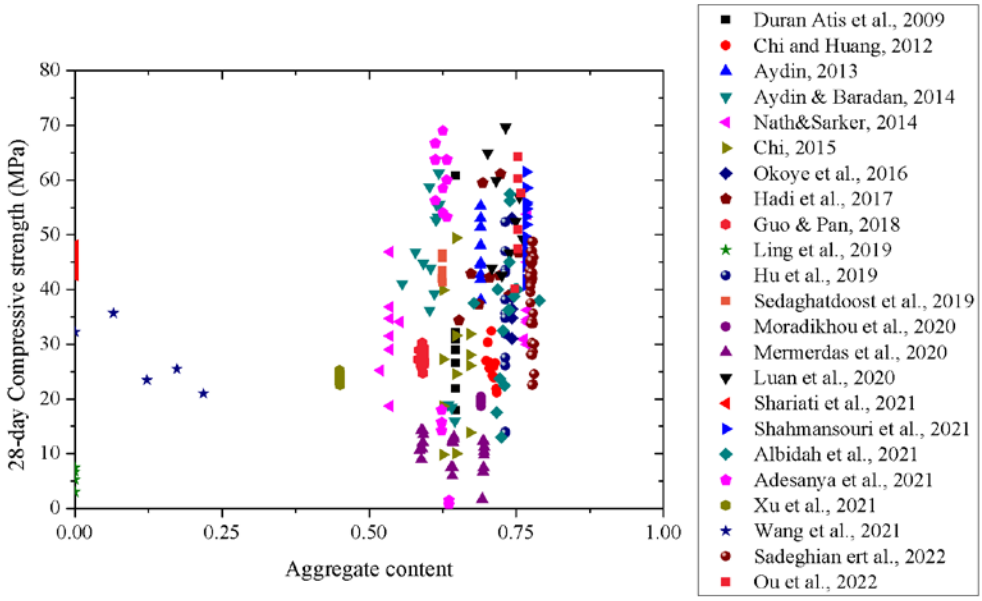

Fig. 4.7. Effect of aggregate content on strength

4.3. Machine learning modelling and discussions

Admittedly, the strength prediction model for AAM-based construction materials has been put forward by building codes and numerous researchers, covering mathematical equations and machine learning-based models. For example, Hamidi et al. [166] proposed the prediction model of the compressive strength for heavy weight aggregate geopolymer based on the size of molds as follows:

$$f_c'(d) = \frac{1.1 f_c'}{\sqrt{1+\frac{d}{l_0}}} + 0.7 f_c' \quad (4.1)$$

where $f_c'(d)$ is the measured compressive strength of specimen with arbitrary size, MPa; f_c' is the compressive strength of the standard cylinder (Ø150×300 mm), MPa; *d* denotes the characteristic specimen dimension and l_0 denotes the characteristic length. Nguyen et al. [92] constructed the Deep Neural Network and Deep Residual Network to calculate the compressive strength of FA geopolymer concrete using the mix design factors. Riahi and Nazari [93] used ANN to predict the effects of nanoparticles on early-age compressive strength of fly ash/rice husk ash-based geopolymer concrete. Nazari and Torgal [94] compared six different ANN-based models for predicting the compressive strength of different types of geopolymers. They found that such modelling mainly depended on the training method rather than the number of neurons in hidden layers. Yadollahi et al. [97] constructed an ANN model for predicting the 28-day compressive strength of alkali-activated natural pumice based on the M_S ratio, Na_2O content, water-to-binder ratio, and ultrasonic pulse velocity results. These models, albeit advanced, were all faced with the problem in generality, since the researchers

only used their own experimental results to construct the models. Hence, it is still of necessity to develop a general model for prediction of compressive strength with high robustness.

Following the instruction mentioned in the previous chapter, a compressive strength-aimed predictive model was constructed by ANN, LGBM and XGBoost algorithms. Due to the totally different database, all parameters related to model should be re-designed. Moreover, the prediction performance was as well largely affected by the database. Finally, the proposed BPNN model for prediction of compressive strength consisted of one input layer (eight input data), two hidden layers (eleven neurons in the first hidden layer and seven neurons in the second hidden layer), and one output layer (one output data). The structure of the proposed model was illustrated in Fig. 4.8, and the detailed parameters were listed in Table 4.3. As for the LGBM and XGBoost models, the hyperparameter selection was tabulated in Tables 4.4 and 4.5, respectively.

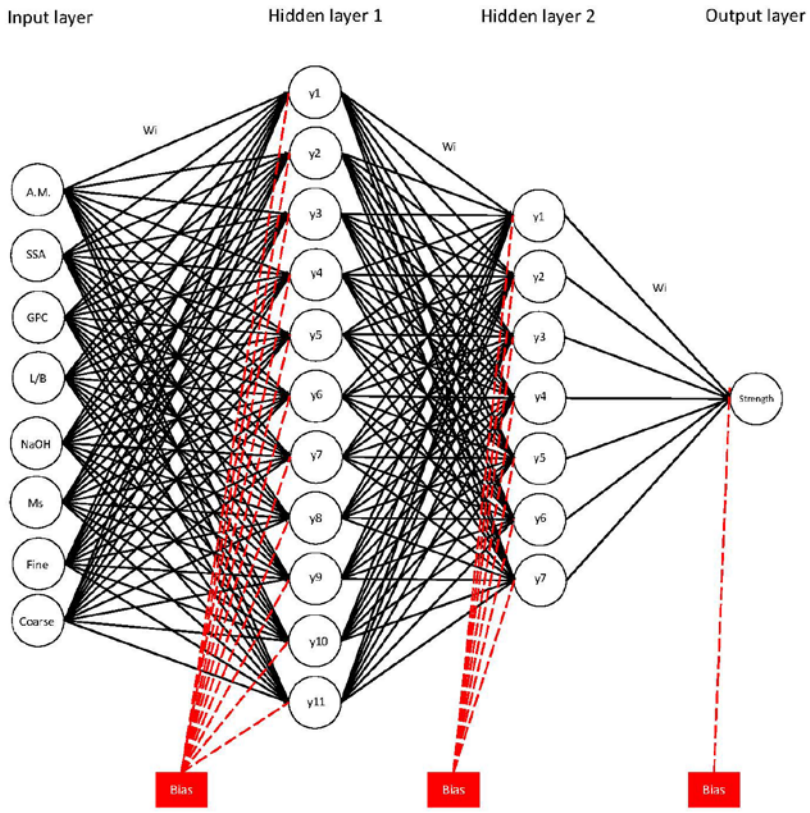

Fig. 4.8. Structure of the proposed BPNN model for compressive strength.

Table 4.3. Properties of BPNN model for compressive strength

Details	Selection
Network architecture	Backpropagation network
Number of input layer	1
Number of hidden layer	2
Number of output layer	1
Number of neurons in input layer	8
Number of neurons in hidden layer 1	11
Number of neurons in hidden layer 2	7
Number of neurons in output layer	1

Activation function	Tan-sig
Learning rate	0.00001
Moment rate	0.95
Training algorithm	Trained (gradient descent with momentum)

Table 4.4. Parameters of the proposed LGBM regression model

Hyperparameter	Selection
boosting_type	GBDT
objective	Regression
learning_rate	0.06
max_depth	4
n_estimators	783
num_leaves	14
min_child_samples	8

Table 4.5. Parameters of the proposed XGBoost regression model

Hyperparameter	Selection
boosting_type	GBDT
objective	Regression
learning_rate	0.17
max_depth	7
n_estimators	100

subsample	0.8
Colsample_bytree	0.8
min_child_weight	5

4.4. Model performance evaluation

Fig. 4.9 illustrates the performance of the proposed BPNN, LGBM, and XGBoost models with a best-fitting line and relatively high R^2 values of 0.85, 0.96 and 0.97, respectively. The MAE values were calculated as 3.67, 1.37 and 1.24, while the RMSE were 2.52, 2.43 and 5.95, respectively. The data points from independent test results by different researchers closely align with the dashed line of y = x, indicating high accuracy in the drying shrinkage model. Notably, no data were intentionally omitted in this model. Herein, the better performance of tree-based algorithms, in which XGBoost showed the best performance. Meanwhile, a MLR model was also constructed for comparative analysis. The MLR equation was expressed in Eq. 4.2.

$$\text{Strength (MPa)} = -0.51\text{Activity moduli} + 0.002\text{SSA} + 520.03\text{GPC} - 5.66\text{L/B} - 0.25\text{NaOH} + 13.31\text{Ms} + 504.20\text{Fine agg.} + 538.75\text{Coarse agg.} - 487.57 \quad (4.2)$$

where the notation for each key factor was the same as those in the previous chapter. Also, the coefficients of MLR can demonstrate the effects of key factors on compressive strength of AAMs. On the other hand, some coefficients of each key factors (e.g.,

activity moduli, GPC, aggregate content) may be opposite to the correlation analysis raised in the previous section. It is because that when conducting MLR analysis, the regression algorithm was constructed based on all key factors.

The predictive performance of the MLR model is illustrated in Fig. 4.10. In comparison to the other three models, the MLR model exhibited significantly lower prediction performance. Notably, the data points of the MLR model were more scattered, and a majority of them deviated considerably from the equality line. Statistically, the accuracy of MLR model was lower than that of BPNN with much lower R^2 of 0.29, higher MAE of 9.78 and higher RMSE of 12.94. A summary of the comparison results is presented in Table 4.6. Although MLR model showed a much lower prediction performance, its convenience in model construction and reflection of effects of each input data on output data cannot be neglected.

Table 4.6. Prediction performance comparison

Model	R^2	MAE	RMSE
BPNN model	0.85	3.67	5.95
LGBM model	0.96	1.37	2.52
XGBoost model	0.97	1.24	2.43
MLR model	0.29	7.30	11.18

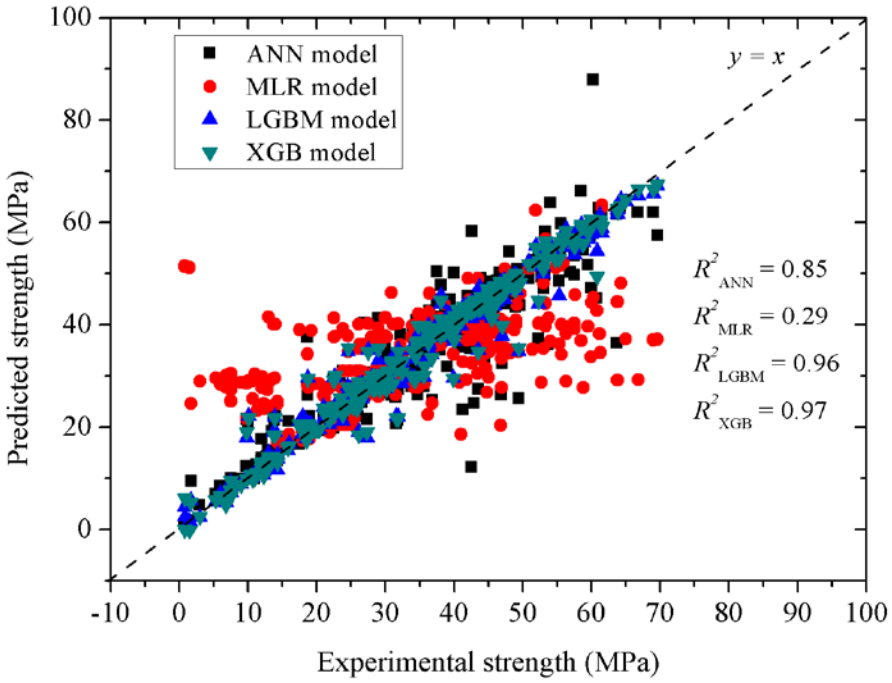

Fig. 4.9. Prediction performance of the BPNN, LGBM, XGBoost and MLR models.

4.5. Feature importance analysis

For illustrating the influencing attributes of each variable in the XGBoost model, feature importance analysis was conducted and the normalized feature importance scores were plotted in Fig. 4.10a, and MLR-based importance analysis results were plotted in Fig. 4.10b. Obviously, coarse aggregate took a dominant place in the XGBoost prediction model for compressive strength of AAMs, which can be explained by enhancement of packing density and compressive strength. The second most important variable lied in the activity moduli of precursors, indicating the unneglectable effect of precursor type on the strength development. However, MLR-based importance analysis results demonstrated a relatively higher importance of silicate modulus and

SSA of the precursors. Apart from the potential reason caused by the different regression mechanisms, the physical meaning of high importance of these two variables can be explained by that different types of precursor and alkali activator led to totally different hydration product. Moreover, it can be observed that in MLR-based analysis, coarse aggregate still took the third most important variable, showing a good agreement with the machine learning-based importance analysis. Such phenomenon further proved the significant role of coarse aggregate in AAM mix design. Addition of coarse aggregate can simultaneously improve the mechanical properties, and reduce the material cost and environmental burden.

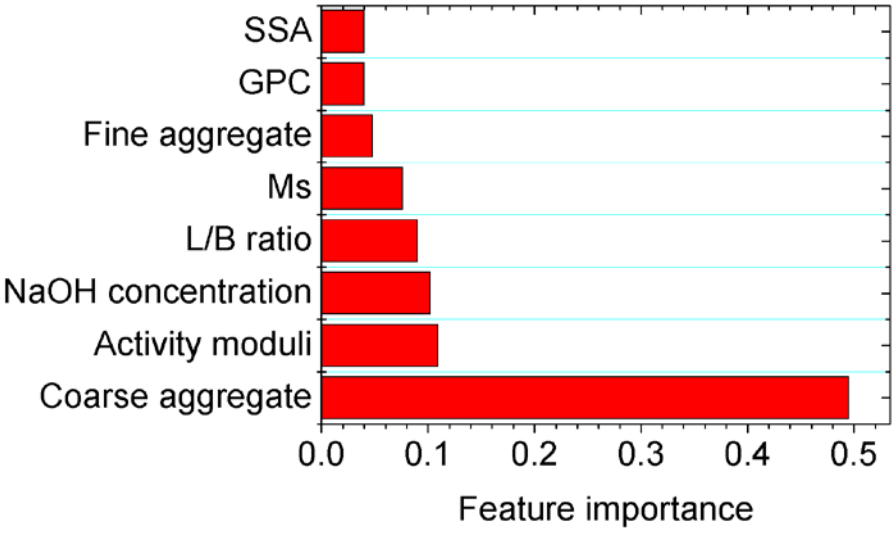

(a)

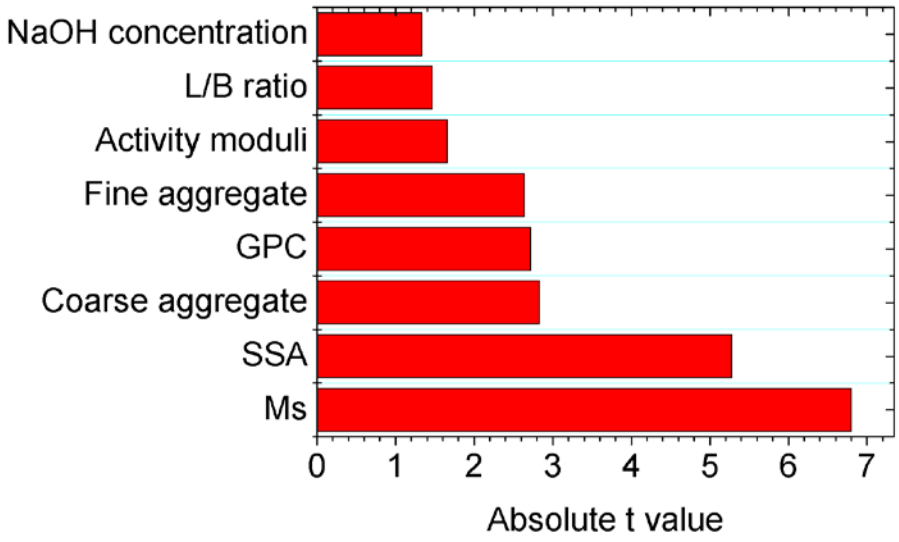

(b)

Fig. 4.10. Feature importance analysis results based on (a) Machine learning algorithm; and (b) MLR regression.

4.6. A summary of key conclusions in this chapter

In this chapter, qualitative and quantitative analysis were performed utilizing extensive data on a total of 301 AAM mixtures extracted from the literature. The key factors were identified, including activity moduli and SSA of precursor, alkali activator properties (i.e., NaOH concentration and Ms), geopolymer paste content, liquid-to-binder ratio and aggregate content.

Qualitative analysis revealed that a higher L/B ratio and a larger GPC may have adverse effects on the strength of AAM, while a higher reactivity of precursor, a higher Ms and a higher NaOH concentration may have positive effects on the strength of AAM. Among these factors, NaOH concentration showed a limit of 12-14 M beyond which the strength improving effects would be hindered. Meantime, the influence of aggregate types shall be taken into account.

Quantitative analysis yielded an XGBoost-based model for strength prediction of AAM with the highest accuracy in comparison to BPNN and LightGBM-based models. A high R^2 value of 0.97 has been attained for the model accompanied with low MAE of 1.24 and RMSE of 2.43. Furthermore, feature importance analysis revealed a relatively higher importance of coarse aggregate on the model. Meantime, activity moduli of precursor also had unneglectable importance on it. MLR-based importance analysis revealed the relatively high importance of Ms on the model. The strength model could be used to predict the strength of new AAM mixtures, guide the scientific mix design of AAM and deepen the understanding of AAM.

Chapter 5: Machine learning-based model for predicting drying shrinkage of AAMs

5.1. Data collection and processing

In this chapter, machine learning-based algorithm was used to construct the predictive model for ultimate drying shrinkage (UDS) of AAMs. For analysis and modelling, this chapter adopted 438 individual experimental mixes from 43 different papers [17, 35, 54, 72, 151, 154-162, 164, 167-194]. Table 5.1 listed out the chemical compositions of raw materials in these researches. Different from the flow and strength, drying shrinkage measurement always considered the curing conditions, including room temperature and relative humidity. Moreover, the curing conditions considered curing temperature, relative humidity (RH) and volume-to-surface (V/S) ratio of specimens. The selected key factors were listed in Table 5.2.

For the selection of drying shrinkage results, the author only focused on the ultimate drying shrinkage results expressed by strain, regardless of the drying period [114]. The curing conditions, i.e., curing temperature and relative humidity, are always concerned and studied in drying shrinkage-related researches. Moreover, different from the compressive strength results, there is no such coefficients for converting drying shrinkage results tested by different molds into the ones tested by the same mold. As for the reason for choosing UDS strain, it is that if the predicted UDS is not satisfied with the requirements, a certain shrinkage at a certain time is not helpful to the mixture

design. In accordance with this method, the processed data and ultimate drying shrinkage results were tabulated in Supplementary Table 3.

Table 5.1. Chemical compositions of raw materials (Ref. [17, 35, 54, 72, 151, 154-162, 164, 167-194]).

Reference	Precursor type	SiO_2	Al_2O_3	CaO	MgO	Na_2O	SO_3	K_2O	Fe_2O_3	LOI
Duran Atiş et al., 2009	GGBFS	36.70	14.21	32.61	10.12	0.42	0.99	0.76	0.98	NA
Ridtirud et al., 2011	FA C	33.66	18.25	19.23	2.84	1.53	2.74	2.08	16.35	2.45
Chi and Huang, 2012	GGBFS	34.58	13.69	40.67	7.05	0.48	0.56	0.64	0.44	1.13
Aydın & Baradan, 2013	GGBFS	40.20	11.66	35.90	5.88	0.30	0.90	1.47	1.68	0.88
	SF	96.100	-	-	-	-	-	-	-	1.81
Aydın, 2013	GGBFS	40.20	11.66	35.90	5.88	0.30	0.90	1.47	1.68	0.88
	FA F	51.31	23.92	6.09	2.63	0.43	1.72	3.21	6.50	2.40
	SF	74.90	1.15	2.20	9.57	2.43	0.18	2.26	1.31	5.70
Aydın & Baradan, 2014	GGBFS	40.20	11.66	35.90	5.88	0.30	0.90	1.47	1.68	0.88
Deb et al., 2015	GGBFS	29.96	12.25	45.45	-	0.31	3.62	0.38	0.52	2.39
	FA F	53.71	27.20	1.90	-	0.36	0.30	0.54	11.17	0.68
Chi, 2015	FA F	56.48	20.34	2.82	0.93	0.33	0.25	0.80	6.61	2.76
Marjanović et al., 2015	GGBFS	37.50	7.27	38.48	10.86	0.54	1.51	0.26	0.73	2.13
	FA F	55.23	21.43	7.94	2.61	-	-	-	7.42	1.66
Chi et al., 2015	GGBFS	34.58	13.69	40.67	7.05	0.15	0.56	0.32	0.44	1.13
	FA F	56.48	20.34	2.82	0.93	0.33	0.25	0.80	6.61	2.76
Ye & Radlińska, 2016	GGBFS	30.04	12.74	43.83	4.79	0.24	3.11	0.40	1.16	2.56

Gao et al., 2016	GGBFS	34.44	13.31	37.42	9.89	0.34	1.23	0.47	0.47	1.65
	FA F	54.62	24.42	4.44	1.43	0.73	0.46	1.75	7.21	2.80
Thomas et al., 2016	GGBFS	36.00	10.50	39.80	7.90	0.30	2.10	0.20	0.70	0.00
	FA C	37.70	20.00	23.40	4.30	1.70	2.40	0.60	5.60	0.31
Yang et al., 2017	FA F	53.00	30.58	4.57	1.25	0.52	-	1.43	3.81	2.29
	MK	55.87	42.25	0.04	0.04	0.26	-	1.43	3.81	0.61
Ye et al., 2017	GGBFS	30.04	12.74	43.83	4.79	0.24	3.11	0.40	1.16	2.56
Hojati & Radlińska, 2017	FA F	48.90	25.25	2.54	0.86	1.41	1.47	-	16.16	1.58
	GGBFS	30.80	11.45	47.50	3.65	0.42	3.03	-	1.81	1.17
Gao et al., 2017	GGBFS	30.23	12.58	40.51	9.05	-	3.47	0.43	0.60	1.94
	FA F	54.62	24.42	4.44	1.43	0.73	0.46	1.75	7.21	2.80
Punurai et al., 2018	FA F	33.40	17.80	17.00	2.05	1.52	3.57	2.36	11.90	1.23
Jiao et al., 2018	GGBFS	32.83	17.19	36.69	8.20	0.65	1.94	0.37	0.38	-
Wang & Ma, 2018	GGBFS	31.20	13.80	45.30	5.20	0.20	2.60	0.20	0.90	-
	FA F	49.10	34.80	4.90	0.40	0.40	0.30	1.30	4.50	-
Taghvayi et al., 2018	GGBFS	35.50	9.50	36.00	9.50	-	-	-	0.50	-
Xiang et al., 2018	MK	52.39	44.35	0.01	0.10	0.71	0.41	0.50	0.81	-
Al-mashhadani et al., 2018	GGBFS	40.55	12.83	35.58	5.87	0.79	0.18	-	1.1	0.03
	FA F	54.08	26.08	2.00	2.68	0.79	0.74	-	6.68	1.36
Lee et al., 2018	GGBFS	29.10	11.70	45.70	3.08	0.19	2.80	0.46	0.45	1.49

Xiang et al., 2018	GGBFS	19.20	9.50	57.40	3.30	0.30	5.00	0.50	2.90	0.50
	FA F	66.30	15.80	5.20	0.90	0.60	0.30	2.40	2.80	4.90
Jiao et al., 2018	GGBFS	32.83	17.19	36.69	8.20	0.65	1.94	0.37	0.38	-
Hu et al., 2019	GGBFS	33.00	13.91	39.11	10.04	-	0.16	1.91	0.82	0.08
Humad et al., 2019	GGBFS	35.00	14.30	30.40	16.10	0.60	0.70	0.70	0.30	0.90
	FA F	48.10	18.90	6.10	1.80	1.10	-	2.30	7.80	1.60
Ling et al., 2019	FA C	30.70	16.00	28.80	6.74	2.97	3.50	0.27	6.80	0.49
Mermerdaş et al., 2020	FA F	55.89	17.54	11.25	1.86	0.9	0.65	2.09	6.7	-
Gong and Qu, 2020	GGBFS	33.80	14.80	38.80	7.10	0.30	2.50	0.40	0.40	1.40
	SF	95.20	-	1.85	0.27	0.17	-	0.86	0.59	1.03
Xiang et al., 2020	GGBFS	19.24	9.45	57.36	3.32	0.27	5.00	0.47	2.86	-
Si et al., 2020	MK	56.61	39.16	0.05	0.09	0.01	0.05	0.30	1.87	-
Xu et al., 2020	GGBFS	26.50	18.20	43.70	4.90	-	2.70	0.80	1.00	-
Behforouz et al., 2020	MK	52.10	43.80	0.20	0.21	0.11	0.00	0.32	2.60	0.99
Chen et al., 2021	GGBFS	30.29	13.53	40.55	8.59	-	3.43	0.57	0.49	1.02
Adesanya et al., 2021	GGBFS	32.30	9.50	38.50	10.20	0.50	4.00	0.50	1.23	-1.30
	FA C	33.40	10.10	42.60	2.00	0.80	1.90	1.20	5.50	2.90
Fu et al., 2021	GGBFS	35.88	10.65	33.54	11.43	0.73	0.13	0.83	0.46	1.30
	MK	49.78	34.63	-	2.58	0.41	-	0.44	0.93	1.10

Sun et al., 2021	MK	53.97	39.43	0.31	0.08	-	-	-	1.34	4.70
Xu et al., 2021	GGBFS	26.50	18.20	43.70	4.90	-	2.70	0.80	1.00	-
Wang et al., 2021	GGBFS	36.77	13.56	37.60	7.45	0.25	1.82	0.55	0.41	0.80
	FA F	49.80	25.08	4.65	1.67	0.66	1.35	3.30	11.67	0.58
Sadeghian et al., 2022	GGBFS	36.50	11.00	38.50	7.80	0.65	0.30	0.80	1.00	0.50
	SF	85.00	1.00	1.50	1.50	-	-	-	2.00	3.50
Ou et al., 2022	GGBFS	33.81	14.78	38.81	7.09	0.26	2.49	0.44	0.36	1.40
	FA F	52.64	34.11	1.32	0.50	0.03	0.33	1.38	3.25	3.25
	SF	94.90	0.49	0.56	0.70	-	-	-	1.07	1.61

Note: LOI = Loss of ignition.

Table 5.2. Key factor selections for prediction models

Properties	Activity moduli	Specific surface area	Geopolymer paste content	Liquid-to-binder ratio	NaOH concentration	Silicate modulus	Fine agg. content	Coarse agg. content	Temperature	RH	V/S ratio

Shrinkage	√		√		√		√		√		√		√		√		√		√		√	

Note: √ represents that this factor was selected as the key factor; × represents that this factor was not considered; and Unified represents that this factor was considered though, it has been controlled as the similar value.

5.2. Data analysis and discussions

5.2.1. Effect of activity moduli on drying shrinkage

Fig. 5.1 illustrates the effect of the reactivity of the binder on the drying shrinkage of AAM. Most data were located in the reactivity range from 0 to 5, and some results showed a relatively high reactivity over 25.00 due to the addition of SF in the binder. To clearly display the influence of reactivity on the UDS ranging from 0 to 5, the shrinkage results in this range were amplified and are inserted in Fig. 5.1. Although there was no strong relationship between the reactivity of the binder and the UDS, the shrinkage generally demonstrated a higher magnitude when the reactivity was approximately 2.00; Jiao et al. [176] reported the highest UDS result of 35748 με for alkali-activated slag paste at a reactivity of 1.89. When the reactivity was lower than 2.00, an increasing trend between drying shrinkage was observed by Ma et al. [30]; the shrinkage results of alkali-activated coal gangue–slag mortar increased from 1782 to 3339 με as the reactivity increased from 0.67 to 1.36. Moreover, the average shrinkage result of Adesanya et al. [35] at a reactivity of 1.80 (4480 με) was also higher than that observed by Duran Atis et al. [158] at a reactivity of 1.55 (3235 με). In contrast, a decreasing tendency of drying shrinkage with regard to the reactivity of the binder, larger than 2.00, was observed. For instance, Ye and Radlińska [17], Chi [162], Mermerdaş et al. [151] and Aydın and Baradan [168] reported drying shrinkage results of 12200, 6006, 1064, and 452 με at reactivities of 2.04, 2.78, 3.19, and 28.52, respectively. In addition, a slight reduction in shrinkage from 3850 to 3740 με was

observed by Adesanya et al. [35] with an increase in reactivity from 2.10 to 2.40. The above results show that the positive influence of reactivity on drying shrinkage had a boundary of 2.00, beyond which drying shrinkage development was inhibited, indicating that using a binder with a high reactivity may reduce the drying shrinkage, which is in line with the existing literature [89,90]. Chindaprasirt et al. [195] increased the fineness of high-calcium fly ash, improving both fineness and pozzolanic reactivity, which led to a reduction in the drying shrinkage rate and enhancement in the compressive strength of alkali-activated FA mortars. The lower reactivity of the binder, for example, FA, may also be advantageous for reducing drying shrinkage; however, the low strength gain of geopolymers adopting such binders cannot be neglected [196]. For alkali-activated slag, the high drying shrinkage is attributed to the absence of crystal phases such as portlandite due to the low Ca/Si ratio of the binder (0.8–1.1) [197].

5.2.2. Effect of specific surface area on drying shrinkage

Another major property of raw materials lies in the SSA. The influence of SSA on drying shrinkage magnitude of AAMs was plotted in Fig. 5.2. Same as the previous sections, there were some data points locating in the area over 15000 m^2/kg, which represents the addition of silica fume or other nano-particles in the matrix. Si et al. [189] introduced glass powder into MK-based geopolymer and found the reduced water loss rate of samples leading to a reduction of UDS. For better illustration, an amplified figure for the range between 0 and 5000 m^2/kg was inserted in Fig. 5.2. Similar to the results displayed in Fig. 5.1, most data points located in the range approximately

between 400 and 500 m^2/kg. These mix designs were generally AAS-based paste, mortar and concrete. Meantime, higher SSA of raw materials could mitigate the UDS magnitude. Specifically, Sadeghian et al. manufactured one-part AAS concrete. The results demonstrated that the addition of silica fume (SSA = 140000 cm^2/g) could considerably decrease UDS. Gong and Qu [187] investigated the mechanical properties and drying shrinkage of AAS mortar mixed with silica fume, nano silica and water glass powder. They found that the 3-day drying shrinkage was increased by 59.6% with the addition of 25 wt.% of silica fume, while the 56-day drying shrinkage was significantly reduced. They explained that the higher reactivity of silica fume needed higher water demand, leading to increased early shrinkage. However, when the amount of silica fume is over certain content (e.g., 10 wt.%), some of the particles filled in the pores rather than participated in the hydration, resulting in the reduction of drying shrinkage. Normally, raw materials with high SSA display relatively high reactivity, having impact on water consumption and pore structure. Drying shrinkage is triggered by the water loss in the pores, which may be mitigated or slowed down with the higher degree of matrix polymerization and loss of water dispersion [187]. In this sense, high SSA materials such as silica fume could improve the resistance of AAMs to the drying shrinkage.

5.2.3. Effect of alkali activator on drying shrinkage

Fig. 5.3 shows the influence of Ms on the drying shrinkage of the AAMs. A pronounced positive correlation of drying shrinkage with Ms was identified. Clearly,

the drying shrinkage of AAM pastes in Jiao et al.'s research increased as the Ms value changed from 1.00 to 1.80 [176]. Additionally, Adesanya et al. [35] also reported low drying shrinkage values with Ms = 0, whereas an increasing shrinkage occurred in some of the mortar as the sodium concentration increased, resulting in a decrease in Ms from 2.5 to 1. Similar experimental results were reported by Duran Atiş et al. [158] and Ye et al. [54]. Thomas et al. [171] investigated the influence of alkali activator concentration on the drying shrinkage of alkali-activated concrete and also revealed a higher magnitude shrinkage when Ms increased from 0.75 to 1.5. For sodium hydroxide alkali-activated slag, an increased dosage of Na_2O can lead to a higher magnitude of drying shrinkage, reduced mass loss, and a refined pore structure, which can be attributed to the increased degree of hydration [54].

Fig. 5.4 presents the effect of NaOH concentration of alkali activator on the drying shrinkage magnitude of AAMs. Different from the effect of Ms, a non-pronounced decreasing trend between NaOH concentration and drying shrinkage was found, especially for the experimental results by Jiao et al. [176]. They reported a significant reduction in UDS when NaOH concentration increased from around 4 M to 8 M. Meantime, Mermerdaş et al. [198] as well reported a negative effect of NaOH concentration on drying shrinkage behavior of MK and calcined kaolin blended concretes. Similarly, Hojati and Radlińska [173] reported their highest UDS (around 2750 με) at NaOH concentration of 2 M, while the lowest UDS (around 2060 2750 με) was found at NaOH concentration of 6 M.

Although increasing Ms may be beneficial to the development of compressive strength of AAM owing to the formation of smaller pore sizes, the tensile stresses of capillary pores would be increased, consequently leading to higher drying shrinkage rates [178]. Moreover, higher NaOH concentration normally causes a higher pH environment in system, which could make drying shrinkage and mass change of the matrix reach to plateau at a later age [173]. However, unlike alkali-activated slag mixtures, increasing the content of Na_2O in alkali activators contributes to a reduction in the drying shrinkage of alkali-activated FA mixtures, which may be related to the reduced porosity and improved strength and stiffness, as reported by Thomas et al. [171].

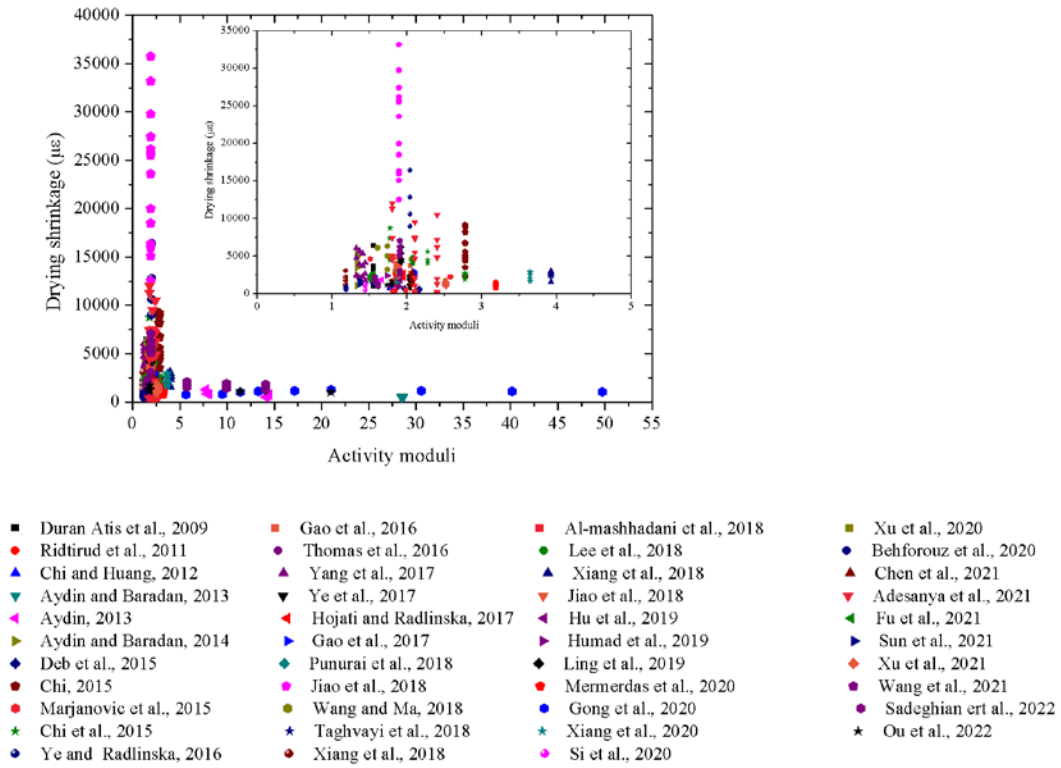

Fig. 5.1. Effect of activity moduli on drying shrinkage

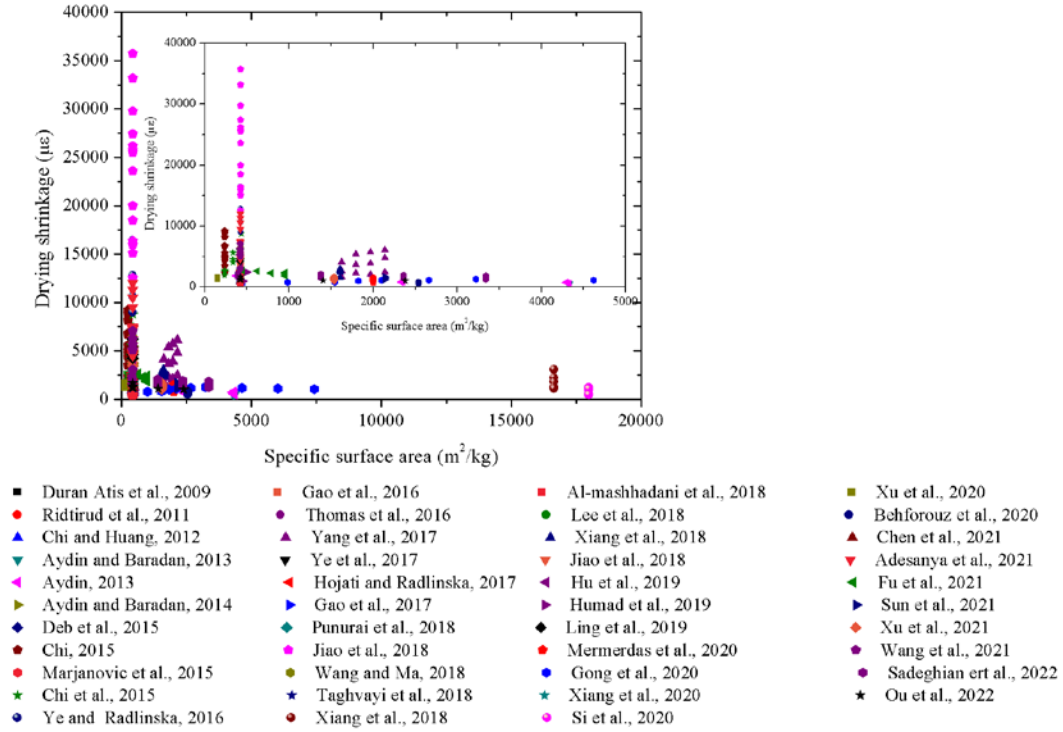

Fig. 5.2. Effect of specific surface area on drying shrinkage

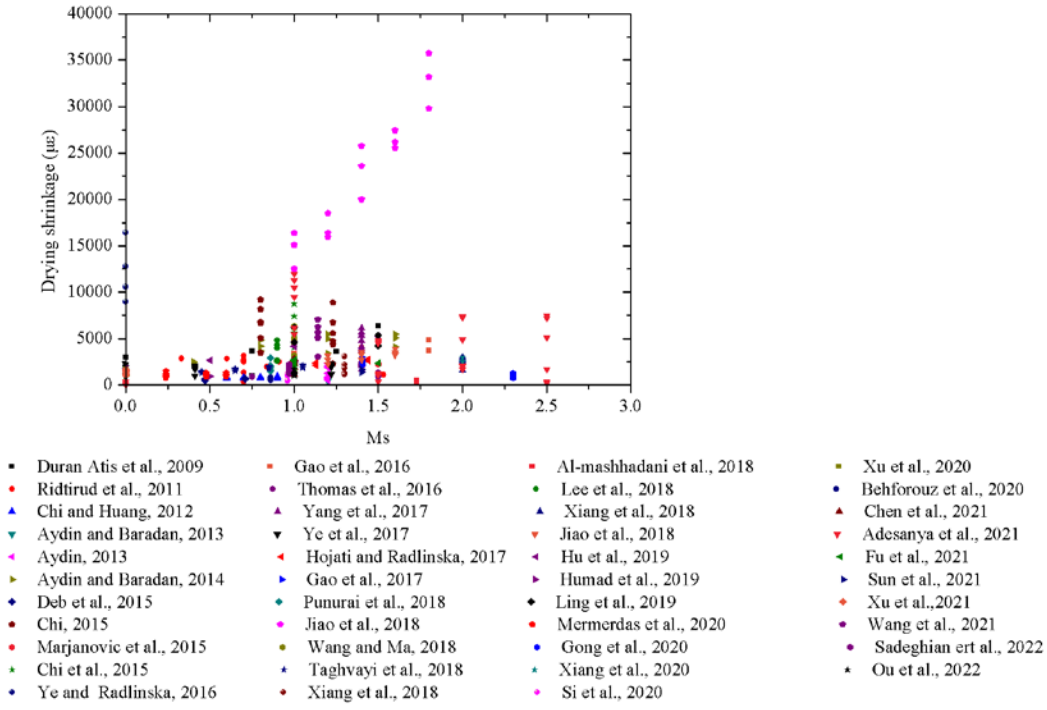

Fig. 5.3. Effect of Ms on drying shrinkage

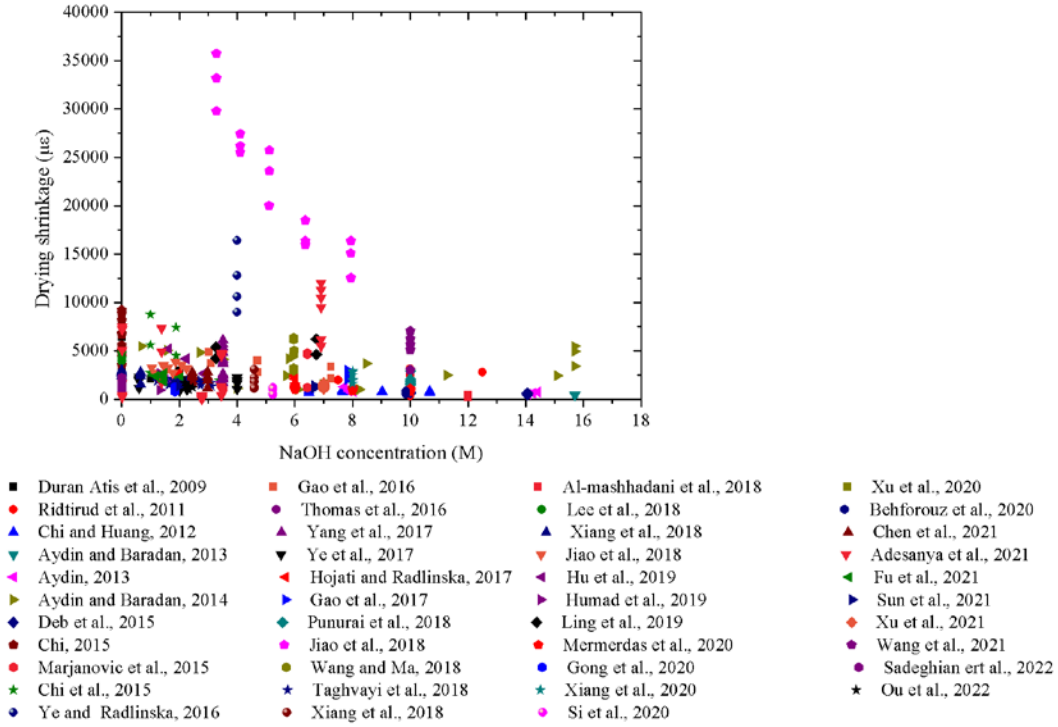

Fig. 5.4. Effect of NaOH concentration on drying shrinkage

5.2.4. Effect of liquid-to-binder ratio on drying shrinkage

Fig. 5.5 shows how the L/B ratio affected the UDS of the AAMs. No obvious tendency was observed; nevertheless, some specific rules could be drawn out by investigating the data of individual experiments. The UDS results of Gao et al. [72] showed an increasing trend with the L/B ratio. The UDS of alkali-activated slag–FA composites increased from 2159 to 4871 με when the L/B ratio increased from 0.43 to 0.44. In addition, Chi and Huang [159] reported that alkali-activated slag mortar showed a relatively low drying shrinkage magnitude when the L/B ratio was lower than 0.30. Adesanya et al. [35] also revealed a positive relationship between the drying shrinkage and L/B ratio, which could be observed in the L/B ratio range of 0.36 to 0.39. Aydın and Baradan reported the similar trend that the UDS increased from 1000 με to

5477 με when L/B ratio increased from 0.36 to 0.38 [168]. Interestingly, the experimental results by Aydın and Baradan also displayed a negative effect of L/B ratio on the UDS when L/B ratio was higher than 0.39. When take a close look into these points, it could be found that the Ms values were different that the high UDS were normally observed when Ms was 1.6. They explained that the higher Ms easily resulted in porous microstructure and existence of higher volume of mesopores [168]. Hence, the possible synergistic effect of other key factors may be considered. As mentioned previously, drying shrinkage is involved in moisture movement in mixtures. In general, the high magnitude drying shrinkage of AAMs caused by the higher L/B ratio could be attributed to a greater volumetric ratio of cementitious material paste and less restraint of deformation; under some conditions, the L/B ratio may not be as remarkable as it was supposed to be. The pore size distribution, porosity of mixtures, and elastic modulus may compensate for the overall effect of drying shrinkage.

5.2.5. Effect of geopolymer paste content and aggregate content on drying shrinkage

Figs. 5.6 and 5.7 demonstrate the influence of the geopolymer paste content and aggregate amount on shrinkage development. The tendency of shrinkage with respect to the aggregate volumetric ratio in general was opposite to that with respect to GPC. However, the influence of aggregate amount and GPC are two independent variables. Notably, the aggregate volumetric ratio, herein, was not directly calculated by 1 – GPC because of the existence of fibers and fillers that are separately calculated in some studies. Moreover, the shrinkage performances of geopolymer paste and aggregates are

completely different: the volume of geopolymer paste may shrink due to moisture loss, but the aggregate volume cannot be changed. As previously discussed, the internal restraint caused by the addition of aggregates can remarkably improve the volume stability. Therefore, the average drying shrinkage strains of all AAM mortar and concrete with a value of 2199 με were lower than that of the AAM paste with a value of 10450 με, indicating a significantly decreasing trend in shrinkage with the aggregate volumetric ratio. AAM paste mixtures manufactured by Jiao et al. [176] and Ye and Radlińska [17] exhibited a fairly high UDS over 10000 με. Yang et al. [172] compared the differences in pore structures and shrinkage characteristics of FA–metakaolin-based geopolymer pastes and mortars. The observed volume change of the metakaolin-based geopolymer was mainly caused by the drying shrinkage rather than autogenous shrinkage, and the geopolymer mortars could provide better compressive strength and lower total shrinkage compared to the geopolymer pastes. Moreover, a sharp reduction in the shrinkage due to the increasing amount of aggregate was also shown in Adesanya et al.'s experiment [35], in which a reduction of drying shrinkage up to 98.3% was observed when the aggregate volumetric ratio increased from 0.53 to 0.56. The introduction of lightweight aggregates in FA–based geopolymer mortar studied by Mermerdaş et al. [151] should be specifically noted. The average UDS of fly-ash–based lightweight geopolymer mortar was 1064 με, which is relatively small compared to those of other geopolymer mortars or concrete. Such effectiveness in mitigating drying shrinkage can be ascribed to the internal curing property of lightweight aggregates [151]. The absorbed water in saturated lightweight aggregates can be released into the

spaces owing to chemical shrinkage, which increases the internal RH and reduces self-desiccation [199]. Behforouz et al. [191] mixed recycled aggregate in metakaolin-based AAMs to produce an eco-friendly geopolymer concrete and reported a fairly low drying shrinkage results. Furthermore, the adoption of fine and coarse aggregates not only enhances the mechanical properties of AAM mixtures, but also decreases the paste volume, lowering the environmental impacts owing to the production of alkali activators [12].

5.2.6. Effect of curing conditions on drying shrinkage

Fig. 5.8 shows the effect of temperature on the development of drying shrinkage of the AAM mixtures. The curing temperature was normally set in the range of 20–60 °C, and the reduction in the UDS with elevated temperature is shown in this figure. The fairly low average shrinkage strain of 1060 με at a temperature of 22 °C should be due to the existence of coarse aggregates, which enhance the stiffness of alkali-activated FA and slag geopolymer [171]. Similarly, the relatively low shrinkage value reported by Aydın and Baradanv [168] at a temperature of 20 °C should be assigned to the addition of steel fibers. The other low values of UDS (< 1000 με) reported by Adesanya et al. [35] may be related to the Ms value of 0. Moreover, the highest temperature of 60 °C reported by Adesanya et al. [35] also demonstrated a mitigation effect on the drying shrinkage of AAMs.

The influence of RH on the UDS should inevitably be mentioned, as demonstrated in Fig. 5.9. Generally, a higher RH could prevent a high drying shrinkage occurring in

AAMs. Most research data on drying shrinkage were obtained from the AAM mixtures exposed to 50% RH, beyond which the collected shrinkage were basically lower [54, 158, 182]. This phenomenon could be explained by capillary pressure theory, which states that the surface tension of the pore solution in the pores, generated in the meniscus formed by pore water evaporation, is the driving force of drying shrinkage, leading to volume reduction of mixtures [79]. Above 40%–50% RH, capillary pressure is the main force and the radius of the meniscus decreases with lower RH [200]. However, when RH continues to decrease, the driving force of the drying shrinkage changes, which is also reflected in Fig. 9. Ye and Radlińska [17] reported a decreasing trend in the drying shrinkage of alkali-activated slag paste when the RH decreased from 50% to 11% RH. Moreover, the drying shrinkage strains measured at 11%, 30%, 50%, and 70% RH were 9000, 10600, 16400, and 12800 με, respectively, indicating that the RH significantly affected the hydration products and the shrinkage kinetics of alkali-activated slag; thus, it is governed by the experienced RH. At high RH, a viscous characteristic of AAM was observed, possibly due to the rearrangement and reorganization of C-A-S-H. Ye and Radlińska [17] also found that micropore closure, silicate polymerization, and new interlayer formation occurred during the rearrangement of the microstructure. Because of the structural incorporation of alkali cations (Na^+) in C-A-S-H, the stacking regularity of the C-A-S-H layers was weakened, resulting in the potential collapse of C-A-S-H, and subsequently, a large drying shrinkage occurred. The lower shrinkage observed at 11% RH may be because the C-A-S-H particles densified, leading to a reduction in the interlayer spacing. RH control is important for AAM mixture curing;

if sufficient water is provided (RH is close to 100%), the drying shrinkage problem may be greatly improved.

Last but not least, size effect of specimen that was always neglected in the previous researches should also be considered. Here, the effect of specimen size on the drying shrinkage has been converted into the V/S ratio. V/S ratio is also regarded as the effective drying thickness of the cementitious material. Fig. 5.10 illustrates the effect of V/S ratio on the drying shrinkage performance of AAMs. It can be seen that the most specimen size was set as 5.99 that is a standard prismatic shrinkage bar according to ASTM C596 [114]. Also, there were some specimens with the V/S ratio of 5.95 and 5.98. Such specimens had the same cross section but varied in the height compared to the standard shrinkage bar. Ye used a modified shrinkage bar with the size of 12.7 mm × 12.7 mm × 139.7 mm for reaching the equilibrium shrinkage in a relatively short period in Refs [54, 201]. From this figure, a decreasing trend of drying shrinkage with the higher V/S ratio could be observed, indicating that larger specimen size may show a lower shrinkage magnitude. Deb et al. [164] reported a fairly low shrinkage result with the largest specimen size of 75 mm × 75 mm × 285 mm. Such finding showed a good agreement with the existing literature [9]. The effect of specimen size on the drying shrinkage could be assigned to the internal humidity distribution that the deeper effective drying thickness, the higher internal humidity. In the practical construction work, V/S ratio could be easily controlled according to the formwork size.

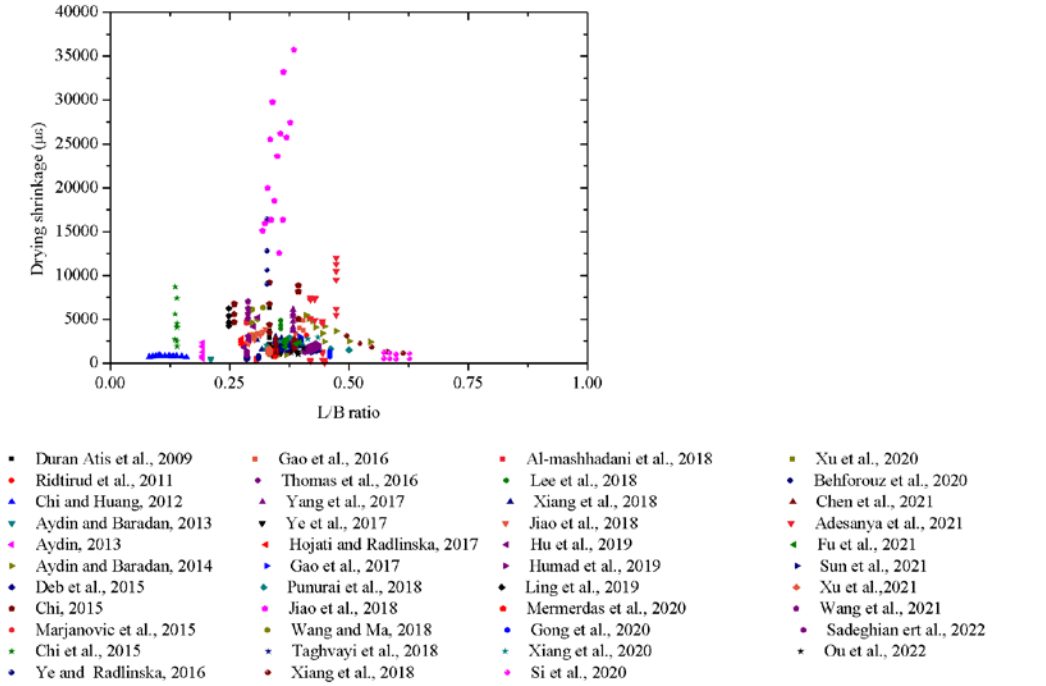

Fig. 5.5. Effect of L/B ratio on drying shrinkage

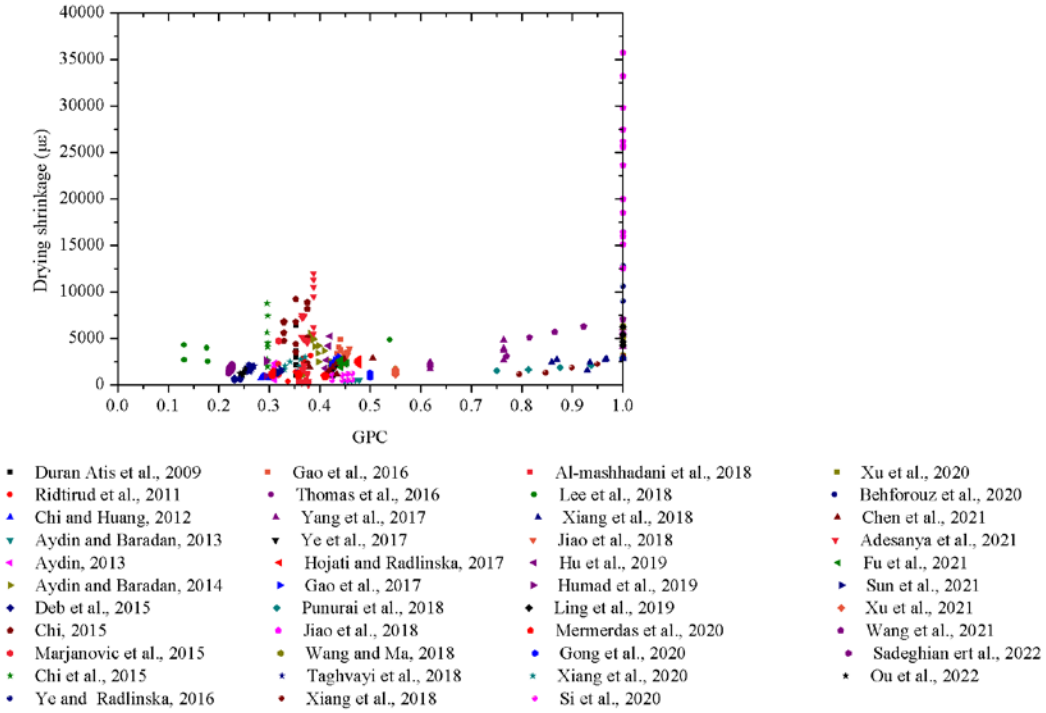

Fig. 5.6. Effect of GPC on drying shrinkage

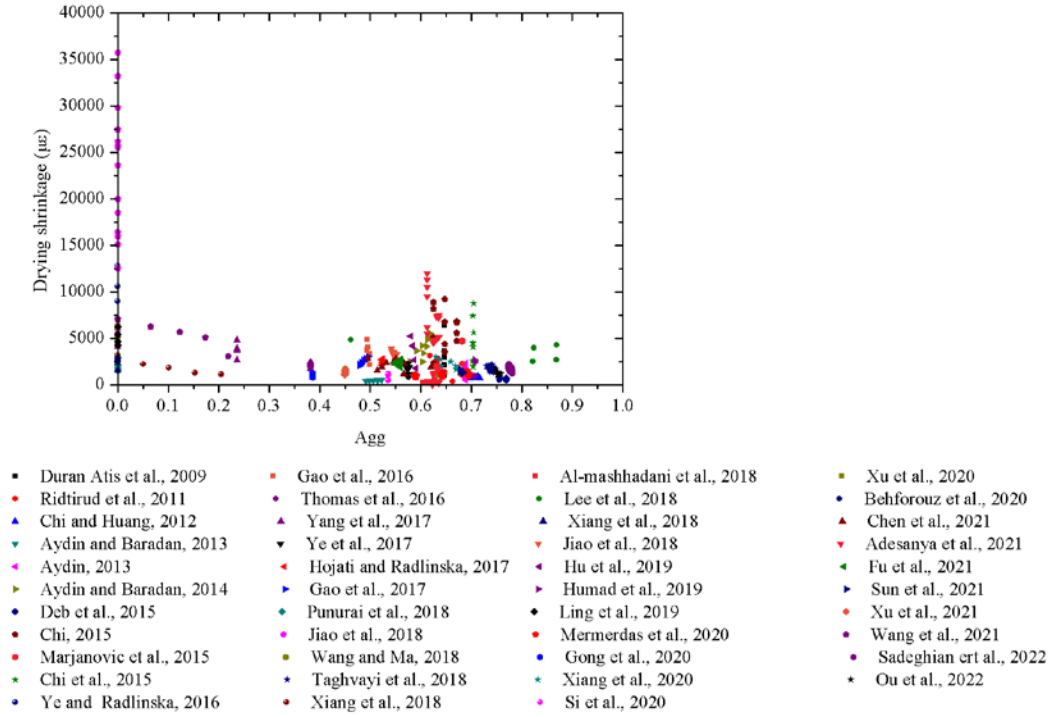

Fig. 5.7. Effect of aggregate content on drying shrinkage

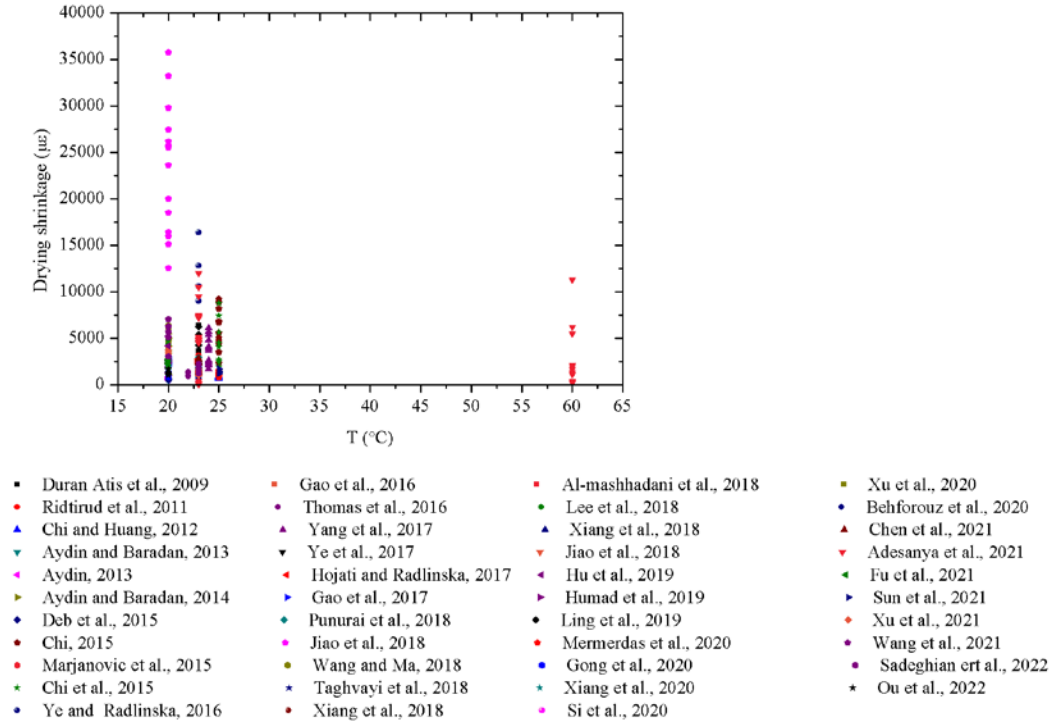

Fig. 5.8. Effect of curing temperature on drying shrinkage

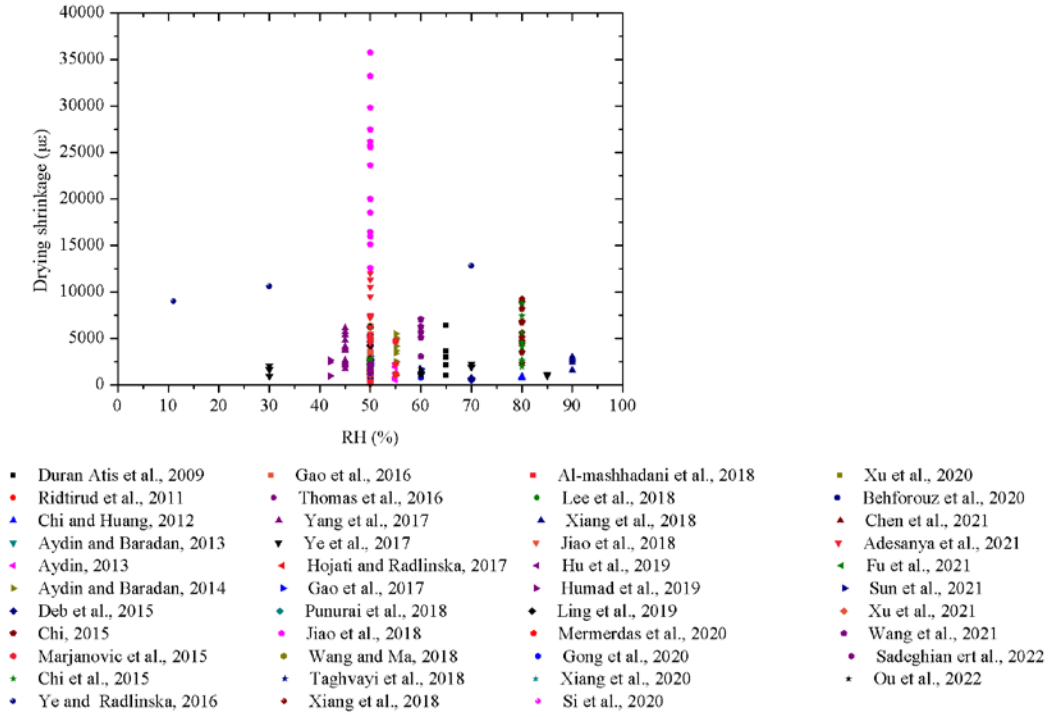

Fig. 5.9. Effect of relative humidity on drying shrinkage

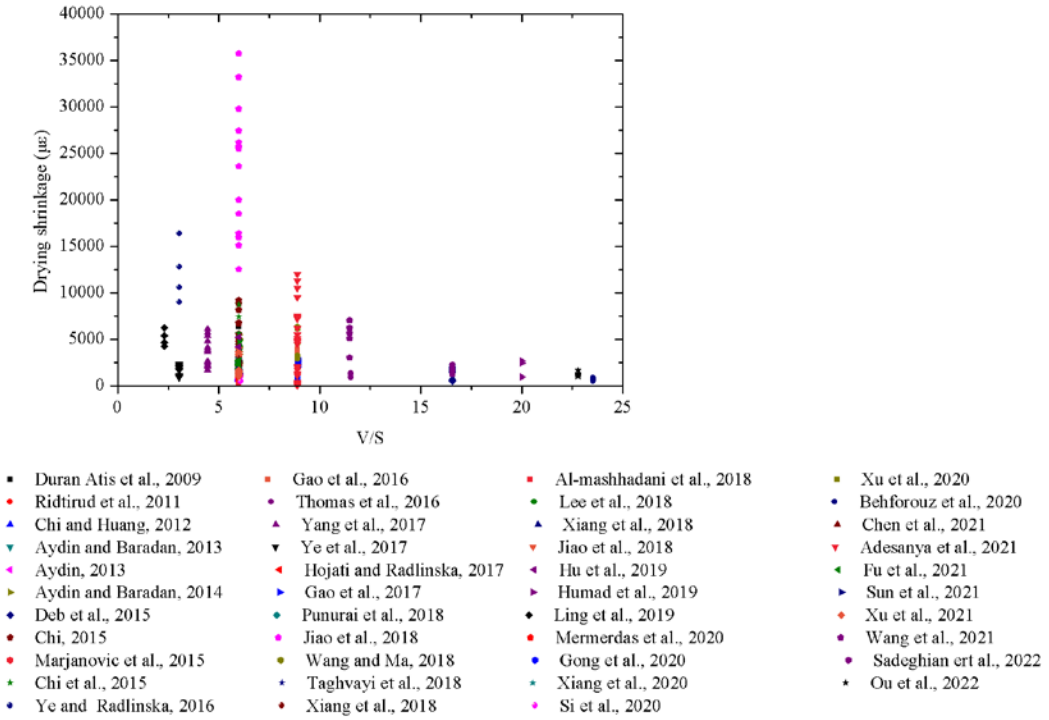

Fig. 5.10. Effect of volume-to-surface ratio on drying shrinkage

5.3. Machine learning modelling and discussions

According to the former analysis on the effect of mix design on the drying shrinkage magnitude of AAMs, a total of eleven key factors were concluded, including the activity moduli and SSA of the binder, GPC, L/B ratio, NaOH concentration, Ms, fine and coarse aggregate content ratio, curing temperature, RH and V/S ratio. As mentioned above, the existing models for predicting the drying shrinkage of AAM have several problems and limitations lying in the limited generality. Therefore, in general, these models do not agree with each other. It is strongly recommended that a drying shrinkage model should be established based on the key factors of AAM as identified in this research, which can be directly designed or controlled before manufacturing the mixtures. In this sense, three prediction models for UDS using BPNN, LGBM and XGBoost were proposed. The obtained 438 AAM mixtures from literature were all used for the model construction. The key factors of AAM were set as input data that could be easily obtained in predicting shrinkage performance. The hyperparameters for each algorithm were listed in Tables 5.3-5.5, in which BPNN model was illustrated in Fig. 5.11. Moreover, the machine learning-based mathematical model is user-friendly, even for practitioners with no computational skills.

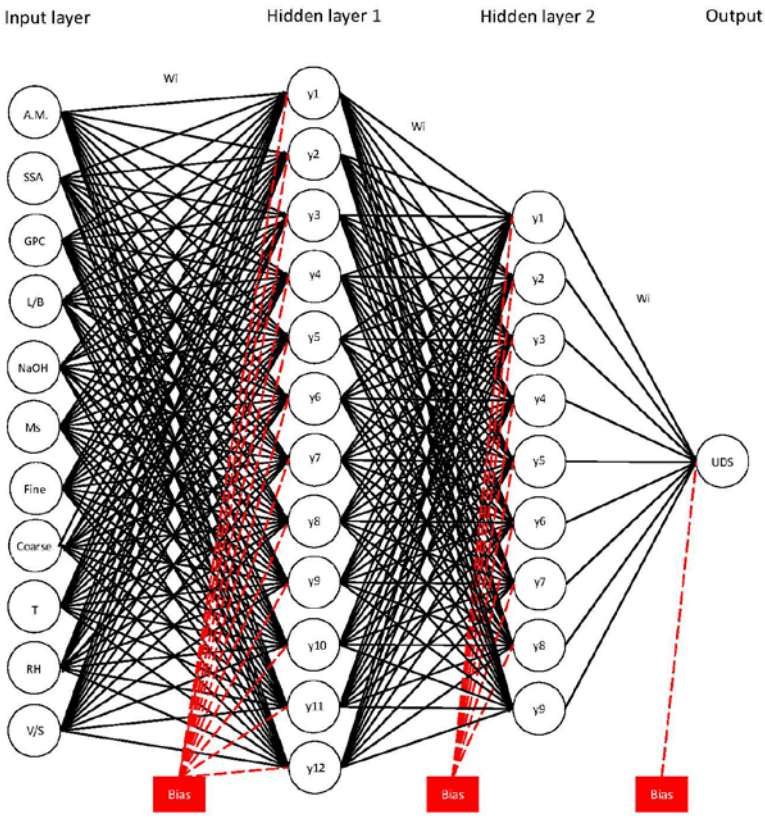

Fig. 5.11. Structure of the proposed BPNN model for UDS.

Table 5.3. Properties of BPNN model for drying shrinkage

Details	Selection
Network architecture	Backpropagation network
Number of input layer	1
Number of hidden layer	2
Number of output layer	1
Number of neurons in input layer	11
Number of neurons in hidden layer 1	12
Number of neurons in hidden layer 2	9
Number of neurons in output layer	1

Activation function	Tan-sig
Learning rate	0.00001
Moment rate	0.95
Training algorithm	Trained (gradient descent with momentum)

Table 5.4. Parameters of the proposed LGBM regression model

Hyperparameter	Selection
boosting_type	GBDT
objective	Regression
learning_rate	0.1
max_depth	10
n_estimators	958
num_leaves	64
min_child_samples	8

Table 5.5. Parameters of the proposed XGBoost regression model

Hyperparameter	Selection
boosting_type	GBDT
objective	Regression
learning_rate	0.11
max_depth	8
n_estimators	550

subsample	0.7
Colsample_bytree	0.75
min_child_weight	1

5.4. Model performance evaluation

Fig. 5.12 illustrates the performance of the proposed BPNN, LGBM and XGBoost models, revealing a relatively high R^2 value of 0.94, 0.99 and 0.99, respectively. Moreover, data points from independent test results by different researchers consistently align with the dashed line of y = x, affirming the high accuracy of the drying shrinkage model. Importantly, same as the previous models, the proposed UDS prediction model also did not deliberately exclude any data points. For comparison, a MLR model was constructed showing as Eq. 5.1.

$$\text{UDS } (\mu\varepsilon) = 9.58\text{Activity moduli} - 0.393\text{SSA} + 56475\text{GPC} + 7423\text{L/B} - 37.3\text{NaOH} + 1239\text{Ms} + 45013\text{Fine agg.} + 41711\text{Coarse agg.} - 64.68\text{T} + 12\text{RH} + 106.47\text{V/S} - 49499 \quad (5.1)$$

where T represents the curing temperature (℃), RH represents the relative humidity (%), and V/S is the volume-to-surface ratio of the sample. The evaluation results were listed in Table 5.6. Compared to the MLR models constructed in Chapters 3 and 4, MLR model for UDS contained three other key factors related to the curing conditions. In the

MLR model, positive effects of GPC and L/B ratio on the drying shrinkage development were revealed by their coefficients. However, several coefficients of key factors (e.g., aggregate content, RH) were opposite to the previous qualitative analysis, which was caused by the regression algorithm based on all key factors. Compared to the prediction performance of MLR models for workability and strength, MLR model for UDS interestingly showed a higher accuracy with statistic R^2 value of 0.41. When predicting the UDS smaller than 10000 με, MLR also displayed a quite good prediction performance, while the predicted UDS were always underestimated when the UDS larger than 15000 με.

Table 5.6. Prediction performance comparison

Model	R^2	MAE	RMSE
BPNN model	0.94	591.58	1062.47
LGBM model	0.99	146.91	423.22
XGBoost model	0.99	128.01	413.32
MLR model	0.41	2098.03	3515.80

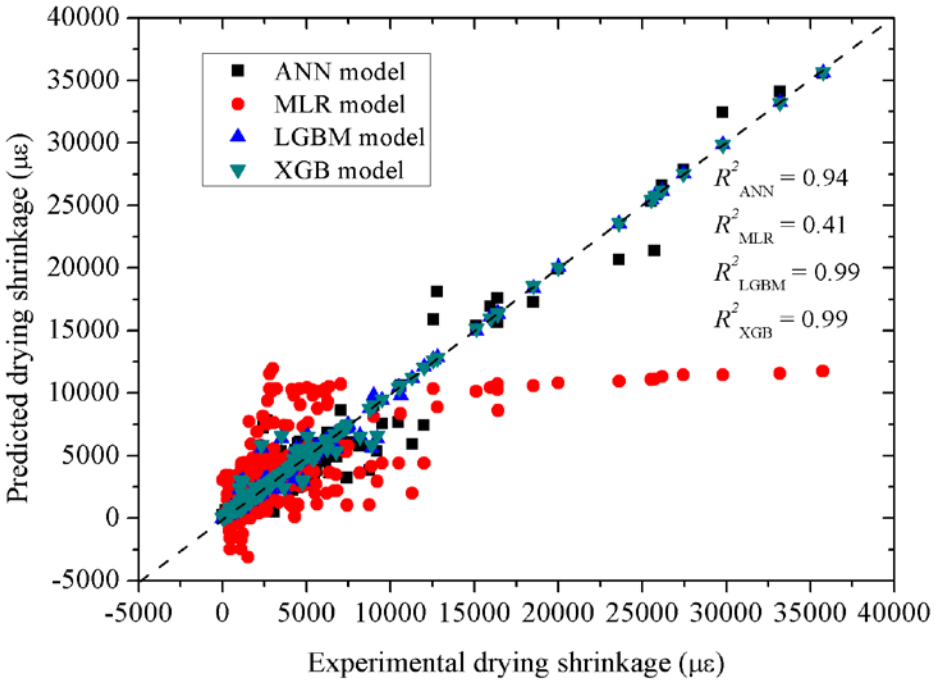

Fig. 5.12. Prediction performance of the BPNN, LGBM, XGBoost and MLR models.

5.5. Feature importance analysis

From the previous section, XGBoost algorithm showed the highest performance in predicting ultimate drying shrinkage of AAMs among these three algorithms. Fig. 5.13 plotted the normalized feature importance score results for the input variables used in the proposed XGBoost model and MLR model. This time, it can be clearly seen that GPC demonstrated the highest feature importance score (0.277) compared to other key factors. Regarding the MLR-based feature importance analysis results, GPC also displayed the highest absolute value among the features, showing a good agreement with that of machine learning-based feature importance analysis. The relatively higher

importance of GPC was because drying shrinkage only happens in the geopolymer paste part.

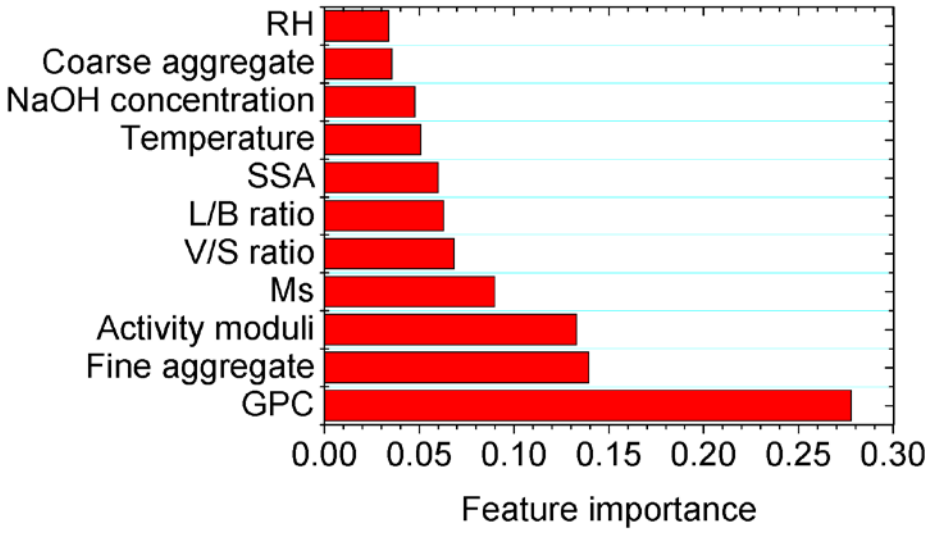

(a)

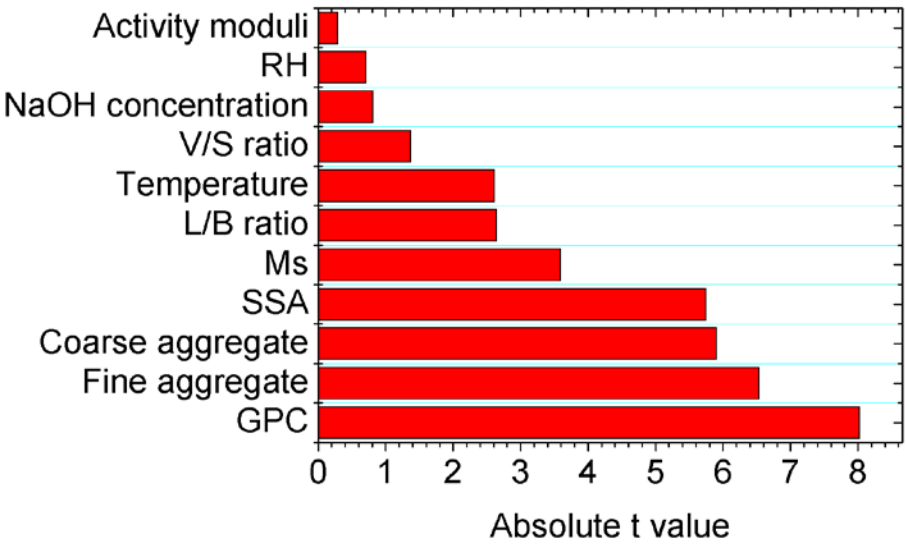

(b)

Fig. 5.13. Feature importance analysis results based on (a) Machine learning algorithm; and (b) MLR regression.

5.6. Comparison of ANN, XGBoost, LightGBM and MLR

According to the model performance evaluation results in Chapters 3, 4 and 5, it can be concluded that machine learning-based models always outperformed than MLR model. This phenomenon can be explained by that machine learning can capture non-linearity between input and output data, while MLR only assumes a linear relationship leading to weaker prediction.

Another interesting finding is that GBDT algorithm (used in XGBoost and LightGBM models) always showed better performance than deep learning algorithm (used in ANN model). There are two major reasons for that. (1) Feature engineering and data preprocessing: GBDT models require minimal feature scaling and transformation, handling categorical features naturally without complex encodings. In contrast, deep learning models need significant preprocessing, normalization, and often complex embeddings for categorical data. (2) Interpretability: GBDT models offer high interpretability with clear feature importance, essential for understanding decision-making processes. Deep learning models, especially deep neural networks, are often considered "black boxes" due to their complexity, making their predictions harder to interpret.

5.7. A summary of key conclusions in this chapter

In this study, the UDS of AAMs was qualitatively and quantitatively analyzed using a total of 438 AAM mixtures extracted from 43 papers. Eleven key factors governing

the drying shrinkage performance of AAMs from the perspectives of mix design and curing conditions were identified, including the activity moduli and SSA of the binder, GPC, L/B ratio, NaOH concentration, Ms, fine and coarse aggregate content ratio, curing temperature, RH and V/S ratio.

Qualitative analysis indicated that the resistance to drying shrinkage of AAMs generally increased with NaOH concentration, aggregate ratio, curing temperature, RH, and V/S ratio, whereas it decreased with GPC, L/B ratio, and Ms. The reactivity of the binder expressed by activity moduli had an upper limit of 2.00 in increasing shrinkage, beyond which the drying shrinkage could be mitigated. The influence of fibers on the shrinkage should be considered, which could enhance the volume stability of AAMs.

Quantitative analysis was conducted by constructing a model for predicting the UDS of AAM mixtures based on ANN, LightGBM and XGBoost models. The key factors were set as input data, and the UDS results were set as the output data. Among these three prediction models, the XGBoost showed good performance in predicting the UDS of various types of AAM with a high R^2 value of 0.99. For comparison, the MLR model was also conducted. MLR model showed an efficient prediction when the shrinkage magnitude was low, but could not precisely predict the high shrinkage magnitude. The much lower R^2 values, and higher MAE and RMSE values of the MLR model than those of the machine learning-based models indicated a better prediction performance of the machine learning model. Moreover, feature importance analysis was conducted for the proposed model, and the results showed that GPC left the highest importance on the drying shrinkage prediction, both for machine learning and MLR.

Meantime, fine aggregate content and activity moduli also displayed a fairly higher importance compared to other variables. The superior performance of machine learning algorithm compared to MLR can be attributed to the ability of capturing non-linearity. Additionally, due to the different feature engineering and interpretability, GBDT algorithm demonstrated a better performance than deep learning algorithm. This study fills the research gap in comparing and predicting the drying shrinkage of various types of AAMs by compiling the valuable data extracted from the literature and constructing a prediction model with high accuracy. Hence, this study will significantly improve the understanding of AAMs in optimizing the mix design for civil engineering applications.

Chapter 6: Prediction of AAM mix design based on the target properties and life cycle assessment

In the former chapters, the forward prediction models for workability, compressive strength, and drying shrinkage were successfully constructed using artificial neural networks. According to the workflow mentioned in the previous chapters, the pre-constructed machine learning model could be used in the inverse prediction by calculating the mechanical properties of random mixes. In this chapter, data generation and inverse prediction were conducted for producing an index of AAM mixes for searching. Following that, a life cycle assessment is conducted to evaluate the environmental impacts of the predicted mix designs. Combining desired properties and environmental impacts, a workflow of choosing optimal AAM mixes for decision-makers was put forward.

6.1. Concept of performance-based prediction for mix design

6.1.1. Importance and idea of inverse prediction

In the previous chapters, three proposed machine learning-based prediction models were constructed for fulfilling the research gap lying in the generality and convenience. In the real construction work, these models can immediately predict the fresh and hardened properties of certain AAM mix designs for decision makers without any experiment, saving cost in time, labor and materials. However, as mentioned in

Introduction part, most decision makers favor more on the “best” mix design that can satisfy their requirements rather than knowing the exact properties of a certain mix. In this situation, the forward prediction models cannot provide one or more back-up mix designs for decision makers. Unfortunately, determining a proper mix design for AAM is much more difficult than that for cement-based materials, which is the biggest barrier to commercial applications of AAMs. Fig. 6.1 shows the difference in determining mix design between OPC and AAM by giving the same requirements. For cement-based mix, OPC is standardized and classified for different usage. Second, the raw material component is mainly associated with only cement, water and aggregate. Most importantly, due to the mature development of OPC, there exist sufficient design codes helping mix design. In contrast, AAM mixes are faced with two major problems. First, the components are much more complicated than OPC-based mix, attributed to various types and dosages of precursors and alkali activators. Second, up to now, there is still no such a systematical design code or guideline for AAMs. Hence, researchers still need conduct trial-and-error experiment to determine the mix design. Therefore, it is urgent to develop a workflow/program of inverse prediction for making the AAM mix design based on the target properties.

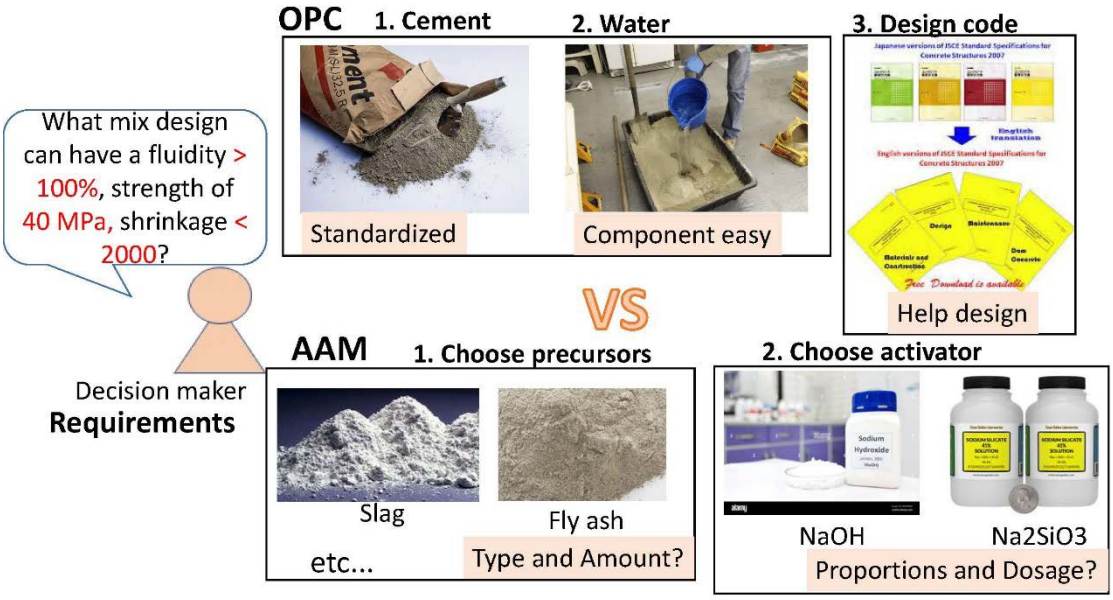

Fig. 6.1. Comparison in determining the mix design between OPC-based and AAM-based.

The main idea of the proposed inverse prediction is using the pre-constructed models to predict new AAM mixes for finding the requirements-satisfied ones. The inverse prediction for predicting sustainable AAM mix design follows this workflow: (i) Construction of forward prediction models for strength of AAMs based on the machine learning algorithm; (ii) Generation of new mix design data using random method or Gaussian mixture model (GMM); and (iii) Calculation of strength results for new mix designs; and (iv) Filtration out the mixes satisfying the required strength. An illustrative workflow was plotted in Fig. 6.2. Here, step (i) has been completed in previous sections. Hence, the analysis of this part mainly lied in the latter three steps.

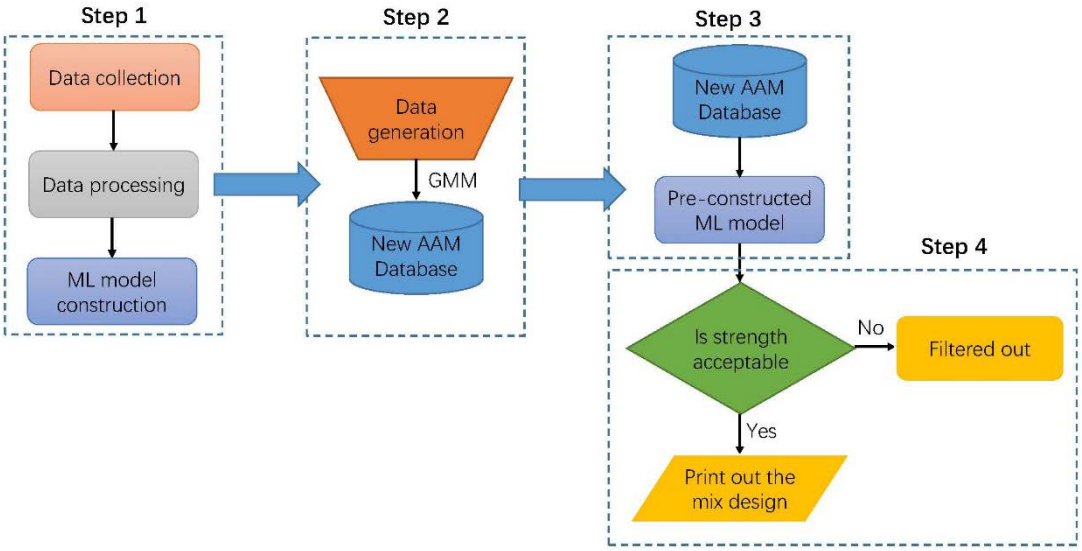

Fig. 6.2. Illustrative workflow for inverse prediction

Finally, the available mix design generated by the Kaneko's python code were used as the new input data in the pre-constructed machine learning model to acquire the predicted strength. A desired property (e.g., 28-day compressive strength of 40 MPa) and an acceptable error (e.g., +10%) were set for filtration out the satisfied mix design.

6.1.2. Data generation

For generating new mixes, a python-based Gaussian Mixture Method (GMM) program developed by Kaneko[1]. The code performs model selection for a GMM using Bayesian Information Criterion (BIC), fits the optimal model to the data, and generates synthetic samples from the learned model. Note that the data used for GMM was same as the previous data in BPNN model construction. In this code, a Gaussian mixture

[1] https://github.com/hkaneko1985/dcekit

model (GMM) was used for generating random data. A GMM, one of the categories of unsupervised learning, is a probabilistic model that assumes all the data points are generated from a mixture of a finite number of Gaussian distributions with unknown parameters, where each data point is assigned to the most probable cluster showing in Fig. 6.3 [202]. GMMs are commonly used for clustering and density estimation tasks. Mixture models can be viewed as an extension of k-means clustering that integrates insights into both the covariance structure of the data and the central tendencies of the latent Gaussians [203]. The probability distribution for the GMM is given in the following equation [204]:

$$P(x) = \sum_{k=1}^{k} \pi_k N(x|\mu_k, \sigma_k) \quad (6.1)$$

where π_k represents the probability weight of the k-th submodel that meets $\sum_{k=1}^{k} \pi k = 1$; $N(x|\mu_k, \sigma_k)$ is the k-th Gaussian distribution of this model in which μ_k and σ_k represent the mean and covariance, respectively. μ_k and σ_k describe the geometric characteristics of clusters.

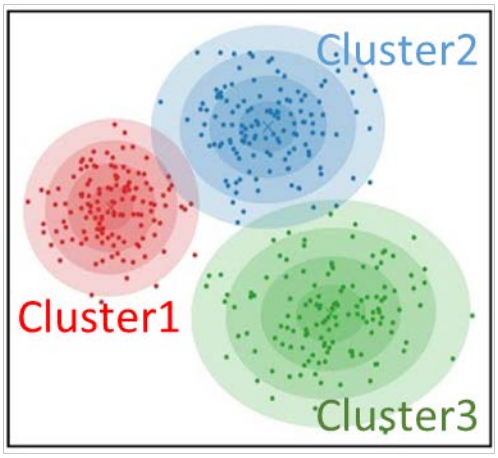

Fig. 6.3. Illustration for Gaussian Mixture Model.

The clusters are ellipsoidal with the center determined by the mean μ_k. Covariance matrix determines the volume, shape and orientation. Therefore, finding the optimal number of components and covariance type becomes the primary task for clustering analysis using GMM. Here, a grid search using BIC was conducted, which is a criterion for model selection among a finite set of models [205]. The BIC values were computed as Eq. 6.2 for different combinations of covariance types and numbers of components, balancing the goodness of fit of a model and its complexity [205].

$$\text{BIC} = -2\times\text{log-likelihood} + k\times\log(n) \tag{6.2}$$

where log-likelihood is the logarithm of the maximum likelihood of the model given the data; k represents the number of free parameters in the model; and n is the number of data points. From the BIC calculation formula, it can be seen that the optimal model

is the one that minimizes the BIC, indicating a good fit to the data while avoiding overfitting.

After obtaining the optimal GMM, a total number of 1000000 synthetic mixes were generated. Note that there existed several negative (< 0) or unreasonable values (e.g., GPC > 1) in generated data, which is impossible in real construction work. Therefore, data filtration for the generated samples was conducted. Meantime, we also provided a random generation dataset for comparison. The randomly generated database were constructed based on the same dataset used for GMM algorithm. The range for each key factor was set lying in the biggest cluster according to the original dataset. Specifically, Activity moduli range was set between 1 and 5; SSA range was set between 300 and 3000 m^2/kg; GPC range was set between 0.2 and 1; L/B ratio range was set between 0.1 and 1.2; NaOH concentration range was set between 0 and 14 M; Ms range was set between 0 and 1; Fine aggregate content was set between 0 and 0.7; and Coarse aggregate content range was set between 0 and 0.5.

6.1.3. Distribution of generated data

According to the abovementioned method, a total number of 614234 available synthetic mix designs were automatically generated by GMM. Meantime, random generated database was also analyzed for comparison. Prior to calculating the mechanical properties of these mixes, a data analysis was firstly conducted. For comparison, original database on mix and strength of AAMs was as well analyzed. Tables 6.1, 6.2 and 6.3 listed out the data description of the original dataset, GMM-

generated dataset and random generated dataset. Apart from the difference in the number of data, other features in original and GMM generated key factors were generally close. Among these key factors, the largest difference occurred to SSA, in which the average value increased by 36.1% in data generation. Compared to the original data, another major difference lied in the minimum values of activity moduli and SSA. Specifically, these two minimum values were extremely close to 0.00, which was not realistic. In contrast, random generated data showed similar average values compared to original dataset lying in the SSA, L/B ratio, NaOH concentration and coarse aggregate content, while activity moduli, GPC and fine aggregate content showed quite different values. The minimum and maximum values for each key factor were determined by the given range, controlling the average values. However, when focusing on the data distribution results, the results between the GMM and random generated dataset were totally different. For GMM, the first, median and third quartiles were generally close to the original database. For instance, the first, median and third quartiles of GPC in original dataset were 0.23, 0.31 and 0.38, respectively. Likewise, the first, median and third quartiles of GPC in GMM generated dataset were 0.23, 0.29 and 0.36, respectively. However, for random method, all these values displayed different. Specifically, the first, median and third quartiles of GPC in random generated dataset were 0.39, 0.50 and 0.60, respectively. Figs. 6.2 and 6.3 display the Pearson correlation coefficient matrix and scatter matrix plot, respectively. The Pearson correlation coefficient is a statistical measure that quantifies the strength and direction of the linear relationship between two variables. Values close to 1 (-1) indicate a strong

positive (negative) linear relationship, while values close to 0 indicate a weak or no linear relationship. Same as the data summary results listed in Tables 6.1, 6.2 and 6.3, the Pearson correlation coefficient matrix (Figs. 6.4a, b and c) and scatter matrix plot (Figs. 6.5 a, b and c) were in generality similar for original and GMM database. On the other hand, the Pearson correlation coefficient matrix and scatter matrix plot of random generated database were totally different from original database. In Fig. 6.4c, except the GPC and aggregate content, all individual variables showed nearly no linear relationship. Moreover, in Fig. 6.5c the data points randomly located everywhere for most variables. Therefore, it could be seen that GMM generated database showed a good agreement with the original dataset, which can provide traditional mix design for decision makers. In contrast, random generated dataset did not follow the data distribution of original one, which can help researchers explore new mix design that not adopted before. Both of these two data generation methods can be applied to the real construction work, this dissertation used GMM generated dataset as the example to display the AAM mix design prediction workflow in the following parts. Notably, although GMM can provide similar dataset with original one, there were several Pearson correlation coefficients demonstrating quite a large difference. For example, the coefficients in original data and generated data for L/B ratio and NaOH concentration were -0.0084 and 0.092, respectively. The difference can be explained by the sensitivity of GMM to initialization [202]. GMM training was sensitive to initial parameter values. Different initializations may lead to different local minima, affecting the quality of the learned model. Specifically, the initial values in SSA of precursors

varied in a large range from 420 to 19815, which was caused by the adoption of rarely used precursors such as silica fume and nano-particles in system. Due to the existence of these data points in the initial dataset, the GMM might capture these patterns during training, affecting the quality of generated samples. Overall, these generated samples could be used for the further calculation in the pre-constructed model.

Table 6.1. Data description of original mix design

	Activity moduli	SSA	GPC	L/B	NaOH concentration	Ms	Fine aggregate	Coarse aggregate
Mean	3.83	1500.23	0.35	0.60	7.10	0.72	0.42	0.22
Std	3.91	3028.27	0.18	0.21	5.32	0.47	0.19	0.21
Min	1.20	237.00	0.21	0.09	0.00	0.00	0.00	0.00
25%	1.70	420.00	0.23	0.48	1.40	0.48	0.27	0.00
50%	1.92	424.00	0.31	0.55	7.00	0.64	0.47	0.15
75%	3.19	1760.00	0.38	0.74	12.00	0.97	0.59	0.47
Max	20.98	19815.00	1.00	1.20	16.00	2.50	0.72	0.62

Note: Count: Number of data; Mean: Average value of the total data; Std: Standard deviation; Min: Minimum value; 25%: First quartile (25th percentile); 50%: Median (50th percentile); 75%: Third quartile (75th percentile); and Max: Maximum value.

Table 6.2. Data description of GMM generated mix design

	Activity moduli	SSA	GPC	L/B	NaOH concentration	Ms	Fine aggregate	Coarse aggregate
Mean	4.07	2053.94	0.31	0.62	8.37	0.66	0.40	0.29
Std	4.01	3693.11	0.11	0.22	4.97	0.41	0.16	0.20
Min	0.00	0.00	0.10	0.01	0.00	0.00	0.00	0.00
25%	1.77	419.31	0.23	0.48	4.51	0.46	0.26	0.07
50%	2.52	728.89	0.29	0.54	8.91	0.59	0.44	0.31
75%	3.50	2137.92	0.36	0.74	13.24	0.97	0.52	0.49
Max	33.35	24650.80	1.00	1.50	23.09	4.66	0.74	0.66

Table 6.3. Data description of random generated mix design

	Activity moduli	SSA	GPC	L/B	NaOH concentration	Ms	Fine aggregate	Coarse aggregate
Mean	3.00	1650.96	0.50	0.65	7.00	0.50	0.29	0.21
Std	1.15	779.46	0.15	0.32	4.05	0.29	0.15	0.12
Min	1.00	300.00	0.14	0.10	0.00	0.00	0.00	0.00
25%	2.00	975.93	0.39	0.37	3.49	0.25	0.17	0.12
50%	3.00	1651.93	0.50	0.65	7.00	0.50	0.29	0.21
75%	4.00	2325.73	0.60	0.93	10.51	0.75	0.39	0.29
Max	5.00	3000.00	1.00	1.20	14.00	1.00	0.77	0.70

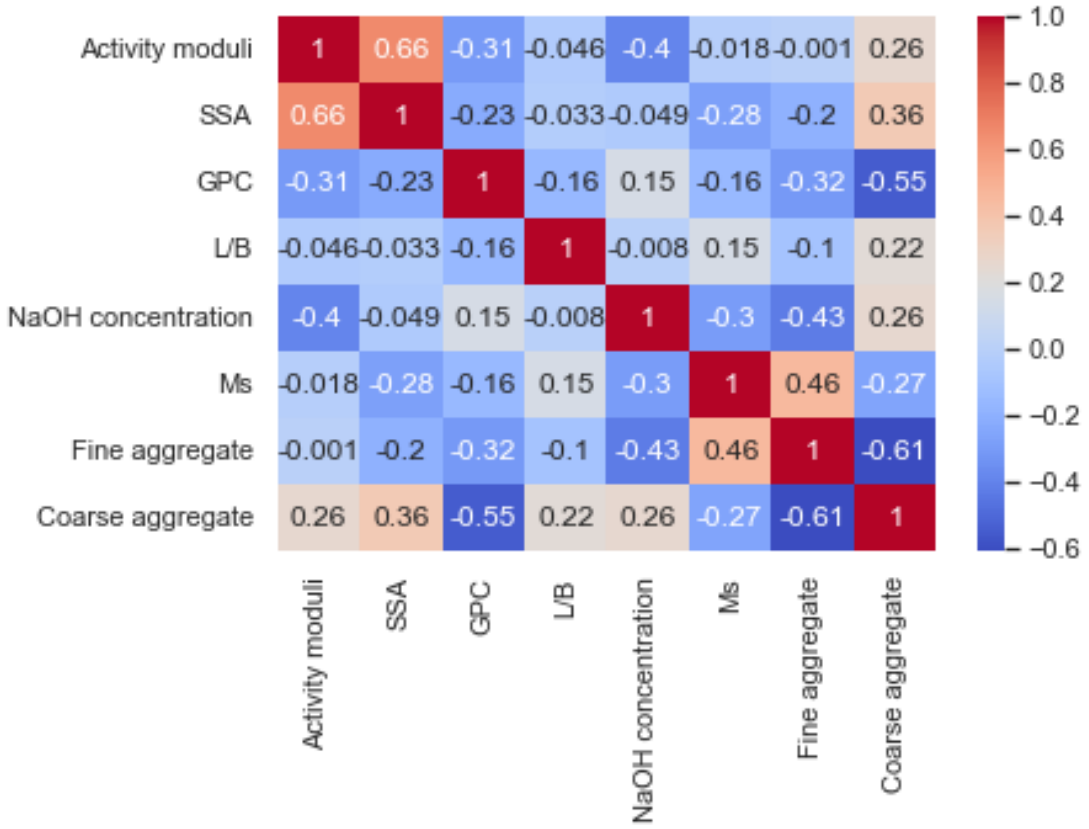
Activity moduli 1 0.66 -0.31 -0.046 -0.4 -0.018 -0.001 0.26
SSA 0.66 1 -0.23 -0.033 -0.049 -0.28 -0.2 0.36
GPC -0.31 -0.23 1 -0.16 0.15 -0.16 -0.32 -0.55
L/B -0.046 -0.033 -0.16 1 -0.008 0.15 -0.1 0.22
NaOH concentration -0.4 -0.049 0.15 -0.008 1 -0.3 -0.43 0.26
Ms -0.018 -0.28 -0.16 0.15 -0.3 1 0.46 -0.27
Fine aggregate -0.001 -0.2 -0.32 -0.1 -0.43 0.46 1 -0.61
Coarse aggregate 0.26 0.36 -0.55 0.22 0.26 -0.27 -0.61 1
Activity moduli
SSA
GPC
L/B
NaOH concentration
Ms
Fine aggregate
Coarse aggregate
1.0
0.8
0.6
0.4
0.2
0.0
−0.2
−0.4
−0.6

(a)

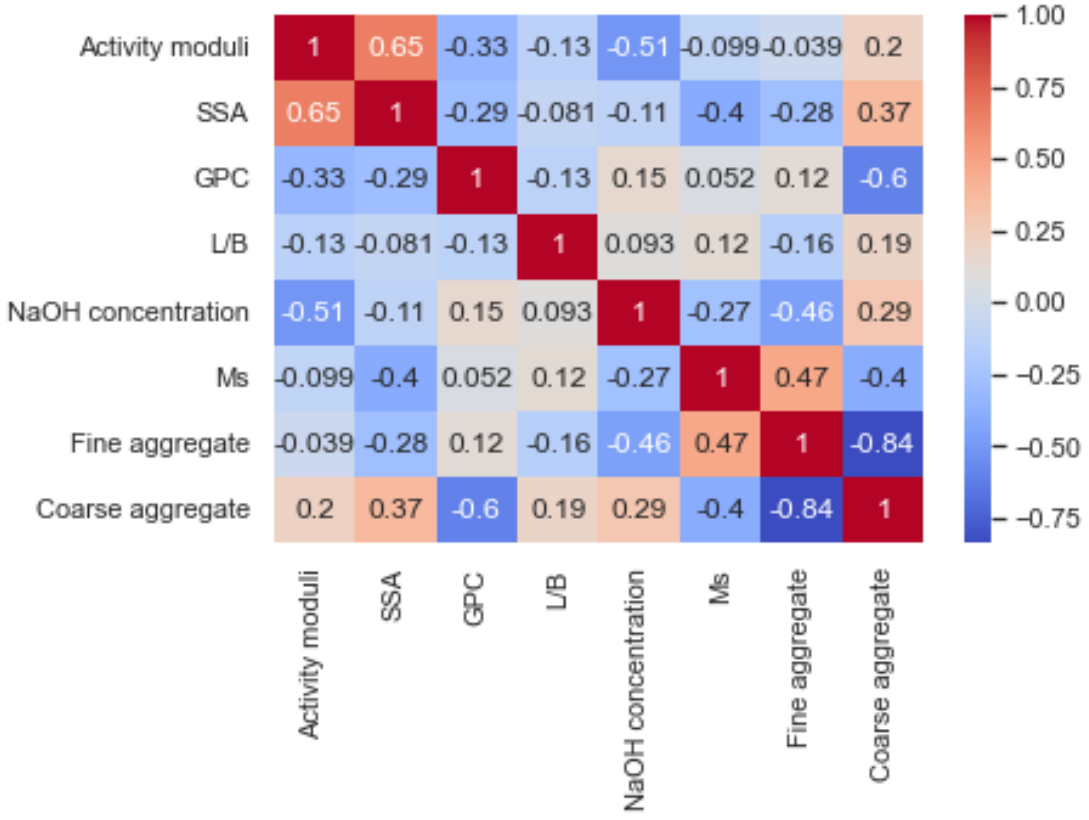
Activity moduli 1 0.65 -0.33 -0.13 -0.51 -0.099 -0.039 0.2
SSA 0.65 1 -0.29 -0.081 -0.11 -0.4 -0.28 0.37
GPC -0.33 -0.29 1 -0.13 0.15 0.052 0.12 -0.6
L/B -0.13 -0.081 -0.13 1 0.093 0.12 -0.16 0.19
NaOH concentration -0.51 -0.11 0.15 0.093 1 -0.27 -0.46 0.29
Ms -0.099 -0.4 0.052 0.12 -0.27 1 0.47 -0.4
Fine aggregate -0.039 -0.28 0.12 -0.16 -0.46 0.47 1 -0.84
Coarse aggregate 0.2 0.37 -0.6 0.19 0.29 -0.4 -0.84 1
Activity moduli
SSA
GPC
L/B
NaOH concentration
Ms
Fine aggregate
Coarse aggregate
1.00
0.75
0.50
0.25
0.00
−0.25
−0.50
−0.75

(b)

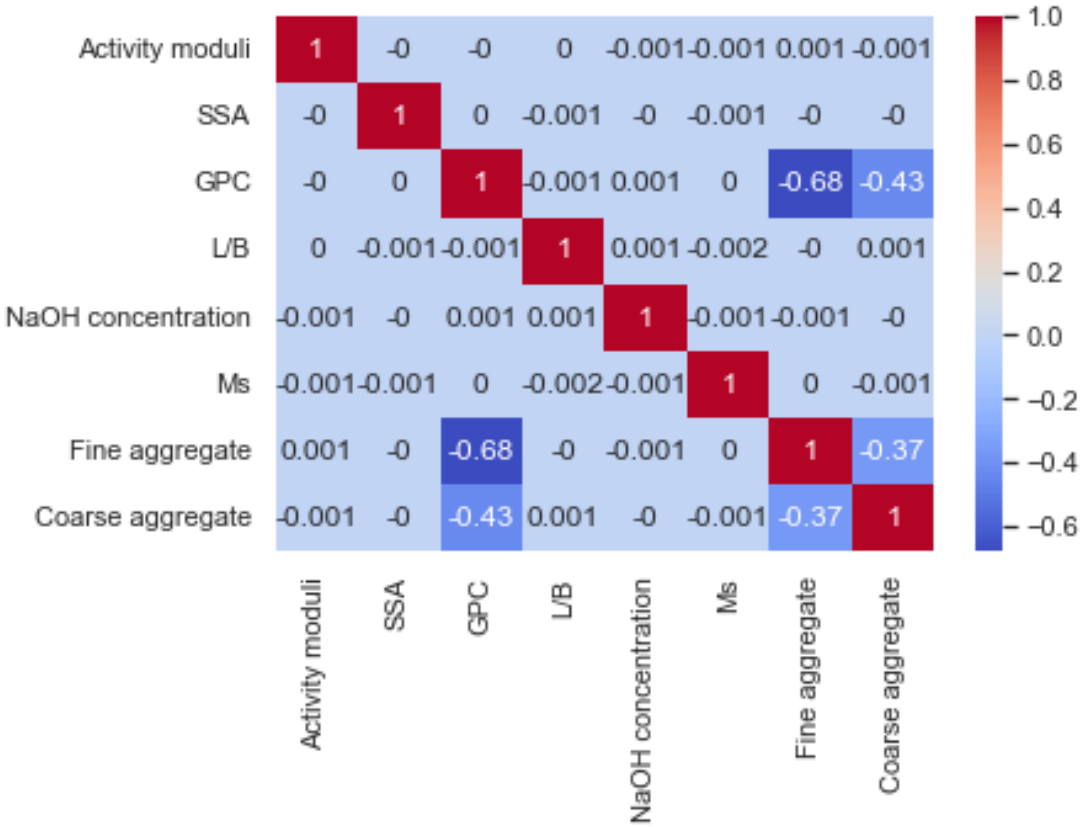

(c)

Fig. 6.4. Pearson correlation coefficient matrix for (a) original dataset; (b) GMM generated dataset; and (c) random generated dataset.

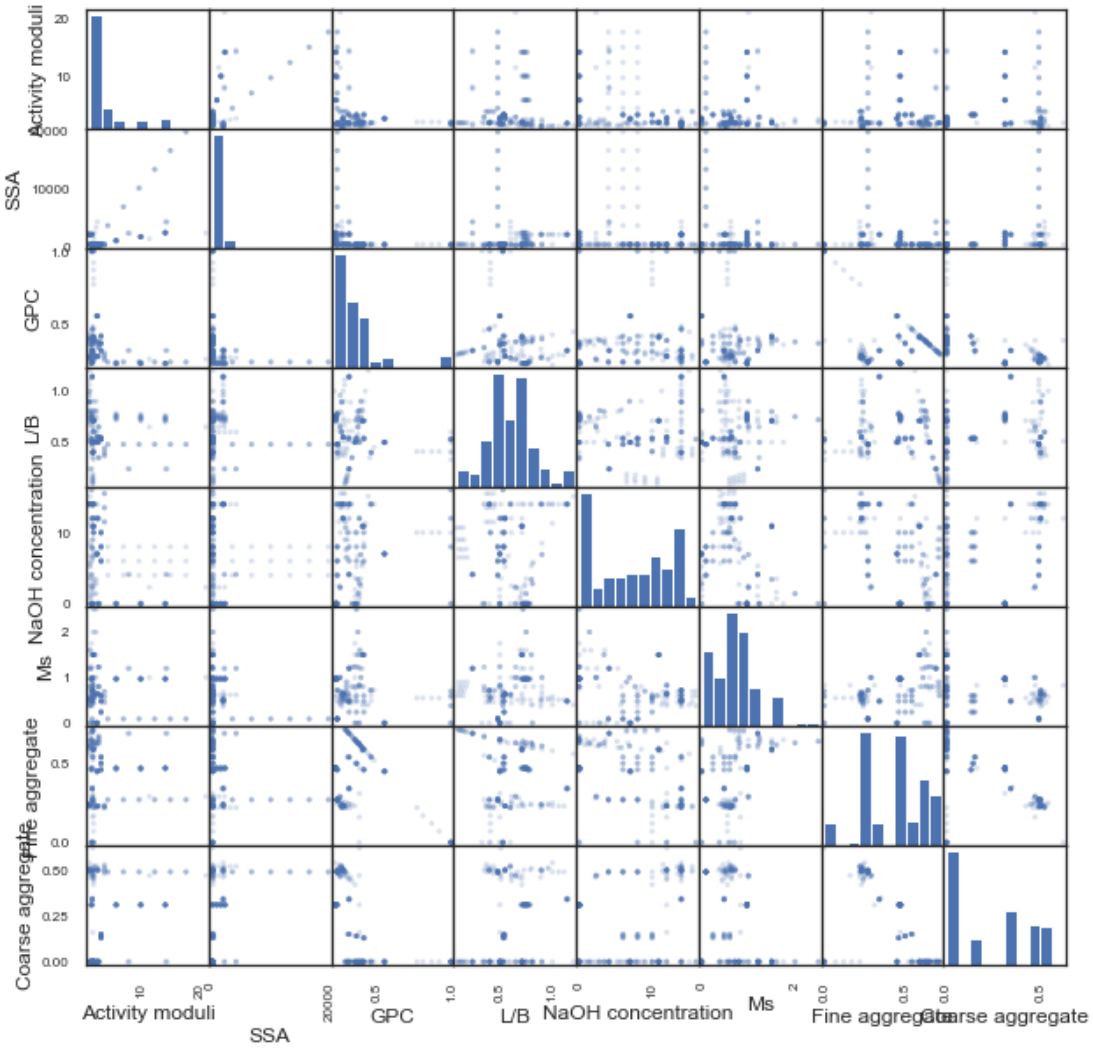
Activity moduli
SSA
GPC
L/B
NaOH concentration
Ms
Fine aggregate
Coarse aggregate

(a)

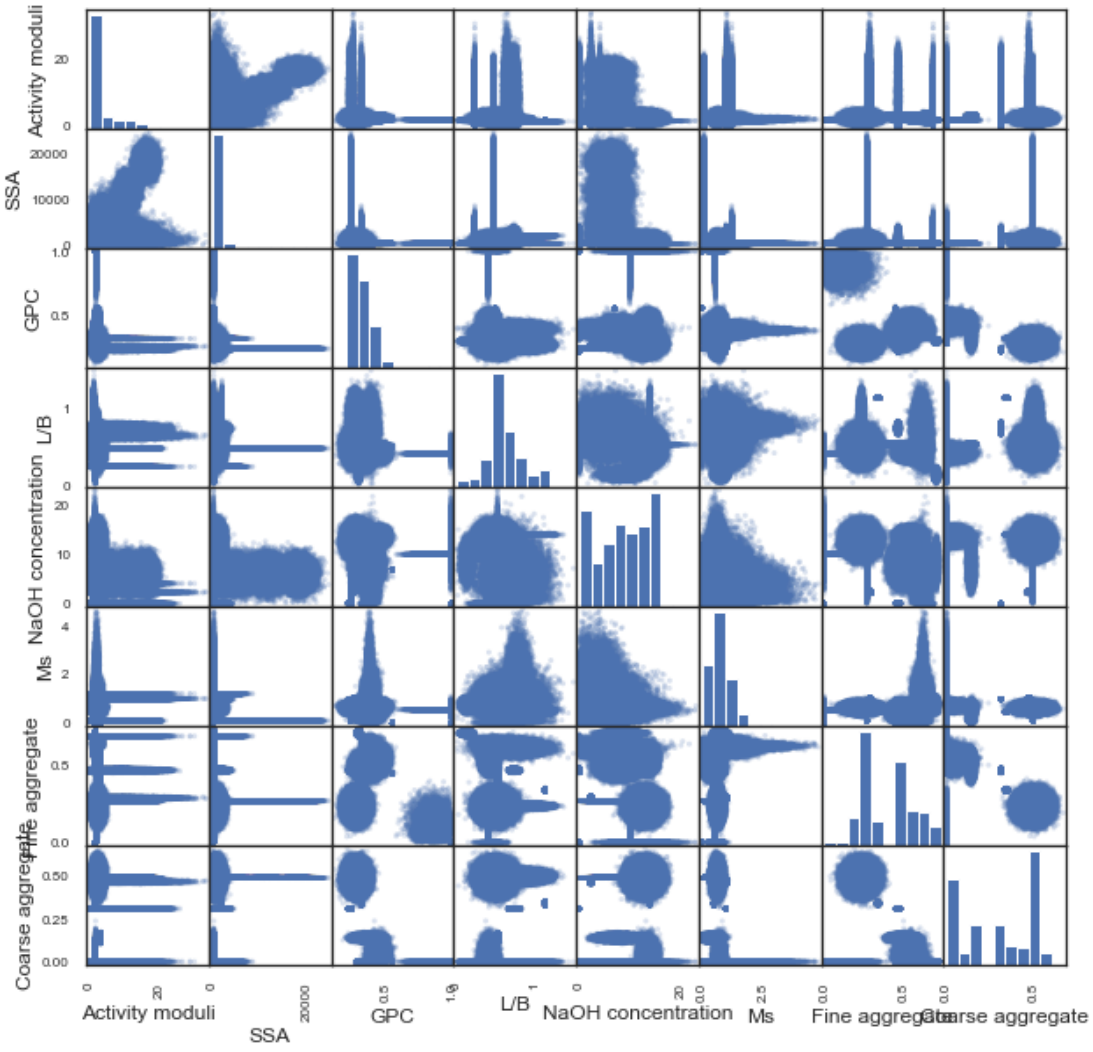
Activity moduli
SSA
GPC
L/B
NaOH concentration
Ms
Fine aggregate
Coarse aggregate

(b)

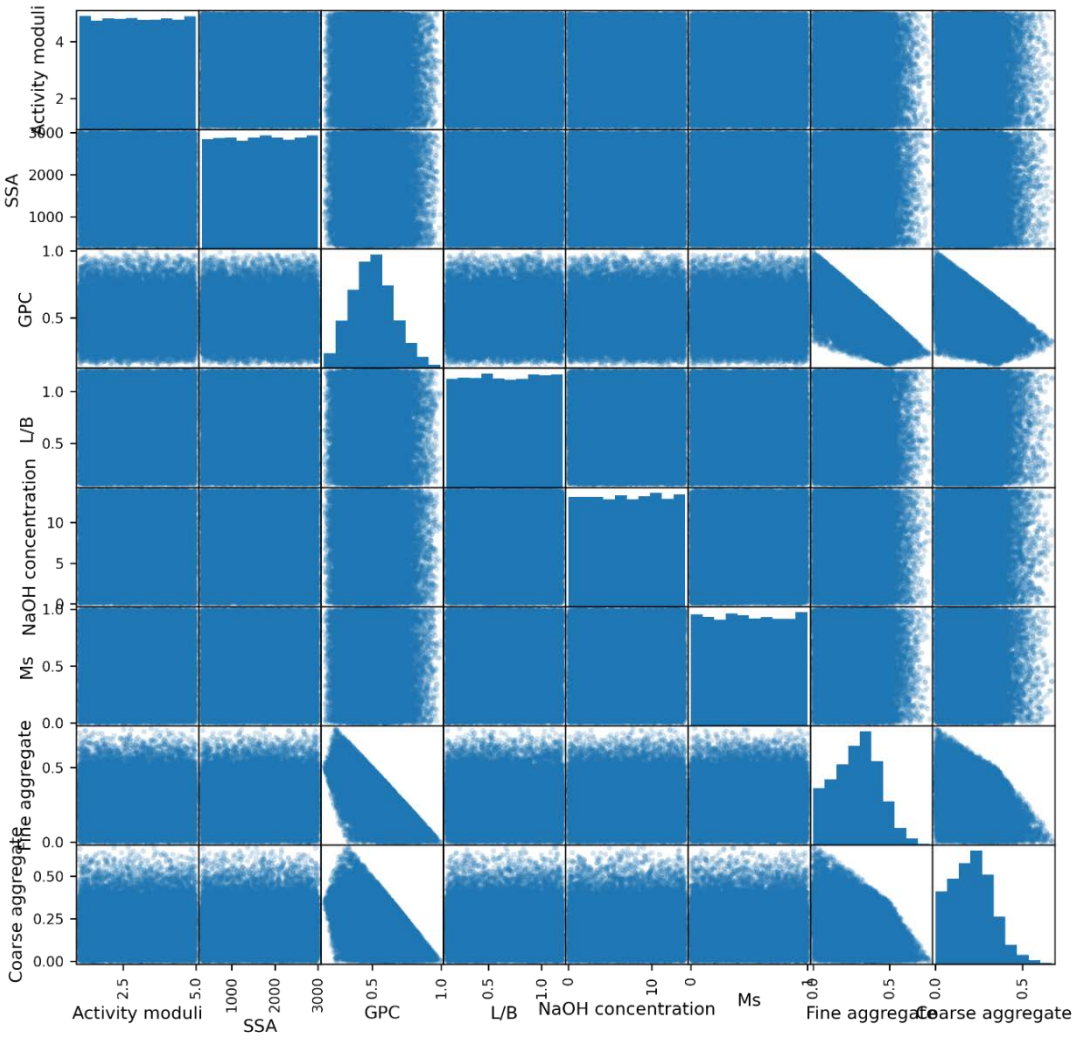

(c)

Fig. 6.5. Scatter matrix plot of data for (a) original dataset; (b) GMM generated dataset; and (c) random generated dataset.

6.2. Inverse prediction

In the previous step, a total number of 614234 available synthetic mix designs were collected. According to the prediction performance of ANN, LGBM and XGBoost models, XGBoost algorithm showed the best in predicting workability, strength and shrinkage among these three algorithms. Hence, the pre-constructed XGBoost model

in the former chapter was re-used to predict the fresh and hardened properties of these generated mix designs.

6.2.1. Distribution of the predicted properties of AAMs

Fig. 6.6 plots the data distribution results of predicted workability in pre-constructed XGBoost model. Generally, the XGBoost algorithm-predicted flow showed a good agreement with the previous data analysis discussion. From Fig. 6.6a and Fig. 6.6b, it can be seen a significantly decreasing trend between the workability and reactivity of precursor (i.e., activity moduli and SSA). Similarly, the higher coarse aggregate content as well inhibited the flowability of AAMs, which was shown in Fig. 6.6h. Fig. 6.6c plots the flowability against the GPC, and a pronounced increasing trend could be seen, especially when GPC was ranging from 0.2 to 0.4. Although when GPC was larger than 0.6 showed a lower average flow values than that of GPC equal to 0.4, a least flowability over 200 was achieved, still showing a good workability. Fig. 6.6d displays the positive influence of L/B ratio on the predicted workability. Fig. 6.6e and Fig. 6.6f revealed the effects of alkali activator on the predicted workability of AAMs. A negative effect of NaOH concentration and a promoting effect of Ms ratio on the workability was demonstrated, which was in line with the previous discussion.

Fig. 6.7 displays the data distribution of the predicted compressive strength results. From the figure, some obvious tendency could be found. First, a pronounced trend between activity moduli and strength cannot be observed in Fig. 6.7a. On the other, a significantly increasing trend between predicted 28-day compressive strength and SSA

could be found in Fig. 6.7b, which was in line with the previous discussion on data analysis in Chapter 4. Fig. 6.7c plots the compressive strength of AAMs against the GPC, and a pronounced decreasing trend could be seen. The highest compressive strength was observed at GPC around 0.25 and the relatively lower strength results were generally observed at GPC beyond 0.6. This finding was as well consistent with the existing literature [68, 153]. Regarding Figs. 6.7d, e, and f, the influences of L/B ratio, NaOH concentration and Ms on the predicted compressive strength were not clearly detected, which can be explained by the synergetic effect of these three key factors related to alkali activator. Lastly, Figs. 6.7g and h demonstrate how fine and coarse aggregate contents affect the predicted compressive strength of AAMs. No obvious potential between fine aggregate and strength could be found in Fig. 6.7g though, a remarkable improvement on strength with higher addition of coarse aggregate could be seen in Fig. 6.7h. Such data point location was in agreement with the experimental results reported by numerous researchers that higher content of coarse aggregates could simultaneously improve the mechanical properties and volume stability of AAM concrete mixtures [31, 151].

Finally, Fig. 6.8 illustrates the data distribution of drying shrinkage results. In the previous chapter, there were eleven key factors of AAMs for drying shrinkage were summarized, in which curing temperature, relative humidity and volume-to-surface ratio were considered. However, most researchers selected a room temperature of 23 ℃ and RH of 50% for the experiment, leading to the generated data mostly lying in these two values. Therefore, these two values were not evaluated here. Also, the data

distribution of the predicted shrinkage results shows a high consistence with the data analysis in the previous chapter. Fig. 6.8a shows the influence of activity moduli on the drying shrinkage of AAMs, in which a higher activity moduli resulted in a lower drying shrinkage. Meantime, higher SSA also led to the lower predicted drying shrinkage values, which was reflected in Fig. 6.8b. These two findings were the same as the experimental results reported by other researchers. Fig. 6.8c displays the effect of GPC on the drying shrinkage development, in which the AAM paste (GPC = 1.0) showed the highest ultimate drying shrinkage value. Interestingly, in Fig. 6.8d drying shrinkage firstly increased and then decreased with L/B ratio. This finding is highly consistent with that in the previous chapter, which was explained by the synergetic effects brought by alkali content. The mitigation effect of NaOH concentration was also revealed, but the effect of Ms was not so clear, illustrated in Figs. 6.8e and f. Fig. 6.8g and h shows the strong mitigation effects of aggregate contents on drying shrinkage, especially for coarse aggregate. Lastly, Fig. 6.8i demonstrates the influence of volume-to-surface ratio on the predicted ultimate drying shrinkage magnitude. In good agreement with the experimental results reported by researchers, higher volume-to-surface ratio (also called effective thickness) can inhibit the predicted shrinkage development in AAMs.

According to these data distribution results, it can be seen that the XGBoost-predicted workability, compressive strength and drying shrinkage generally followed the tendency analyzed in the previous chapters, proving the robustness and availability of XGBoost in inverse prediction.

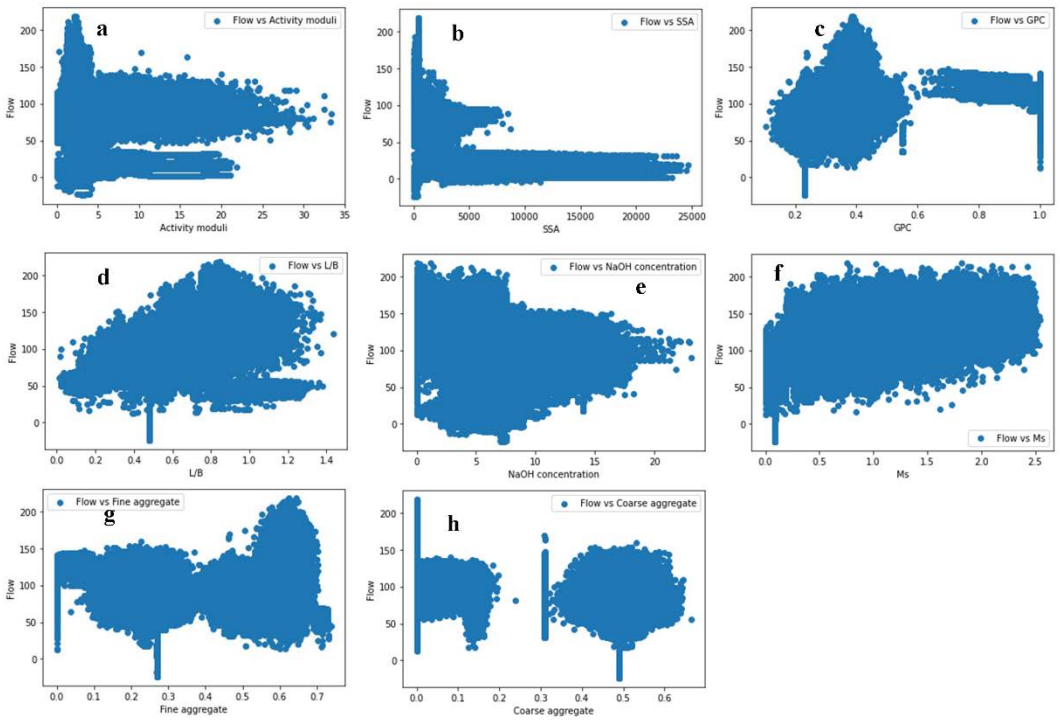

Fig. 6.6. Predicted flow distribution vs. (a) activity moduli; (b) SSA; (c) GPC; (d) L/B ratio; (e) NaOH concentration; (f) Ms; (g) fine aggregate content; and (h) coarse aggregate content.

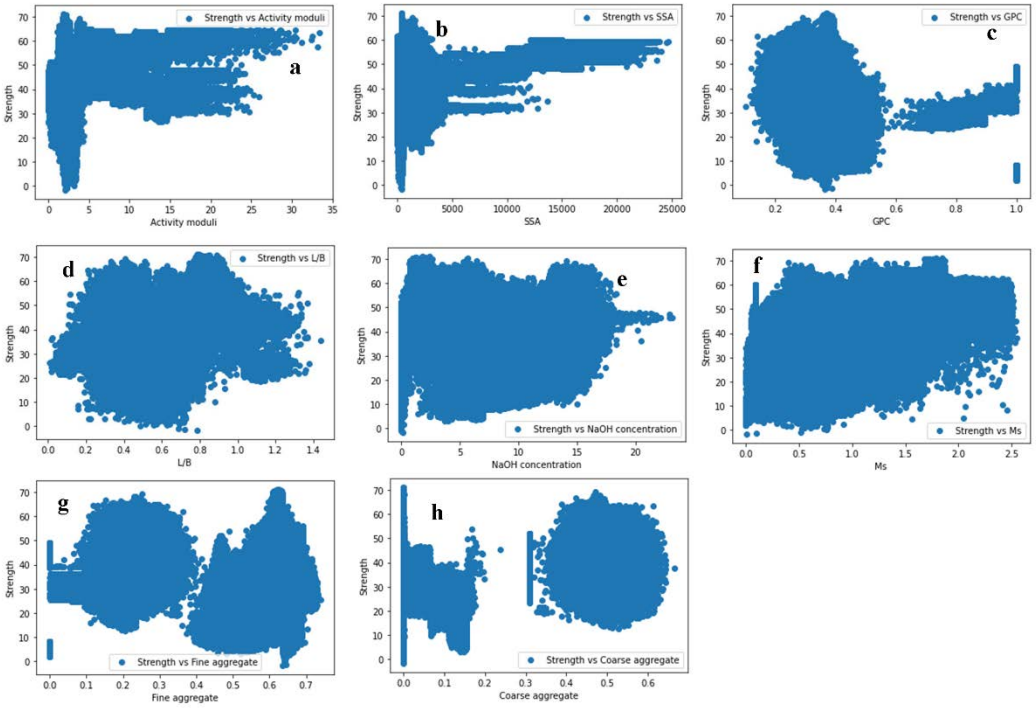

Fig. 6.7. Predicted compressive strength distribution vs. (a) activity moduli; (b) SSA; (c) GPC; (d) L/B ratio; (e) NaOH concentration; (f) Ms; (g) fine aggregate content; and (h) coarse aggregate content.

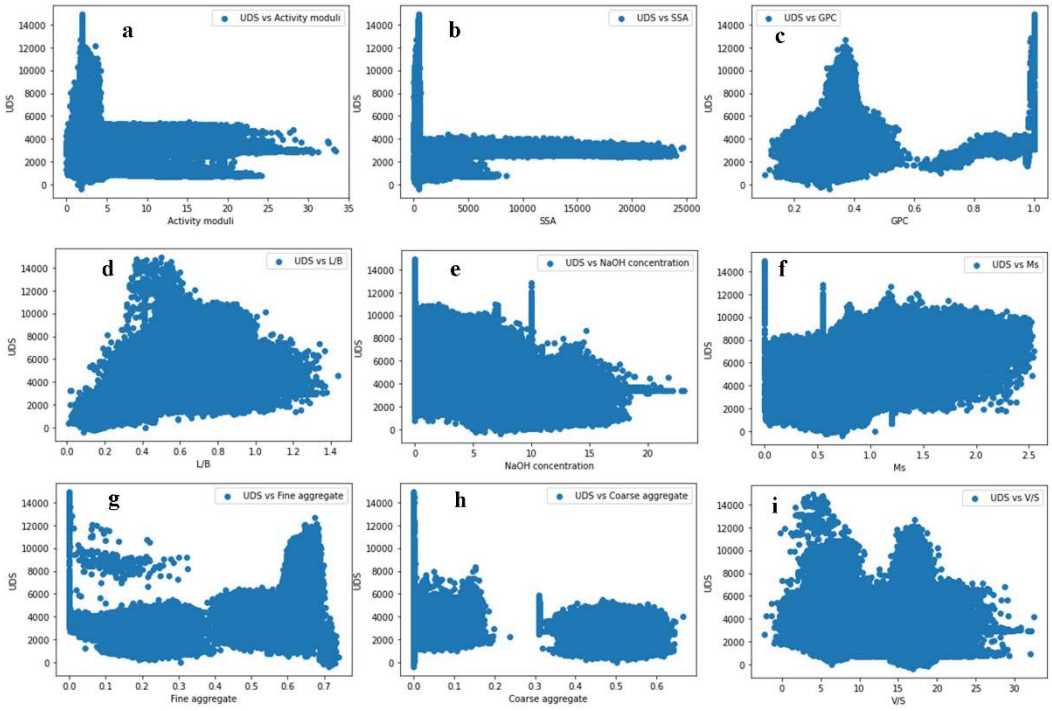

Fig. 6.8. Predicted ultimate drying shrinkage distribution vs. (a) activity moduli; (b) SSA; (c) GPC; (d) L/B ratio; (e) NaOH concentration; (f) Ms; (g) fine aggregate content; (h) coarse aggregate content; and (i) volume-to-surface ratio.

6.2.2. Filtration out the desired mixes

After acquiring the predicted strength results, the final step was to filter out the mix designs with the desired properties, e.g., flowability ≥ 100%, strength = 40 (+ 10% error) MPa, drying shrinkage ≤ 2000 με. Table 6.4 and Table 6.5 list out the statistic summary for the predicted and original mix design with the target properties. It should be noted that the average values listed in Table 6.5 were calculated from individual dataset used in the previous three chapters. According to the target properties, there were 1043

individual mix designs filtered out, in which the average flowability, compressive strength and ultimate drying shrinkage were 109.12%, 41.52 MPa and 1377 με, respectively. From the table, it could be seen that the average values for each mix design key factor were close to the experimental values reported by other researchers. First, the average values of compressive strength and drying shrinkage for the predicted and original mix designs were generally close. Specifically, the absolute difference ratios of compressive strength and drying shrinkage between the predicted and original mixes were 0.6% and 2.0%, respectively. Second, the sum of average values of GPC, fine aggregate and coarse aggregate was 1.02, which basically satisfied the real situation. Furthermore, average GPC values for compressive strength (0.30) and drying shrinkage (0.34) in real cases both were close to the predicted one (0.30). However, due to the different dataset in the original mix design, there still existed unneglectable difference. The difference in the average flowability results between the predicted and original data was not small (28.16%), which was because of the existence of AAM paste with high workability over 300% in the original data. Moreover, the predicted NaOH concentration and Ms was quite different from the original ones, which was caused by the complicated effect of alkali activation on the different properties of AAMs. Overall, the XGBoost algorithm showed a relatively confident prediction on the AAM mix design.

Table 6.4. Data summary for the predicted mix (target flow ≥ 100%, target strength = 40 (+ 10% error) MPa, target drying shrinkage ≤ 2000 με)

	Flowability (%)	Strength (MPa)	Drying shrinkage (με)	Activity moduli	SSA (m^2/kg)	GPC	L/B	NaOH concentration (M)	Ms	Fine aggregate	Coarse aggregate	V/S*
Mean	109.12	41.52	1377	2.66	517.34	0.30	0.41	11.94	0.65	0.29	0.43	10.36
Std	10.45	0.88	351	1.65	547.90	0.05	0.11	3.15	0.18	0.14	0.16	5.26
Min	100.01	40.00	608	0.68	0.02	0.19	0.24	0.51	0.09	0.09	0.00	3.30
25%	102.18	40.74	1071	1.99	158.08	0.27	0.36	11.71	0.54	0.22	0.45	6.01
50%	105.72	41.52	1363	2.31	335.92	0.29	0.42	12.77	0.64	0.25	0.49	6.83
75%	112.30	42.29	1692	2.66	562.18	0.31	0.44	13.73	0.69	0.29	0.51	16.31
Max	186.50	42.99	1999	10.05	2462.26	0.49	1.05	16.78	2.21	0.69	0.61	24.46

Note: *V/S ratio is only considered for calculation of drying shrinkage.

Table 6.5. Average values for experimental data.

Properties	Value*	Activity moduli	SSA	GPC	L/B	NaOH concentration	Ms	Fine aggregate	Coarse aggregate	V/S*
Flowability	151.90	4.24	649.77	0.68	0.53	4.67	1.15	0.29	0.02	-
Strength	41.76	3.17	984.43	0.30	0.66	6.73	0.74	0.36	0.34	-
Drying shrinkage	1350	4.21	2378.27	0.34	0.39	4.06	0.80	0.45	0.21	12.45

Note: The units used in this table is the same as Table 6.3.

6.3. Validation of the predicted mix design

To prove the applicability of the proposed program, a batch of the predicted mix designs were chosen to be produced and measured for their flowability and 28-day compressive strength. Drying shrinkage was influenced by the curing conditions and sample shape, which were totally different from different usage in real construction work (e.g., column, beam, etc.). Hence, the drying shrinkage value was only for checking. This time, we chose mortar samples to be used as the validation group.

6.3.1. Materials

A Nippon Steel-provided GGBFS (ST40 compliant with JIS A 6206) was used in this experiment with the specific density of 2.91 g/cm^3 and SSA of 397 m^2/kg. The chemical composition was listed in Table 6.6. According to the activity moduli calculation equation, the activity moduli of this GGBFS was 1.89. Therefore, in the data generation step, these two key factors for raw materials were set in advance, and the negative values were also removed. Hence, a total of 64697 random data were selected for the further calculation. Note that because of the newly-generated samples with the pre-determined values, the dataset was not the same as the previous one. Sodium hydroxide pellet (purity > 97%) and commercial sodium silicate solution (9.4% Na_2O, 29.4% SiO_2, 61.2% H_2O) were adopted for producing the alkali activator. The standard fine aggregate (compliant with JIS R 5201) was used with the specific gravity of 2.64. The mortar samples were prepared by a Hobart mixer. The precursors were firstly mixed

with fine aggregate at a slow speed for 30 seconds, and the alkali activator was then added and mixed for 1 minute. After that, the mortar samples were homogenized by a trowel for 30 seconds and re-mixed at a high speed for 2 minutes. The samples were cast in a cylinder mold with the size of 50 mm × 50 mm × 100 mm for compressive strength test. Meantime, part of samples were cast in a prism mold with the size of 40 mm × 40 mm × 160 mm for drying shrinkage test.

Table 6.6. Chemical compositions of GGBFS (wt.%)

Component	GGBFS
SiO_2	33.03
TiO_2	0.57
Al_2O_3	12.50
Fe_2O_3	1.23
MnO	0.18
MgO	6.65
CaO	43.42
Na_2O	0.16
K_2O	0.25
P_2O_5	0.02
LOI	0.1%

6.3.2. Mix proportions

Mix proportions were determined by the predicted mix design satisfying the desired properties, i.e., flowability ≥ 100%, compressive strength = 40 (+ 10% error) MPa. Note that extremely small value (< 0.0001) may also appear, which was all regarded as 0. Moreover, these mix design were generated based on the obtained data from existing literature, in which the type of materials varied among individual researches. Therefore, the performance of raw materials when mixing, such as the viscosity of alkali activator, may also be different from the authors' raw materials. Hence, the mix proportions may need further tailored considering the difficulty of material preparation and mixing procedure. In this sense, Table 6.7 listed out the satisfied mix design with the predicted properties, and Table 6.8 listed out the mix proportions of the validation groups. It should be mentioned that the predicted mix designs were not only limited in the mixes listed in Table 6.7. The other mixes may not be appropriate to be prepared. For example, some predicted mixes required a fairly high Ms ratio over 2.00, which needs increase SiO_2 in the system by adding silica fume to achieve this goal. However, with the addition of silica fume also influence the raw material properties, which cannot meet the pre-determined conditions. Therefore, for Mix 1 the key factors were set as activity moduli of 1.89, SSA of 397 m^2/kg, GPC of 0.40 ± 0.05, L/B ratio of 0.85 ± 0.05, NaOH concentration 8.0 ± 0.05 M, Ms of 0.5 ± 0.05, and fine aggregate content of 0.60 ± 0.05; while for Mix 2 the key factors were set as activity moduli of 1.89, SSA of 397 m^2/kg, GPC of 0.40 ± 0.05, L/B ratio of 0.85 ± 0.05, NaOH concentration 6.0 ± 0.05 M, Ms of 0.5 ± 0.05, and fine aggregate content of 0.60 ± 0.05.

Table 6.7. Predicted mix design

Mix	A.M.	SSA	GPC	L/B	NaOH	Ms	Fine agg.	Coarse agg.	Predicted flow/%	Predicted strength/MPa	Predicted shrinkage/με
1	1.89	397	0.41	0.89	8.08	0.55	0.59	0.00	119.36	40.45	4137
2	1.89	397	0.40	0.82	6.14	0.52	0.60	0.00	145.94	43.65	4367

Table 6.8. Mix proportions

Mix	GGBFS/g	NaOH pellet/g	Na_2SiO_3 solution/g	Water[1]/g	Sand/g	Experimental flow/%	Experimental strength/MPa	Experimental shrinkage/με	Error to predicted strength[2]	Error to target strength[3]	Error to predicted shrinkage[4]
1	100	14.14	22.18	44.18	249.48	119.30	44.37	3751	8.83%	10.92%	10.29%
2	100	11.36	17.82	47.32	249.48	147.75	40.33	3428	6.42%	0.82%	27.39%

Note: [1]Water refers to the additional water, excluding the water content in sodium silicate solution; [2]Error to predicted strength was calculated by $\frac{|\text{Predicted strength}-\text{Experimental strength}|}{\text{Experimental strength}}$; [3]Error to target strength was calculated by $\frac{|\text{Predicted strength}-\text{Target strength}|}{\text{Target strength}}$; 4Error to predicted shrinkage was calculated by $\frac{|\text{Predicted shrinkage}-\text{Experimental shrinkage}|}{\text{Experimental shrinkage}}$.

6.3.3. Testing method

For evaluating the workability of the AAS mortar samples, a slump flow test was conducted using a mortar flow evaluator. To perform the test, fresh mortar mixture was filled into the slump cone on the plate, and the slump cone was then lifted up to make the paste slump and flow. When the flow ceased, two perpendicular flow diameters of the sample were measured and averaged as the slump flow result for each group.

28-day compressive strength of AAS samples were measured by a hydraulic compression machine with a constant load rate of 0.6 $N/mm^2 \cdot s$ in accordance with JIS A 1108. For each mix, triplicated samples were tested and averaged for the compressive strength result.

Drying shrinkage test was conducted by a dial indicators comparison provided by Mitutoyo (No. 2119S-10) with the accuracy of 0.001 mm. As specified in JIS A 1129, shrinkage strain was used to describe the drying shrinkage magnitude [3]. The specimens were placed at the curing chamber with the temperature of 23 °C and relative humidity (RH) of 50%.

6.4. Results and discussions

The testing results were listed in Table 6.8, accompanied with the error compared to the predicted and target values. It can be seen that the error between the experimental and predicted strength results were in general small, less than 10%. Meantime, it was

close to the target strength of 40 MPa. Meantime, both flowability results satisfied the requirements that higher than 100%, achieving fluidity. The drying shrinkage prediction was quite accurate for Mix 1 with the error of around 10%, while for Mix 2 the error was around 27%. Moreover, this inverse prediction was totally built based on the pre-constructed XGBoost model, which means that the training dataset in the forward XGBoost model played a dominant role in the final mix design prediction. Therefore, for improving the accuracy, it is suggested to update the training dataset when new experimental results are acquired.

Compared to the existing inverse prediction models [41, 42], this proposed model had several advantages. First, the training database was acquired from the published research covering a wide range of AAM types, e.g., slag/fly ash/metakaolin-based paste, mortar and concrete, demonstrating higher generality. Second, the inverse prediction by Huo et al. [41] was based on manually adjusting the Na_2O content and $n(H_2O)/n(Na_2O)$ to calculate the $n(SiO_2)/n(Na_2O)$. While, the proposed model can directly predict the mix design by giving the key factors, making it more convenient to calculate the usage of each component. However, there were several drawbacks and limitations to inversely predict the mix design by using BPNN model and GMM data augmentation method. For example, the prediction performance is largely dependent on the data quality of training dataset and generated samples. This part was illustrated in detail in the latter chapter.

6.5. Life cycle assessment for predicted mix designs

After inverse prediction, a life-cycle assessment (LCA) was conducted to evaluate the environmental burdens of the predicted AAS mortar, conventional OPC-based mortar, and normal AAS mortar with the similar 28-day compressive strength of 40 MPa. This part was used as the example to show the LCA calculation for latter calculation for all inversely predicted mix designs. LCA was performance on five categories, i.e., Global warming (GWP), Ozone depletion (ODP), Acidification (AP), Eutrophication (EP), and Ecotoxicity (ETP), according to International Organization for Standardization (ISO) 14040 and the Ecoinvent database. This part was finished according to the traditional LCA workflow, including (i) Defining the goal, scope and boundaries for LCA; (ii) Collecting products and process inventory; (iii) Assessing the environmental impacts in accordance with the inventory; and (iv) Analyzing the results and putting forward future improvements.

6.5.1. Goal, scope and system boundaries for LCA

The goal of this research is to evaluate and compare the environmental impacts of the optimized AAM and conventional mixtures production for advancing the development of next-generation concrete. A typical ‘cradle-to-gate’ perspective considering the potential environmental impacts from collecting raw materials to packing final products was studied as the system boundaries [115]. The functional unit of LCA in this paper was 1 ton of the OPC-based, normal AAM, and the predicted AAM mixtures with the given compressive strength under the similar standard curing

condition. This study focused on the comparison of AAM and OPC-based mixtures with the same hardened properties. For evaluating the environmental impacts of these two materials, one method is to evaluate the environmental impacts per unit of measurable performance, for instance, compressive strength [122]. Therefore, conventional OPC-based mixture (Conv), normal AAS mixture (Norm) and the predicted AAS mixture (Pred) with similar 28-day compressive strengths of 40 MPa were respectively identified [77, 206]. The mix design was listed in Table 6.9. The mix designs and compressive strengths of Conv and Norm were derived from the existing literature [161, 207], while the mix design and experimental data of Pred was reported in the previous part. Fig. 6.9 shows the raw materials and process flow diagrams of OPC mortar and AAM production. The dash line squares are the system boundaries. As a type of by-product from iron and steel production, GGBFS contributed to little environmental impacts [208]. It should be noted that logistics was not considered in this study for clarity.

Table 6.9. Mix proportions from the existing literature and experimental data (by mass).

Mix	Cement/%	GGBFS/%	NaOH/%	Na_2SiO_3/%	Water[1]/%	Aggregate/%	Strength/MPa[2]	Ref.
Conv	22.22	0	0	0	11.11	66.67	43.0	[207]
Norm	0	23.43	0.95	8.79	8.26	58.57	41.3	[149]
Pred	0	23.48	4.18	2.67	11.11	58.57	40.3	Experiment

Note: [1]Water herein referred to the additional water excluding the water content in sodium silicate solution; [2]Strength referred to the 28-day compressive strength

measured by a cylindrical mold with a diameter of 100 mm and height of 200 mm (conversion coefficient of 0.75 for cubic samples).

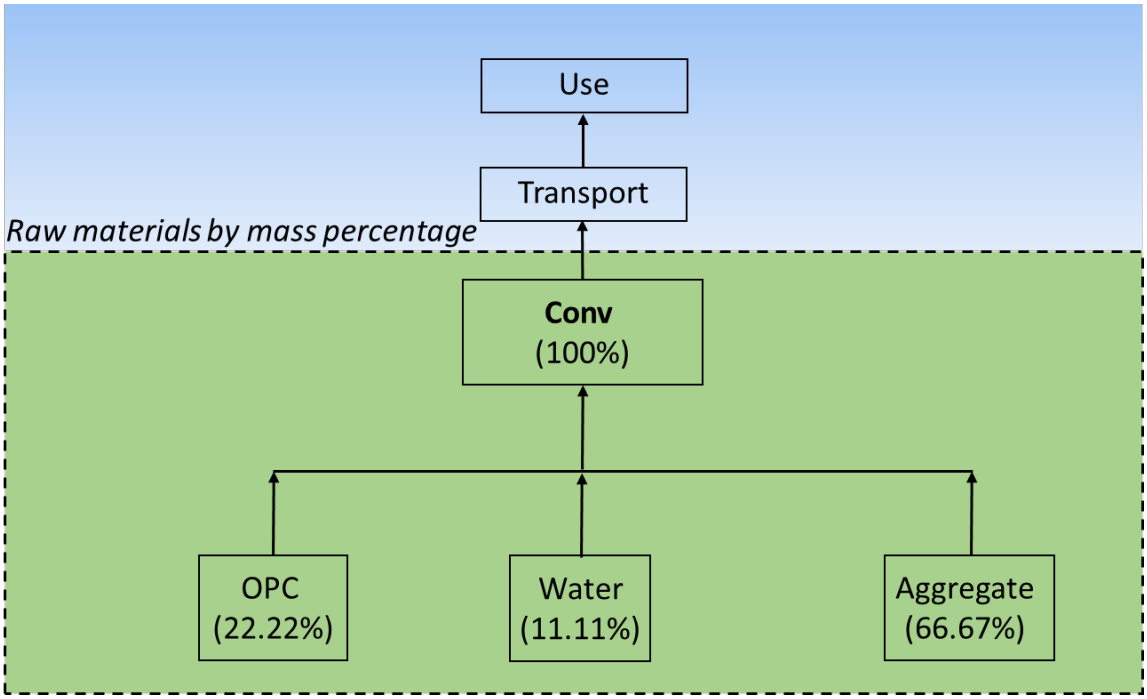

(a)

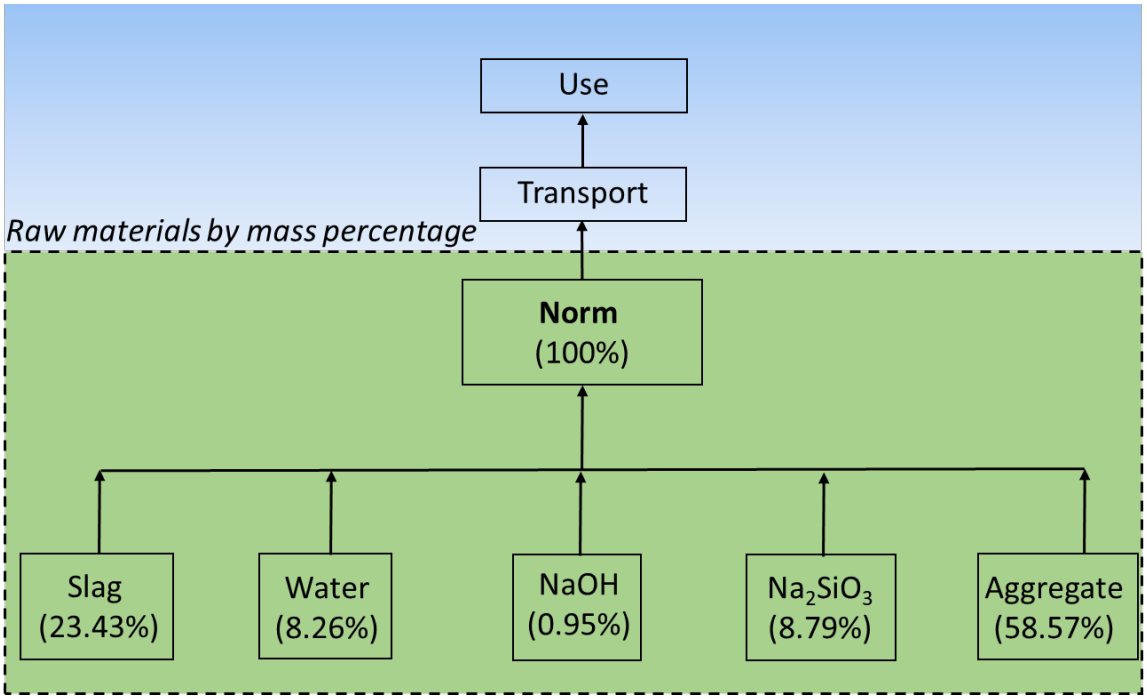

(b)

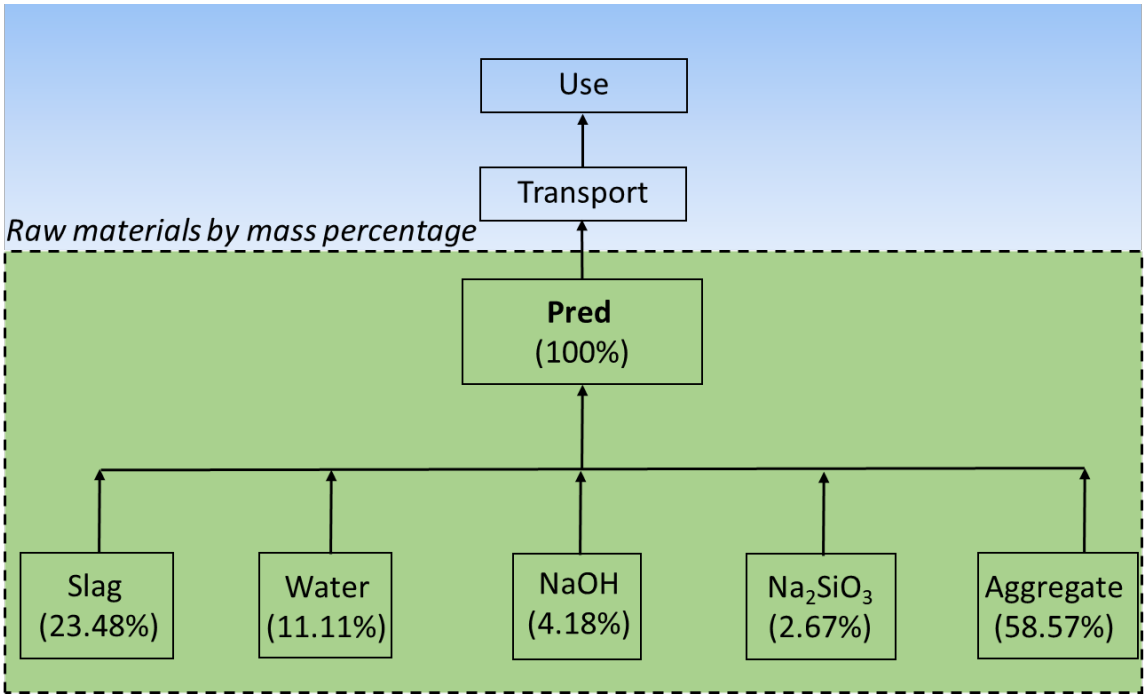

(c)

Fig. 6.9. Flow diagrams for production of (a) Conv, (b) Norm, and (c) Pred.

6.5.2. Inventory

Inventory data for the raw materials and processing procedures were acquired from the LCA conducted by Jiang et al. [12, 209, 210]. Jiang et al. [12] provided possible values of greenhouse gas emissions and potential environmental toxicity for each material. In this proposed LCA, the largest values for greenhouse gas emissions and environmental toxicity were chosen to evaluate the highest environmental burden of Conv, Norm and Pred. The details of raw materials for the production of 1 ton of Conv, Norm and Pred were elaborated as follows.

Cement is produced from the clinker and gypsum which involves raw materials crushing, grinding, blending and calcination [100]. The cement used in Conv mixtures was CEM I 42.5 N OPC [77, 206]. Boesch and Hellweg [211] reported the life cycle

impact assessment (LCIA) results of cement production in Europe and USA. For consistency, it was assumed that the OPC was produced in Europe. GGBFS is the by-products of the iron and steel production and the use of industrial waste in concrete has been prevalent for decades. Moreover, recycling of GGBFS and other industrial wastes is beneficial to the environmental sustainability and thus little environmental burden was included in previous studies [14, 50]. For alkali activator, NaOH pellets and sodium silicate solution were used in AAS mortars, however, it was extremely difficult to identify the inventory data for different types of sodium silicate. Hence, an assumption was made that the inventory data for different sodium silicate solutions were the same. Fine aggregates were used in all mixtures. Environmental impact data for the production of fine aggregate can be directly obtained from the Ecoinvent database. The amount of tap water only considered the water used in the supply chain production, excluding the water in sodium silicate solution. The relevant data were obtained from Ecoinvent database and literatures [12, 209]. Table 6.10 reports the environmental impact for the production of each type of raw material in OPC-based and AAM-based mortars, which were used for the subsequent calculation of total environmental impacts by CML 2002 approach.

Table 6.10. Environmental impact of the production of each raw material per unit of 1 kg.

Materials	GWP/kg CO_2-eq.	ODP/kg CFC-11-eq. ($\times 10^{-8}$)	ETP/kg 2,4-D-eq.	AP/H^+ moles-eq.	EP/kg N-eq. ($\times 10^{-4}$)	Data resources

OPC	1.0	10.0	0.501	0.251	1.71	
GGBFS	0	0	0	0	0	
Coarse aggregate	0.088	0.0468	0.00383	0.00531	0.0479	Ecoinvent [210]; M. Jiang et al., 2014 [12]
Fine aggregate	0.088	0.0242	0.00383	0.00531	0.0479	
Water	0.0010	0.069	0.0084	0.00022	0.00279	
Sodium silicate solution	0.78	6.01	1.88	0.178	3.10	
NaOH pellets	1.2	107	0.777	0.803	3.73	

6.5.3. Impact assessment of raw materials

The aforementioned CML 2002 approach was adopted in the present study due to its capability to quantify the environmental impacts brought by the production of Conv, Norm and Pred in different categories. Five acknowledged baseline categories, i.e., Global warming (GWP), Ozone depletion (ODP), Ecotoxicity (ETP), Acidification (AP) and Eutrophication (EP), were selected for evaluating the environmental impacts [121, 211, 212]. In order, the functional unit of these five categories were kilogram CO_2 equivalent (kg CO_2-eq.) for GWP, kilogram CO_2 equivalent (kg CFC-11-eq.) for ODP, kilogram 2,4-D equivalent (kg 2,4-D-eq.) for ETP, H^+ moles equivalent (H^+ moles-eq.) for AP, and kilogram N equivalent (kg N-eq.) for EP.

6.5.4. Sensitivity analysis

Sensitivity analysis was carried out on the LCA of Conv, Norm and Pred by varying the variables by 10% because the variations in the amount of raw materials could influence the environmental impacts [12]. Herein, cement/geopolymer paste mass content was defined as the ratio of the mass of OPC/GGBFS, water, and alkali activator to the total mass of concrete. Two scenarios were considered as follows: Scenario 1: Increasing/decreasing 10% of cement/geopolymer paste content; Scenario 2: Increasing/decreasing 10% of the aggregate content by mass.

6.6. Environmental impact results

6.6.1. Environmental impacts of individual raw materials in 1 ton of Conv, Norm and Pred

In accordance with the inventories and assumptions mentioned in previous sections, the environmental impacts of individual raw material in 1 ton of Conv, Norm and Pred were listed in Table 6.11. The table revealed that different raw materials in OPC or AAM-based mixtures exhibited different levels of GWP, ODP, ETP, AP and EP. Due to no content of cement in AAMs, the environmental impacts brought by OPC were all 0 in the five categories. On the other hand, Norm and Pred both adopted alkali activator (sodium silicate solution + NaOH pellets) that was not added in Conv. For Conv, the GWP score of OPC (222.222 kg CO_2-eq.) was much higher than that of fine aggregate (58.667 kg CO_2-eq.) and water (0.111 kg CO_2-eq.) production. Similarly, for ODP, ETP,

AP and EP, production of cement resulted in the major ecological impacts in comparison to the production of aggregate and water in Conv. For AAM-based mortar, global warming was mainly caused by production of sodium silicate solution (68.548 kg CO_2-eq.) in production of Norm, while for production of 1 ton Pred aggregate production led to a higher GWP score (51.538 kg CO_2-eq.) compared to others. The global warming caused by cement production was much more severe than aggregate and alkali activator production, which is the major reason why AAM can alleviate greenhouse gas emission. However, for ODP, ETP, AP and EP, the environmental impacts were mainly caused by production of silicate solution and NaOH pellets. Due to different amount of sodium silicate solution and NaOH dry pellets in Norm and Pred, the ecological impacts were slightly different. Specifically, production of NaOH pellets in 1 ton Pred led to higher ozone depletion potential compared to cement production in 1 ton Conv. Moreover, ETP score of production of sodium silicate solution (165.218 kg 2,4-D-eq.) in 1 ton Norm was even higher than that of production of OPC (111.333 kg 2,4-D-eq.) in 1 ton Conv.

Table 6.11. The LCIA results of individual component in 1 ton of Conv, Norm and Pred.

Materials	Mixture type	GWP/kg CO_2-eq.	ODP/kg CFC-11-eq.	ETP/kg 2,4-D-eq.	AP/H^+ moles-eq.	EP/kg N-eq.
OPC	Conv	222.222	2.222E-05	111.333	55.778	3.800E-02
	Norm	0	0	0	0	0

	Pred	0	0	0	0	0
Fine aggregate	Conv	58.667	1.613E-07	2.553	3.540	3.193E-03
	Norm	51.544	1.417E-07	2.243	3.110	2.806E-03
	Pred	51.538	1.417E-07	2.243	3.110	2.805E-03
Water	Conv	0.111	7.667E-08	0.933	0.024	3.100E-05
	Norm	0.083	5.700E-08	0.694	0.018	2.305E-05
	Pred	0.111	7.665E-08	0.933	0.024	3.099E-05
Sodium silicate solution	Conv	0	0	0	0	0
	Norm	68.548	5.282E-06	165.218	15.643	2.724E-02
	Pred	32.630	2.514E-06	78.646	7.446	1.297E-02
NaOH pellets	Conv	0	0	0	0	0
	Norm	11.400	1.017E-05	7.382	7.629	3.544E-03
	Pred	32.002	2.853E-05	20.721	21.414	9.947E-03

6.6.2. Environmental impacts of 1 ton of Conv, Norm and Pred with equivalent strength

Based on the data of raw materials in Conv, Norm and Pred, the environmental impacts of producing 1 ton of these three mixtures can then be evaluated. The relative environmental impacts of producing the same quantity of Conv, Norm and Pred were listed in Table 6.12. The global warming caused by production of aggregate and alkali activator cannot be neglected though, the total GWP score of Conv was nearly 2.5 times higher than that of Norm and Pred. Additionally, manufacturing 1 ton Conv also left

relatively higher ecological impacts in acidification and eutrophication, ascribing to the existence of cement. However, the environmental burden caused by production of alkali activator was reflected in ozone depletion and ecotoxicity, showing the highest ODP score of 3.127E-05 kg CFC-11-eq. and highest ETP score of 175.536 kg 2,4-D-eq. in Pred and Norm, respectively. The degree of individual environmental impact when producing the same quantity of Conv, Norm and Pred production was plotted in Fig. 6.10. It can be obviously seen that production of OPC was a major source for the global warming and ecological toxicity, in which cement production took account 79.08%, 98.94%, 96.96%, 93.99% and 92.18% in GWP, ODP, ETP, AP and EP, respectively. This phenomenon was in line with the previous LCIA results. For AAM-based mortar, production of fine aggregate and alkali activator both left considerable impacts on global warming, in which the GWP score of fine aggregate took account for nearly 45% in total GWP score of Pred. The environmental impacts brought by aggregates were mainly caused by the crushing and screening phases [1]. Nevertheless, manufacturing of alkali activator resulted in the highest burden in ODP, ETP, AP and EP (88.99%~98.73%).

Finally, for reflecting the difference in each category of the LCIA results, a comparative environmental burden results for OPC-based and AAM-based mixtures were plotted in Fig. 6.11. Meantime, a radar chart was as well plotted in Fig. 6.12. The inner location of the pentagon represents lower total environmental impacts. The difference ratio was calculated based on the LCIA results of Conv. It can be seen that Norm and Pred generally demonstrated lower environmental impacts compared to

cement mortar. Manufacturing of alkali activator admittedly led to higher ecological toxicity in ODP and ETP though, using 100% industrial waste as the binder can remarkably reduce the environmental burden brought by production of OPC. Nevertheless, a higher ODP score still should be controlled, meaning that the predicted mix design can be further improved based on the environmental impact results. Moreover, the machine learning algorithm predicted mix design even showed lower environmental impacts in GWP, EP and ETP in comparison to the normal AAS mortar.

Table 6.12. Environmental impact of 1 ton of Conv, Norm and Pred.

Mixture type	GWP/kg CO_2-eq.	ODP/kg CFC-11-eq.	ETP/kg 2,4-D-eq.	AP/H^+ moles-eq.	EP/kg N-eq.
Conv	281.000	2.246E-05	114.820	59.342	4.122E-02
Norm	131.574	1.565E-05	175.536	26.400	3.362E-02
Pred	116.280	3.127E-05	102.543	31.995	2.575E-02

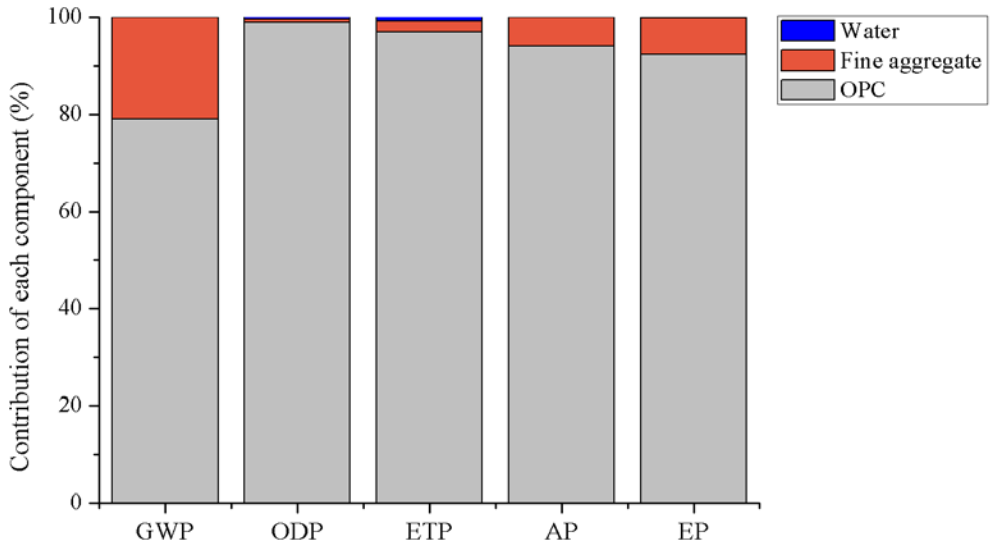
Contribution of each component (%)
100
80
60
40
20
0
GWP
ODP
ETP
AP
EP
Water
Fine aggregate
OPC

(a)

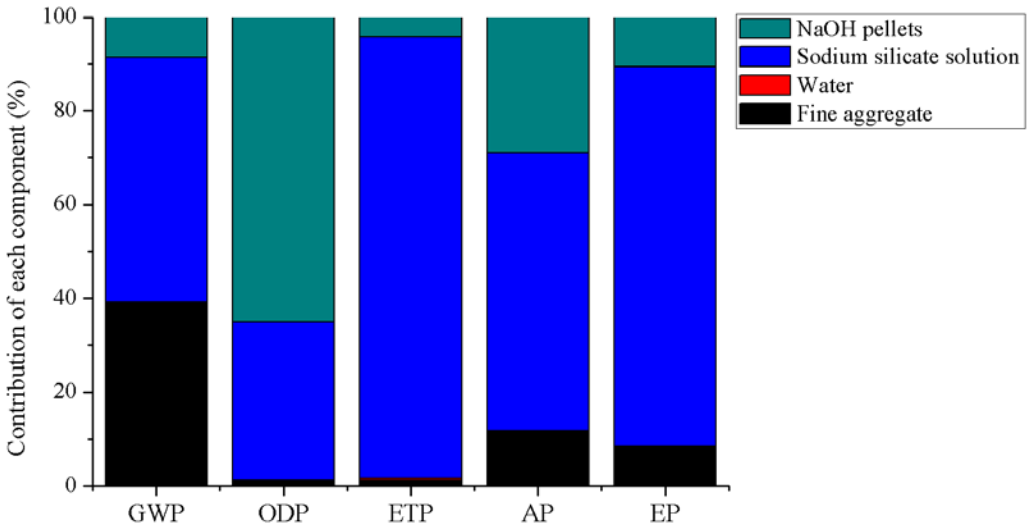
Contribution of each component (%)
100
80
60
40
20
0
GWP
ODP
ETP
AP
EP
NaOH pellets
Sodium silicate solution
Water
Fine aggregate

(b)

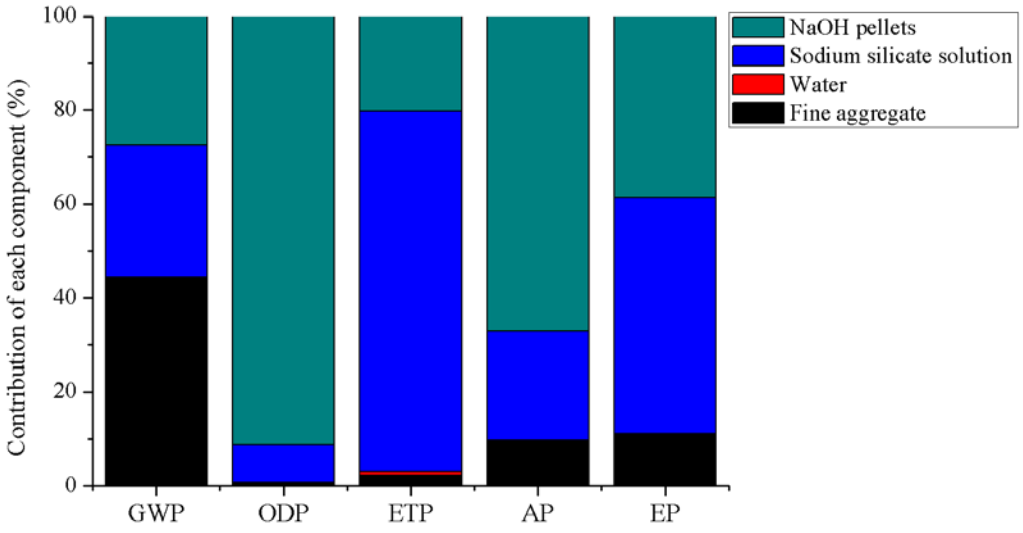

(c)

Fig. 6.10. The environmental impacts of individual component in production 1 ton of (a) Conv, (b) Norm, and (c) Pred.

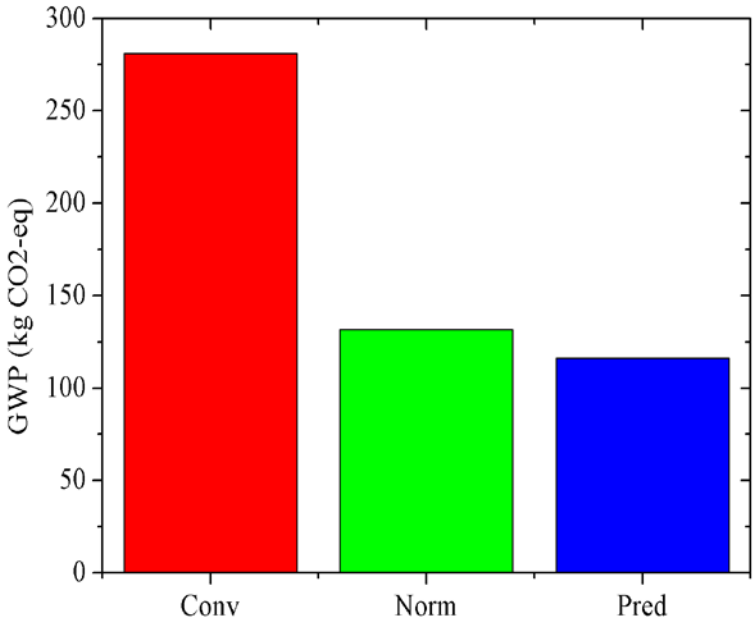

(a)

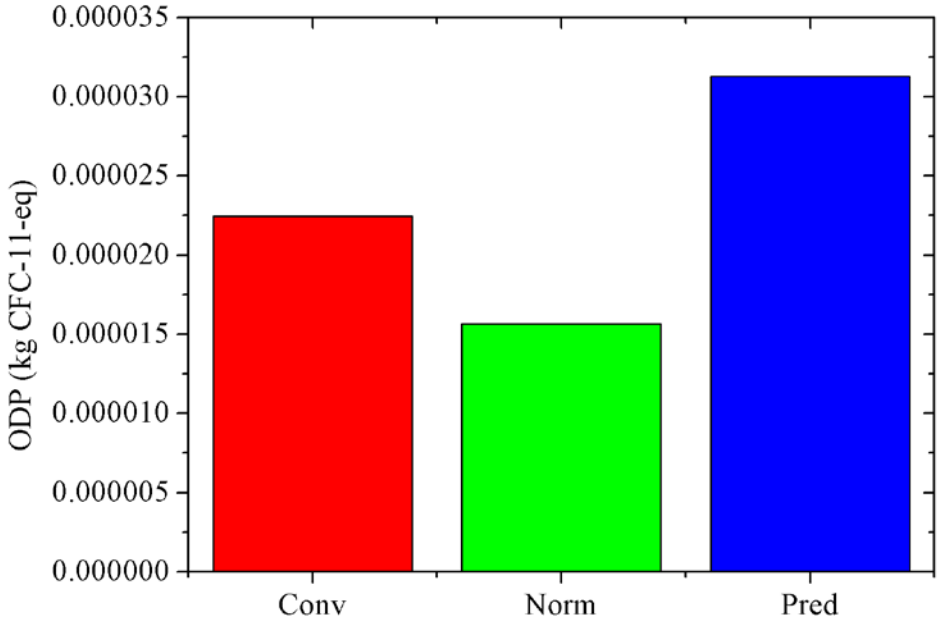
ODP (kg CFC-11-eq)
0.000035
0.000030
0.000025
0.000020
0.000015
0.000010
0.000005
0.000000
Conv
Norm
Pred

(b)

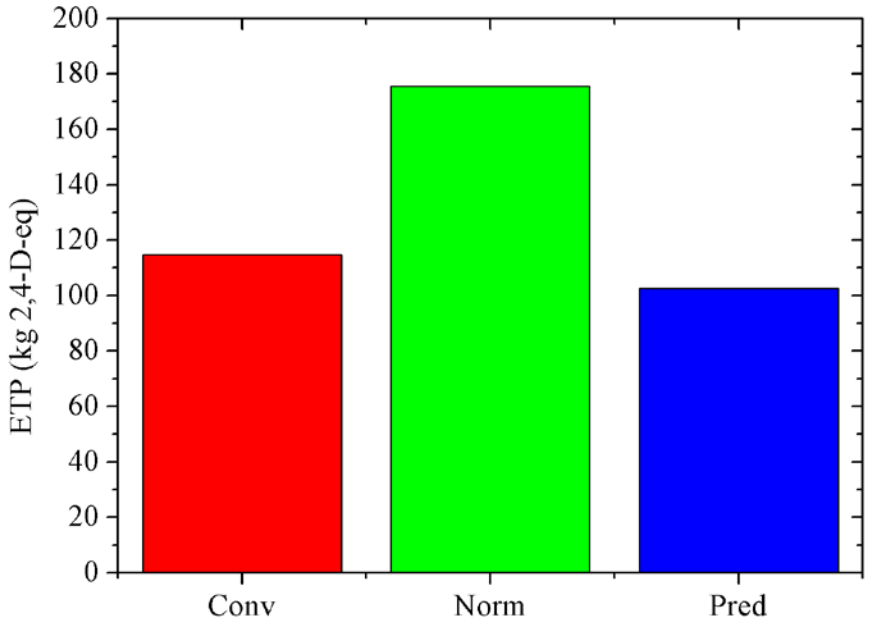
ETP (kg 2,4-D-eq)
200
180
160
140
120
100
80
60
40
20
0
Conv
Norm
Pred

(c)

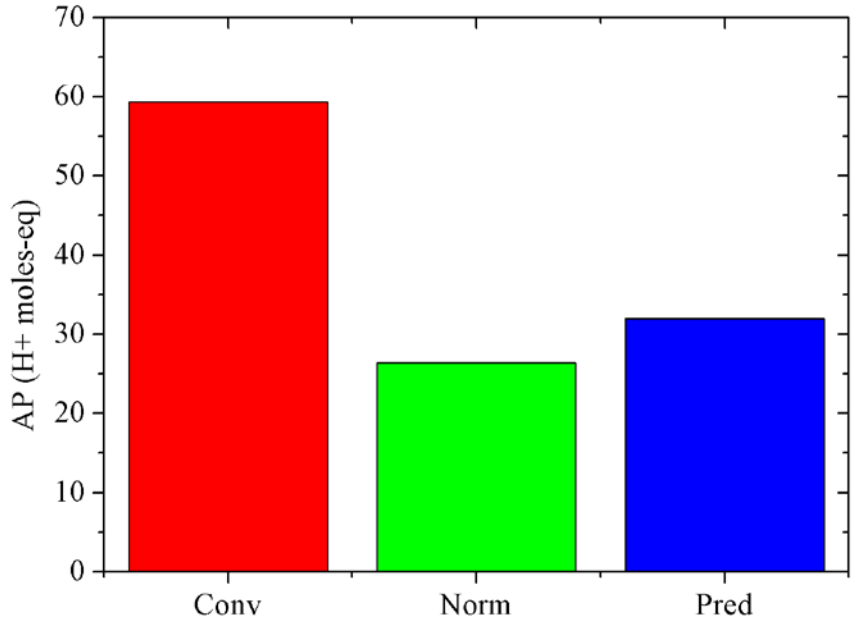

(d)

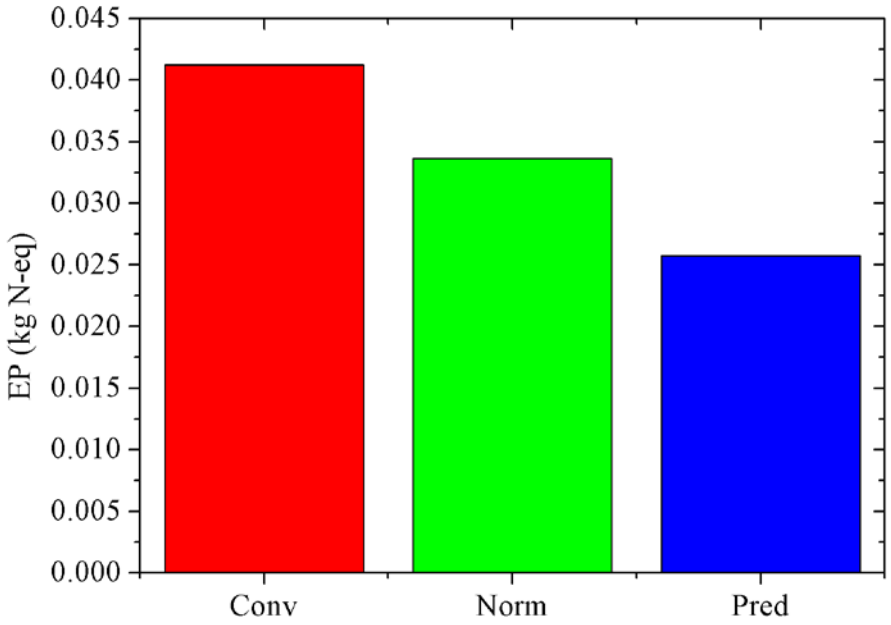

(e)

Fig. 6.11. Comparative environmental burden results for Conv, Norm, and Pred, including (a) GWP; (b) ODP; (c) ETP; (d) AP; and (e) EP.

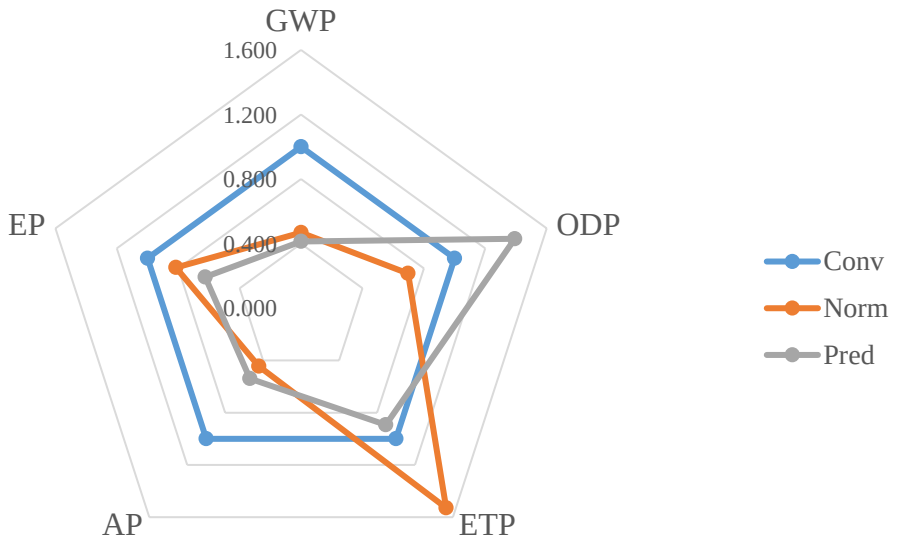

Fig. 6.12. Radar chart for the environmental impacts of Conv, Norm and Pred.

6.6.3. Sensitivity analysis for Conv, Norm and Pred

For illustrating the environmental impacts in different scenarios, sensitivity analysis was conducted. Scenarios 1 and 2 display the influence of adjusting cement/geopolymer paste content and aggregate content by 10%, respectively. Table 6.13 listed out the sensitivity analysis. In general, the global warming and ecological toxicity were increased with the selected variables. Meantime, the environmental burden caused by increasing aggregate content (scenario 2) were all less harmful than increasing paste content (scenario 1). Specifically, the average change ratios of five categories of Conv, Norm and Pred in scenario 1 were 9.25%, 8.77% and 8.65%, respectively, while the average ratios in scenario 2 were 0.75%, 1.23% and 1.35%, respectively, indicating that the inclusion of aggregate into OPC- or AAM-based

mixtures can provide internal restraint without sacrificing sustainability. In scenario 1, global warming potential change was more sensitive to increasing cement paste content in Conv (7.91%) compared to Norm (6.08%) and Pred (5.57%). Furthermore, the increase ratios of AP and EP scores for Conv were also higher than those for Norm and Pred. However, ODP of Pred (9.95%) and ETP of Norm (9.87%) became more sensitive with the increasing geopolymer paste content. It was because that increment of paste content resulted in the higher content of NaOH pellets and sodium silicate solution, echoing the individual LCA results in which alkali activator dominated the ODP and ETP. In scenario 2, interestingly, the change ratios of these five environmental impact categories for Conv were always smaller than those of AAMs. The sensitivity analysis results revealed that the strategy of introduction of aggregate into cement- and AAM-based mixtures is strongly suggested for higher strength dimensional stability and low environmental burden.

Table 6.13. Sensitivity analysis results

Mixture	Conv				Norm				Pred			
Scenario	1		2		1		2		1		2	
Change (%)	+10	-10	+10	-10	+10	-10	+10	-10	+10	-10	+10	-10
GWP (%)	7.91	-7.91	2.09	-2.09	6.08	-6.08	3.92	-3.92	5.57	-5.57	4.43	-4.43
ODP (%)	9.93	-9.93	0.07	-0.07	9.91	-9.91	0.09	-0.09	9.95	-9.95	0.05	-0.05
ETP (%)	9.78	-9.78	0.22	-0.22	9.87	-9.87	0.13	-0.13	9.78	-9.78	0.22	-0.22

AP (%)	9.40	-9.40	0.60	-0.60	8.82	-8.82	1.18	-1.18	9.03	-9.03	0.97	-0.97
EP (%)	9.23	-9.23	0.77	-0.77	9.17	-9.17	0.83	-0.83	8.91	-8.91	1.09	-1.09

6.7. Optimization of AAM mix design based on algorithm and LCA results

Based on the comparative environmental burden results between OPC-based and AAS-based mixtures, the predicted AAS mix showed lower GWP, ETP, AP, and EP scores. However, the ODP score was still higher than that of traditional cement mixtures due to the presence of the alkali activator, according to the sensitivity analysis. Therefore, it was suggested to decrease the geopolymer paste content and increase the aggregate content for lowering down the ecotoxicity and ensuring the desired mechanical properties. Hence, we traced back to the GMM generated mix design database to filter out the satisfied mix design with required properties (i.e., flowability > 100% and compressive strength = 40 MPa) and lower environmental burden than Conv. Table 6.14 listed out the optimized AAS mix design, noted as Opt, with the predicted properties. Different from the previous AAS mix, optimized mix design adopted coarse aggregate to lower down the paste content. The comparative environmental impact results between Conv and Opt were plotted in Fig. 6.13, accompanied with a radar chart illustrated in Fig. 6.14. According to the evaluation results, it can be clearly seen that the scores of all environmental impact categories were lower in optimized AAS mix than traditional cement mixtures. Thus, one of the major advantages of using machine

learning algorithm and data generation method is that optimization of AAM mix design can be conducted as well.

Table 6.14. Optimized AAS mix design

GGBFS/ %	Na_2SiO_3/ %	NaOH/%	Water/%	Fine aggregate/%	Coarse aggregate/%	Flow/%	Strength/ MPa	Shrinkage/ με
19.57	3.48	1.41	2.89	24.34	48.28	102.93	40.23	1900

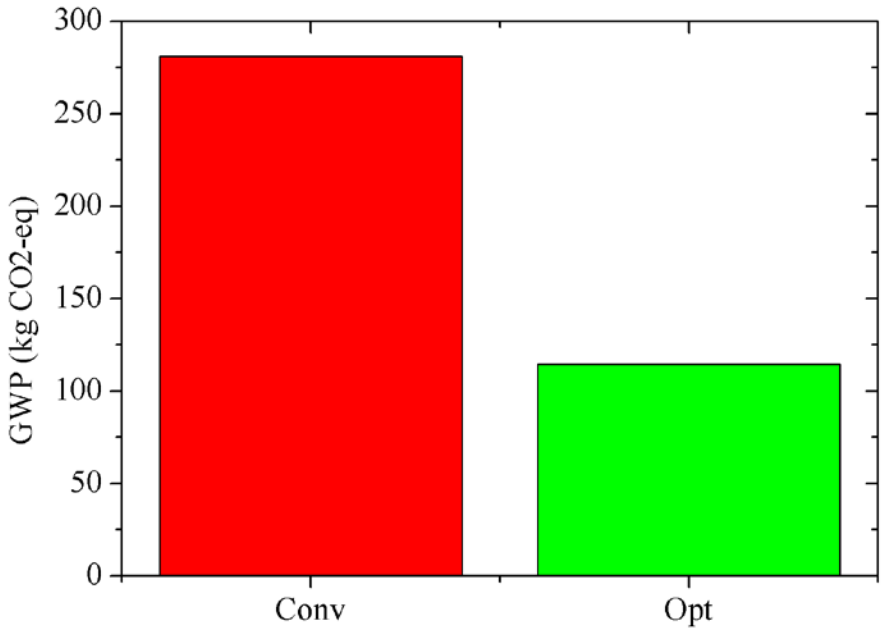

(a)

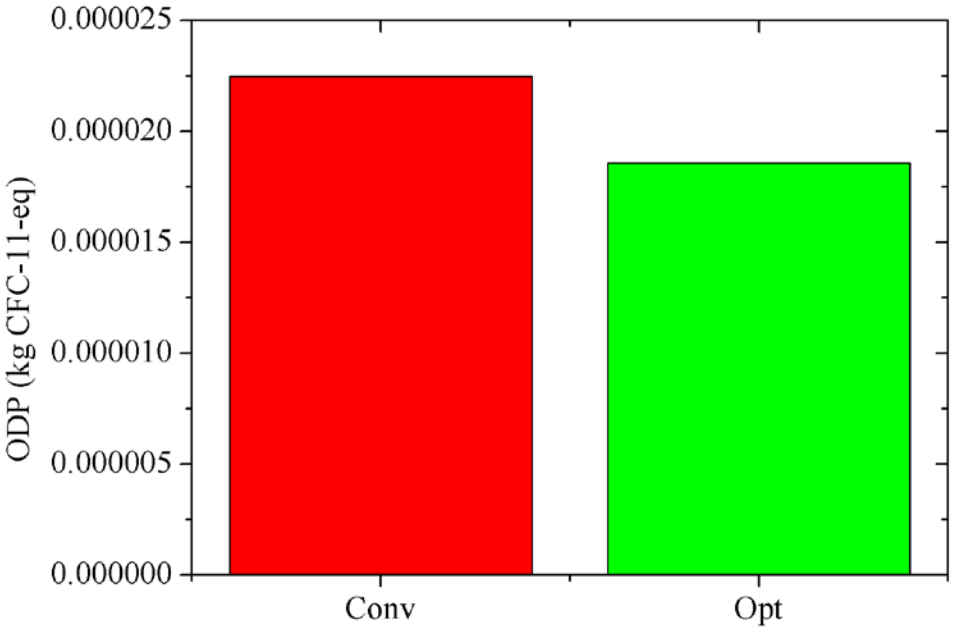
0.000025
0.000020
0.000015
0.000010
0.000005
0.000000
ODP (kg CFC-11-eq)
Conv
Opt

(b)

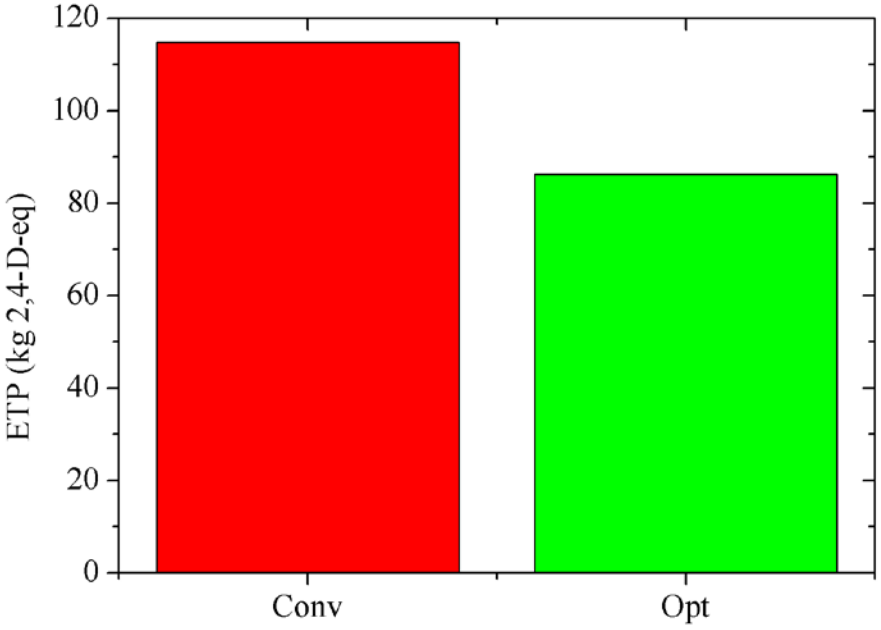
120
100
80
60
40
20
0
ETP (kg 2,4-D-eq)
Conv
Opt

(c)

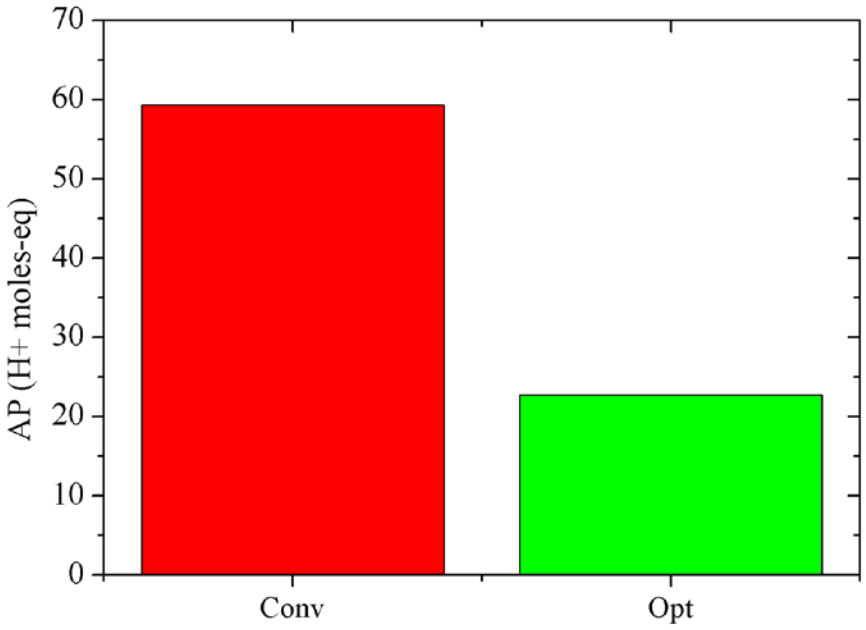

(d)

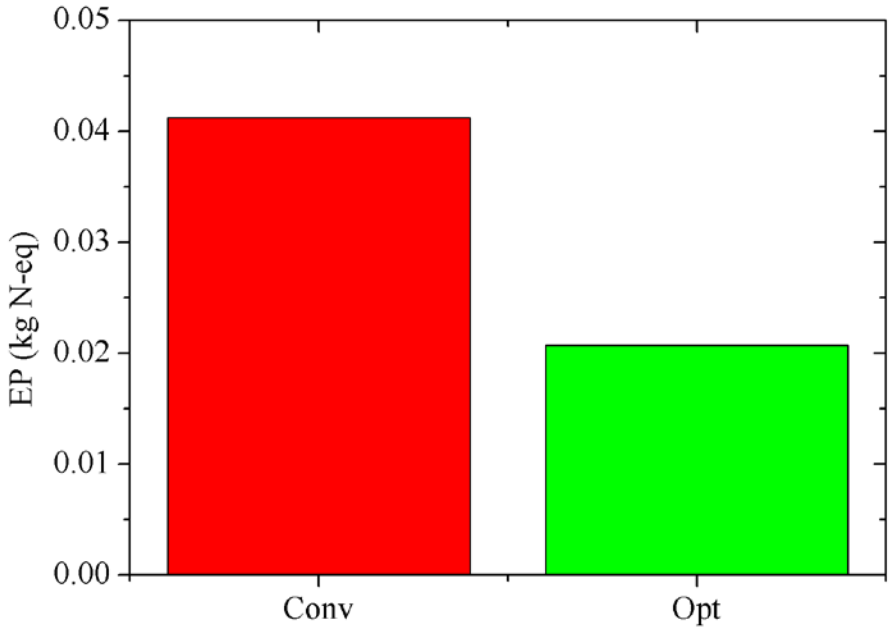

(e)

Fig. 6.13. Comparative environmental burden results for Conv and Opt, including (a) GWP; (b) ODP; (c) ETP; (d) AP; and (e) EP.

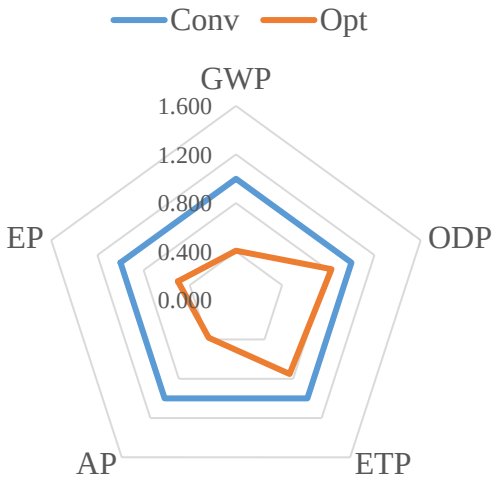

Fig. 6.14. Radar chart for the environmental impacts of Conv and Opt.

6.8. Workflow of determining optimal mix for decision-makers

According to the aforementioned mix design prediction and life cycle assessment, an index for various types of AAMs with different mix proportions and associated environmental impacts could be put forward. The workflow was shown in Fig. 6.15. The concept of this workflow is to combine inverse prediction and LCA method for determining the AAM mix design with the desired properties and environmental burdens. First, a quick index of different AAM mixes constructed by GMM method was put forward. In this database, the fresh and hardened properties (e.g., flowability, compressive strength, drying shrinkage) were as well predicted for individual mixes, accompanied with the environmental burden represented by impact categories (e.g., GWP, ODP, AP, EP, ETP). For decision-makers, the desired fresh and hardened

properties are varied from different conditions. Therefore, based on the application, data filtration was conducted for achieving the required properties. Considering the sustainability, the environmental impacts of selected mix designs were further checked to meet the waste emission requirements. Finally, only the AAM mixes that simultaneously satisfied the desired properties and environmental criteria were chosen for decision-makers. There are several advantages in the proposed workflow. Firstly, the dataset encompasses a wide range of AAM types and can be continuously updated with new data. Secondly, due to the adoption of advanced machine learning algorithm, the prediction is more accurate compared to other empirical models. Thirdly, the proposed program is user-friendly and easy to use, even for practitioners with little to no mathematical skills. Most importantly, it is the first time to simultaneously consider properties and sustainability during AAM mix design, which can largely reduce the cost in time and labor for rigorous experimental preparation.

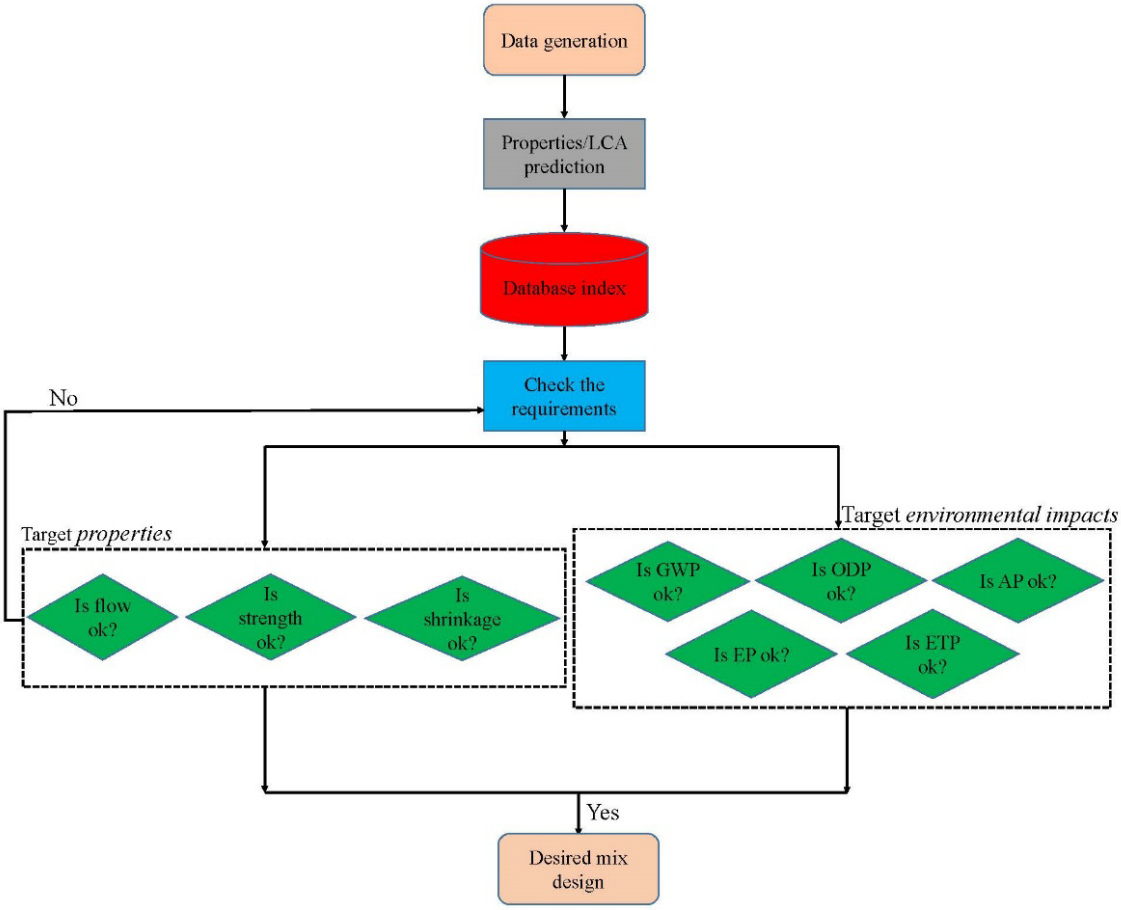

Fig. 6.15. Workflow for determining the sustainable AAM mix design

6.9. A summary of key conclusions in this chapter

In this chapter, an inverse prediction model for determining the mix design of AAM by providing key factors was constructed based on the pre-constructed XGBoost model. Meantime, a life cycle assessment (LCA) of production of 1 ton cement mortar (i.e., Conv) and alkali-activated slag mortar (i.e., Norm and Pred) with similar strength was also conducted for evaluating the environmental impacts of the predicted mixes. Five commonly used categories of environmental impacts were evaluated for Conv, Norm and Pred, including GWP, ODP, ETP, AP and EP. Moreover, a sensitivity analysis was

conducted as well, considering two scenarios that were adjusting cement/geopolymer paste content and aggregate content by 10%. There were three major steps in the workflow of this inverse prediction including forward prediction model construction, random mix design generation, and inverse prediction. A GMM algorithm was adopted to generate abundant samples that were used for inverse prediction. Finally, a workflow for decision-makers to determine the AAM mixes was presented.

The GMM algorithm showed high efficiency in data augmentation following similar data distribution, and random generation can provide abundant new mix design that not used before. Available synthetic mix designs were automatically generated by GMM. Except for SSA, other generated key factors were in general close to the original ones. For predicting the mix design with the target flow of ≥ 100%, target strength of 40 (+ 10% error) MPa, and a target drying shrinkage ≤ 2000 με, a total number of 1043 AAM mixes were filtered out after calculation using XGBoost model. The inversely predicted mix design displayed similar data distribution compared to the original mix design dataset. Finally, two AAS mortars were manufactured according to the predicted mix designs. The experimental results were generally close to the predicted results and target properties, indicating the availability of this model in the real construction work.

The LCA on the environmental impact of cement, water and aggregate in Conv revealed that global warming and ecological toxicity were dominated by production of OPC, while production of water and aggregate exhibited minor environmental impacts. On the other hand, GWP of AAMs was controlled by alkali activator and aggregate, but ODP, ETP, AP and EP were mainly governed by NaOH pellet and sodium silicate

solution. The sensitivity analysis results displayed the individual effects on the environmental burden of Conv, Norm and Pred brought by cement/geopolymer paste content and aggregate content. The environmental burden of Conv, Norm and Pred was sensitive to change of cement/geopolymer paste content due to the existence of OPC in Conv and alkali activator in Norm and Pred. Additionally, adjusting aggregate content resulted in the average LCIA increasing by 9.25%, 8.77% and 8.65% in Conv, Norm and Pred, respectively, demonstrating less harmful than paste content (0.75%, 1.23% and 1.35% in Conv, Norm and Pred, respectively). For solving the environmental toxicity problem, the predicted AAM mix design was further optimized based on the GMM generated dataset. The optimized AAM mix design adopted coarse aggregate to lower down the paste content and maintain the desired properties.

To be honest, it is still a tough task for researchers in the field of civil engineering to design sustainable AAM mixes with low cost and high performance. This research probes this issue by combining machine learning algorithm and GMM data augmentation method to construct an inverse prediction program.

Chapter 7: Conclusions

This thesis focused on determining and optimizing the sustainable mix design of alkali-activated materials (AAMs) using machine learning methods. A typical 'cradle-to-gate' life cycle assessment (LCA) analysis was conducted to evaluate the environmental burden of the predicted mix design by machine learning algorithm. Starting with the introduction and statement of problems on current research of AAMs in Chapter 1, the need to use machine learning method for helping design the mix proportions of AAMs was identified. The current prediction models for AAMs were faced with two major problems, including low generality and lack of inverse prediction. Specifically, numerous researchers constructed the forward prediction models, namely, using mix design to predict mechanical properties of AAMs, based on their own experimental data, leading to limited applicability to other researchers' data. Meantime, inverse prediction from the required properties to mix design of AAMs is seldom touched, which still inhibits the commercial development of AAMs. LCA was recommended for AAM design to ensure its sustainability. Then, three main research goals were put forward based on prediction of properties of AAMs, prediction of mix design of AAMs and LCA of AAMs. Chapter 2 offered a literature review on the influence of key factors in mix design on the fresh and hardened properties of AAMs, the calculation mechanism behind artificial neural networks, and environmental impacts of each component in AAMs.

Chapters 3, 4 and 5 provided three forward prediction models for the flowability, compressive strength and drying shrinkage of AAMs based on the collected data from existing literature. A typical workflow for constructing the prediction models was adopted, including data collection, data processing, data analysis and model construction. In Chapter 3, the workability of AAMs were evaluated using 402 mixtures from 26 papers. Eight key factors were identified, including activity moduli and specific surface area of precursors, geopolymer paste content (GPC), NaOH concentration, silicate modulus of alkali activator (Ms), liquid-to-binder (L/B) ratio, fine and coarse aggregate content. Backpropagation neural networks (BPNN), LightGBM, and XGBoost regression models were developed to predict flowability. The prediction performance was evaluated by the mean absolute error (MAE), root mean squared error (RMSE), and R^2 statistics (also used in the following two chapters). Analysis showed that Ms and GPC generally improved workability, while reactivity of precursors, NaOH concentration, and aggregate ratio reduced it. Among the three abovementioned algorithms, the LightGBM algorithm exhibited the strongest performance, demonstrating high robustness and accuracy in predicting the workability of AAMs. It achieved an impressive R^2 value of 0.96, with an MAE of 5.64 and RMSE of 11.20. The results of feature importance analysis displayed a relatively higher importance of Ms on the workability of AAMs.

Chapter 4 analyzed 301 AAM mixtures, identifying key factors same as the ones in Chapter 3 such as precursor properties, activator characteristics, L/B ratios and aggregate contents. Qualitative analysis showed that higher L/B ratios and larger GPC

might weaken AAM strength, while higher precursor reactivity, Ms, and NaOH concentration could enhance it, with NaOH concentration having a threshold of 12-14 M. A model based on XGBoost has achieved the highest accuracy compared to models using BPNN and LightGBM for predicting the strength of AAM. It has attained a notably high R^2 value of 0.97, along with low MAE of 1.24 and RMSE of 2.43. Feature importance analysis results showed the dominant importance of coarse aggregate on the strength prediction.

The last forward prediction model lied in the ultimate drying shrinkage of AAMs in Chapter 5. This chapter studied 438 AAM mixtures from 43 papers to understand drying shrinkage. Different from the previous two chapters, eleven key factors were identified including the activity moduli and SSA of the binder, GPC, L/B ratio, NaOH concentration, Ms, fine and coarse aggregate content ratio, curing temperature, RH and V/S ratio. Qualitative analysis showed shrinkage resistance increased with NaOH concentration, aggregate ratio, curing temperature, RH, and V/S ratio, but decreased with GPC, L/B ratio, and Ms. An XGBoost model predicted UDS with high accuracy (R^2 = 0.99, MAE = 128.01, RMSE = 413.32), outperforming other two algorithms. Meantime, the feature importance analysis pointed out that GPC left the highest significance on the drying shrinkage of AAMs. These three chapters filled research gaps, aided in cost-effective and sustainable AAM development, bridging scientific knowledge with practical implementation and improving AAM mix design understanding for civil engineering applications. Although the proposed models demonstrated higher generality and accuracy compared to existing ones, they still have

limitations. Hypothetical values for key factors like specific surface area may introduce errors. Additionally, the models may face challenges in predicting certain precursors with limited data. Furthermore, the complexity of machine learning models makes interpretation difficult, and important parameters such as raw material origin are not fully captured without manual preprocessing.

Chapter 6 introduced an inverse prediction model for sustainable AAM mix design, utilizing the pre-constructed XGBoost model in previous chapters and life cycle assessment method. The workflow involved constructing a forward prediction model, generating random mix designs using a Gaussian mixture method (GMM) algorithm, and performing inverse prediction. For evaluating the environmental impacts, CML 2002 approach was conducted to evaluate and compare the environmental burden among conventional cement mortar, normal alkali-activated slag mortar, and predicted alkali-activated slag (AAS) mortar based on five environmental impact categories including Global warming (GWP), Ozone depletion (ODP), Acidification (AP), Eutrophication (EP), and Ecotoxicity (ETP). Sensitivity analysis considered adjustments of cement/geopolymer paste and aggregate content by 10%. This LCA method was then applied to all predicted mixes to provide indexes in sustainability. The GMM algorithm generated synthetic mix designs, closely resembled original data distributions. For a target flowability of higher than 100%, target strength of 40 (+ 10% error) MPa, target drying shrinkage less than 2000 με, 1043 AAM mixes were filtered using the XGBoost model. The inversely predicted mix designs demonstrated similar data distribution to the original dataset. Regarding the limitations of GMM, it's sensitive

to initialization and outliers, which can lead to suboptimal solutions and computational inefficiencies. GMM's computational complexity makes it challenging to impose constraints on generated data, such as maintaining positive values or specific relationships. Two AAS mortars were manufactured based on predicted mix designs, with experimental results closely matching predictions and achieving the target properties. Regarding the environmental impact results, Conv, production of OPC dominated global warming and ecological toxicity, while water and aggregate had minor impacts. For AAMs, GWP was influenced by alkali activator and aggregate, while ODP, ETP, AP, and EP were mainly affected by NaOH pellet and sodium silicate solution. Sensitivity analysis showed that changes in cement/geopolymer paste content significantly affected Conv, Norm, and Pred due to OPC and alkali activator presence. Adjusting aggregate content resulted in a slight increase in environmental burden for all mixes. According to the environmental impact results, an improvement on mix design was conducted by addition of coarse aggregate. The improved mix design was derived from the GMM generated dataset based on the target properties and environmental burdens. The improved mix design remained the desired properties and displayed lower greenhouse gas emission and potential environmental toxicity. Lastly, a workflow on how to determine desired AAM mixes for decision-makers was put forward. This research aimed to address the challenge of designing sustainable, cost-effective AAM mixes in civil engineering by combining machine learning algorithms and LCA method, thus advancing practical development and commercial application of AAM in construction projects.

In the future research, several points are worthy of notice lying in the improvement of forward/inverse prediction model and LCA analysis. First, in the forward prediction model, namely using mix design to predict the properties, several key factors (categorical features) were not taken into consideration such as the origin of raw material due to their complexity in mathematical representation. Thus, it is suggested to use special codes to distinguish these parameters. Second, the dataset should be updated in order to cover rarely used materials and find more new AAM mixes, in which random generation method is suggested to generate abundant new mixes that are not adopted before. Third, it's crucial to consider the variability in properties of raw materials across different locations, as well as the associated logistical costs, in the sensitivity analysis. Additionally, thorough examination of structural design incorporating AAM is necessary, given its relatively recent introduction and limited field applications. It's recommended that future studies delve into the structural responses and LCA of AAM-based structures across various application scenarios such as buildings, bridges, dams, blast-resistant and impact-resistant structures, as well as mass concrete projects.

Reference

[1] Y.K. Kong, S. Ruan, K. Kurumisawa, Recycling of calcined carbonated cement pastes as cementitious materials: Proposed ccus technology for calcium looping, J. Environ. Chem. Eng. 10 (5) (2022) 108247. https://doi.org/10.1016/j.jece.2022.108247.

[2] Y.K. Kong, Y. Song, K. Kurumisawa, T. Wang, D. Yan, Q. Zeng, X. Zhou, S. Ruan, Use of hydrated cement pastes (hcp) as a CO_2 sponge, J. CO2 Util. 55 (2022) 101804. https://doi.org/10.1016/j.jcou.2021.101804.

[3] Y.K. Kong, Y. Song, Y. Weng, K. Kurumisawa, D. Yan, X. Zhou, S. Wang, S. Ruan, Influences of CO_2-cured cement powders on hydration of cement paste, Greenhouse Gases: Sci. Technol. 12 (2) (2022) https://doi.org/10.1002/ghg.2141.

[4] NOAA, earth system research laboratory's (esrl), global greenhouse gas reference network.

[5] C. Chen, G. Habert, Y. Bouzidi, A. Jullien, Environmental impact of cement production: Detail of the different processes and cement plant variability evaluation, J. Clean. Prod. 18 (2010) 478-485. https://doi.org/10.1016/j.jclepro.2009.12.014.

[6] H. Ye, Z. Chen, L. Huang, Mechanism of sulfate attack on alkali-activated slag: The role of activator composition, Cem. Concr. Res. 125 (2019) 105868. https://doi.org/10.1016/j.cemconres.2019.105868.

[7] R. Snellings, G. Mertens, J. Elsen, Supplementary cementitious materials, Rev. Mineral. Geochem. 74 (2012) 211-278. https://doi.org/10.2138/rmg.2012.74.6.

[8] M. Schneider, M. Romer, M. Tschudin, H. Bolio, Sustainable cement production—present and future, Cem. Concr. Res. 41 (7) (2011) 642-650. https://doi.org/10.1016/j.cemconres.2011.03.019.

[9] P. Fernando, C. João, J. Said, Alkali-activated binders: A review: Part 1. Historical background, terminology, reaction mechanisms and hydration products, Constr. Build. Mater. 22 (7) (2008) 1305-1314. https://doi.org/10.1016/j.conbuildmat.2007.10.015.

[10] A.R.G. de Azevedo, A.S.A. Cruz, M.T. Marvila, L.B. de Oliveira, S.N. Monteiro, C.M.F. Vieira, R. Fediuk, R. Timokhin, N. Vatin, M. Daironas, Natural fibers as an alternative to synthetic fibers in reinforcement of geopolymer matrices: A comparative review, Polymers 13 (15) (2021) 2493. https://doi.org/10.3390/polym13152493.

[11] B.C. Mendes, L.G. Pedroti, C.M.F. Vieira, M. Marvila, A.R.G. Azevedo, J.M. Franco de Carvalho, J.C.L. Ribeiro, Application of eco-friendly alternative activators in alkali-activated materials: A review, J. Build. Eng. 35 (2021) 102010. https://doi.org/10.1016/j.jobe.2020.102010.

[12] M. Jiang, X. Chen, F. Rajabipour, C.T. Hendrickson, Comparative life cycle assessment of conventional, glass powder, and alkali-activated slag concrete and mortar, J. Infrastruct. Syst. 20 (4) (2014) 04014020. http://doi.org/doi:10.1061/(ASCE)IS.1943-555X.0000211.

[13] M. Fawer, M. Concannon, W. Rieber, Life cycle inventories for the production of sodium silicates, Int. J. Life Cycle Asses. 4 (4) (1999) 207. https://doi.org/10.1007/BF02979498.

[14] G. Habert, J.-B. d'Espinose de Lacaillerie, N. Roussel, An environmental evaluation of geopolymer based concrete production: Reviewing current research trends, J. Clean. Prod. 19 (2011) 1229-1238. https://doi.org/10.1016/j.jclepro.2011.03.012.

[15] L.K. Turner, F.G. Collins, Carbon dioxide equivalent (CO_2-e) emissions: A comparison between geopolymer and opc cement concrete, Constr. Build. Mater. 43 (2013) 125-130. https://doi.org/10.1016/j.conbuildmat.2013.01.023.

[16] R. Robayo-Salazar, J. Mejía-Arcila, R. Mejía de Gutiérrez, E. Martínez, Life cycle assessment (lca) of an alkali-activated binary concrete based on natural volcanic pozzolan: A comparative analysis to OPC concrete, Constr. Build. Mater. 176 (2018) 103-111. https://doi.org/10.1016/j.conbuildmat.2018.05.017.

[17] H. Ye, A. Radlińska, Shrinkage mechanisms of alkali-activated slag, Cem. Concr. Res. 88 (2016) 126-135. https://doi.org/10.1016/j.cemconres.2016.07.001.

[18] I. Garcia-Lodeiro, A. Palomo, A. Fernández-Jiménez, D.E. Macphee, Compatibility studies between n-a-s-h and c-a-s-h gels. Study in the ternary diagram Na_2O–CaO–Al_2O_3–SiO_2–H_2O, Cem. Concr. Res. 41 (9) (2011) 923-931. https://doi.org/10.1016/j.cemconres.2011.05.006.

[19] T. Bakharev, J.G. Sanjayan, Y.B. Cheng, Resistance of alkali-activated slag concrete to carbonation, Cem. Concr. Res. 31 (9) (2001) 1277-1283. https://doi.org/10.1016/S0008-8846(01)00574-9.

[20] T. Huyen Vu, L.C. Dang, G. Kang, V. Sirivivatnanon, Chloride induced corrosion of steel reinforcement in alkali activated concretes: A critical review, Case Stud. Constr. Mater. (2022) e01112. https://doi.org/10.1016/j.cscm.2022.e01112.

[21] S.-D. Wang, X.-C. Pu, K.L. Scrivener, P.L. Pratt, Alkali-activated slag cement and concrete: A review of properties and problems, Adv. Cem. Res. 7 (27) (1995) 93-102. https://doi.org/10.1680/adcr.1995.7.27.93.

[22] S.H. Chu, Effect of paste volume on fresh and hardened properties of concrete, Constr. Build. Mater. 218 (2019) 284-294. https://doi.org/10.1016/j.conbuildmat.2019.05.131.

[23] F. Kuang, Z. Long, D. Kuang, X. Liu, R. Guo, Application of back propagation neural network to the modeling of slump and compressive strength of composite geopolymers, Comp. Mater. Sci. 206 (2022) 111241. https://doi.org/10.1016/j.commatsci.2022.111241.

[24] P. Zhang, Z. Gao, J. Wang, J. Guo, T. Wang, Influencing factors analysis and optimized prediction model for rheology and flowability of nano-SiO_2 and pva fiber reinforced alkali-activated composites, J. Clean. Prod. 366 (2022) 132988. https://doi.org/10.1016/j.jclepro.2022.132988.

[25] S. Nazar, J. Yang, X.-E. Wang, K. Khan, M.N. Amin, M.F. Javed, F. Althoey, M. Ali, Estimation of strength, rheological parameters, and impact of raw constituents of alkali-activated mortar using machine learning and shapely additive explanations (shap), Constr. Build. Mater. 377 (2023) 131014. https://doi.org/10.1016/j.conbuildmat.2023.131014.

[26] E. Gomaa, T. Han, M. ElGawady, J. Huang, A. Kumar, Machine learning to predict properties of fresh and hardened alkali-activated concrete, Cem. Concr. Compos. 115 (2021) 103863. https://doi.org/10.1016/j.cemconcomp.2020.103863.

[27] ACI 318M-14, Building code requirements for structural concrete and commentary, 2014. USA.

[28] AS 3600-2009, Concrete structures, Standards Australia, 2009.

[29] W. Prachasaree, S. Limkatanyu, A. Hawa, P. Sukontasukkul, P. Chindaprasirt, Manuscript title: Development of strength prediction models for fly ash based geopolymer concrete, J. Build. Eng. 32 (2020) 101704. https://doi.org/10.1016/j.jobe.2020.101704.

[30] H. Ma, H. Chen, H. Zhu, y. Shi, Y. Ni, Q. Huo, Z. Hang, Study on the drying shrinkage of alkali-activated coal gangue-slag mortar and its mechanisms, Constr. Build. Mater. 225 (2019) 204-213. https://doi.org/10.1016/j.conbuildmat.2019.07.258.

[31] S.H. Chu, Y.K. Kong, Mathematical model for strength of alkali-activated materials, J. Build. Eng. 44 (2021) 103189. https://doi.org/10.1016/j.jobe.2021.103189.

[32] Y.K. Kong, K. Kurumisawa, Prediction of the drying shrinkage of alkali-activated materials using artificial neural networks, Case Stud. Constr. Mater. 17 (2022) e01166. https://doi.org/10.1016/j.cscm.2022.e01166.

[33] EN 1992-1-1: Eurocode 2: Design of concrete structures, Part 1. General rules and rules for buildings, 2004.

[34] CEB Bulletin D'information, CEB-FIP model code 2010, Germany, 2010.

[35] E. Adesanya, A. Aladejare, A. Adediran, A. Lawal, M. Illikainen, Predicting shrinkage of alkali-activated blast furnace-fly ash mortars using artificial neural network (ann), Cem. Concr. Compos. 124 (2021) 104265. https://doi.org/10.1016/j.cemconcomp.2021.104265.

[36] L. Huang, Z. Chen, H. Ye, A mechanistic model for the time-dependent autogenous shrinkage of high performance concrete, Constr. Build. Mater. 255 (2020) 119335. https://doi.org/10.1016/j.conbuildmat.2020.119335.

[37] H. Zhang, Y. Wang, D.E. Lehman, Y. Geng, K. Kuder, Time-dependent drying shrinkage model for concrete with coarse and fine recycled aggregate, Cem. Concr. Compos. 105 (2020) 103426. https://doi.org/10.1016/j.cemconcomp.2019.103426.

[38] I.C. Yeh, Computer-aided design for optimum concrete mixtures, Cem. Concr. Compos. 29 (3) (2007) 193-202. https://doi.org/10.1016/j.cemconcomp.2006.11.001.

[39] Y. Huang, J. Zhang, F. Tze Ann, G. Ma, Intelligent mixture design of steel fibre reinforced concrete using a support vector regression and firefly algorithm

based multi-objective optimization model, Constr. Build. Mater. 260 (2020) 120457. https://doi.org/10.1016/j.conbuildmat.2020.120457.
[40] X. Ke, Y. Duan, A bayesian machine learning approach for inverse prediction of high-performance concrete ingredients with targeted performance, Constr. Build. Mater. 270 (2021) 121424. https://doi.org/10.1016/j.conbuildmat.2020.121424.
[41] W. Huo, Z. Zhu, H. Sun, B. Ma, L. Yang, Development of machine learning models for the prediction of the compressive strength of calcium-based geopolymers, J. Clean. Prod. 380 (2022) 135159. https://doi.org/10.1016/j.jclepro.2022.135159.
[42] Y. Sun, H. Cheng, S. Zhang, M.K. Mohan, G. Ye, G. De Schutter, Prediction & optimization of alkali-activated concrete based on the random forest machine learning algorithm, Constr. Build. Mater. 385 (2023) 131519. https://doi.org/10.1016/j.conbuildmat.2023.131519.
[43] I. Jawed, J. Skalny, Alkalies in cement: A review: II. Effects of alkalies on hydration and performance of portland cement, Cem. Concr. Res. 8 (1) (1978) 37-51.
[44] C. Shi, X. Wu, M. Tang, Research on alkali-activated cementitious systems in china: A review, Adv. Cem. Res. 5 (17) (1993) 1-7. https://doi.org/10.1680/adcr.1993.5.17.1.
[45] F. Farooq, X. Jin, M. Faisal Javed, A. Akbar, M. Izhar Shah, F. Aslam, R. Alyousef, Geopolymer concrete as sustainable material: A state of the art review, Constr. Build. Mater. 306 (2021) 124762. https://doi.org/10.1016/j.conbuildmat.2021.124762.
[46] M. Ahmaruzzaman, A review on the utilization of fly ash, Prog. Energy Combust. Sci. 36 (3) (2010) 327-363. https://doi.org/10.1016/j.pecs.2009.11.003.
[47] J.M. Paris, J.G. Roessler, C.C. Ferraro, H.D. DeFord, T.G. Townsend, A review of waste products utilized as supplements to portland cement in concrete, J. Clean. Prod. 121 (2016) 1-18. https://doi.org/10.1016/j.jclepro.2016.02.013.
[48] M.R. Karim, M.F.M. Zain, M. Jamil, F.C. Lai, Fabrication of a non-cement binder using slag, palm oil fuel ash and rice husk ash with sodium hydroxide, Constr. Build. Mater. 49 (2013) 894-902. https://doi.org/10.1016/j.conbuildmat.2013.08.077.
[49] B.L. Damineli, F.M. Kemeid, P.S. Aguiar, V.M. John, Measuring the eco-efficiency of cement use, Cem. Concr. Compos. 32 (8) (2010) 555-562. https://doi.org/10.1016/j.cemconcomp.2010.07.009.
[50] R. Bajpai, K. Choudhary, A. Srivastava, K.S. Sangwan, M. Singh, Environmental impact assessment of fly ash and silica fume based geopolymer concrete, J. Clean. Prod. 254 (2020) 120147. https://doi.org/10.1016/j.jclepro.2020.120147.
[51] D.A. Salas, A.D. Ramirez, N. Ulloa, H. Baykara, A.J. Boero, Life cycle assessment of geopolymer concrete, Constr. Build. Mater. 190 (2018) 170-177. https://doi.org/10.1016/j.conbuildmat.2018.09.123.
[52] M. Rowles, B. O'connor, Chemical optimisation of the compressive strength of aluminosilicate geopolymers synthesised by sodium silicate activation of

metakaolinite, J. Mater. Chem. 13 (5) (2003) 1161-1165. https://doi.org/10.1039/B212629J.

[53] A. Albidah, M. Alghannam, H. Abbas, T. Almusallam, Y. Al-Salloum, Characteristics of metakaolin-based geopolymer concrete for different mix design parameters, J. Mater. Res. Technol. 10 (2021) 84-98. https://doi.org/10.1016/j.jmrt.2020.11.104.

[54] H. Ye, C. Cartwright, F. Rajabipour, A. Radlińska, Understanding the drying shrinkage performance of alkali-activated slag mortars, Cem. Concr. Compos. 76 (2017) 13-24. https://doi.org/10.1016/j.cemconcomp.2016.11.010.

[55] M. Moranville-Regourd, Cements made from blastfurnace slag, Lea's chemistry of cement and concrete, Elsevier1998, pp. 637-678.

[56] M.M. Alonso, S. Gismera, M.T. Blanco, M. Lanzón, F. Puertas, Alkali-activated mortars: Workability and rheological behaviour, Constr. Build. Mater. 145 (2017) 576-587. https://doi.org/10.1016/j.conbuildmat.2017.04.020.

[57] B.G. Kutchko, A.G. Kim, Fly ash characterization by sem-eds, FUEL - GUILDFORD - (2006).

[58] X. Gao, Q.L. Yu, H.J.H. Brouwers, Properties of alkali activated slag–fly ash blends with limestone addition, Cem. Concr. Compos. 59 (2015) 119-128. https://doi.org/10.1016/j.cemconcomp.2015.01.007.

[59] E. Aprianti S, A huge number of artificial waste material can be supplementary cementitious material (scm) for concrete production – a review part ii, J. Clean. Prod. 142 (2017) 4178-4194. https://doi.org/10.1016/j.jclepro.2015.12.115.

[60] H. Alanazi, J. Hu, Y.-R. Kim, Effect of slag, silica fume, and metakaolin on properties and performance of alkali-activated fly ash cured at ambient temperature, Constr. Build. Mater. 197 (2019) 747-756. https://doi.org/10.1016/j.conbuildmat.2018.11.172.

[61] M. Ibrahim, M.A.M. Johari, M. Maslehuddin, M.K. Rahman, Influence of nano-sio2 on the strength and microstructure of natural pozzolan based alkali activated concrete, Constr. Build. Mater. 173 (2018) 573-585. https://doi.org/10.1016/j.conbuildmat.2018.04.051.

[62] Y. Ling, K. Wang, X. Wang, S. Hua, Effects of mix design parameters on heat of geopolymerization, set time, and compressive strength of high calcium fly ash geopolymer, Constr. Build. Mater. 228 (2019) 116763. https://doi.org/10.1016/j.conbuildmat.2019.116763.

[63] M.N.S. Hadi, H. Zhang, S. Parkinson, Optimum mix design of geopolymer pastes and concretes cured in ambient condition based on compressive strength, setting time and workability, J. Build. Eng. 23 (2019) 301-313. https://doi.org/10.1016/j.jobe.2019.02.006.

[64] J. Zhang, C. Shi, Z. Zhang, Z. Ou, Durability of alkali-activated materials in aggressive environments: A review on recent studies, Constr. Build. Mater. 152 (2017) 598-613. https://doi.org/10.1016/j.conbuildmat.2017.07.027.

[65] M. Jafari Nadoushan, A.A. Ramezanianpour, The effect of type and concentration of activators on flowability and compressive strength of natural pozzolan and

slag-based geopolymers, Constr. Build. Mater. 111 (2016) 337-347. https://doi.org/10.1016/j.conbuildmat.2016.02.086.

[66] F. Pacheco-Torgal, D. Moura, Y. Ding, S. Jalali, Composition, strength and workability of alkali-activated metakaolin based mortars, Constr. Build. Mater. 25 (9) (2011) 3732-3745. https://doi.org/10.1016/j.conbuildmat.2011.04.017.

[67] W. Hu, Y. Ma, M. Koehler, H. Gong, B. Huang, Mix design optimization and early strength prediction of unary and binary geopolymer from multiple waste streams, J. Hazard. Mater. 403 (2021) 123632. https://doi.org/10.1016/j.jhazmat.2020.123632.

[68] C. Luan, X. Shi, K. Zhang, N. Utashev, F. Yang, J. Dai, Q. Wang, A mix design method of fly ash geopolymer concrete based on factors analysis, Constr. Build. Mater. (2020) 121612. https://doi.org/10.1016/j.conbuildmat.2020.121612.

[69] Y. Alrefaei, Y.-S. Wang, J.-G. Dai, Effect of mixing method on the performance of alkali-activated fly ash/slag pastes along with polycarboxylate admixture, Cem. Concr. Compos. 117 (2021) 103917. https://doi.org/10.1016/j.cemconcomp.2020.103917.

[70] M. Nedeljković, Z. Li, G. Ye, Setting, strength, and autogenous shrinkage of alkali-activated fly ash and slag pastes: Effect of slag content, Mater. 11 (11) (2018) 2121. https://doi.org/10.3390/ma11112121.

[71] J.G. Jang, N.K. Lee, H.K. Lee, Fresh and hardened properties of alkali-activated fly ash/slag pastes with superplasticizers, Constr. Build. Mater. 50 (2014) 169-176. https://doi.org/10.1016/j.conbuildmat.2013.09.048.

[72] X. Gao, Q.L. Yu, H.J.H. Brouwers, Assessing the porosity and shrinkage of alkali activated slag-fly ash composites designed applying a packing model, Constr. Build. Mater. 119 (2016) 175-184. https://doi.org/10.1016/j.conbuildmat.2016.05.026.

[73] M. Tuyan, L.V. Zhang, M.L. Nehdi, Development of sustainable alkali-activated slag grout for preplaced aggregate concrete, J. Clean. Prod. 277 (2020) 123488. https://doi.org/10.1016/j.jclepro.2020.123488.

[74] L.B. de Oliveira, A.R.G. de Azevedo, M.T. Marvila, E.C. Pereira, R. Fediuk, C.M.F. Vieira, Durability of geopolymers with industrial waste, Case Stud. Constr. Mater. 16 (2022) e00839. https://doi.org/10.1016/j.cscm.2021.e00839.

[75] A.K.H. Kwan, S.K. Ling, Lowering paste volume of scc through aggregate proportioning to reduce carbon footprint, Constr. Build. Mater. 93 (2015) 584-594. https://doi.org/10.1016/j.conbuildmat.2015.06.034.

[76] B. Bennett, P. Visintin, T. Xie, Global warming potential of recycled aggregate concrete with supplementary cementitious materials, J. Build. Eng. 52 (2022) 104394. https://doi.org/10.1016/j.jobe.2022.104394.

[77] S.H. Chu, Development of infilled cementitious composites (icc), Compos. Struct. 267 (2021) 113885. https://doi.org/10.1016/j.compstruct.2021.113885.

[78] T. Bakharev, J.G. Sanjayan, Y.B. Cheng, Effect of elevated temperature curing on properties of alkali-activated slag concrete, Cem. Concr. Res. 29 (10) (1999) 1619-1625. https://doi.org/10.1016/S0008-8846(99)00143-X.

[79] D. Huang, P. Chen, H. Peng, Y. Yang, Q. Yuan, M. Su, A review and comparison study on drying shrinkage prediction between alkali-activated fly ash/slag and ordinary portland cement, Constr. Build. Mater. 305 (2021) 124760. https://doi.org/10.1016/j.conbuildmat.2021.124760.

[80] H. Ye, A. Radlińska, A review and comparative study of existing shrinkage prediction models for portland and non-portland cementitious materials, Adv. Mater. Sci. Eng. 2016 (2016) https://doi.org/10.1155/2016/2418219.

[81] Y. Ohama, S. Kan, Effects of specimen size on strength and drying shrinkage of polymer-modified concrete, Int. J. Cem. Compos. Lightweight Concr. 4 (4) (1982) 229-233. https://doi.org/10.1016/0262-5075(82)90026-4.

[82] M. Ba, C. Qian, H. Wang, Effects of specimen shape and size on water loss and drying shrinkage of cement-based materials, Journal of Wuhan University of Technology-Mater. Sci. Ed. 28 (4) (2013) 733-740. http://doi.org/10.1007/s11595-013-0761-y.

[83] Z. Li, J. Yoon, R. Zhang, F. Rajabipour, W.V. Srubar Iii, I. Dabo, A. Radlińska, Machine learning in concrete science: Applications, challenges, and best practices, npj Comput. Mater. 8 (1) (2022) 127. https://doi.org/10.1038/s41524-022-00810-x.

[84] K. van Breugel, Numerical simulation of hydration and microstructural development in hardening cement-based materials (i) theory, Cem. Concr. Res. 25 (2) (1995) 319-331. https://doi.org/10.1016/0008-8846(95)00017-8.

[85] B.H. Cho, W. Chung, B.H. Nam, Molecular dynamics simulation of calcium-silicate-hydrate for nano-engineered cement composites—a review, Nanomaterials 10 (11) (2020) 2158. https://www.mdpi.com/2079-4991/10/11/2158.

[86] Y.K. Kong, K. Kurumisawa, Application of machine learning in predicting workability for alkali-activated materials, Case Stud. Constr. Mater. 18 (2023) e02173. https://doi.org/10.1016/j.cscm.2023.e02173.

[87] S.H. Chu, K. Kurumisawa, Y.K. Kong, Physically explicable mathematical model for strength prediction of uhpfrc, Eng. Struct. 275 (2023) 115191. https://doi.org/10.1016/j.engstruct.2022.115191.

[88] A. Shehadeh, O. Alshboul, R.E. Al Mamlook, O. Hamedat, Machine learning models for predicting the residual value of heavy construction equipment: An evaluation of modified decision tree, lightgbm, and xgboost regression, Autom. Constr. 129 (2021) 103827. https://doi.org/10.1016/j.autcon.2021.103827.

[89] M.A. DeRousseau, J.R. Kasprzyk, W.V. Srubar, Computational design optimization of concrete mixtures: A review, Cem. Concr. Res. 109 (2018) 42-53. https://doi.org/10.1016/j.cemconres.2018.04.007.

[90] A. Abdulalim Alabdullah, M. Iqbal, M. Zahid, K. Khan, M. Nasir Amin, F.E. Jalal, Prediction of rapid chloride penetration resistance of metakaolin based high strength concrete using light gbm and xgboost models by incorporating shap analysis, Constr. Build. Mater. 345 (2022) 128296. https://doi.org/10.1016/j.conbuildmat.2022.128296.

[91] B. Hilloulin, V.Q. Tran, Using machine learning techniques for predicting autogenous shrinkage of concrete incorporating superabsorbent polymers and supplementary cementitious materials, J. Build. Eng. 49 (2022) 104086. https://doi.org/10.1016/j.jobe.2022.104086.

[92] K.T. Nguyen, Q.D. Nguyen, T.A. Le, J. Shin, K. Lee, Analyzing the compressive strength of green fly ash based geopolymer concrete using experiment and machine learning approaches, Constr. Build. Mater. 247 (2020) 118581. https://doi.org/10.1016/j.conbuildmat.2020.118581.

[93] S. Riahi, A. Nazari, Predicting the effects of nanoparticles on early age compressive strength of ash-based geopolymers by artificial neural networks, Neural. Comput. Appl. 31 (2012) https://doi.org/10.1007/s00521-012-1085-0.

[94] A. Nazari, F.P. Torgal, Predicting compressive strength of different geopolymers by artificial neural networks, Ceram. Intl. 39 (2013) 2247–2257. https://doi.org/10.1016/j.ceramint.2012.08.070.

[95] J.A. Anderson, Cognitive and psychological computation with neural models, IEEE Trans. Syst. Man Cybern. SMC-13 (5) (1983) 799-815. https://doi.org/10.1109/TSMC.1983.6313074.

[96] R. Ince, Prediction of fracture parameters of concrete by artificial neural networks, Eng. Fract. Mech. 71 (15) (2004) 2143-2159. https://doi.org/10.1016/j.engfracmech.2003.12.004.

[97] M. Mohabbi Yadollahi, A. Benli, R. Demirboga, Prediction of compressive strength of geopolymer composites using an artificial neural network, Mater. Res. Innov. 19 (2015) 1433075X15Y.000. http://doi.org/10.1179/1433075X15Y.0000000020.

[98] H.M. Mushgil, H.A. Alani, L.E. George, Comparison between resilient and standard back propagation algorithms efficiency in pattern recognition, Int. J. Sci. Eng. Res. 6 (3) (2015) 29-34. http://doi.org/10.1109/CIMSim.2013.14.

[99] F. Demir, Prediction of elastic modulus of normal and high strength concrete by artificial neural networks, Constr. Build. Mater. 22 (7) (2008) 1428-1435. https://doi.org/10.1016/j.conbuildmat.2007.04.004.

[100] D. Huntzinger, T. Eatmon, A life-cycle assessment of portland cement manufacturing: Comparing the traditional process with alternative technologies, J. Clean. Prod. 17 (2009) 668-675. https://doi.org/10.1016/j.jclepro.2008.04.007.

[101] K. Gäbel, P. Forsberg, A.-M. Tillman, The design and building of a life cycle-based process model for simulating environmental performance, product performance and cost in cement manufacturing, J. Clean. Prod. 12 (1) (2004) 77-93. https://doi.org/10.1016/S0959-6526(02)00196-8.

[102] C. Chen, G. Habert, Y. Bouzidi, A. Jullien, A. Ventura, Lca allocation procedure used as an incitative method for waste recycling: An application to mineral additions in concrete, Resour. Conserv. Recycl. 54 (2010) 1231-1240. https://doi.org/10.1016/j.resconrec.2010.04.001.

[103] S. Ross, D. Evans, M. Webber, How lca studies deal with uncertainty, Int. J. Life Cycle Asses. 7 (1) (2002) 47. https://doi.org/10.1007/BF02978909.

[104] P.S. Matheu, K. Ellis, B. Varela, Comparing the environmental impacts of alkali activated mortar and traditional portland cement mortar using life cycle assessment, IOP Conference Series: Materials Science and Engineering 96 (2015) 012080. 10.1088/1757-899x/96/1/012080.

[105] E. Batuecas, I. Ramón-Álvarez, S. Sánchez-Delgado, M. Torres-Carrasco, Carbon footprint and water use of alkali-activated and hybrid cement mortars, J. Clean. Prod. 319 (2021) 128653. https://doi.org/10.1016/j.jclepro.2021.128653.

[106] Y. Patrisia, D.W. Law, C. Gunasekara, A. Wardhono, Life cycle assessment of alkali-activated concretes under marine exposure in an australian context, Environ. Impact Assess. Rev. 96 (2022) 106813. https://doi.org/10.1016/j.eiar.2022.106813.

[107] Y.K. Kong, S.H. Chu, Modeling the drying shrinkage of cement paste prepared with wastewater, J. Mater. Civ. Eng. 34 (6) (2022) 04022104. http://doi.org/10.1061/(ASCE)MT.1943-5533.0004249.

[108] S. Oyebisi, A. Ede, F. Olutoge, D. Olukanni, Assessment of activity moduli and acidic resistance of slag-based geopolymer concrete incorporating pozzolan, Case Stud. Constr. Mater. 13 (2020) e00394. https://doi.org/10.1016/j.cscm.2020.e00394.

[109] A. Dehghani, F. Aslani, N. Ghaebi Panah, Effects of initial SiO_2/Al_2O_3 molar ratio and slag on fly ash-based ambient cured geopolymer properties, Constr. Build. Mater. 293 (2021) 123527. https://doi.org/10.1016/j.conbuildmat.2021.123527.

[110] D.A.H. Hanaor, M. Ghadiri, W. Chrzanowski, Y. Gan, Scalable surface area characterization by electrokinetic analysis of complex anion adsorption, Langmuir 30 (50) (2014) 15143-15152. https://doi.org/10.1021/la503581e.

[111] B. Nematollahi, J. Sanjayan, Effect of different superplasticizers and activator combinations on workability and strength of fly ash based geopolymer, Mater. Des. 57 (2014) 667-672. https://doi.org/10.1016/j.matdes.2014.01.064.

[112] Z. Deng, Z. Yang, J. Bian, J. Lin, Z. Long, G. Hong, Z. Yang, Y. Ye, Advantages and disadvantages of pva-fibre-reinforced slag- and fly ash-blended geopolymer composites: Engineering properties and microstructure, Constr. Build. Mater. 349 (2022) 128690. https://doi.org/10.1016/j.conbuildmat.2022.128690.

[113] S. Hicks, Design shear resistance of headed studs embedded in solid slabs and encasements, J. Constr. Steel Res. 139 (2017) 339-352. 10.1016/j.jcsr.2017.09.018.

[114] ASTM International, West Conshohocken, PA, ASTM C596-09, Standard test method for drying shrinkage of mortar containing hydraulic cement, 2017.

[115] ISO, Environmental management. Life cycle assessmentdprinciples and framework, Geneva, 2006.

[116] C. Valderrama, R. Granados, J.L. Cortina, C.M. Gasol, M. Guillem, A. Josa, Implementation of best available techniques in cement manufacturing: A life-cycle assessment study, J. Clean. Prod. 25 (2012) 60-67. https://doi.org/10.1016/j.jclepro.2011.11.055.

[117] M. Hauschild, H. Wenzel, Environmental assessment of products, vol. 2: Scientific background, 1998, Chapman & Hall, London). 1998.
[118] J.B. Guinée, E. Lindeijer, Handbook on life cycle assessment: Operational guide to the iso standards, Springer Science & Business Media 2002.
[119] M.J. Goedkoop, The eco-indicator 99 a damage oriented method for life cycle impact assessment methodology report, Pre Concultants (1999).
[120] C. Lamnatou, F. Motte, G. Notton, D. Chemisana, C. Cristofari, Building-integrated solar thermal system with/without phase change material: Life cycle assessment based on recipe, usetox and ecological footprint, J. Clean. Prod. 193 (2018) 672-683. https://doi.org/10.1016/j.jclepro.2018.05.032.
[121] P. Van den Heede, N. De Belie, Environmental impact and life cycle assessment (lca) of traditional and 'green' concretes: Literature review and theoretical calculations, Cem. Concr. Compos. 34 (4) (2012) 431-442. https://doi.org/10.1016/j.cemconcomp.2012.01.004.
[122] S. Ruan, C. Unluer, Comparative life cycle assessment of reactive MgO and Portland cement production, J. Clean. Prod. 137 (2016) 258-273. https://doi.org/10.1016/j.jclepro.2016.07.071.
[123] K.-H. Yang, J.-K. Song, Workability loss and compressive strength development of cementless mortars activated by combination of sodium silicate and sodium hydroxide, J. Mater. Civ. Eng. 21 (3) (2009) 119-127. https://doi.org/10.1061/(ASCE)0899-1561(2009)21:3(119).
[124] K.-H. Yang, J.-K. Song, K.-S. Lee, A.F. Ashour, Flow and compressive strength of alkali-activated mortars, (2009) http://hdl.handle.net/10454/7741.
[125] P. Nath, P.K. Sarker, Effect of ggbfs on setting, workability and early strength properties of fly ash geopolymer concrete cured in ambient condition, Constr. Build. Mater. 66 (2014) 163-171. https://doi.org/10.1016/j.conbuildmat.2014.05.080.
[126] X. Gao, Q.L. Yu, H.J.H. Brouwers, Characterization of alkali activated slag–fly ash blends containing nano-silica, Constr. Build. Mater. 98 (2015) 397-406. https://doi.org/10.1016/j.conbuildmat.2015.08.086.
[127] G. Fang, W.K. Ho, W. Tu, M. Zhang, Workability and mechanical properties of alkali-activated fly ash-slag concrete cured at ambient temperature, Constr. Build. Mater. 172 (2018) 476-487. https://doi.org/10.1016/j.conbuildmat.2018.04.008.
[128] M. Najimi, N. Ghafoori, M. Sharbaf, Alkali-activated natural pozzolan/slag mortars: A parametric study, Constr. Build. Mater. 164 (2018) 625-643. https://doi.org/10.1016/j.conbuildmat.2017.12.222.
[129] A.A. Ramezanianpour, M.A. Moeini, Mechanical and durability properties of alkali activated slag coating mortars containing nanosilica and silica fume, Constr. Build. Mater. 163 (2018) 611-621. https://doi.org/10.1016/j.conbuildmat.2017.12.062.
[130] S. Yousefi Oderji, B. Chen, M.R. Ahmad, S.F.A. Shah, Fresh and hardened properties of one-part fly ash-based geopolymer binders cured at room

temperature: Effect of slag and alkali activators, J. Clean. Prod. 225 (2019) 1-10. https://doi.org/10.1016/j.jclepro.2019.03.290.

[131] Y. Alrefaei, Y.-S. Wang, J.-G. Dai, The effectiveness of different superplasticizers in ambient cured one-part alkali activated pastes, Cem. Concr. Compos. 97 (2019) 166-174. https://doi.org/10.1016/j.cemconcomp.2018.12.027.

[132] W. Song, Z. Zhu, S. Pu, Y. Wan, X. Xu, S. Song, J. Zhang, K. Yao, L. Hu, Multi-technical characterization and correlations between properties of standard cured alkali-activated high-calcium fa binders with ggbs as additive, Constr. Build. Mater. 241 (2020) 117996. https://doi.org/10.1016/j.conbuildmat.2020.117996.

[133] S.F.A. Shah, B. Chen, S.Y. Oderji, M. Aminul Haque, M.R. Ahmad, Comparative study on the effect of fiber type and content on the performance of one-part alkali-activated mortar, Constr. Build. Mater. 243 (2020) 118221. https://doi.org/10.1016/j.conbuildmat.2020.118221.

[134] S.F.A. Shah, B. Chen, S.Y. Oderji, M.A. Haque, M.R. Ahmad, Improvement of early strength of fly ash-slag based one-part alkali activated mortar, Constr. Build. Mater. 246 (2020) 118533. https://doi.org/10.1016/j.conbuildmat.2020.118533.

[135] E. Paul, Influence of superplasticizer on workability and strength of ambient cured alkali activated mortar, Clean. Mater. 6 (2022) 100152. https://doi.org/10.1016/j.clema.2022.100152.

[136] M.H. Dheyaaldin, M.A. Mosaberpanah, R. Alzeebaree, Performance of fiber-reinforced alkali-activated mortar with/without nano silica and nano alumina, Sustainability 14 (5) (2022) 2527. https://www.mdpi.com/2071-1050/14/5/2527.

[137] B.H. Tekle, K. Holschemacher, Alkali activated cement mixture at ambient curing: Strength, workability, and setting time, Struct. Concr. 23 (4) (2022) 2496-2509. https://doi.org/10.1002/suco.202100274.

[138] Y.K. Kong, K. Kurumisawa, S.H. Chu, Infilled cementitious composites (icc) – a comparative life cycle assessment with uhpc, J. Clean. Prod. (2022) 134051. https://doi.org/10.1016/j.jclepro.2022.134051.

[139] A.K.H. Kwan, W.W.S. Fung, Packing density measurement and modelling of fine aggregate and mortar, Cem. Concr. Compos. 31 (6) (2009) 349-357. https://doi.org/10.1016/j.cemconcomp.2009.03.006.

[140] M. Hunger, H.J.H. Brouwers, Flow analysis of water–powder mixtures: Application to specific surface area and shape factor, Cem. Concr. Compos. 31 (1) (2009) 39-59. https://doi.org/10.1016/j.cemconcomp.2008.09.010.

[141] Y. Qing, Z. Zenan, K. Deyu, C. Rongshen, Influence of nano-SiO_2 addition on properties of hardened cement paste as compared with silica fume, Constr. Build. Mater. 21 (3) (2007) 539-545. https://doi.org/10.1016/j.conbuildmat.2005.09.001.

[142] R. Jia, Q. Wang, T. Luo, Understanding the workability of alkali-activated phosphorus slag pastes: Effects of alkali dose and silicate modulus on early-age hydration reactions, Cem. Concr. Compos. 133 (2022) 104649. https://doi.org/10.1016/j.cemconcomp.2022.104649.

[143] K. Somna, C. Jaturapitakkul, P. Kajitvichyanukul, P. Chindaprasirt, Naoh-activated ground fly ash geopolymer cured at ambient temperature, Fuel 90 (6) (2011) 2118-2124. https://doi.org/10.1016/j.fuel.2011.01.018.

[144] A.A. Adewumi, M.A.M. Ariffin, M.O. Yusuf, M. Maslehuddin, M. Ismail, Effect of sodium hydroxide concentration on strength and microstructure of alkali-activated natural pozzolan and limestone powder mortar, Constr. Build. Mater. 271 (2021) 121530. https://doi.org/10.1016/j.conbuildmat.2020.121530.

[145] F.N. Okoye, J. Durgaprasad, N.B. Singh, Effect of silica fume on the mechanical properties of fly ash based-geopolymer concrete, Ceram. Intl. 42 (2, Part B) (2016) 3000-3006. https://doi.org/10.1016/j.ceramint.2015.10.084.

[146] M.N.S. Hadi, N.A. Farhan, M.N. Sheikh, Design of geopolymer concrete with ggbfs at ambient curing condition using taguchi method, Constr. Build. Mater. 140 (2017) 424-431. https://doi.org/10.1016/j.conbuildmat.2017.02.131.

[147] X. Guo, X. Pan, Mechanical properties and mechanisms of fiber reinforced fly ash–steel slag based geopolymer mortar, Constr. Build. Mater. 179 (2018) 633-641. https://doi.org/10.1016/j.conbuildmat.2018.05.198.

[148] Y. Hu, Z. Tang, W. Li, Y. Li, V.W.Y. Tam, Physical-mechanical properties of fly ash/ggbfs geopolymer composites with recycled aggregates, Constr. Build. Mater. 226 (2019) 139-151. https://doi.org/10.1016/j.conbuildmat.2019.07.211.

[149] A. Sedaghatdoost, K. Behfarnia, M. Bayati, M.s. Vaezi, Influence of recycled concrete aggregates on alkali-activated slag mortar exposed to elevated temperatures, J. Build. Eng. 26 (2019) 100871. https://doi.org/10.1016/j.jobe.2019.100871.

[150] A.B. Moradikhou, A. Esparham, M. Jamshidi Avanaki, Physical & mechanical properties of fiber reinforced metakaolin-based geopolymer concrete, Constr. Build. Mater. 251 (2020) 118965. https://doi.org/10.1016/j.conbuildmat.2020.118965.

[151] K. Mermerdaş, Z. Algın, Ş. Ekmen, Experimental assessment and optimization of mix parameters of fly ash-based lightweight geopolymer mortar with respect to shrinkage and strength, J. Build. Eng. 31 (2020) 101351. https://doi.org/10.1016/j.jobe.2020.101351.

[152] M. Shariati, A. Shariati, N.T. Trung, P. Shoaei, F. Ameri, N. Bahrami, S.N. Zamanabadi, Alkali-activated slag (aas) paste: Correlation between durability and microstructural characteristics, Constr. Build. Mater. 267 (2021) 120886. https://doi.org/10.1016/j.conbuildmat.2020.120886.

[153] A.A. Shahmansouri, M. Nematzadeh, A. Behnood, Mechanical properties of ggbfs-based geopolymer concrete incorporating natural zeolite and silica fume with an optimum design using response surface method, J. Build. Eng. 36 (2021) 102138. https://doi.org/10.1016/j.jobe.2020.102138.

[154] Y. Xu, G. Xing, J. Zhao, Y. Zhang, The effect of polypropylene fiber with different length and dosage on the performance of alkali-activated slag mortar, Constr. Build. Mater. 307 (2021) 124978. https://doi.org/10.1016/j.conbuildmat.2021.124978.

[155] Y. Wang, Y. Wang, M. Zhang, Effect of sand content on engineering properties of fly ash-slag based strain hardening geopolymer composites, J. Build. Eng. 34 (2021) 101951. https://doi.org/10.1016/j.jobe.2020.101951.
[156] G. Sadeghian, K. Behfarnia, M. Teymouri, Drying shrinkage of one-part alkali-activated slag concrete, J. Build. Eng. 51 (2022) 104263. https://doi.org/10.1016/j.jobe.2022.104263.
[157] Z. Ou, R. Feng, F. Li, G. Liu, N. Li, Development of drying shrinkage model for alkali-activated slag concrete, Constr. Build. Mater. 323 (2022) 126556. https://doi.org/10.1016/j.conbuildmat.2022.126556.
[158] C. Duran Atiş, C. Bilim, Ö. Çelik, O. Karahan, Influence of activator on the strength and drying shrinkage of alkali-activated slag mortar, Constr. Build. Mater. 23 (1) (2009) 548-555. https://doi.org/10.1016/j.conbuildmat.2007.10.011.
[159] M. Chi, R. Huang, Effects of dosage and modulus ratio of alkali-activated solution on the properties of slag mortars, Adv. Sci. Lett. 16 (2012) 7-12. https://doi.org/10.1166/asl.2012.3313.
[160] S. Aydın, A ternary optimisation of mineral additives of alkali activated cement mortars, Constr. Build. Mater. 43 (2013) 131-138. https://doi.org/10.1016/j.conbuildmat.2013.02.005.
[161] S. Aydın, B. Baradan, Effect of activator type and content on properties of alkali-activated slag mortars, Compos. Part B Eng. 57 (2014) 166-172. https://doi.org/10.1016/j.compositesb.2013.10.001.
[162] M. Chi, Effects of modulus ratio and dosage of alkali-activated solution on the properties and micro-structural characteristics of alkali-activated fly ash mortars, Constr. Build. Mater. 99 (2015) 128-136. http://doi.org/10.1016/j.conbuildmat.2015.09.029.
[163] F. Matalkah, R. Aqel, A. Ababneh, Enhancement of the mechanical properties of kaolin geopolymer using sodium hydroxide and calcium oxide, Procedia Manuf. 44 (2020) 164-171. https://doi.org/10.1016/j.promfg.2020.02.218.
[164] P.S. Deb, P. Nath, P.K. Sarker, Drying shrinkage of slag blended fly ash geopolymer concrete cured at room temperature, Procedia Eng. 125 (2015) 594-600. https://doi.org/10.1016/j.proeng.2015.11.066.
[165] Y.-F. Cao, Z. Tao, Z. Pan, R. Wuhrer, Effect of calcium aluminate cement on geopolymer concrete cured at ambient temperature, Constr. Build. Mater. 191 (2018) 242-252. https://doi.org/10.1016/j.conbuildmat.2018.09.204.
[166] F. Hamidi, F. Aslani, A. Valizadeh, Compressive and tensile strength fracture models for heavyweight geopolymer concrete, Eng. Fract. Mech. 231 (2020) 107023. https://doi.org/10.1016/j.engfracmech.2020.107023.
[167] C. Ridtirud, P. Chindaprasirt, K. Pimraksa, Factors affecting the shrinkage of fly ash geopolymers, Int. J. Miner. Metall. Mater. 18 (1) (2011) 100-104. http://doi.org/10.1007/s12613-011-0407-z.
[168] S. Aydın, B. Baradan, The effect of fiber properties on high performance alkali-activated slag/silica fume mortars, Compos. Part B Eng. 45 (1) (2013) 63-69. https://doi.org/10.1016/j.compositesb.2012.09.080.

[169] N. Marjanović, M. Komljenović, Z. Baščarević, V. Nikolić, R. Petrović, Physical–mechanical and microstructural properties of alkali-activated fly ash–blast furnace slag blends, Ceram. Intl. 41 (1, Part B) (2015) 1421-1435. https://doi.org/10.1016/j.ceramint.2014.09.075.

[170] M. Chi, Y. Liu, R. Huang, Mechanical and microstructural characterization of alkali-activated materials based on fly ash and slag, Int. J. Eng. Technol. 7 (2015) 59-64. http://doi.org/10.7763/IJET.2015.V7.767.

[171] R. Thomas, D. Lezama, S. Peethamparan, On drying shrinkage in alkali-activated concrete: Improving dimensional stability by aging or heat-curing, Cem. Concr. Res. 91 (2016) http://doi.org/10.1016/j.cemconres.2016.10.003.

[172] T. Yang, H. Zhu, Z. Zhang, Influence of fly ash on the pore structure and shrinkage characteristics of metakaolin-based geopolymer pastes and mortars, Constr. Build. Mater. 153 (2017) 284-293. https://doi.org/10.1016/j.conbuildmat.2017.05.067.

[173] M. Hojati, A. Radlińska, Shrinkage and strength development of alkali-activated fly ash-slag binary cements, Constr. Build. Mater. 150 (2017) 808-816. https://doi.org/10.1016/j.conbuildmat.2017.06.040.

[174] X. Gao, Q.L. Yu, R. Yu, H.J.H. Brouwers, Evaluation of hybrid steel fiber reinforcement in high performance geopolymer composites, Mater. Struct. 50 (2) (2017) 165. https://doi.org/10.1617/s11527-017-1030-x.

[175] W. Punurai, W. Kroehong, A. Saptamongkol, P. Chindaprasirt, Mechanical properties, microstructure and drying shrinkage of hybrid fly ash-basalt fiber geopolymer paste, Constr. Build. Mater. 186 (2018) 62-70. https://doi.org/10.1016/j.conbuildmat.2018.07.115.

[176] Z. Jiao, Y. Wang, W. Zheng, W. Huang, Effect of dosage of alkaline activator on the properties of alkali-activated slag pastes, Adv. Mater. Sci. Eng. 2018 (2018) https://doi.org/10.1155/2018/8407380.

[177] G. Wang, Y. Ma, Drying shrinkage of alkali-activated fly ash/slag blended system, J. Sustainable Cem.-Based Mater. 7 (4) (2018) 203-213. https://doi.org/10.1080/21650373.2018.1471424.

[178] H. Taghvayi, K. Behfarnia, M. Khalili, The effect of alkali concentration and sodium silicate modulus on the properties of alkali-activated slag concrete, J. Adv. Concr. Technol. 16 (7) (2018) 293-305. https://doi.org/10.3151/jact.16.293.

[179] J. Xiang, L. Liu, X. Cui, Y. He, G. Zheng, C. Shi, Effect of fuller-fine sand on rheological, drying shrinkage, and microstructural properties of metakaolin-based geopolymer grouting materials, Cem. Concr. Compos. 104 (2019) 103381. https://doi.org/10.1016/j.cemconcomp.2019.103381.

[180] M.M. Al-mashhadani, O. Canpolat, Y. Aygörmez, M. Uysal, S. Erdem, Mechanical and microstructural characterization of fiber reinforced fly ash based geopolymer composites, Constr. Build. Mater. 167 (2018) 505-513. https://doi.org/10.1016/j.conbuildmat.2018.02.061.

[181] N.K. Lee, S.Y. Abate, H.-K. Kim, Use of recycled aggregates as internal curing agent for alkali-activated slag system, Constr. Build. Mater. 159 (2018) 286-296. https://doi.org/10.1016/j.conbuildmat.2017.10.110.

[182] J. Xiang, L. Liu, X. Cui, Y. He, G. Zheng, C. Shi, Effect of limestone on rheological, shrinkage and mechanical properties of alkali – activated slag/fly ash grouting materials, Constr. Build. Mater. 191 (2018) 1285-1292. https://doi.org/10.1016/j.conbuildmat.2018.09.209.

[183] Z. Jiao, Y. Wang, W. Zheng, W. Huang, Pottery sand as fine aggregate for preparing alkali-activated slag mortar, Adv. Mater. Sci. Eng. 2018 (2018) 3037498. https://doi.org/10.1155/2018/3037498.

[184] X. Hu, C. Shi, Z. Zhang, Z. Hu, Autogenous and drying shrinkage of alkali-activated slag mortars, J. Am. Ceram. Soc. 102 (8) (2019) 4963-4975. https://doi.org/10.1111/jace.16349.

[185] A.M. Humad, A. Kothari, J.L. Provis, A. Cwirzen, The effect of blast furnace slag/fly ash ratio on setting, strength, and shrinkage of alkali-activated pastes and concretes, Front. Mater. 6 (2019) http://doi.org/10.3389/fmats.2019.00009.

[186] Y. Ling, K. Wang, C. Fu, Shrinkage behavior of fly ash based geopolymer pastes with and without shrinkage reducing admixture, Cem. Concr. Compos. 98 (2019) 74-82. https://doi.org/10.1016/j.cemconcomp.2019.02.007.

[187] J. Gong, Z. Qu, Mechanical properties and drying shrinkage investigation of alkali-activated mortar using waste glass powder, Adv. Civ. Eng. 2020 (2020) 8892474. https://doi.org/10.1155/2020/8892474.

[188] J. Xiang, Y. He, L. Liu, H. Zheng, X. Cui, Exothermic behavior and drying shrinkage of alkali-activated slag concrete by low temperature-preparation method, Constr. Build. Mater. 262 (2020) 120056. https://doi.org/10.1016/j.conbuildmat.2020.120056.

[189] R. Si, Q. Dai, S. Guo, J. Wang, Mechanical property, nanopore structure and drying shrinkage of metakaolin-based geopolymer with waste glass powder, J. Clean. Prod. 242 (2020) 118502. https://doi.org/10.1016/j.jclepro.2019.118502.

[190] Y. Xu, H. Chen, P. Wang, Effect of polypropylene fiber on properties of alkali-activated slag mortar, Adv. Civ. Eng. 2020 (2020) 4752841. http://doi.or/10.1155/2020/4752841.

[191] B. Behforouz, V.S. Balkanlou, F. Naseri, E. Kasehchi, E. Mohseni, T. Ozbakkaloglu, Investigation of eco-friendly fiber-reinforced geopolymer composites incorporating recycled coarse aggregates, Int. J. Environ. Sci. Technol. 17 (6) (2020) 3251-3260. http://doi.or/10.1007/s13762-020-02643-x.

[192] W. Chen, Y. Xie, B. Li, B. Li, J. Wang, N. Thom, Role of aggregate and fibre in strength and drying shrinkage of alkali-activated slag mortar, Constr. Build. Mater. 299 (2021) 124002. https://doi.org/10.1016/j.conbuildmat.2021.124002.

[193] B. Fu, Z. Cheng, J. Han, N. Li, Understanding the role of metakaolin towards mitigating the shrinkage behavior of alkali-activated slag, Mater. 14 (22) (2021) 6962. https://www.mdpi.com/1996-1944/14/22/6962.

[194] K. Sun, X. Peng, S.H. Chu, S. Wang, L. Zeng, G. Ji, Utilization of bof steel slag aggregate in metakaolin-based geopolymer, Constr. Build. Mater. 300 (2021) 124024. https://doi.org/10.1016/j.conbuildmat.2021.124024.

[195] P. Chindaprasirt, T. Chareerat, S. Hatanaka, T. Cao, High-strength geopolymer using fine high-calcium fly ash, J. Mater. Civ. Eng. 23 (3) (2011) 264-270. https://doi.org/10.1061/(ASCE)MT.1943-5533.0000161.
[196] N. Farzadnia, H. Noorvand, A.M. Yasin, F.N.A. Aziz, The effect of nano silica on short term drying shrinkage of pofa cement mortars, Constr. Build. Mater. 95 (2015) 636-646. https://doi.org/10.1016/j.conbuildmat.2015.07.132.
[197] S. Aydın, B. Baradan, Mechanical and microstructural properties of heat cured alkali-activated slag mortars, Mater. Des. 35 (2012) 374-383. https://doi.org/10.1016/j.matdes.2011.10.005.
[198] K. Mermerdaş, E. Güneyisi, M. Gesoğlu, T. Özturan, Experimental evaluation and modeling of drying shrinkage behavior of metakaolin and calcined kaolin blended concretes, Constr. Build. Mater. 43 (2013) 337-347. https://doi.org/10.1016/j.conbuildmat.2013.02.047.
[199] P. Shen, J.-X. Lu, L. Lu, Y. He, F. Wang, S. Hu, An alternative method for performance improvement of ultra-high performance concrete by internal curing: Role of physicochemical properties of saturated lightweight fine aggregate, Constr. Build. Mater. 312 (2021) 125373. https://doi.org/10.1016/j.conbuildmat.2021.125373.
[200] K. Kovler, S. Zhutovsky, Overview and future trends of shrinkage research, Mater. Struct. 39 (9) (2006) 827-847. https://doi.org/10.1617/s11527-006-9114-z.
[201] H. Ye, A. Radlińska, Shrinkage mitigation strategies in alkali-activated slag, Cem. Concr. Res. 101 (2017) 131-143. https://doi.org/10.1016/j.cemconres.2017.08.025.
[202] G. Jouan, A. Cuzol, V. Monbet, G. Monnier, Gaussian mixture models for clustering and calibration of ensemble weather forecasts, Discrete Contin. Dyn. Syst. - S 16 (2) (2023) 309-328. https://doi.org/10.3934/dcdss.2022037.
[203] G.J. McLachlan, S. Rathnayake, On the number of components in a gaussian mixture model, WIREs Data Min. Knowl. Discovery 4 (5) (2014) 341-355. https://doi.org/10.1002/widm.1135.
[204] Z. Zivkovic, Improved adaptive gaussian mixture model for background subtraction, Proceedings of the 17th International Conference on Pattern Recognition, 2004. ICPR 2004., IEEE, 2004, pp. 28-31.
[205] X. Liu, J. Yang, L. Wang, J. Wu, Bayesian information criterion based data-driven state of charge estimation for lithium-ion battery, J. Energy Storage 55 (2022) 105669. https://doi.org/10.1016/j.est.2022.105669.
[206] H. Huang, X. Gao, D. Jia, Effects of rheological performance, antifoaming admixture, and mixing procedure on air bubbles and strength of uhpc, J. Mater. Civ. Eng. 31 (4) (2019) 04019016. https://doi.org/10.1061/(ASCE)MT.1943-5533.0002651.
[207] K. Yildirim, M. Sümer, Effects of sodium chloride and magnesium sulfate concentration on the durability of cement mortar with and without fly ash, Compos. Part B Eng. 52 (2013) 56-61. https://doi.org/10.1016/j.compositesb.2013.03.040.

[208] D.J.M. Flower, J.G. Sanjayan, Green house gas emissions due to concrete manufacture, Int. J. Life Cycle Asses. 12 (5) (2007) 282. https://doi.org/10.1065/lca2007.05.327.

[209] T. Stengel, P. Schießl, 22 - life cycle assessment (lca) of ultra high performance concrete (uhpc) structures, in: F. Pacheco-Torgal, L.F. Cabeza, J. Labrincha, A. de Magalhães (Eds.), Eco-efficient construction and building materials, Woodhead Publishing2014, pp. 528-564.https://doi.org/10.1533/9780857097729.3.528.

[210] Ecoinvent, List of ecoinvent reports, 2012.

[211] M.E. Boesch, S. Hellweg, Identifying improvement potentials in cement production with life cycle assessment, Environ. Sci. Technol. 44 (23) (2010) 9143-9149. https://doi.org/10.1021/es100771k.

[212] L.C. Dreyer, A.L. Niemann, M.Z. Hauschild, Comparison of three different lcia methods: Edip97, cml2001 and eco-indicator 99, Int. J. Life Cycle Asses. 8 (4) (2003) 191-200. https://doi.org/10.1007/BF02978471.

[213] J.G. Carbonell, R.S. Michalski, T.M. Mitchell, 1 - an overview of machine learning, in: R.S. Michalski, J.G. Carbonell, T.M. Mitchell (Eds.), Machine learning, Morgan Kaufmann, San Francisco (CA), 1983, pp. 3-23.https://doi.org/10.1016/B978-0-08-051054-5.50005-4.

Appendix

Supplementary Table 1. Mix design key factors and flowability of AAM mixes

Year	Author	Mix ID	A.M.	SSA	GPC	L/B ratio	NaOH concentration/M	Ms	Fine agg.	Coarse agg.	Flow (%)
2009	Yang et al.	1	1.81	420	0.25	0.37	0.67	0.75	0.75	0.00	0.0
		2	1.81	420	0.25	0.50	3.92	0.75	0.75	0.00	0.0
		3	1.81	420	0.25	0.47	0.50	0.75	0.75	0.00	13.8
		4	1.81	420	0.25	0.60	2.94	0.75	0.75	0.00	11.0
		5	1.81	420	1.00	0.57	0.40	0.75	0.00	0.00	180.0
		6	1.81	420	0.40	0.57	0.40	0.75	0.60	0.00	161.0
		7	1.81	420	0.33	0.57	0.40	0.75	0.67	0.00	155.0

		8	1.81	420	0.29	0.57	0.40	0.75	0.71	0.00	135.0
		9	1.81	420	0.25	0.57	0.40	0.75	0.75	0.00	97.4
		10	1.81	420	0.22	0.57	0.40	0.75	0.78	0.00	30.5
		11	1.81	420	1.00	0.70	2.35	0.75	0.00	0.00	177.0
		12	1.81	420	0.40	0.70	2.35	0.75	0.60	0.00	163.0
		13	1.81	420	0.33	0.70	2.35	0.75	0.67	0.00	152.0
		14	1.81	420	0.29	0.70	2.35	0.75	0.71	0.00	142.5
		15	1.81	420	0.25	0.70	2.35	0.75	0.75	0.00	80.0
		16	1.81	420	0.22	0.70	2.35	0.75	0.78	0.00	24.5
		17	1.81	420	0.25	0.67	0.33	0.75	0.75	0.00	147.0
		18	1.81	420	0.25	0.80	1.96	0.75	0.75	0.00	133.0
		19	2.02	339	0.25	0.36	0.60	0.75	0.75	0.00	5.0
		20	2.02	339	0.25	0.46	1.50	0.75	0.75	0.00	0.0

		21	2.02	339	0.25	0.46	0.45	0.75	0.75	0.00	25.0
		22	2.02	339	0.25	0.56	1.13	0.75	0.75	0.00	17.0
		23	2.02	339	1.00	0.56	0.36	0.75	0.00	0.00	200.0
		24	2.02	339	0.40	0.56	0.36	0.75	0.60	0.00	177.0
		25	2.02	339	0.33	0.56	0.36	0.75	0.67	0.00	163.0
		26	2.02	339	0.29	0.56	0.36	0.75	0.71	0.00	145.5
		27	2.02	339	0.25	0.56	0.36	0.75	0.75	0.00	110.0
		28	2.02	339	0.22	0.56	0.36	0.75	0.78	0.00	35.5
		29	2.02	339	1.00	0.66	0.90	0.75	0.00	0.00	200.0
		30	2.02	339	0.40	0.66	0.90	0.75	0.60	0.00	175.0
		31	2.02	339	0.33	0.66	0.90	0.75	0.67	0.00	169.0
		32	2.02	339	0.29	0.66	0.90	0.75	0.71	0.00	146.0
		33	2.02	339	0.25	0.66	0.90	0.75	0.75	0.00	97.0

		34	2.02	339	0.22	0.66	0.90	0.75	0.78	0.00	45.0
		35	2.02	339	0.25	0.66	0.30	0.75	0.75	0.00	160.0
		36	2.02	339	0.25	0.76	0.75	0.75	0.75	0.00	150.0
		37	1.81	420	0.25	0.38	0.00	0.90	0.75	0.00	0.0
		38	1.81	420	0.25	0.48	0.00	0.90	0.75	0.00	0.0
		39	1.81	420	0.25	0.48	0.00	0.90	0.75	0.00	22.5
		40	1.81	420	0.25	0.58	0.00	0.90	0.75	0.00	20.0
		41	1.81	420	1.00	0.58	0.00	0.90	0.00	0.00	185.0
		42	1.81	420	0.40	0.58	0.00	0.90	0.60	0.00	163.0
		43	1.81	420	0.33	0.58	0.00	0.90	0.67	0.00	154.0
		44	1.81	420	0.29	0.58	0.00	0.90	0.71	0.00	137.0
		45	1.81	420	0.25	0.58	0.00	0.90	0.75	0.00	86.0
		46	1.81	420	0.22	0.58	0.00	0.90	0.78	0.00	31.0

		47	1.81	420	1.00	0.68	0.00	0.90	0.00	0.00	180.0
		48	1.81	420	0.40	0.68	0.00	0.90	0.60	0.00	162.0
		49	1.81	420	0.33	0.68	0.00	0.90	0.67	0.00	150.0
		50	1.81	420	0.29	0.68	0.00	0.90	0.71	0.00	132.0
		51	1.81	420	0.25	0.68	0.00	0.90	0.75	0.00	72.0
		52	1.81	420	0.22	0.68	0.00	0.90	0.78	0.00	30.0
		53	1.81	420	0.25	0.68	0.00	0.90	0.75	0.00	150.0
		54	1.81	420	0.25	0.78	0.00	0.90	0.75	0.00	147.5
2009	Yang et al.	2	2.02	663	0.36	0.47	1.00	0.55	0.64	0.00	87.5
		3	2.02	669	0.36	0.49	1.00	0.75	0.64	0.00	82.5
		4	2.02	674	0.36	0.50	1.00	0.85	0.64	0.00	89.0
		5	2.02	674	0.36	0.52	1.00	0.55	0.64	0.00	85.5
		6	2.02	687	0.36	0.56	1.00	0.75	0.64	0.00	82.5

		7	2.02	702	0.36	0.61	1.00	0.85	0.64	0.00	87.5
		8	1.81	717	0.37	0.45	1.00	0.55	0.63	0.00	81.0
		9	1.81	727	0.36	0.48	1.00	0.75	0.64	0.00	79.5
		10	1.87	887	0.36	0.48	1.00	0.75	0.64	0.00	57.5
		11	1.93	1053	0.36	0.48	1.00	0.75	0.64	0.00	47.5
		12	1.81	733	0.36	0.49	1.00	0.85	0.64	0.00	78.0
		13	1.81	732	0.37	0.51	1.00	0.55	0.63	0.00	75.5
		14	1.81	745	0.36	0.55	1.00	0.75	0.64	0.00	80.5
		15	1.87	903	0.36	0.55	1.00	0.75	0.64	0.00	54.0
		16	1.93	1067	0.36	0.55	1.00	0.75	0.64	0.00	44.0
		17	1.81	759	0.36	0.60	1.00	0.85	0.64	0.00	71.5
2011	Pacheco-Torgal et al.	10-0	1.17	2140	0.48	1.00	10.00	0.28	0.52	0.00	20.0
		12-0	1.17	2140	0.48	1.00	12.00	0.28	0.52	0.00	12.0

		14-0	1.17	2140	0.48	1.00	14.00	0.28	0.52	0.00	13.0
		16-0	1.17	2140	0.48	1.00	16.00	0.28	0.52	0.00	13.0
		10-1%	1.17	2140	0.48	1.03	10.00	0.28	0.52	0.00	24.0
		12-1%	1.17	2140	0.48	1.03	12.00	0.28	0.52	0.00	16.0
		14-1%	1.17	2140	0.48	1.03	14.00	0.28	0.52	0.00	12.0
		16-1%	1.17	2140	0.48	1.03	16.00	0.28	0.52	0.00	10.0
		10-2%	1.17	2140	0.49	1.06	10.00	0.28	0.51	0.00	30.0
		12-2%	1.17	2140	0.49	1.06	12.00	0.28	0.51	0.00	25.0
		14-2%	1.17	2140	0.49	1.06	14.00	0.28	0.51	0.00	11.0
		16-2%	1.17	2140	0.49	1.06	16.00	0.28	0.51	0.00	12.0
		10-3%	1.17	2140	0.49	1.09	10.00	0.28	0.51	0.00	40.0
		12-3%	1.17	2140	0.49	1.09	12.00	0.28	0.51	0.00	34.0
		14-3%	1.17	2140	0.49	1.09	14.00	0.28	0.51	0.00	28.0

		16-3%	1.17	2140	0.49	1.09	16.00	0.28	0.51	0.00	12.0
2014	Jang et al.	S50	2.44	388	1.00	0.50	4.00	0.71	0.00	0.00	27.9
		S50P1	2.44	388	1.00	0.51	4.00	0.71	0.00	0.00	40.0
		S50P2	2.44	388	1.00	0.51	4.00	0.71	0.00	0.00	54.4
		S50P3	2.44	388	1.00	0.52	4.00	0.71	0.00	0.00	68.3
		S50P4	2.44	388	1.00	0.53	4.00	0.71	0.00	0.00	75.3
		S50N1	2.44	388	1.00	0.51	4.00	0.71	0.00	0.00	32.1
		S50N2	2.44	388	1.00	0.51	4.00	0.71	0.00	0.00	47.4
		S50N3	2.44	388	1.00	0.52	4.00	0.71	0.00	0.00	54.4
		S50N4	2.44	388	1.00	0.53	4.00	0.71	0.00	0.00	67.0
		S0P4	1.39	290	1.00	0.53	4.00	0.71	0.00	0.00	106.0
		S30P4	2.02	349	1.00	0.53	4.00	0.71	0.00	0.00	85.1
		S70P4	2.85	427	1.00	0.53	4.00	0.71	0.00	0.00	50.0

		S100P4	3.48	485	1.00	0.53	4.00	0.71	0.00	0.00	27.9
		S0N4	1.39	290	1.00	0.53	4.00	0.71	0.00	0.00	107.0
		S30N4	2.02	349	1.00	0.53	4.00	0.71	0.00	0.00	83.7
		S70N4	2.85	427	1.00	0.53	4.00	0.71	0.00	0.00	40.0
		S100N4	3.48	485	1.00	0.53	4.00	0.71	0.00	0.00	25.1
2014	Nath & Sarker	1 mortar	1.77	420	0.46	0.40	14.00	1.07	0.54	0.00	110.0
		2 mortar	1.78	421	0.46	0.40	14.00	1.07	0.54	0.00	110.0
		3 mortar	1.79	421	0.46	0.40	14.00	1.07	0.54	0.00	100.0
		4 mortar	1.81	422	0.46	0.40	14.00	1.07	0.54	0.00	85.0
		5 mortar	1.78	421	0.45	0.35	14.00	1.07	0.55	0.00	73.0
		6 mortar	1.78	421	0.48	0.45	14.00	1.07	0.52	0.00	123.0
		7 mortar	1.78	421	0.46	0.40	14.00	0.76	0.54	0.00	120.0
		8 mortar	1.78	421	0.46	0.40	14.00	0.93	0.54	0.00	115.0

2014	Nematollahi & Sanjayan	1	1.81	420	1.00	0.30	8.00	0.00	0.00	0.00	61.6
		2	1.81	420	1.00	0.30	8.00	0.85	0.00	0.00	92.6
		3	1.81	420	1.00	0.31	8.00	0.00	0.00	0.00	119.0
		4	1.81	420	1.00	0.31	8.00	0.85	0.00	0.00	222.0
		5	1.81	420	1.00	0.31	8.00	0.85	0.00	0.00	119.0
		6	1.81	420	1.00	0.31	8.00	0.85	0.00	0.00	118.0
		7	1.81	420	1.00	0.31	8.00	0.85	0.00	0.00	96.9
		8	1.81	420	1.00	0.31	8.00	0.85	0.00	0.00	97.9
		9	1.81	420	1.00	0.31	8.00	0.85	0.00	0.00	90.5
2015	Gao et al.	S60F40L0P	1.95	423	1.00	0.35	5.11	1.40	0.00	0.00	191.0
		S50F50L0P	2.00	423	1.00	0.35	5.11	1.40	0.00	0.00	205.0
		S40F60L0P	2.05	422	1.00	0.35	5.11	1.40	0.00	0.00	213.0
		S60F30L10P	1.92	423	0.93	0.39	5.11	1.40	0.00	0.00	205.0

		S50F40L10P	1.97	423	0.93	0.39	5.11	1.40	0.00	0.00	213.0
		S40F50L10P	2.03	422	0.93	0.39	5.11	1.40	0.00	0.00	220.0
		S60F20L20P	1.88	424	0.85	0.44	5.11	1.40	0.00	0.00	213.0
		S50F30L20P	1.94	423	0.85	0.44	5.11	1.40	0.00	0.00	220.0
		S40F40L20P	2.00	423	0.85	0.44	5.11	1.40	0.00	0.00	227.0
		S60F10L30P	1.83	424	0.78	0.50	5.11	1.40	0.00	0.00	227.0
		S50F20L30P	1.90	424	0.78	0.50	5.11	1.40	0.00	0.00	235.0
		S40F30L30P	1.97	423	0.78	0.50	5.11	1.40	0.00	0.00	235.0
		S60F40L0M	1.95	423	0.81	0.45	5.11	1.40	0.19	0.00	130.0
		S50F50L0M	2.00	423	0.81	0.45	5.11	1.40	0.19	0.00	144.0
		S40F60L0M	2.05	422	0.81	0.45	5.11	1.40	0.19	0.00	152.0
		S60F30L10M	1.92	423	0.76	0.50	5.11	1.40	0.19	0.00	144.0
		S50F40L10M	1.97	423	0.76	0.50	5.11	1.40	0.19	0.00	152.0

		S40F50L10M	2.03	422	0.76	0.50	5.11	1.40	0.19	0.00	156.0
		S60F20L20M	1.88	424	0.70	0.56	5.11	1.40	0.19	0.00	156.0
		S50F30L20M	1.94	423	0.70	0.56	5.11	1.40	0.19	0.00	163.0
		S40F40L20M	2.00	423	0.70	0.56	5.11	1.40	0.19	0.00	167.0
		S60F10L30M	1.83	424	0.64	0.64	5.11	1.40	0.19	0.00	163.0
		S50F20L30M	1.90	424	0.64	0.64	5.11	1.40	0.19	0.00	167.0
		S40F30L30M	1.97	423	0.64	0.64	5.11	1.40	0.19	0.00	174.0
2015	Gao et al.	A730	1.90	424	1.00	0.48	4.89	1.40	0.00	0.00	205.0
		A370	2.09	422	1.00	0.48	4.89	1.40	0.00	0.00	220.0
		A731	4.60	1219	1.00	0.47	5.02	1.40	0.00	0.00	152.0
		A371	4.79	1217	1.00	0.47	5.02	1.40	0.00	0.00	169.0
		A732	7.35	2015	1.00	0.47	5.16	1.40	0.00	0.00	108.0
		A372	7.54	2013	1.00	0.47	5.16	1.40	0.00	0.00	124.0

		A733	10.15	2811	1.00	0.46	5.31	1.40	0.00	0.00	67.0
		A373	10.34	2809	1.00	0.46	5.31	1.40	0.00	0.00	88.0
2016	Jafari Nadoushan & Ramezanianpour	1	1.53	338	1.00	0.40	6.00	0.00	0.00	0.00	40.0
		2	1.53	338	1.00	0.40	6.00	0.15	0.00	0.00	65.0
		3	1.53	338	1.00	0.40	6.00	0.31	0.00	0.00	150.0
		4	1.53	338	1.00	0.40	6.00	0.48	0.00	0.00	160.0
		5	1.53	338	1.00	0.40	6.00	0.66	0.00	0.00	160.0
		6	1.53	338	1.00	0.40	6.00	0.00	0.00	0.00	40.0
		7	1.53	338	1.00	0.40	6.00	0.18	0.00	0.00	55.0
		8	1.53	338	1.00	0.40	6.00	0.38	0.00	0.00	65.0
		9	1.53	338	1.00	0.40	6.00	0.58	0.00	0.00	90.0
		10	1.53	338	1.00	0.40	6.00	0.79	0.00	0.00	140.0
		11	1.53	338	1.00	0.40	6.00	0.00	0.00	0.00	40.0

		12	1.53	338	1.00	0.40	6.00	0.18	0.00	0.00	50.0
		13	1.53	338	1.00	0.40	6.00	0.38	0.00	0.00	55.0
		14	1.53	338	1.00	0.40	6.00	0.59	0.00	0.00	58.0
		15	1.53	338	1.00	0.40	6.00	0.83	0.00	0.00	60.0
		16	1.53	338	1.00	0.40	8.00	0.00	0.00	0.00	5.0
		17	1.53	338	1.00	0.40	8.00	0.11	0.00	0.00	50.0
		18	1.53	338	1.00	0.40	8.00	0.24	0.00	0.00	143.0
		19	1.53	338	1.00	0.40	8.00	0.38	0.00	0.00	160.0
		20	1.53	338	1.00	0.40	8.00	0.54	0.00	0.00	160.0
		21	1.53	338	1.00	0.40	8.00	0.00	0.00	0.00	5.0
		22	1.53	338	1.00	0.40	8.00	0.14	0.00	0.00	48.0
		23	1.53	338	1.00	0.40	8.00	0.30	0.00	0.00	145.0
		24	1.53	338	1.00	0.40	8.00	0.46	0.00	0.00	150.0

		25	1.53	338	1.00	0.40	8.00	0.65	0.00	0.00	150.0
		26	1.53	338	1.00	0.40	8.00	0.00	0.00	0.00	5.0
		27	1.53	338	1.00	0.40	8.00	0.14	0.00	0.00	10.0
		28	1.53	338	1.00	0.40	8.00	0.29	0.00	0.00	120.0
		29	1.53	338	1.00	0.40	8.00	0.47	0.00	0.00	123.0
		30	1.53	338	1.00	0.40	8.00	0.67	0.00	0.00	125.0
		31	1.53	338	1.00	0.40	10.00	0.00	0.00	0.00	35.0
		32	1.53	338	1.00	0.40	10.00	0.09	0.00	0.00	40.0
		33	1.53	338	1.00	0.40	10.00	0.20	0.00	0.00	130.0
		34	1.53	338	1.00	0.40	10.00	0.32	0.00	0.00	130.0
		35	1.53	338	1.00	0.40	10.00	0.46	0.00	0.00	140.0
		36	1.53	338	1.00	0.40	10.00	0.00	0.00	0.00	35.0
		37	1.53	338	1.00	0.40	10.00	0.11	0.00	0.00	100.0

		38	1.53	338	1.00	0.40	10.00	0.24	0.00	0.00	105.0
		39	1.53	338	1.00	0.40	10.00	0.39	0.00	0.00	110.0
		40	1.53	338	1.00	0.40	10.00	0.55	0.00	0.00	115.0
		41	1.53	338	1.00	0.40	10.00	0.00	0.00	0.00	35.0
		42	1.53	338	1.00	0.40	10.00	0.11	0.00	0.00	35.0
		43	1.53	338	1.00	0.40	10.00	0.24	0.00	0.00	95.0
		44	1.53	338	1.00	0.40	10.00	0.39	0.00	0.00	100.0
		45	1.53	338	1.00	0.40	10.00	0.56	0.00	0.00	115.0
2016	Gao et al.	M1-820	1.22	424	0.45	0.71	5.11	1.00	0.49	0.00	64.0
		M2-824	1.22	424	0.44	0.69	5.11	1.40	0.49	0.00	136.0
		M3-828	1.22	424	0.44	0.68	5.11	1.80	0.49	0.00	165.0
		M4-640	0.92	423	0.45	0.71	5.11	1.00	0.49	0.00	81.0
		M5-644	0.92	423	0.44	0.69	5.11	1.40	0.49	0.00	146.0

		M6-648	0.92	423	0.44	0.68	5.11	1.80	0.49	0.00	179.0
		M7-460	0.61	422	0.45	0.71	5.11	1.00	0.49	0.00	87.0
		M8-464	0.61	422	0.44	0.69	5.11	1.40	0.49	0.00	165.0
		M9-468	0.61	422	0.44	0.68	5.11	1.80	0.49	0.00	200.0
2018	Nedeljković et al.	S0i	2.39	420	1.00	0.40	4.00	1.45	0.00	0.00	271.0
		S30i	2.19	422	1.00	0.40	4.00	1.45	0.00	0.00	202.0
		S50i	2.06	423	1.00	0.40	4.00	1.45	0.00	0.00	150.0
		S70i	1.92	424	1.00	0.40	4.00	1.45	0.00	0.00	12.2
		S100i	1.73	425	1.00	0.40	4.00	1.45	0.00	0.00	12.2
		S0ii	2.39	420	1.00	0.50	4.00	1.45	0.00	0.00	314.2
		S30ii	2.19	422	1.00	0.50	4.00	1.45	0.00	0.00	271.0
		S50ii	2.06	423	1.00	0.50	4.00	1.45	0.00	0.00	245.2
		S70ii	1.92	424	1.00	0.50	4.00	1.45	0.00	0.00	202.0

		S100ii	1.73	425	1.00	0.50	4.00	1.45	0.00	0.00	115.7
2018	Fang et al.	1	1.97	421	0.23	0.41	10.00	1.21	0.27	0.50	138.7
		2	1.95	421	0.23	0.41	10.00	1.21	0.27	0.50	135.7
		3	1.93	421	0.23	0.41	10.00	1.21	0.27	0.50	130.6
		4	1.91	421	0.23	0.41	10.00	1.21	0.27	0.50	124.8
		5	1.89	422	0.23	0.41	10.00	1.21	0.27	0.50	121.9
		6	1.95	421	0.23	0.41	12.00	1.10	0.27	0.50	119.0
		7	1.93	421	0.23	0.41	12.00	1.10	0.27	0.50	107.4
		8	1.91	421	0.23	0.41	12.00	1.10	0.27	0.50	101.6
		9	1.95	421	0.23	0.36	10.00	1.20	0.27	0.50	81.3
		10	1.93	421	0.22	0.36	10.00	1.20	0.27	0.50	72.6
		11	1.91	421	0.22	0.36	10.00	1.20	0.27	0.51	69.7
		12	1.95	421	0.24	0.41	10.00	1.03	0.27	0.50	139.4

		13	1.91	421	0.23	0.41	10.00	1.33	0.27	0.50	81.3
2018	Najimi et al.	2M-SL30-SS30-0.60	0.58	478	0.44	0.60	2.00	1.00	0.56	0.00	111.0
		2M-SL50-SS30-0.60	0.97	496	0.44	0.60	2.00	1.00	0.56	0.00	111.0
		2M-SL70-SS30-0.60	1.35	515	0.44	0.60	2.00	1.00	0.56	0.00	111.0
		1M-SL30-SS30-0.60	0.58	478	0.44	0.60	1.00	1.33	0.56	0.00	144.0
		1M-SL50-SS30-0.60	0.97	496	0.44	0.60	1.00	1.33	0.56	0.00	124.0
		1M-SL70-SS30-0.60	1.35	515	0.44	0.60	1.00	1.33	0.56	0.00	86.0

		0.5M-SL30-SS30-0.60	0.58	478	0.44	0.60	0.50	1.60	0.56	0.00	127.0
		0.5M-SL50-SS30-0.60	0.97	496	0.44	0.60	0.50	1.60	0.56	0.00	89.0
		0.5M-SL70-SS30-0.60	1.35	515	0.44	0.60	0.50	1.60	0.56	0.00	67.0
		1M-SL30-SS30-0.56	0.58	478	0.44	0.56	1.00	1.33	0.56	0.00	116.0
		1M-SL50-SS30-0.56	0.97	496	0.44	0.56	1.00	1.33	0.56	0.00	95.0
		1M-SL70-SS30-0.56	1.35	515	0.44	0.56	1.00	1.33	0.56	0.00	76.0

		1M-SL30-SS30-0.52	0.58	478	0.40	0.36	1.00	1.56	0.60	0.00	102.0
		1M-SL50-SS30-0.52	0.97	496	0.40	0.36	1.00	1.56	0.60	0.00	79.0
		1M-SL70-SS30-0.52	1.35	515	0.40	0.36	1.00	1.56	0.60	0.00	41.0
		1M-SL30-SS20-0.60	0.58	478	0.44	0.60	1.00	1.08	0.56	0.00	152.0
		1M-SL50-SS20-0.60	0.97	496	0.44	0.60	1.00	1.08	0.56	0.00	152.0
		1M-SL70-SS20-0.60	1.35	515	0.44	0.60	1.00	1.08	0.56	0.00	151.0

		1M-SL30-SS25-0.60	0.58	478	0.44	0.60	1.00	1.22	0.56	0.00	152.0
		1M-SL50-SS25-0.60	0.97	496	0.44	0.60	1.00	1.22	0.56	0.00	152.0
		1M-SL70-SS25-0.60	1.35	515	0.44	0.60	1.00	1.22	0.56	0.00	130.0
2018	Ramezanianpour & Moeini	Control NaOH-0.9	1.53	338	0.06	0.90	6.00	0.79	0.94	0.00	85.0
		NaOH-N0M5-0.9	1.45	1321	0.06	0.90	6.00	0.79	0.94	0.00	90.0
		NaOH-N0M7.5-0.9	1.41	1813	0.06	0.90	6.00	0.79	0.94	0.00	105.0

		NaOH-N0M10-0.9	1.37	2304	0.06	0.90	6.00	0.79	0.94	0.00	110.0
		Control NaOH-1	1.53	338	0.07	1.00	6.00	0.79	0.93	0.00	130.0
		NaOH-N0M5-1	1.45	1321	0.07	1.00	6.00	0.79	0.93	0.00	140.0
		NaOH-N0M7.5-1	1.41	1813	0.07	1.00	6.00	0.79	0.93	0.00	130.0
		NaOH-N0M10-1	1.37	2304	0.07	1.00	6.00	0.79	0.93	0.00	140.0
		NaOH-N2M0-0.9	6.88	1932	0.06	0.90	6.00	0.79	0.94	0.00	70.0

		NaOH-N4M0-0.9	12.22	3525	0.06	0.90	6.00	0.79	0.94	0.00	55.0
		NaOH-N2M0-1	6.88	1932	0.07	1.00	6.00	0.79	0.93	0.00	110.0
		NaOH-N4M0-1	12.22	3525	0.07	1.00	6.00	0.79	0.93	0.00	100.0
		NaOH-N2M5-0.9	6.80	2915	0.06	0.90	6.00	0.79	0.94	0.00	80.0
		NaOH-N2M7.5-0.9	6.66	3346	0.07	0.88	6.00	0.79	0.93	0.00	85.0
		NaOH-N2M10-0.9	6.62	3828	0.07	0.88	6.00	0.79	0.93	0.00	85.0

		NaOH-N2M5-1	6.70	2864	0.07	0.98	6.00	0.79	0.93	0.00	100.0
		NaOH-N2M7.5-1	6.66	3346	0.07	0.98	6.00	0.79	0.93	0.00	110.0
		NaOH-N2M10-1	6.62	3828	0.07	0.98	6.00	0.79	0.93	0.00	110.0
2018	Ibrahim et al.	M0	3.14	442	0.25	0.57	14.00	1.10	0.26	0.49	64.0
		M1	5.80	1238	0.25	0.57	14.00	1.10	0.26	0.49	70.0
		M2	9.80	2431	0.25	0.56	14.00	1.10	0.26	0.48	72.0
		M3	16.47	4420	0.26	0.55	14.00	1.10	0.26	0.48	58.0
		M4	23.13	6409	0.26	0.54	14.00	1.10	0.26	0.48	52.0
2019	Yousefi Oderji et al.	AA1	2.20	420	1.00	0.08	0.00	0.92	0.00	0.00	200.0
		AA2	2.15	421	1.00	0.08	0.00	0.92	0.00	0.00	150.0

		AA3	2.12	421	1.00	0.08	0.00	0.92	0.00	0.00	140.0
		AA4	2.10	421	1.00	0.08	0.00	0.92	0.00	0.00	122.0
2019	Alanazi et al.	FA-1	2.48	420	1.00	0.40	12.00	0.61	0.00	0.00	132.8
		FA-2.5	2.48	420	1.00	0.40	12.00	1.17	0.00	0.00	124.2
		FA-1S10	2.40	421	1.00	0.40	12.00	0.61	0.00	0.00	115.7
		FA-2.5S10	2.40	421	1.00	0.40	12.00	1.17	0.00	0.00	115.5
		FA-1S15	2.37	421	1.00	0.40	12.00	0.61	0.00	0.00	111.4
		FA-2.5S15	2.37	421	1.00	0.40	12.00	1.17	0.00	0.00	109.2
		FA-1SF5	69.85	1399	1.00	0.40	12.00	0.61	0.00	0.00	120.0
		FA-2.5SF5	69.85	1399	1.00	0.40	12.00	1.17	0.00	0.00	115.7
		FA-1SF10	137.22	2378	1.00	0.40	12.00	0.61	0.00	0.00	102.8
		FA-2.5SF10	137.22	2378	1.00	0.40	12.00	1.17	0.00	0.00	94.3
		FA-1MK5	2.43	506	1.00	0.40	12.00	0.61	0.00	0.00	107.1

		FA-2.5MK5	2.43	506	1.00	0.40	12.00	1.17	0.00	0.00	98.6
		FA-1MK10	2.37	592	1.00	0.40	12.00	0.61	0.00	0.00	98.6
		FA-2.5MK10	2.37	592	1.00	0.40	12.00	1.17	0.00	0.00	90.0
2019	Alrefaei et al.	M1-0.4-control	1.98	423	1.00	0.52	0.00	0.94	0.00	0.00	69.7
		M1-0.4-N	1.98	423	1.00	0.53	0.00	0.94	0.00	0.00	166.9
		M1-0.4-M	1.98	423	1.00	0.53	0.00	0.94	0.00	0.00	175.0
		M1-0.4-PC	1.98	423	1.00	0.53	0.00	0.94	0.00	0.00	179.5
		M1-0.38-N	1.98	423	1.00	0.51	0.00	0.94	0.00	0.00	153.9
		M1-0.38-M	1.98	423	1.00	0.51	0.00	0.94	0.00	0.00	142.9
		M1-0.38-PC	1.98	423	1.00	0.51	0.00	0.94	0.00	0.00	155.0
		M1-0.36-N	1.98	423	1.00	0.49	0.00	0.94	0.00	0.00	122.0
		M1-0.36-M	1.98	423	1.00	0.49	0.00	0.94	0.00	0.00	121.1

		M1-0.36-PC	1.98	423	1.00	0.49	0.00	0.94	0.00	0.00	129.7
		M1-0.34-N	1.98	423	1.00	0.47	0.00	0.94	0.00	0.00	105.4
		M1-0.34-M	1.98	423	1.00	0.47	0.00	0.94	0.00	0.00	83.0
		M1-0.34-PC	1.98	423	1.00	0.47	0.00	0.94	0.00	0.00	106.6
2020	Song et al.	Control	1.55	420	1.00	0.65	1.83	1.60	0.00	0.00	153.3
		10GGSS	1.65	421	1.00	0.65	1.83	1.60	0.00	0.00	150.0
		20GGSS	1.74	421	1.00	0.65	1.83	1.60	0.00	0.00	141.7
		30GGSS	1.84	422	1.00	0.65	1.83	1.60	0.00	0.00	106.7
		40GGSS	1.94	422	1.00	0.65	1.83	1.60	0.00	0.00	81.1
		50GGSS	2.03	423	1.00	0.65	1.83	1.60	0.00	0.00	59.6
2020	Shah et al.	Control	2.10	421	0.59	0.42	0.00	0.90	0.41	0.00	200.0
		Mix-S1	2.10	421	0.59	0.42	0.00	0.90	0.41	0.00	194.0
		Mix-S2	2.10	421	0.58	0.42	0.00	0.90	0.41	0.00	185.0

		Mix-S3	2.10	421	0.58	0.42	0.00	0.90	0.41	0.00	176.0
		Mix-S4	2.10	421	0.58	0.42	0.00	0.90	0.40	0.00	159.0
		Mix-B1	2.10	421	0.59	0.42	0.00	0.90	0.41	0.00	180.0
		Mix-B2	2.10	421	0.58	0.42	0.00	0.90	0.41	0.00	180.0
		Mix-B3	2.10	421	0.58	0.42	0.00	0.90	0.41	0.00	150.0
		Mix-B4	2.10	421	0.58	0.42	0.00	0.90	0.40	0.00	129.0
		Mix-P1	2.10	421	0.59	0.42	0.00	0.90	0.41	0.00	170.0
		Mix-P2	2.10	421	0.58	0.42	0.00	0.90	0.41	0.00	159.0
		Mix-P3	2.10	421	0.58	0.42	0.00	0.90	0.41	0.00	112.0
		Mix-P4	2.10	421	0.58	0.42	0.00	0.90	0.40	0.00	88.0
2020	Shah et al.	AM1	2.05	422	0.59	0.42	0.00	0.90	0.41	0.00	86.0
		AM2	2.05	422	0.59	0.43	0.00	0.90	0.41	0.00	128.0
		AM3	2.05	422	0.59	0.44	0.00	0.90	0.41	0.00	146.0

		AM4	2.00	422	0.59	0.42	0.00	0.90	0.41	0.00	56.0
		AM5	2.00	422	0.59	0.43	0.00	0.90	0.41	0.00	122.0
		AM6	2.00	422	0.59	0.44	0.00	0.90	0.41	0.00	152.0
		AM7	1.95	423	0.59	0.42	0.00	0.90	0.41	0.00	56.0
		AM8	1.95	423	0.59	0.43	0.00	0.90	0.41	0.00	107.0
		AM9	1.95	423	0.59	0.44	0.00	0.90	0.41	0.00	149.0
2021	Alrefaei et al.	0.4-1GP-12%	1.74	423	1.00	0.88	0.00	0.94	0.00	0.00	183.9
		0.4-2GP-12%	1.74	423	1.00	0.88	0.00	1.94	0.00	0.00	190.6
		0.4-H-12%	1.74	423	1.00	0.88	0.00	2.94	0.00	0.00	200.0
		0.4-H-9%	1.74	423	1.00	0.83	0.00	3.94	0.00	0.00	190.5
		0.3-1GP-12%	1.74	423	1.00	0.71	0.00	4.94	0.00	0.00	58.5
		0.3-2GP-12%	1.74	423	1.00	0.71	0.00	5.94	0.00	0.00	104.7
		0.3-H-12%	1.74	423	1.00	0.71	0.00	6.94	0.00	0.00	111.3

		0.3-H-9%	1.74	423	1.00	0.66	0.00	7.94	0.00	0.00	98.1
2022	Paul	M0	1.62	373	0.78	0.25	8.00	1.99	0.22	0.00	50.0
		M0.5S	1.62	373	0.78	0.25	8.00	1.99	0.22	0.00	53.0
		M1S	1.62	373	0.78	0.25	8.00	1.99	0.22	0.00	57.0
		M1.5S	1.62	373	0.78	0.25	8.00	1.99	0.22	0.00	59.0
		M2S	1.62	373	0.78	0.26	8.00	1.99	0.22	0.00	61.0
		M2.5S	1.62	373	0.78	0.26	8.00	1.99	0.22	0.00	64.0
		M3S	1.62	373	0.78	0.26	8.00	1.99	0.22	0.00	66.0
		M0.5N	1.62	373	0.78	0.25	8.00	1.99	0.22	0.00	58.0
		M1N	1.62	373	0.78	0.25	8.00	1.99	0.22	0.00	65.0
		M1.5N	1.62	373	0.78	0.25	8.00	1.99	0.22	0.00	73.0
		M2N	1.62	373	0.78	0.26	8.00	1.99	0.22	0.00	78.0
		M2.5N	1.62	373	0.78	0.26	8.00	1.99	0.22	0.00	79.0

		M3N	1.62	373	0.78	0.26	8.00	1.99	0.22	0.00	80.0
		M0.5P	1.62	373	0.78	0.25	8.00	1.99	0.22	0.00	64.0
		M1P	1.62	373	0.78	0.25	8.00	1.99	0.22	0.00	75.0
		M1.5P	1.62	373	0.78	0.25	8.00	1.99	0.22	0.00	87.0
		M2P	1.62	373	0.78	0.26	8.00	1.99	0.22	0.00	103.0
		M2.5P	1.62	373	0.78	0.26	8.00	1.99	0.22	0.00	104.0
		M3P	1.62	373	0.78	0.26	8.00	1.99	0.22	0.00	104.0
2022	Deng et al.	AAF	2.28	420	0.50	0.60	8.00	1.15	0.50	0.00	158.8
		AAFF3	2.28	420	0.50	0.60	8.00	1.15	0.50	0.00	98.3
		AAFF6	2.28	420	0.50	0.60	8.00	1.15	0.50	0.00	87.5
		AASF	2.09	422	0.50	0.60	8.00	1.15	0.50	0.00	154.6
		AASFF3	2.09	422	0.50	0.60	8.00	1.15	0.50	0.00	94.9
		AASFF6	2.09	422	0.50	0.60	8.00	1.15	0.50	0.00	83.6

2022	Dheyaaldin et al.	M1	2.34	774	0.52	0.55	12.00	0.86	0.48	0.00	75.0
		M2	2.34	774	0.51	0.55	12.00	0.86	0.47	0.00	70.0
		M3	2.48	389	0.51	0.57	12.00	0.86	0.47	0.00	77.0
		M4	17.35	5230	0.53	0.53	12.00	0.86	0.47	0.00	75.0
		M5	2.20	5230	0.52	0.53	12.00	0.86	0.47	0.00	70.0
		M6	18.06	5031	0.52	0.55	12.00	0.86	0.48	0.00	73.0
		M7	2.48	389	0.52	0.57	12.00	0.86	0.48	0.00	82.0
		M8	18.06	5031	0.51	0.55	12.00	0.86	0.47	0.00	70.0
		M9	2.34	2897	0.52	0.55	12.00	0.86	0.48	0.00	78.0
		M10	9.97	3040	0.52	0.54	12.00	0.86	0.47	0.00	75.0
		M11	10.19	2898	0.52	0.55	12.00	0.86	0.47	0.00	80.0
		M12	10.41	2749	0.52	0.56	12.00	0.86	0.48	0.00	70.0
		M13	2.41	586	0.52	0.56	12.00	0.86	0.48	0.00	65.0

		M14	9.97	5135	0.52	0.54	12.00	0.86	0.47	0.00	75.0
		M15	10.19	2897	0.52	0.55	12.00	0.86	0.47	0.00	65.0
2022	Tekle & Holschemacher	T1	1.83	454	0.49	0.45	7.14	1.86	0.51	0.00	70.0
		T2	1.85	452	0.49	0.45	7.14	1.86	0.51	0.00	80.0
		T3	21.19	2348	0.49	0.45	7.14	1.86	0.51	0.00	190.0
		T4	21.18	2349	0.49	0.45	7.14	1.86	0.51	0.00	160.0
		T5	21.20	2572	0.49	0.45	7.14	1.86	0.51	0.00	120.0
		T6	21.18	2574	0.49	0.45	7.14	1.86	0.51	0.00	120.0
		TM1	11.50	1402	0.36	0.47	7.14	1.44	0.64	0.00	75.0
		TM2	11.50	1402	0.39	0.58	7.14	1.68	0.61	0.00	155.0
		TM3	11.50	1402	0.44	0.70	7.14	1.87	0.56	0.00	200.0
		TM4	11.50	1402	0.49	0.59	7.14	1.68	0.51	0.00	190.0
		TM5	11.50	1402	0.45	0.52	7.14	1.86	0.55	0.00	140.0

		TM6	11.50	1402	0.50	0.63	7.14	1.45	0.50	0.00	185.0
		TM7	11.50	1402	0.55	0.53	7.14	1.86	0.45	0.00	180.0
		TM8	11.50	1402	0.62	0.64	7.14	1.45	0.38	0.00	220.0
		TM9	11.50	1402	0.55	0.57	7.14	1.68	0.45	0.00	160.0
		TM-S	11.50	1402	0.35	0.45	7.14	2.09	0.65	0.00	90.0
		TM-set	11.50	1402	0.55	0.57	7.14	1.45	0.45	0.00	150.0
		TM-F	11.50	1402	0.64	0.70	7.14	1.87	0.36	0.00	235.0
		TM 10	11.50	1402	0.55	0.57	7.14	1.87	0.45	0.00	165.0
		TM 11	11.50	1402	0.48	0.58	7.14	1.86	0.52	0.00	185.0
		TM 12	11.50	1402	0.53	0.70	7.14	1.45	0.47	0.00	210.0
		TM 13	11.50	1402	0.57	0.58	7.14	1.45	0.43	0.00	190.0
		TM 14	11.50	1402	0.64	0.70	7.14	1.68	0.36	0.00	230.0

Note: A.M. = Activity moduli; SSA = Specific surface area, GPC = Geopolymer paste content; L/B = Liquid-to-binder; Agg. = Aggregate.

Supplementary Table 2. Mix design key factors and strength of AAM mixes

Year	Author	Mix ID	A.M.	SSA	GPC	L/B ratio	NaOH concentration	Ms	Fine agg.	Coarse agg.	Compressive strength/MPa
2009	Duran Atiş et al.	1 concrete	1.55	425	0.35	0.50	0	0.75	0.65	0.00	26.6
		2 concrete	1.55	425	0.35	0.50	0	1.00	0.65	0.00	30.9
		3 concrete	1.55	425	0.35	0.50	0	1.25	0.65	0.00	32.2
		4 concrete	1.55	425	0.35	0.50	0	1.50	0.65	0.00	29.0
		5 concrete	1.55	425	0.35	0.50	0	1.75	0.65	0.00	60.8
		6 concrete	1.55	425	0.35	0.50	1	0.00	0.65	0.00	17.9
		7 concrete	1.55	425	0.35	0.50	2	0.00	0.65	0.00	21.9
2012	Chi and Huang	8 concrete	1.78	435	0.28	0.09	11	0.60	0.72	0.00	21.2
		1 mortar	1.78	435	0.28	0.10	9	0.70	0.72	0.00	21.8
		2 mortar	1.78	435	0.29	0.11	8	0.80	0.71	0.00	26.6

		3 mortar	1.78	435	0.29	0.11	6	0.90	0.71	0.00	23.9
		4 mortar	1.78	435	0.29	0.12	11	0.60	0.71	0.00	25.9
		5 mortar	1.78	435	0.29	0.13	9	0.70	0.71	0.00	24.2
		6 mortar	1.78	435	0.29	0.14	8	0.80	0.71	0.00	32.4
		7 mortar	1.78	435	0.29	0.15	6	0.90	0.71	0.00	26.6
		8 mortar	1.78	435	0.29	0.15	11	0.60	0.71	0.00	25.6
		GPF	1.78	435	0.30	0.16	9	0.70	0.70	0.00	25.6
		GP1	1.78	435	0.30	0.18	8	0.80	0.70	0.00	30.3
		GP2	1.78	435	0.30	0.19	6	0.90	0.70	0.00	26.9
2013	Aydın	GP3	1.33	410	0.31	0.24	4	1.20	0.69	0.00	53.0
		GP4	7.71	2369	0.31	0.24	4	1.20	0.69	0.00	55.3
		TM1	14.09	4328	0.31	0.24	4	1.20	0.69	0.00	44.9
		TM2	1.49	393	0.31	0.24	4	1.20	0.69	0.00	51.4

		TM3	1.66	375	0.31	0.24	4	1.20	0.69	0.00	48.1
		TM4	7.87	2352	0.31	0.24	4	1.20	0.69	0.00	44.5
		TM5	8.04	2334	0.31	0.24	4	1.20	0.69	0.00	38.1
		TM6	14.25	4311	0.31	0.24	4	1.20	0.69	0.00	42.8
		TM7	14.42	4293	0.31	0.24	4	1.20	0.69	0.00	41.9
2014	Aydın & Baradan	TM8	1.33	410	0.35	0.51	4	0.00	0.65	0.00	16.0
		TM9	1.33	410	0.36	0.55	5	0.00	0.64	0.00	18.5
		Control sample	1.33	410	0.37	0.58	7	0.00	0.63	0.00	19.0
		PP-1	1.33	410	0.44	1.20	15	0.40	0.56	0.00	41.0
		PP-2	1.33	410	0.42	1.00	11	0.40	0.58	0.00	46.8
		PP-3	1.33	410	0.40	0.81	6	0.40	0.60	0.00	36.2
		PP-4	1.33	410	0.41	0.90	8	0.80	0.59	0.00	44.8

		BF-1	1.33	410	0.40	0.82	6	0.80	0.60	0.00	58.8
		BF-2	1.33	410	0.39	0.74	3	0.80	0.61	0.00	52.7
		BF-3	1.33	410	0.40	0.80	5	1.20	0.60	0.00	43.9
		BF-4	1.33	410	0.39	0.73	2	1.20	0.61	0.00	55.6
		BF-5	1.33	410	0.38	0.70	1	1.20	0.62	0.00	61.3
		SF-1	1.33	410	0.39	0.75	4	1.60	0.61	0.00	39.2
		SF-2	1.33	410	0.38	0.71	2	1.60	0.62	0.00	53.3
		SF-3	1.33	410	0.38	0.69	1	1.60	0.62	0.00	55.6
2014	Nath&Sarker	SF-4	1.77	420	0.23	0.40	14	0.72	0.27	0.50	30.0
		SF-5	1.78	421	0.23	0.40	14	0.72	0.27	0.50	36.3
		0-0%-0.33-23	1.79	421	0.23	0.40	14	0.72	0.27	0.50	43.8

		0-0%-0.40-23	1.81	422	0.23	0.40	14	0.72	0.27	0.50	53.8
		0-0%-0.50-23	1.78	421	0.23	0.35	14	0.72	0.27	0.50	45.5
		0-0%-0.60-23	1.78	421	0.24	0.45	14	0.72	0.27	0.50	30.9
		S00	1.78	421	0.23	0.40	14	0.49	0.27	0.50	34.5
		S10	1.78	421	0.23	0.40	14	0.61	0.27	0.50	34.0
		S20	1.77	420	0.46	0.40	14	0.72	0.54	0.00	18.8
		S30	1.78	421	0.46	0.40	14	0.72	0.54	0.00	29.1
		S00R50	1.79	421	0.46	0.40	14	0.72	0.54	0.00	34.7
		S10R50	1.81	422	0.46	0.40	14	0.72	0.54	0.00	46.9
		S20R50	1.78	421	0.45	0.35	14	0.72	0.55	0.00	34.1

		S30R50	1.78	421	0.48	0.45	14	0.72	0.52	0.00	25.2
		S00R100	1.78	421	0.46	0.40	14	0.49	0.54	0.00	36.8
		S10R100	1.78	421	0.46	0.40	14	0.61	0.54	0.00	31.5
2015	Chi	S20R100	2.78	237	0.33	0.35	0	1.23	0.67	0.00	28.1
		S30R100	2.78	237	0.33	0.35	0	0.80	0.67	0.00	13.9
		RA0	2.78	237	0.33	0.35	0	1.23	0.67	0.00	26.1
		RA25	2.78	237	0.33	0.35	0	0.80	0.67	0.00	31.9
		RA50	2.78	237	0.35	0.50	0	1.23	0.65	0.00	24.6
		RA75	2.78	237	0.35	0.50	0	0.80	0.65	0.00	10.1
		RA100	2.78	237	0.35	0.50	0	1.23	0.65	0.00	49.4
		Control (MR1.5)	2.78	237	0.35	0.50	0	0.80	0.65	0.00	31.6
		MP-0.15	2.78	237	0.37	0.65	0	1.23	0.63	0.00	18.7

		MP-0.2	2.78	237	0.37	0.65	0	0.80	0.63	0.00	9.8
		MP-0.25	2.78	237	0.37	0.65	0	1.23	0.63	0.00	39.9
		M2-0.15	2.78	237	0.37	0.65	0	0.80	0.63	0.00	27.3
2016	Okoye et al.	M2-0.2	1.76	420	0.26	0.60	14	0.62	0.22	0.52	31.1
		M2-0,25	1.93	1399	0.26	0.60	14	0.62	0.22	0.52	34.8
		M4-0.15	2.12	2378	0.26	0.60	14	0.62	0.22	0.52	38.6
		M4-0.2	2.32	3357	0.26	0.60	14	0.62	0.22	0.52	36.4
		M4-0.25	2.56	4336	0.26	0.60	14	0.62	0.22	0.52	53.0
2017	Hadi et al.	M1	1.90	425	0.25	0.51	10	0.44	0.26	0.49	46.8
		M2	1.90	425	0.26	0.61	12	0.55	0.26	0.48	39.0
		M3	1.90	425	0.28	0.71	14	0.64	0.25	0.47	42.6
		M4	1.90	425	0.28	0.51	14	0.55	0.25	0.47	61.2
		M5	1.90	425	0.30	0.61	10	0.64	0.25	0.46	42.2

		M6	1.90	425	0.31	0.71	12	0.44	0.24	0.45	37.3
		M7	1.90	425	0.31	0.51	12	0.64	0.24	0.45	59.5
		M8	1.90	425	0.33	0.61	14	0.44	0.24	0.44	42.9
		M9	1.90	425	0.35	0.71	10	0.55	0.23	0.42	34.4
2018	Guo & Pan	M10	1.88	378	0.41	0.71	11	1.50	0.59	0.00	26.6
		M11	1.88	378	0.41	0.71	11	1.50	0.59	0.00	27.0
		M12	1.88	378	0.41	0.71	11	1.50	0.59	0.00	29.3
		M13	1.88	378	0.41	0.71	11	1.50	0.59	0.00	28.5
		M14	1.88	378	0.41	0.71	11	1.50	0.59	0.00	28.1
		M15	1.88	378	0.41	0.71	11	1.50	0.59	0.00	26.3
		M16	1.88	378	0.41	0.71	11	1.50	0.59	0.00	27.2
		M17	1.88	378	0.40	0.71	11	1.50	0.59	0.00	28.5
		M18	1.88	378	0.40	0.71	11	1.50	0.59	0.00	30.2

		M19	1.88	378	0.40	0.71	11	1.50	0.59	0.00	29.1
		M20	1.88	378	0.40	0.71	11	1.50	0.59	0.00	24.8
		M21	1.88	378	0.40	0.71	11	1.50	0.59	0.00	25.9
		M22	1.88	378	0.40	0.71	11	1.50	0.59	0.00	26.3
		M23	1.88	378	0.40	0.71	11	1.50	0.58	0.00	29.0
		M24	1.88	378	0.40	0.71	11	1.50	0.58	0.00	27.2
2019	Ling et al.	M25	1.92	420	1.00	0.33	0	0.00	0.00	0.00	7.5
		M26	1.92	420	1.00	0.40	0	0.00	0.00	0.00	6.8
		M27	1.92	420	1.00	0.50	0	0.00	0.00	0.00	5.3
		T1	1.92	420	1.00	0.60	0	0.00	0.00	0.00	3.0
2019	Hu et al.	T2	2.75	420	0.27	0.55	12	0.64	0.23	0.50	26.1
		T3	2.64	421	0.27	0.55	12	0.64	0.23	0.50	43.5
		T4	2.54	421	0.27	0.55	12	0.64	0.23	0.50	47.0

		T5	2.44	422	0.27	0.55	12	0.64	0.23	0.50	52.3
		T6	2.75	420	0.27	0.55	12	0.64	0.23	0.50	14.0
		T7	2.64	421	0.27	0.55	12	0.64	0.23	0.50	31.9
		T8	2.54	421	0.27	0.55	12	0.64	0.23	0.50	35.6
		T9	2.44	422	0.27	0.55	12	0.64	0.23	0.50	43.0
		M8-R1	2.75	420	0.27	0.55	12	0.64	0.23	0.50	13.7
		M12-R1	2.64	421	0.27	0.55	12	0.64	0.23	0.50	27.5
		M16-R1	2.54	421	0.27	0.55	12	0.64	0.23	0.50	34.8
		M8-R2.5	2.44	422	0.27	0.55	12	0.64	0.23	0.50	38.1
2019	Sedaghatdoost et al.	M12-R2.5	1.78	360	0.38	0.50	12	0.83	0.63	0.00	41.3
		M16-R2.5	1.78	360	0.38	0.50	12	0.83	0.47	0.16	46.5
		M8-R4	1.78	360	0.38	0.50	12	0.83	0.31	0.31	45.8
		M12-R4	1.78	360	0.38	0.50	12	0.83	0.16	0.47	43.5

		M16-R4	1.78	360	0.38	0.51	12	0.83	0.00	0.62	42.0
2020	Moradikhou et al.	1	1.70	2140	0.31	1.14	14	0.48	0.35	0.35	19.2
		2	1.70	2140	0.31	1.14	14	0.48	0.34	0.34	18.7
		3	1.70	2140	0.31	1.14	14	0.48	0.34	0.34	19.5
		4	1.70	2140	0.31	1.14	14	0.48	0.34	0.34	18.8
		5	1.70	2140	0.31	1.14	14	0.48	0.34	0.34	19.5
		6	1.70	2140	0.31	1.14	14	0.48	0.34	0.34	20.1
		7	1.70	2140	0.31	1.14	14	0.48	0.34	0.34	19.7
		14	1.70	2140	0.31	1.14	14	0.48	0.34	0.34	19.7
		15	1.70	2140	0.31	1.14	14	0.48	0.34	0.34	20.4
		16	1.70	2140	0.31	1.14	14	0.48	0.34	0.34	19.9
2020	Mermerdaş et al.	17	3.19	420	0.31	0.54	6	0.24	0.54	0.15	1.7
		18	3.19	420	0.31	0.54	8	0.24	0.54	0.15	12.3

		19	3.19	420	0.31	0.54	10	0.24	0.54	0.15	12.3
		20	3.19	420	0.36	0.54	6	0.24	0.50	0.14	7.5
		27	3.19	420	0.36	0.54	8	0.24	0.50	0.14	12.3
		28	3.19	420	0.36	0.54	10	0.24	0.50	0.14	13.0
		29	3.19	420	0.41	0.54	6	0.24	0.46	0.13	10.7
		30	3.19	420	0.41	0.54	8	0.24	0.46	0.13	14.3
		31	3.19	420	0.41	0.54	10	0.24	0.46	0.13	14.3
		32	3.19	420	0.31	0.54	6	0.48	0.54	0.15	6.8
		33	3.19	420	0.31	0.54	8	0.48	0.54	0.15	7.5
		M1	3.19	420	0.30	0.54	10	0.48	0.54	0.15	9.8
		M2	3.19	420	0.36	0.53	6	0.48	0.50	0.14	6.0
		M3	3.19	420	0.36	0.53	8	0.48	0.50	0.14	12.0
		M4	3.19	420	0.36	0.53	10	0.48	0.50	0.14	12.8

		M5	3.19	420	0.41	0.54	6	0.48	0.46	0.13	9.0
		M6	3.19	420	0.41	0.54	8	0.48	0.46	0.13	12.0
		M7	3.19	420	0.41	0.54	10	0.48	0.46	0.13	12.0
		M8	3.19	420	0.31	0.54	6	0.60	0.54	0.15	7.5
		M9	3.19	420	0.31	0.54	8	0.60	0.54	0.15	10.5
		M10	3.19	420	0.30	0.54	10	0.60	0.54	0.15	11.3
		M11	3.19	420	0.36	0.54	6	0.60	0.50	0.14	7.5
		M12	3.19	420	0.36	0.54	8	0.60	0.50	0.14	12.0
		M13	3.19	420	0.36	0.54	10	0.60	0.50	0.14	13.1
		M14	3.19	420	0.41	0.53	6	0.60	0.46	0.13	11.0
		M15	3.19	420	0.41	0.53	8	0.60	0.46	0.13	12.1
		M16	3.19	420	0.41	0.53	10	0.60	0.46	0.13	13.5
2020	Luan et al.	M17	3.76	420	0.24	0.37	12	0.46	0.24	0.53	49.2

		M1	3.76	420	0.25	0.40	14	0.58	0.23	0.52	56.9
		M2	3.76	420	0.25	0.44	16	0.69	0.23	0.52	52.4
		M3	3.76	420	0.26	0.37	14	0.69	0.23	0.51	46.7
		M4	3.76	420	0.27	0.40	16	0.46	0.23	0.50	69.6
		M5	3.76	420	0.28	0.44	12	0.58	0.22	0.50	42.6
		M6	3.76	420	0.28	0.37	16	0.58	0.22	0.49	59.9
		M7	3.76	420	0.29	0.40	12	0.69	0.22	0.49	43.9
		M8	3.76	420	0.30	0.44	14	0.46	0.22	0.48	65.0
2021	Shariati et al.	M9	1.58	360	1.00	0.53	8	0.38	0.00	0.00	42.6
		M10	1.58	360	1.00	0.53	12	0.38	0.00	0.00	44.6
		M11	1.58	360	1.00	0.53	16	0.38	0.00	0.00	43.4
		M12	1.58	360	1.00	0.53	8	0.60	0.00	0.00	47.4
		M13	1.58	360	1.00	0.53	12	0.60	0.00	0.00	48.1

		M14	1.58	360	1.00	0.53	16	0.60	0.00	0.00	46.9
		M15	1.58	360	1.00	0.53	8	0.70	0.00	0.00	43.7
		Control	1.58	360	1.00	0.53	12	0.70	0.00	0.00	46.3
		P3-5	1.58	360	1.00	0.53	16	0.70	0.00	0.00	45.2
2021	Shahmansouri et al.	P3-10	1.68	450	0.23	0.48	4	0.09	0.27	0.49	45.0
		P3-15	4.33	3678	0.23	0.48	4	0.09	0.27	0.49	46.8
		P3-20	6.98	6905	0.23	0.48	4	0.09	0.27	0.49	49.0
		P9-5	9.63	10133	0.23	0.48	4	0.09	0.27	0.49	48.8
		P9-10	12.28	13360	0.23	0.48	4	0.09	0.27	0.49	55.9
		P9-15	14.94	16588	0.23	0.48	4	0.09	0.27	0.49	58.6
		P9-20	17.59	19815	0.23	0.48	4	0.09	0.27	0.49	61.5
		P15-5	1.68	450	0.23	0.48	6	0.09	0.27	0.49	41.8
		P15-10	4.33	3678	0.23	0.48	6	0.09	0.27	0.49	44.2

		P15-15	6.98	6905	0.23	0.48	6	0.09	0.27	0.49	47.3
		P15-20	9.63	10133	0.23	0.48	6	0.09	0.27	0.49	49.6
		SHGC0	12.28	13360	0.23	0.48	6	0.09	0.27	0.49	55.5
		SHGC1	14.94	16588	0.23	0.48	6	0.09	0.27	0.49	58.5
		SHGC2	17.59	19815	0.23	0.48	6	0.09	0.27	0.49	61.5
		SHGC3	1.68	450	0.23	0.48	8	0.09	0.27	0.49	40.8
		SHGC4	4.33	3678	0.23	0.48	8	0.09	0.27	0.49	44.5
		G1-00-50-W	6.98	6905	0.23	0.48	8	0.09	0.27	0.49	49.0
		G1-05-50-W	9.63	10133	0.23	0.48	8	0.09	0.27	0.49	45.4
		G1-10-50-W	12.28	13360	0.23	0.48	8	0.09	0.27	0.49	54.8
		G1-15-50-W	14.94	16588	0.23	0.48	8	0.09	0.27	0.49	53.3
		G1-00-52-W	17.59	19815	0.23	0.48	8	0.09	0.27	0.49	51.9
2021	Albidah et al.	G1-05-52-W	1.20	2140	0.26	0.89	14	0.36	0.24	0.50	56.3

		G1-10-52-W	1.20	2140	0.26	0.89	14	0.43	0.24	0.50	57.5
		G1-15-52-W	1.20	2140	0.26	0.89	14	0.51	0.24	0.50	57.5
		G1-00-54-W	1.20	2140	0.26	0.90	14	0.59	0.24	0.50	45.0
		G1-05-54-W	1.20	2140	0.26	0.90	14	0.68	0.24	0.50	36.3
		G1-10-54-W	1.20	2140	0.25	0.96	14	0.51	0.24	0.51	38.8
		G1-15-54-W	1.20	2140	0.26	0.79	14	0.51	0.24	0.50	36.3
		G2-00-50-W	1.20	2140	0.27	0.73	14	0.51	0.23	0.50	22.5
		G2-05-50-W	1.20	2140	0.28	0.67	14	0.51	0.23	0.49	13.0
		G2-10-50-W	1.20	2140	0.32	0.89	14	0.51	0.22	0.46	37.5
		G2-15-50-W	1.20	2140	0.28	0.90	14	0.51	0.23	0.49	40.0
		G2-00-52-W	1.20	2140	0.25	0.96	14	0.55	0.24	0.51	40.0
		G2-05-52-W	1.20	2140	0.21	1.00	14	0.58	0.25	0.54	38.0
		G2-10-52-W	1.20	2140	0.25	0.80	14	0.40	0.24	0.51	40.0

		G2-15-52-W	1.20	2140	0.27	1.00	14	0.51	0.23	0.49	32.5
		G2-00-54-W	1.20	2140	0.28	1.06	14	0.51	0.23	0.49	23.8
		G2-05-54-W	1.20	2140	0.28	1.11	14	0.51	0.23	0.49	17.5
2021	Adesanya et al.	G2-10-54-W	1.80	425	0.38	0.81	3	0.00	0.62	0.00	18.0
		G2-15-54-W	2.10	424	0.38	0.81	3	0.00	0.62	0.00	15.8
		G1-00-50-P	2.40	423	0.38	0.81	3	0.00	0.62	0.00	14.3
		G1-05-50-P	1.80	425	0.39	0.90	7	1.00	0.61	0.00	66.8
		G1-10-50-P	2.10	424	0.39	0.90	7	1.00	0.61	0.00	63.8
		G1-15-50-P	2.40	423	0.39	0.90	7	1.00	0.61	0.00	56.3
		G1-00-52-P	1.80	425	0.37	0.80	3	1.50	0.63	0.00	69.0
		G1-05-52-P	2.10	424	0.37	0.80	3	1.50	0.63	0.00	58.5
		G1-10-52-P	2.40	423	0.37	0.80	3	1.50	0.63	0.00	54.0
		G1-15-52-P	1.80	425	0.37	0.75	1	2.00	0.63	0.00	63.8

		G1-00-54-P	2.10	424	0.37	0.75	1	2.00	0.63	0.00	60.0
		G1-05-54-P	2.40	423	0.37	0.75	1	2.00	0.63	0.00	53.3
		G1-10-54-P	1.80	425	0.36	0.72	0	2.50	0.64	0.00	0.8
		G1-15-54-P	2.10	424	0.36	0.72	0	2.50	0.64	0.00	0.8
		G2-00-50-P	2.40	423	0.36	0.72	0	2.50	0.64	0.00	1.5
2021	Xu et al.	G2-05-50-P	2.52	425	0.55	0.50	7	0.00	0.45	0.00	23.7
		G2-10-50-P	2.52	425	0.55	0.50	7	0.00	0.45	0.00	22.6
		G2-15-50-P	2.52	425	0.55	0.50	7	0.00	0.45	0.00	23.1
		G2-00-52-P	2.52	425	0.55	0.50	7	0.00	0.45	0.00	23.5
		G2-05-52-P	2.52	425	0.55	0.50	7	0.00	0.45	0.00	23.4
		G2-10-52-P	2.52	425	0.55	0.50	7	0.00	0.45	0.00	24.2
		G2-15-52-P	2.52	425	0.55	0.50	7	0.00	0.45	0.00	24.2
		G2-00-54-P	2.52	425	0.55	0.50	7	0.00	0.45	0.00	24.2

		G2-05-54-P	2.52	425	0.55	0.50	7	0.00	0.45	0.00	24.2
		G2-10-54-P	2.52	425	0.55	0.50	7	0.00	0.45	0.00	24.5
		G2-15-54-P	2.52	425	0.55	0.50	7	0.00	0.45	0.00	24.7
		44F0S0	2.52	425	0.55	0.50	7	0.00	0.45	0.00	25.3
		47F0S0	2.52	425	0.55	0.50	7	0.00	0.45	0.00	24.7
2021	Wang et al.	50F0S0	1.91	421	1.00	0.41	10	0.55	0.00	0.00	32.3
		47F25S0	1.91	421	0.92	0.41	10	0.55	0.07	0.00	35.7
		47F0S5	1.91	421	0.87	0.41	10	0.55	0.12	0.00	23.5
		47F0S10	1.91	421	0.81	0.41	10	0.55	0.17	0.00	25.5
		Slag LSS 4% Na,Ms=0.75	1.91	421	0.77	0.41	10	0.55	0.22	0.00	21.0
2022	Sadeghian ert al.	Slag LSS 4% Na,Ms=1.00	1.57	400	0.22	0.73	0	0.97	0.47	0.31	43.0

		Slag LSS 4% Na,Ms=1.25	5.74	1080	0.22	0.72	0	0.97	0.47	0.31	48.8
		Slag LSS 4% Na,Ms=1.50	9.91	1760	0.22	0.71	0	0.97	0.47	0.31	45.9
		Slag LSS 8% Na,Ms=0.75	14.08	2440	0.22	0.70	0	0.97	0.47	0.31	24.5
		Slag SH 4%	1.57	400	0.22	0.75	0	0.97	0.47	0.31	42.4
		Slag SH 8%	5.74	1080	0.22	0.74	0	0.97	0.47	0.31	47.0
		M36	9.91	1760	0.22	0.73	0	0.97	0.47	0.31	45.0
		M37	14.08	2440	0.22	0.72	0	0.97	0.47	0.31	22.7
		M38	1.57	400	0.23	0.77	0	0.97	0.46	0.31	41.3
		M39	5.74	1080	0.22	0.76	0	0.97	0.47	0.31	45.3
		M46	9.91	1760	0.22	0.75	0	0.97	0.47	0.31	45.0

		M47	14.08	2440	0.22	0.74	0	0.97	0.47	0.31	22.5
		M48	1.57	400	0.22	0.75	0	0.97	0.47	0.31	45.8
		M49	5.74	1080	0.22	0.74	0	0.97	0.47	0.31	48.8
		M56	9.91	1760	0.22	0.73	0	0.97	0.47	0.31	45.0
		M57	14.08	2440	0.22	0.72	0	0.97	0.47	0.31	33.8
		M58	1.57	400	0.23	0.77	0	0.97	0.46	0.31	45.2
		M59	5.74	1080	0.22	0.76	0	0.97	0.47	0.31	47.0
		GGBFS	9.91	1760	0.22	0.75	0	0.97	0.47	0.31	43.1
		SF10	14.08	2440	0.22	0.74	0	0.97	0.47	0.31	30.2
		SF20	1.57	400	0.23	0.79	0	0.97	0.46	0.31	43.6
		FA20	5.74	1080	0.23	0.78	0	0.97	0.46	0.31	45.3
		FA40	9.91	1760	0.23	0.77	0	0.97	0.46	0.31	39.5
		SF10+FA20	14.08	2440	0.22	0.76	0	0.97	0.47	0.31	28.1

		SF10+FA40	1.57	400	0.22	0.73	0	0.97	0.47	0.31	42.0
		SF20+FA20	5.74	1080	0.22	0.72	0	0.97	0.47	0.31	45.9
		SF20+FA40	9.91	1760	0.22	0.71	0	0.97	0.47	0.31	45.9
		0-4%	14.08	2440	0.22	0.70	0	0.97	0.47	0.31	30.0
		0-6%	1.57	400	0.22	0.75	0	0.97	0.47	0.31	41.4
		0-8%	5.74	1080	0.22	0.74	0	0.97	0.47	0.31	45.3
		0.4-4%	9.91	1760	0.22	0.73	0	0.97	0.47	0.31	45.0
		0.4-6%	14.08	2440	0.22	0.72	0	0.97	0.47	0.31	28.6
		0.4-8%	1.57	400	0.23	0.77	0	0.97	0.46	0.31	40.5
		0.8-4%	5.74	1080	0.22	0.76	0	0.97	0.47	0.31	45.0
		0.8-6%	9.91	1760	0.22	0.75	0	0.97	0.47	0.31	44.7
		0.8-8%	14.08	2440	0.22	0.74	0	0.97	0.47	0.31	28.0
		1.2-4%	1.57	400	0.22	0.75	0	0.97	0.47	0.31	45.0

		1.2-6%	5.74	1080	0.22	0.74	0	0.97	0.47	0.31	48.8
		1.2-8%	9.91	1760	0.22	0.73	0	0.97	0.47	0.31	43.0
		1.6-4%	14.08	2440	0.22	0.72	0	0.97	0.47	0.31	35.6
		1.6-6%	1.57	400	0.23	0.77	0	0.97	0.46	0.31	45.0
		1.6-8%	5.74	1080	0.22	0.76	0	0.97	0.47	0.31	45.3
		LA1	9.91	1760	0.22	0.75	0	0.97	0.47	0.31	43.1
		LB1	14.08	2440	0.22	0.74	0	0.97	0.47	0.31	34.3
		LA2	1.57	400	0.23	0.79	0	0.97	0.46	0.31	42.4
		LB2	5.74	1080	0.23	0.78	0	0.97	0.46	0.31	42.4
		MA1	9.91	1760	0.23	0.77	0	0.97	0.46	0.31	37.5
		MB1	14.08	2440	0.22	0.76	0	0.97	0.47	0.31	33.8
2022	Ou et al.	MA2	1.79	425	0.24	0.61	2	1.00	0.29	0.47	57.6
		MB2	1.79	425	0.25	0.65	2	1.00	0.29	0.47	50.9

		HA1	1.79	425	0.25	0.68	2	1.00	0.28	0.46	40.1
		HB1	1.73	424	0.25	0.65	2	1.00	0.29	0.47	47.4
		HA2	11.39	1404	0.25	0.65	2	1.00	0.29	0.47	64.3
		HB2	20.98	2383	0.25	0.65	2	1.00	0.29	0.47	60.3

Supplementary Table 3. Mix design key factors and ultimate drying shrinkage of AAM mixes

Year	Author	Mix ID	A.M.	SSA	GPC	L/B ratio	NaOH concentration/ M	Ms	Fine agg.	Coarse agg.	T/ ℃	RH/ %	V/S	UDS	Time
2009	Duran Atiş et al.	Slag LSS 4% Na,Ms=0.75	1.55	425	0.35	0.33	0.00	0.75	0.65	0.00	23	65	5.99	1004	180d
		Slag LSS 4% Na,Ms=1.00	1.55	425	0.35	0.33	0.00	1.00	0.65	0.00	23	65	5.99	2926	180d
		Slag LSS 4% Na,Ms=1.25	1.55	425	0.35	0.33	0.00	1.25	0.65	0.00	23	65	5.99	3614	180d
		Slag LSS 4% Na,Ms=1.50	1.55	425	0.35	0.33	0.00	1.50	0.65	0.00	23	65	5.99	6372	180d

		Slag LSS 8% Na,Ms=0.75	1.55	425	0.35	0.33	0.00	0.75	0.65	0.00	23	65	5.99	3642	180d
		Slag SH 4%	1.55	425	0.35	0.33	1.00	0.00	0.65	0.00	23	65	5.99	2119	180d
		Slag SH 8%	1.55	425	0.35	0.33	2.00	0.00	0.65	0.00	23	65	5.99	2968	180d
2011	Ridtirud et al.	S/N0.3	1.84	420	0.37	0.38	10.00	0.33	0.63	0.00	23	50	5.99	2863	71d
		S/N0.67	1.84	420	0.37	0.38	10.00	0.70	0.63	0.00	23	50	5.99	2474	71d
		S/N1.0	1.84	420	0.37	0.38	10.00	0.91	0.63	0.00	23	50	5.99	2474	71d
		S/N1.5	1.84	420	0.37	0.38	10.00	0.99	0.63	0.00	23	50	5.99	2474	71d
		S/N3.0	1.84	420	0.37	0.38	10.00	1.53	0.63	0.00	23	50	5.99	1096	71d
		L/A0.4	1.84	420	0.34	0.29	10.00	0.70	0.66	0.00	23	50	5.99	353	71d
		L/A0.5	1.84	420	0.35	0.33	10.00	0.70	0.65	0.00	23	50	5.99	1378	71d
		L/A0.6	1.84	420	0.37	0.38	10.00	0.70	0.63	0.00	23	50	5.99	2722	71d
		L/A0.7	1.84	420	0.38	0.41	10.00	0.70	0.62	0.00	23	50	5.99	3146	71d

		7.5M NaOH	1.84	420	0.37	0.38	7.50	0.84	0.63	0.00	23	50	5.99	1959	71d
		10M NaOH	1.84	420	0.37	0.38	10.00	0.70	0.63	0.00	23	50	5.99	2602	71d
		12.5M NaoH	1.84	420	0.37	0.38	12.50	0.60	0.63	0.00	23	50	5.99	2816	71d
2012	Chi and Huang	M36	1.78	435	0.28	0.08	10.68	0.60	0.72	0.00	25	80	5.95	700	28d
		M37	1.78	435	0.28	0.09	9.01	0.70	0.72	0.00	25	80	5.95	750	28d
		M38	1.78	435	0.29	0.10	7.65	0.80	0.71	0.00	25	80	5.95	810	28d
		M39	1.78	435	0.29	0.10	6.49	0.90	0.71	0.00	25	80	5.95	930	28d
		M46	1.78	435	0.29	0.11	10.67	0.60	0.71	0.00	25	80	5.95	834	28d
		M47	1.78	435	0.29	0.11	9.02	0.70	0.71	0.00	25	80	5.95	820	28d
		M48	1.78	435	0.29	0.12	7.64	0.80	0.71	0.00	25	80	5.95	880	28d
		M49	1.78	435	0.29	0.13	6.49	0.90	0.71	0.00	25	80	5.95	760	28d
		M56	1.78	435	0.29	0.13	10.66	0.60	0.71	0.00	25	80	5.95	740	28d
		M57	1.78	435	0.30	0.14	9.03	0.70	0.70	0.00	25	80	5.95	810	28d

		M58	1.78	435	0.30	0.15	7.65	0.80	0.70	0.00	25	80	5.95	760	28d
		M59	1.78	435	0.30	0.16	6.49	0.90	0.70	0.00	25	80	5.95	675	28d
2013	Aydın & Baradan	0	28.52	4328	0.48	0.21	15.70	1.20	0.52	0.00	20	50	5.99	518	60d
		0.5%F6	28.52	4328	0.47	0.21	15.70	1.20	0.51	0.00	20	50	5.99	488	60d
		1.0%F6	28.52	4328	0.46	0.21	15.70	1.20	0.51	0.00	20	50	5.99	459	60d
		1.5%F6	28.52	4328	0.46	0.21	15.70	1.20	0.50	0.00	20	50	5.99	441	60d
		2.0%F6	28.52	4328	0.45	0.21	15.70	1.20	0.49	0.00	20	50	5.99	407	60d
		0.5%F13	28.52	4328	0.47	0.21	15.70	1.20	0.51	0.00	20	50	5.99	481	60d
		1.0%F13	28.52	4328	0.46	0.21	15.70	1.20	0.51	0.00	20	50	5.99	450	60d
		1.5%F13	28.52	4328	0.46	0.21	15.70	1.20	0.50	0.00	20	50	5.99	427	60d
		2.0%F13	28.52	4328	0.45	0.21	15.70	1.20	0.49	0.00	20	50	5.99	394	60d
2013	Aydın	GGBFS	1.33	410	0.31	0.19	15.70	1.20	0.69	0.00	20	55	5.99	2330	120d
		SF10	7.71	2369	0.31	0.19	15.70	1.20	0.69	0.00	20	55	5.99	1270	120d

		SF20	14.09	4328	0.31	0.19	15.70	1.20	0.69	0.00	20	55	5.99	510	120d
		FA20	1.49	393	0.31	0.19	15.70	1.20	0.69	0.00	20	55	5.99	1990	120d
		FA40	1.66	375	0.31	0.19	15.70	1.20	0.69	0.00	20	55	5.99	1870	120d
		SF10+FA20	7.87	2352	0.31	0.19	15.70	1.20	0.69	0.00	20	55	5.99	850	120d
		SF10+FA40	8.04	2334	0.31	0.19	15.70	1.20	0.69	0.00	20	55	5.99	820	120d
		SF20+FA20	14.25	4311	0.31	0.19	15.70	1.20	0.69	0.00	20	55	5.99	650	120d
		SF20+FA40	14.42	4293	0.31	0.19	15.70	1.20	0.69	0.00	20	55	5.99	760	120d
2014	Aydın and Baradan	0-4%	1.33	410	0.35	0.34	4.00	0.00	0.65	0.00	20	55	5.99	1142	180d
		0-6%	1.33	410	0.36	0.35	6.11	0.00	0.64	0.00	20	55	5.99	1000	180d
		0-8%	1.33	410	0.37	0.37	8.23	0.00	0.63	0.00	20	55	5.99	1000	180d
		0.4-4%	1.33	410	0.44	0.54	15.08	0.40	0.56	0.00	20	55	5.99	2433	180d
		0.4-6%	1.33	410	0.42	0.50	11.27	0.40	0.58	0.00	20	55	5.99	2516	180d
		0.4-8%	1.33	410	0.40	0.45	5.72	0.40	0.60	0.00	20	55	5.99	2461	180d

		0.8-4%	1.33	410	0.41	0.47	8.47	0.80	0.59	0.00	20	55	5.99	3677	180d
		0.8-6%	1.33	410	0.40	0.45	5.81	0.80	0.60	0.00	20	55	5.99	4203	180d
		0.8-8%	1.33	410	0.39	0.42	2.71	0.80	0.61	0.00	20	55	5.99	4839	180d
		1.2-4%	1.33	410	0.40	0.44	15.70	1.20	0.60	0.00	20	55	5.99	3401	180d
		1.2-6%	1.33	410	0.39	0.42	15.70	1.20	0.61	0.00	20	55	5.99	4977	180d
		1.2-8%	1.33	410	0.38	0.41	15.70	1.20	0.62	0.00	20	55	5.99	5477	180d
		1.6-4%	1.33	410	0.39	0.43	3.51	1.60	0.61	0.00	20	55	5.99	4120	180d
		1.6-6%	1.33	410	0.38	0.42	1.57	1.60	0.62	0.00	20	55	5.99	5060	180d
		1.6-8%	1.33	410	0.38	0.41	0.68	1.60	0.62	0.00	20	55	5.99	5475	180d
2015	Deb et al.	R2.5S10	1.97	421	0.23	0.29	10.01	0.71	0.27	0.50	20	70	16.57	700	180d
		R2.5S20	2.16	421	0.23	0.29	10.01	0.71	0.27	0.50	20	70	16.57	650	180d

		R1.5S10	1.97	421	0.23	0.29	14.06	0.47	0.27	0.50	20	70	16.57	650	180d
		R1.5S20	2.16	421	0.23	0.29	14.06	0.47	0.27	0.50	20	70	16.57	475	180d
2015	Chi	LA1	2.78	237	0.33	0.26	0.00	1.23	0.67	0.00	25	80	5.99	5581	28d
		LB1	2.78	237	0.33	0.26	0.00	0.80	0.67	0.00	25	80	5.99	6811	28d
		LA2	2.78	237	0.33	0.26	0.00	1.23	0.67	0.00	25	80	5.99	4718	28d
		LB2	2.78	237	0.33	0.26	0.00	0.80	0.67	0.00	25	80	5.99	6678	28d
		MA1	2.78	237	0.35	0.33	0.00	1.23	0.65	0.00	25	80	5.99	6755	28d
		MB1	2.78	237	0.35	0.33	0.00	0.80	0.65	0.00	25	80	5.99	9205	28d
		MA2	2.78	237	0.35	0.33	0.00	1.23	0.65	0.00	25	80	5.99	4371	28d
		MB2	2.78	237	0.35	0.33	0.00	0.80	0.65	0.00	25	80	5.99	3510	28d
		HA1	2.78	237	0.37	0.39	0.00	1.23	0.63	0.00	25	80	5.99	8874	28d

		HB1	2.78	237	0.37	0.39	0.00	0.80	0.63	0.00	25	80	5.99	8179	28d
		HA2	2.78	237	0.37	0.39	0.00	1.23	0.63	0.00	25	80	5.99	2318	28d
		HB2	2.78	237	0.37	0.39	0.00	0.80	0.63	0.00	25	80	5.99	5066	28d
2015	Marjanović et al.	FA-BFS 25-75 n=1.0; 10% Na2O; 95C	1.78	424	0.32	0.29	6.43	1.00	0.68	0.00	20	55	8.89	1190	180d
		FA-BFS 25-75 n=1.5; 7% Na2O; 95C	1.78	424	0.32	0.29	3.51	1.50	0.68	0.00	20	55	8.89	1071	180d
		FA 100	2.58	420	0.32	0.29	3.51	1.50	0.68	0.00	20	55	8.89	2261	28d
		BFS 100	1.51	425	0.32	0.29	6.43	1.00	0.68	0.00	20	55	8.89	4642	180d

		FA-BFS 25-75 n=1.0; 10% Na2O; 20C	1.78	424	0.32	0.29	6.43	1.00	0.68	0.00	20	55	8.89	4761	180d
		FA-BFS 25-75 n=1.5; 7% Na2O; 20C	1.78	424	0.32	0.29	3.51	1.50	0.68	0.00	20	55	8.89	4761	180d
2015	Chi et al.	LF	2.78	237	0.30	0.14	3.38	1.00	0.70	0.00	25	80	5.99	1938	28d
		LSF	2.28	336	0.30	0.14	3.38	1.00	0.70	0.00	25	80	5.99	4081	28d
		LS	1.78	435	0.30	0.14	3.38	1.00	0.70	0.00	25	80	5.99	4489	28d
		MF	2.78	237	0.30	0.14	1.88	1.00	0.70	0.00	25	80	5.99	2527	28d
		MSF	2.28	336	0.30	0.14	1.88	1.00	0.70	0.00	25	80	5.99	4505	28d
		MS	1.78	435	0.30	0.14	1.88	1.00	0.70	0.00	25	80	5.99	7425	28d
		HF	2.78	237	0.30	0.14	1.00	1.00	0.70	0.00	25	80	5.99	2708	28d

		HSF	2.28	336	0.30	0.14	1.00	1.00	0.70	0.00	25	80	5.99	5625	28d
		HS	1.78	435	0.30	0.14	1.00	1.00	0.70	0.00	25	80	5.99	8750	28d
2016	Ye & Radlińska	AAS_70% RH	2.04	425	1.00	0.33	4.00	0.00	0.00	0.00	23	70	3.04	12800	70d
		AAS_50% RH	2.04	425	1.00	0.33	4.00	0.00	0.00	0.00	23	50	3.04	16400	70d
		AAS_30% RH	2.04	425	1.00	0.33	4.00	0.00	0.00	0.00	23	30	3.04	10600	70d
		AAS_11% RH	2.04	425	1.00	0.33	4.00	0.00	0.00	0.00	23	11	3.04	9000	70d
2016	Gao et al.	M1-820	1.86	424	0.43	0.39	7.25	1.00	0.50	0.00	20	50	8.89	3358	28d
		M2-824	1.86	424	0.44	0.40	4.71	1.40	0.50	0.00	20	50	8.89	3985	28d
		M3-828	1.86	424	0.44	0.40	3.02	1.80	0.49	0.00	20	50	8.89	4871	28d
		M7-460	2.05	422	0.43	0.39	7.25	1.00	0.50	0.00	20	50	8.89	2159	28d

		M8-464	2.05	422	0.44	0.40	4.71	1.40	0.50	0.00	20	50	8.89	2786	28d
		M9-468	2.05	422	0.44	0.40	3.09	1.80	0.49	0.00	20	50	8.89	3727	28d
2016	Thomas et al.	FC1	1.89	420	0.36	0.29	0.00	1.50	0.29	0.35	22	50	11.55	1325	365d
		FC2	1.89	420	0.36	0.29	0.00	1.50	0.29	0.35	22	50	11.55	990	365d
		FC3	1.89	420	0.36	0.29	0.00	1.50	0.29	0.35	22	50	11.55	863	365d
		SC1	1.62	425	0.36	0.29	0.00	1.50	0.29	0.35	22	50	11.55	1227	365d
		SC2	1.62	425	0.36	0.29	0.00	1.50	0.29	0.35	22	50	11.55	1383	365d

		SC3	1.62	425	0.36	0.29	0.00	0.75	0.29	0.35	22	50	11.55	850	365d
		SC4	1.62	425	0.36	0.29	0.00	0.75	0.29	0.35	22	50	11.55	888	365d
		SC5	1.62	425	0.36	0.29	0.00	0.75	0.29	0.35	22	50	11.55	956	365d
2017	Yang et al.	P0	1.32	2140	1.00	0.38	3.50	1.40	0.00	0.00	24	45	4.44	6113	50d
		P10	1.36	1968	1.00	0.38	3.50	1.40	0.00	0.00	24	45	4.44	5713	50d
		P20	1.40	1796	1.00	0.38	3.50	1.40	0.00	0.00	24	45	4.44	5370	50d
		P30	1.45	1624	1.00	0.38	3.50	1.40	0.00	0.00	24	45	4.44	4130	50d
		M0	1.32	2140	0.76	0.38	3.50	1.40	0.24	0.00	24	45	4.44	4804	50d
		M10	1.36	1968	0.76	0.38	3.50	1.40	0.24	0.00	24	45	4.44	3907	50d
		M20	1.40	1796	0.76	0.38	3.50	1.40	0.24	0.00	24	45	4.44	3689	50d

		M30	1.45	1624	0.76	0.38	3.50	1.40	0.24	0.00	24	45	4.44	2638	50d
		S0	1.32	2140	0.62	0.38	3.50	1.40	0.38	0.00	24	45	4.44	2460	50d
		S10	1.36	1968	0.62	0.38	3.50	1.40	0.38	0.00	24	45	4.44	2087	50d
		S20	1.40	1796	0.62	0.38	3.50	1.40	0.38	0.00	24	45	4.44	2263	50d
		S30	1.45	1624	0.62	0.38	3.50	1.40	0.38	0.00	24	45	4.44	1713	50d
2017	Ye et al.	AAS1_85%RH	2.04	425	0.43	0.35	2.26	0.41	0.57	0.00	23	85	3.04	1000	60d
		AAS1_70%RH	2.04	425	0.43	0.35	2.26	0.41	0.57	0.00	23	70	3.04	1875	70d
		AAS1_50%RH	2.04	425	0.43	0.35	2.26	0.41	0.57	0.00	23	50	3.04	2094	65d
		AAS1_30%RH	2.04	425	0.43	0.35	2.26	0.41	0.57	0.00	23	30	3.04	1687	65d
		AAS2_85%RH	2.04	425	0.43	0.36	0.60	1.22	0.57	0.00	23	85	3.04	1156	70d
		AAS2_70%RH	2.04	425	0.43	0.36	0.60	1.22	0.57	0.00	23	70	3.04	1937	65d
		AAS2_50%RH	2.04	425	0.43	0.36	0.60	1.22	0.57	0.00	23	50	3.04	2312	65d
		AAS2_30%RH	2.04	425	0.43	0.36	0.60	1.22	0.57	0.00	23	30	3.04	2062	65d

		AAS3_85%RH	2.04	425	0.42	0.34	2.00	0.00	0.58	0.00	23	85	3.04	937	55d
		AAS3_70%RH	2.04	425	0.42	0.34	2.00	0.00	0.58	0.00	23	70	3.04	1875	65d
		AAS3_50%RH	2.04	425	0.42	0.34	2.00	0.00	0.58	0.00	23	50	3.04	1125	60d
		AAS3_30%RH	2.04	425	0.42	0.34	2.00	0.00	0.58	0.00	23	30	3.04	906	60d
		AAS4_85%RH	2.04	425	0.43	0.35	4.00	0.00	0.57	0.00	23	85	3.04	1062	60d
		AAS4_70%RH	2.04	425	0.43	0.35	4.00	0.00	0.57	0.00	23	70	3.04	2250	75d
		AAS4_50%RH	2.04	425	0.43	0.35	4.00	0.00	0.57	0.00	23	50	3.04	1900	65d
		AAS4_30%RH	2.04	425	0.43	0.35	4.00	0.00	0.57	0.00	23	30	3.04	1625	65d
2017	Hojati and Radlińska	FS-10-6M	1.95	421	0.48	0.28	6.00	1.13	0.52	0.00	23	50	6.05	2335	140d
		FS-10-2M	1.95	421	0.48	0.28	2.00	1.44	0.52	0.00	23	50	6.05	2608	140d
		FS-15-6M	1.95	421	0.48	0.28	6.00	1.13	0.52	0.00	23	50	6.05	2420	140d
		FS-15-2M	1.95	421	0.48	0.28	2.00	1.44	0.52	0.00	23	50	6.05	2778	140d
		FS-20-6M	1.95	421	0.48	0.28	6.00	1.13	0.52	0.00	23	50	6.05	2131	140d

		FS-20-2M	1.95	421	0.48	0.28	2.00	1.44	0.52	0.00	23	50	6.05	2693	140d
2017	Gao et al.	Ref	2.09	424	0.44	0.40	7.83	1.40	0.50	0.00	20	50	8.89	3013	28d
		SF-0.25	2.09	424	0.43	0.40	7.83	1.40	0.49	0.00	20	50	8.89	2722	28d
		SF-0.5	2.09	424	0.43	0.40	7.83	1.40	0.49	0.00	20	50	8.89	2527	28d
		SF-0.75	2.09	424	0.43	0.40	7.83	1.40	0.48	0.00	20	50	8.89	2260	28d
		SF-1.0	2.09	424	0.42	0.40	7.83	1.40	0.48	0.00	20	50	8.89	2041	28d
		LF-0.25	2.09	424	0.43	0.40	7.83	1.40	0.49	0.00	20	50	8.89	2843	28d
		LF-0.5	2.09	424	0.43	0.40	7.83	1.40	0.49	0.00	20	50	8.89	2649	28d
		LF-0.75	2.09	424	0.43	0.40	7.83	1.40	0.48	0.00	20	50	8.89	2357	28d
		LF-1.0	2.09	424	0.42	0.40	7.83	1.40	0.48	0.00	20	50	8.89	2187	28d
2018	Punurai et al.	FA	1.88	420	1.00	0.38	10.00	0.86	0.00	0.00	23	50	5.99	2941	120d
		10BF90FA	1.88	420	0.94	0.40	10.00	0.86	0.00	0.00	23	50	5.99	2067	120d
		20BF80FA	1.88	420	0.88	0.43	10.00	0.86	0.00	0.00	23	50	5.99	1868	120d

		30BF70FA	1.88	420	0.81	0.46	10.00	0.86	0.00	0.00	23	50	5.99	1629	120d
		40BF60FA	1.88	420	0.75	0.50	10.00	0.86	0.00	0.00	23	50	5.99	1510	120d
2018	Jiao et al.	M1N6	1.89	424	1.00	0.32	7.94	1.00	0.00	0.00	20	50	5.98	1510 6	28d
		M1N8	1.89	424	1.00	0.34	7.94	1.00	0.00	0.00	20	50	5.98	1638 3	28d
		M1N10	1.89	424	1.00	0.35	7.94	1.00	0.00	0.00	20	50	5.98	1255 3	28d
		M1.2N6	1.89	424	1.00	0.32	6.36	1.20	0.00	0.00	20	50	5.98	1595 7	28d
		M1.2N8	1.89	424	1.00	0.34	6.36	1.20	0.00	0.00	20	50	5.98	1851 1	28d

		M1.2N10	1.89	424	1.00	0.36	6.36	1.20	0.00	0.00	20	50	5.98	16383	28d
		M1.4N6	1.89	424	1.00	0.33	5.10	1.40	0.00	0.00	20	50	5.98	20000	28d
		M1.4N8	1.89	424	1.00	0.35	5.12	1.40	0.00	0.00	20	50	5.98	23617	28d
		M1.4N10	1.89	424	1.00	0.37	5.11	1.40	0.00	0.00	20	50	5.98	25745	28d
		M1.6N6	1.89	424	1.00	0.33	4.11	1.60	0.00	0.00	20	50	5.98	25532	28d
		M1.6N8	1.89	424	1.00	0.36	4.11	1.60	0.00	0.00	20	50	5.98	26170	28d

		M1.6N10	1.89	424	1.00	0.38	4.11	1.60	0.00	0.00	20	50	5.98	27447	28d
		M1.8N6	1.89	424	1.00	0.34	3.28	1.80	0.00	0.00	20	50	5.98	29787	28d
		M1.8N8	1.89	424	1.00	0.36	3.28	1.80	0.00	0.00	20	50	5.98	33192	28d
		M1.8N10	1.89	424	1.00	0.38	3.28	1.80	0.00	0.00	20	50	5.98	35748	28d
2018	Wang & Ma	N4F0	2.06	425	1.00	0.30	5.96	1.00	0.00	0.00	20	50	8.89	4587	18d
		N4F3	1.87	424	1.00	0.30	5.96	1.00	0.00	0.00	20	50	8.89	2932	18d
		N4F5	1.74	423	1.00	0.30	5.96	1.00	0.00	0.00	20	50	8.89	3214	18d
		N4F7	1.61	422	1.00	0.30	5.96	1.00	0.00	0.00	20	50	8.89	6148	18d
		N5F5	1.74	423	1.00	0.31	5.97	1.00	0.00	0.00	20	50	8.89	5040	18d

		N6F5	1.74	423	1.00	0.32	5.96	1.00	0.00	0.00	20	50	8.89	6356	18d
2018	Taghvayi et al.	N35M45	1.55	400	0.25	0.34	1.86	0.45	0.32	0.43	23	50	16.57	1273	400d
		N45M45	1.55	400	0.25	0.35	2.31	0.45	0.32	0.43	23	50	16.57	1391	400d
		N55M45	1.55	400	0.26	0.36	2.73	0.45	0.32	0.43	23	50	16.57	1450	400d
		N65M45	1.55	400	0.26	0.37	3.12	0.45	0.31	0.43	23	50	16.57	1361	400d
		N75M45	1.55	400	0.26	0.38	3.49	0.45	0.31	0.42	23	50	16.57	1480	400d
		N35M65	1.55	400	0.25	0.34	1.64	0.65	0.32	0.43	23	50	16.57	1500	400d

		N45M65	1.55	400	0.26	0.35	2.04	0.65	0.32	0.43	23	50	16.57	1628	400d
		N55M65	1.55	400	0.26	0.37	2.41	0.65	0.31	0.43	23	50	16.57	1750	400d
		N65M65	1.55	400	0.26	0.38	2.75	0.65	0.31	0.42	23	50	16.57	1717	400d
		N75M65	1.55	400	0.27	0.39	3.07	0.65	0.31	0.42	23	50	16.57	1687	400d
		N35M85	1.55	400	0.25	0.35	1.43	0.85	0.32	0.43	23	50	16.57	1717	400d
		N45M85	1.55	400	0.26	0.36	1.78	0.85	0.32	0.43	23	50	16.57	1924	400d

		N55M85	1.55	400	0.26	0.37	2.09	0.85	0.31	0.42	23	50	16.57	1983	400d
		N65M85	1.55	400	0.26	0.38	2.39	0.85	0.31	0.42	23	50	16.57	1894	400d
		N75M85	1.55	400	0.27	0.39	2.66	0.85	0.31	0.42	23	50	16.57	1983	400d
		N35M105	1.55	400	0.26	0.35	1.23	1.05	0.32	0.43	23	50	16.57	1865	400d
		N45M105	1.55	400	0.26	0.36	1.52	1.05	0.31	0.43	23	50	16.57	2190	400d
		N55M105	1.55	400	0.26	0.38	1.79	1.05	0.31	0.42	23	50	16.57	2125	400d

		N65M105	1.55	400	0.27	0.39	2.03	1.05	0.31	0.42	23	50	16.57	1983	400d
		N75M105	1.55	400	0.27	0.40	2.26	1.05	0.31	0.42	23	50	16.57	2000	400d
2018	Xiang et al.	100 MK-0FS	1.18	16646	1.00	0.50	4.59	1.30	0.00	0.00	20	50	5.98	3085	91d
		90 MK-10FS	1.18	16646	0.95	0.52	4.59	1.30	0.05	0.00	20	50	5.98	2228	91d
		80 MK-20FS	1.18	16646	0.90	0.55	4.59	1.30	0.10	0.00	20	50	5.98	1800	91d
		70 MK-30FS	1.18	16646	0.85	0.58	4.59	1.30	0.15	0.00	20	50	5.98	1285	91d

		60 MK-40FS	1.18	1664 6	0.80	0.61	4.59	1.30	0.20	0.00	20	50	5.98	1114	91d
2018	Al-mashhadani et al.	Control	1.99	421	0.37	0.31	12.00	1.73	0.63	0.00	23	50	5.99	486	84d
		ST 0.4	1.99	421	0.37	0.31	12.00	1.73	0.62	0.00	23	50	5.99	337	84d
		ST 0.8	1.99	421	0.36	0.31	12.00	1.73	0.61	0.00	23	50	5.99	306	84d
		ST 1.2	1.99	421	0.36	0.31	12.00	1.73	0.60	0.00	23	50	5.99	286	84d
		PP 0.4	1.99	421	0.37	0.31	12.00	1.73	0.63	0.00	23	50	5.99	301	84d
		PP 0.8	1.99	421	0.37	0.31	12.00	1.73	0.63	0.00	23	50	5.99	244	84d
		PP 1.2	1.99	421	0.37	0.31	12.00	1.73	0.62	0.00	23	50	5.99	218	84d
		PVA 0.4	1.99	421	0.37	0.31	12.00	1.73	0.63	0.00	23	50	5.99	270	84d
		PVA 0.8	1.99	421	0.37	0.31	12.00	1.73	0.62	0.00	23	50	5.99	202	84d
		PVA 1.2	1.99	421	0.37	0.31	12.00	1.73	0.62	0.00	23	50	5.99	187	84d
2018	Lee et al.	Control	2.08	420	0.54	0.36	0.00	0.90	0.46	0.00	20	50	6.06	4840	91d

		RA25	2.08	420	0.13	0.36	0.00	0.90	0.84	0.02	20	50	6.06	4295	91d
		RA50	2.08	420	0.18	0.36	0.00	0.90	0.76	0.07	20	50	6.06	3954	91d
		ES25	2.08	420	0.13	0.36	0.00	0.90	0.85	0.02	20	50	6.06	2659	91d
		ES50	2.08	420	0.18	0.36	0.00	0.90	0.77	0.06	20	50	6.06	2522	91d
2018	Xiang et al.	l-LP-0	3.93	1608	1.00	0.30	0.66	2.00	0.00	0.00	20	90	5.98	2804	28d
		l-LP-5	3.93	1608	0.96	0.31	0.66	2.00	0.00	0.00	20	90	5.98	2674	28d
		l-LP-10	3.93	1608	0.93	0.32	0.66	2.00	0.00	0.00	20	90	5.98	1575	28d
		l-LP-20	3.93	1608	0.86	0.34	0.66	2.00	0.00	0.00	20	90	5.98	2416	28d
		s-LP-0	3.93	1608	1.00	0.35	0.00	2.00	0.00	0.00	20	90	5.98	2997	28d
		s-LP-5	3.93	1608	0.97	0.36	0.00	2.00	0.00	0.00	20	90	5.98	2804	28d
		s-LP-10	3.93	1608	0.93	0.37	0.00	2.00	0.00	0.00	20	90	5.98	2416	28d
		s-LP-120	3.93	1608	0.87	0.40	0.00	2.00	0.00	0.00	20	90	5.98	2707	28d
2018	Jiao et al.	M1.2N6M	1.89	424	0.45	0.29	1.29	1.20	0.55	0.00	20	50	5.98	2240	28d

		M1.2N8M	1.89	424	0.45	0.30	1.77	1.20	0.55	0.00	20	50	5.98	2720	28d
		M1.2N10M	1.89	424	0.45	0.31	2.25	1.20	0.55	0.00	20	50	5.98	3200	28d
		M1.4N6M	1.89	424	0.45	0.29	1.16	1.40	0.55	0.00	20	50	5.98	2720	28d
		M1.4N8M	1.89	424	0.45	0.31	1.61	1.40	0.55	0.00	20	50	5.98	3264	28d
		M1.4N10M	1.89	424	0.46	0.32	2.07	1.40	0.54	0.00	20	50	5.98	3552	28d
		M1.6N6M	1.89	424	0.45	0.30	1.04	1.60	0.55	0.00	20	50	5.98	3264	28d
		M1.6N8M	1.89	424	0.45	0.31	1.44	1.60	0.55	0.00	20	50	5.98	3488	28d
		M1.6N10M	1.89	424	0.46	0.33	1.86	1.60	0.54	0.00	20	50	5.98	3904	28d
2019	Hu et al.	M0	1.91	425	0.41	0.28	3.44	0.00	0.59	0.00	20	50	5.98	1773	56d
		M0.5	1.91	425	0.41	0.29	2.83	0.50	0.59	0.00	20	50	5.98	2665	56d
		M1.0	1.91	425	0.42	0.30	2.23	1.00	0.58	0.00	20	50	5.98	4173	56d
		M1.5	1.91	425	0.42	0.31	1.63	1.50	0.58	0.00	20	50	5.98	5223	56d

2019	Humad et al.	100:0-10SS1	1.74	500	0.29	0.35	1.32	1.00	0.53	0.18	20	42	20.00	2440	44d
		80:20-10SS1	1.90	460	0.29	0.35	1.32	1.00	0.53	0.18	20	42	20.00	2660	44d
		80:20-10SS0.5	1.90	460	0.29	0.35	1.32	0.50	0.53	0.18	20	42	20.00	950	44d
2019	Ling et al.	1.0-20%	1.92	420	1.00	0.25	6.74	1.00	0.00	0.00	23	50	2.31	4630	56d
		1.0-25%	1.92	420	1.00	0.25	6.74	1.00	0.00	0.00	23	50	2.31	6230	56d
		1.5-20%	1.92	420	1.00	0.25	3.26	1.50	0.00	0.00	23	50	2.31	4250	56d
		1.5-25%	1.92	420	1.00	0.25	3.26	1.50	0.00	0.00	23	50	2.31	5390	56d
2020	Mermerdaş et al.	M1	3.19	2000	0.31	0.35	6.00	0.24	0.54	0.15	25	50	5.99	1500	90d
		M2	3.19	2000	0.31	0.35	8.00	0.24	0.54	0.15	25	50	5.99	960	90d
		M3	3.19	2000	0.31	0.35	10.00	0.24	0.54	0.15	25	50	5.99	960	90d

		M4	3.19	2000	0.36	0.35	6.00	0.24	0.50	0.14	25	50	5.99	1160	90d
		M5	3.19	2000	0.36	0.35	8.00	0.24	0.50	0.14	25	50	5.99	910	90d
		M6	3.19	2000	0.36	0.35	10.00	0.24	0.50	0.14	25	50	5.99	900	90d
		M7	3.19	2000	0.41	0.35	6.00	0.24	0.46	0.13	25	50	5.99	1000	90d
		M8	3.19	2000	0.41	0.35	8.00	0.24	0.46	0.13	25	50	5.99	850	90d
		M9	3.19	2000	0.41	0.35	10.00	0.24	0.46	0.13	25	50	5.99	800	90d
		M10	3.19	2000	0.31	0.35	6.00	0.48	0.54	0.15	25	50	5.99	1300	90d
		M11	3.19	2000	0.31	0.35	8.00	0.48	0.54	0.15	25	50	5.99	1200	90d
		M12	3.19	2000	0.30	0.35	10.00	0.48	0.54	0.15	25	50	5.99	1080	90d
		M13	3.19	2000	0.36	0.35	6.00	0.48	0.50	0.14	25	50	5.99	1260	90d
		M14	3.19	2000	0.36	0.35	8.00	0.48	0.50	0.14	25	50	5.99	960	90d
		M15	3.19	2000	0.36	0.35	10.00	0.48	0.50	0.14	25	50	5.99	1000	90d
		M16	3.19	2000	0.41	0.35	6.00	0.48	0.46	0.13	25	50	5.99	1100	90d

		M17	3.19	2000	0.41	0.35	8.00	0.48	0.46	0.13	25	50	5.99	1000	90d
		M18	3.19	2000	0.41	0.35	10.00	0.48	0.46	0.13	25	50	5.99	960	90d
		M19	3.19	2000	0.31	0.35	6.00	0.60	0.54	0.15	25	50	5.99	1300	90d
		M20	3.19	2000	0.31	0.35	8.00	0.60	0.54	0.15	25	50	5.99	1100	90d
		M21	3.19	2000	0.30	0.35	10.00	0.60	0.54	0.15	25	50	5.99	1070	90d
		M22	3.19	2000	0.36	0.35	6.00	0.60	0.50	0.14	25	50	5.99	1300	90d
		M23	3.19	2000	0.36	0.35	8.00	0.60	0.50	0.14	25	50	5.99	1010	90d
		M24	3.19	2000	0.36	0.35	10.00	0.60	0.50	0.14	25	50	5.99	1000	90d
		M25	3.19	2000	0.41	0.35	6.00	0.60	0.46	0.13	25	50	5.99	1100	90d
		M26	3.19	2000	0.41	0.35	8.00	0.60	0.46	0.13	25	50	5.99	1000	90d
		M27	3.19	2000	0.41	0.35	10.00	0.60	0.46	0.13	25	50	5.99	960	90d
2020	Gong et al.	A0	1.80	425	0.50	0.46	1.84	2.30	0.39	0.00	20	60	8.89	1117	56d
		S1	11.38	1823	0.50	0.46	1.84	2.30	0.39	0.00	20	60	8.89	1000	56d

		S2	20.97	3222	0.50	0.46	1.84	2.30	0.39	0.00	20	60	8.89	1273	56d
		S3	30.56	4620	0.50	0.46	1.84	2.30	0.39	0.00	20	60	8.89	1146	56d
		S4	40.15	6019	0.50	0.46	1.84	2.30	0.39	0.00	20	60	8.89	1103	56d
		S5	49.73	7417	0.50	0.46	1.84	2.30	0.39	0.00	20	60	8.89	1033	56d
		NS1	5.63	985	0.50	0.46	1.84	2.30	0.39	0.00	20	60	8.89	778	56d
		NS2	9.47	1545	0.50	0.46	1.84	2.30	0.39	0.00	20	60	8.89	790	56d
		NS3	13.29	2102	0.50	0.46	1.84	2.30	0.39	0.00	20	60	8.89	1103	56d
		NS4	17.13	2662	0.50	0.46	1.84	2.30	0.39	0.00	20	60	8.89	1146	56d
		NS5	20.97	3222	0.50	0.46	1.84	2.30	0.39	0.00	20	60	8.89	1245	56d
2020	Xiang et al.	Low - NaOH	3.65	425	0.33	0.32	8.00	0.00	0.67	0.00	20	50	5.98	1633	180d
		Room - NaOH	3.65	425	0.36	0.41	8.00	1.00	0.64	0.00	20	50	5.98	1944	180d
		Low - 1.0 M	3.65	425	0.33	0.33	8.00	1.00	0.67	0.00	20	50	5.98	2022	180d
		Room - 1.0 M	3.65	425	0.36	0.41	8.00	1.00	0.64	0.00	20	50	5.98	2761	180d

		Low - 2.0 M	3.65	425	0.34	0.36	8.00	2.00	0.66	0.00	20	50	5.98	2488	180d
		Room - 2.0 M	3.65	425	0.37	0.44	8.00	2.00	0.63	0.00	20	50	5.98	2955	180d
2020	Si et al.	M-MK0G-A	1.45	17990	0.46	0.57	5.25	0.96	0.54	0.00	23	50	6.08	1200	56d
		M-MK5G-A	1.45	17990	0.45	0.59	5.25	0.96	0.54	0.00	23	50	6.08	1136	56d
		M-MK10G-A	1.45	17990	0.45	0.60	5.25	0.96	0.54	0.00	23	50	6.08	1010	56d
		M-MK20G-A	1.45	17990	0.43	0.63	5.25	0.96	0.54	0.00	23	50	6.08	1105	56d
		M-MK0G-H	1.45	17990	0.46	0.57	5.25	0.96	0.54	0.00	23	50	6.08	526	56d

		M-MK5G-H	1.45	17990	0.45	0.59	5.25	0.96	0.54	0.00	23	50	6.08	482	56d
		M-MK10G-H	1.45	17990	0.45	0.60	5.25	0.96	0.54	0.00	23	50	6.08	453	56d
		M-MK20G-H	1.45	17990	0.43	0.63	5.25	0.96	0.54	0.00	23	50	6.08	468	56d
2020	Xu et al.	Control	2.52	154	0.55	0.33	7.00	0.00	0.45	0.00	23	50	5.99	1676	56d
		P1	2.52	154	0.55	0.33	7.00	0.00	0.45	0.00	23	50	5.99	1517	56d
		P2	2.52	154	0.55	0.33	7.00	0.00	0.45	0.00	23	50	5.99	1429	56d
		P3	2.52	154	0.55	0.33	7.00	0.00	0.45	0.00	23	50	5.99	1305	56d
		P4	2.52	154	0.55	0.33	7.00	0.00	0.45	0.00	23	50	5.99	1235	56d
2020	Behforouz et al.	Control	1.19	2540	0.24	0.31	9.85	0.86	0.25	0.51	23	50	23.53	850	90d

		PP0.3	1.19	2540	0.24	0.31	9.85	0.86	0.25	0.51	23	50	23.53	618	90d
		PP0.5	1.19	2540	0.24	0.31	9.85	0.86	0.25	0.51	23	50	23.53	533	90d
		PP1	1.19	2540	0.24	0.31	9.85	0.86	0.24	0.51	23	50	23.53	506	90d
		PP0.3RCA10	1.19	2540	0.24	0.31	9.85	0.86	0.25	0.51	23	50	23.53	634	90d
		PP0.3RCA20	1.19	2540	0.24	0.31	9.85	0.86	0.25	0.51	23	50	23.53	714	90d
		PP0.3RCA30	1.19	2540	0.24	0.31	9.85	0.86	0.24	0.51	23	50	23.53	768	90d
2021	Chen et al.	AASM-AB-1.5	2.07	425	0.50	0.35	2.98	1.00	0.50	0.00	23	50	5.99	2833	28d

		AASM-AB-2.5	2.07	425	0.38	0.35	2.98	1.00	0.62	0.00	23	50	5.99	1917	28d
		AASM-AB-2.0/AASM-PS-0.6-1.8	2.07	425	0.43	0.35	2.98	1.00	0.57	0.00	23	50	5.99	2333	28d
		AASM-PS-0.075-0.6	2.07	425	0.43	0.35	2.98	1.00	0.57	0.00	23	50	5.99	2277	28d
		AASM-PS-1.18-2.36	2.07	425	0.43	0.35	2.98	1.00	0.57	0.00	23	50	5.99	1166	28d
		AASM-Control	2.07	425	0.45	0.39	2.45	1.00	0.55	0.00	23	50	5.99	2777	28d
		AASM-PP-1.0	2.07	425	0.45	0.39	2.45	1.00	0.55	0.00	23	50	5.99	2277	28d
		AASM-PP-1.5	2.07	425	0.45	0.39	2.45	1.00	0.55	0.00	23	50	5.99	2405	28d
		AASM-PP-2.0	2.07	425	0.45	0.39	2.45	1.00	0.55	0.00	23	50	5.99	2500	28d
		AASM-SF-1.0	2.07	425	0.43	0.39	2.45	1.00	0.53	0.00	23	50	5.99	2333	28d

		AASM-SF-1.5	2.07	425	0.43	0.39	2.45	1.00	0.52	0.00	23	50	5.99	1888	28d
		AASM-SF-2.0	2.07	425	0.42	0.39	2.45	1.00	0.51	0.00	23	50	5.99	1555	28d
2021	Adesanya et al.	M1	1.80	425	0.38	0.45	2.77	0.00	0.62	0.00	23	50	8.89	400	28d
		M2	2.10	424	0.38	0.45	2.77	0.00	0.62	0.00	23	50	8.89	100	28d
		M3	2.40	423	0.38	0.45	2.77	0.00	0.62	0.00	23	50	8.89	0	28d
		M4	1.80	425	0.39	0.47	6.91	1.00	0.61	0.00	23	50	8.89	1200 0	28d
		M5	2.10	424	0.39	0.47	6.91	1.00	0.61	0.00	23	50	8.89	9500	28d
		M6	2.40	423	0.39	0.47	6.91	1.00	0.61	0.00	23	50	8.89	1050 0	28d
		M7	1.80	425	0.37	0.44	3.45	1.50	0.63	0.00	23	50	8.89	4500	28d
		M8	2.10	424	0.37	0.44	3.45	1.50	0.63	0.00	23	50	8.89	4700	28d
		M9	2.40	423	0.37	0.44	3.45	1.50	0.63	0.00	23	50	8.89	4800	28d

		M10	1.80	425	0.37	0.43	1.38	2.00	0.63	0.00	23	50	8.89	7400	28d
		M11	2.10	424	0.37	0.43	1.38	2.00	0.63	0.00	23	50	8.89	7300	28d
		M12	2.40	423	0.37	0.43	1.38	2.00	0.63	0.00	23	50	8.89	4900	28d
		M13	1.80	425	0.36	0.42	0.01	2.50	0.64	0.00	23	50	8.89	5100	28d
		M14	2.10	424	0.36	0.42	0.01	2.50	0.64	0.00	23	50	8.89	7500	28d
		M15	2.40	423	0.36	0.42	0.01	2.50	0.64	0.00	23	50	8.89	7200	28d
		M16	1.80	425	0.38	0.45	2.77	0.00	0.62	0.00	60	50	8.89	300	28d
		M17	2.10	424	0.38	0.45	2.77	0.00	0.62	0.00	60	50	8.89	300	28d
		M18	2.40	423	0.38	0.45	2.77	0.00	0.62	0.00	60	50	8.89	300	28d
		M19	1.80	425	0.39	0.47	6.91	1.00	0.61	0.00	60	50	8.89	1130 0	28d
		M20	2.10	424	0.39	0.47	6.91	1.00	0.61	0.00	60	50	8.89	5500	28d
		M21	2.40	423	0.39	0.47	6.91	1.00	0.61	0.00	60	50	8.89	6200	28d

		M22	1.80	425	0.37	0.44	3.45	1.50	0.63	0.00	60	50	8.89	400	28d
		M23	2.10	424	0.37	0.44	3.45	1.50	0.63	0.00	60	50	8.89	1100	28d
		M24	2.40	423	0.37	0.44	3.45	1.50	0.63	0.00	60	50	8.89	1300	28d
		M25	1.80	425	0.37	0.43	1.38	2.00	0.63	0.00	60	50	8.89	1700	28d
		M26	2.10	424	0.37	0.43	1.38	2.00	0.63	0.00	60	50	8.89	2100	28d
		M27	2.40	423	0.37	0.43	1.38	2.00	0.63	0.00	60	50	8.89	2000	28d
		M28	1.80	425	0.36	0.42	0.01	2.50	0.64	0.00	60	50	8.89	1700	28d
		M29	2.10	424	0.36	0.42	0.01	2.50	0.64	0.00	60	50	8.89	400	28d
		M30	2.40	423	0.36	0.42	0.01	2.50	0.64	0.00	60	50	8.89	200	28d
2021	Fu et al.	S-6-1	1.55	450	0.44	0.37	1.47	1.00	0.56	0.00	20	50	5.98	2688	90d
		M1S-6-1	1.54	621	0.44	0.37	1.47	1.00	0.56	0.00	20	50	5.98	2603	90d
		M2S-6-1	1.53	788	0.44	0.37	1.47	1.00	0.56	0.00	20	50	5.98	2264	90d
		M3S-6-1	1.52	957	0.44	0.37	1.47	1.00	0.56	0.00	20	50	5.98	1867	90d

		M3S-8-1	1.52	957	0.45	0.39	2.01	1.00	0.55	0.00	20	50	5.98	2210	90d
		M3S-6-1.5	1.52	957	0.45	0.40	1.19	1.50	0.55	0.00	20	50	5.98	2368	90d
2021	Sun et al.	NaOH+Limestone	1.37	2140	0.32	0.42	6.68	0.00	0.42	0.26	25	60	5.98	1420	128d
		NaOH+BOF SSA	1.37	2140	0.32	0.42	6.68	0.00	0.42	0.26	25	60	5.98	1200	128d
		Water glass+Limestone	1.37	2140	0.32	0.43	2.01	1.40	0.42	0.26	25	60	5.98	1700	128d
		Water glass+BOF SSA	1.37	2140	0.32	0.43	2.01	1.40	0.42	0.26	25	60	5.98	1380	128d
2021	Xu et al.	Control	2.52	1535	0.55	0.33	7.00	0.00	0.45	0.00	23	50	5.99	1678	56d
		P3-5	2.52	1535	0.55	0.33	7.00	0.00	0.45	0.00	23	50	5.99	1593	56d
		P3-10	2.52	1535	0.55	0.33	7.00	0.00	0.45	0.00	23	50	5.99	1538	56d
		P3-15	2.52	1535	0.55	0.33	7.00	0.00	0.45	0.00	23	50	5.99	1483	56d

		P3-20	2.52	1535	0.55	0.33	7.00	0.00	0.45	0.00	23	50	5.99	1447	56d
		P9-5	2.52	1535	0.55	0.33	7.00	0.00	0.45	0.00	23	50	5.99	1496	56d
		P9-10	2.52	1535	0.55	0.33	7.00	0.00	0.45	0.00	23	50	5.99	1410	56d
		P9-15	2.52	1535	0.55	0.33	7.00	0.00	0.45	0.00	23	50	5.99	1313	56d
		P9-20	2.52	1535	0.55	0.33	7.00	0.00	0.45	0.00	23	50	5.99	1240	56d
		P15-5	2.52	1535	0.55	0.33	7.00	0.00	0.45	0.00	23	50	5.99	1204	56d
		P15-10	2.52	1535	0.55	0.33	7.00	0.00	0.45	0.00	23	50	5.99	1161	56d
		P15-15	2.52	1535	0.55	0.33	7.00	0.00	0.45	0.00	23	50	5.99	1094	56d
		P15-20	2.52	1535	0.55	0.33	7.00	0.00	0.45	0.00	23	50	5.99	1045	56d
2021	Wang et al.	SHGC0	1.91	421	1.00	0.29	10.00	1.14	0.00	0.00	20	60	11.48	7054	28d
		SHGC1	1.91	421	0.92	0.29	10.00	1.14	0.07	0.00	20	60	11.48	6254	28d

		SHGC2	1.91	421	0.87	0.29	10.00	1.14	0.12	0.00	20	60	11.48	5672	28d
		SHGC3	1.91	421	0.81	0.29	10.00	1.14	0.17	0.00	20	60	11.48	5090	28d
		SHGC4	1.91	421	0.77	0.29	10.00	1.14	0.22	0.00	20	60	11.48	3054	28d
2022	Sadeghian et al.	G1-00-50-W	1.57	400	0.22	0.42	0.00	0.97	0.47	0.31	23	50	16.57	1626	180d
		G1-05-50-W	5.74	1380	0.22	0.41	0.00	0.97	0.47	0.31	23	50	16.57	1573	180d
		G1-10-50-W	9.91	2360	0.22	0.41	0.00	0.97	0.47	0.31	23	50	16.57	1573	180d

		G1-15-50-W	14.08	3340	0.22	0.41	0.00	0.97	0.47	0.31	23	50	16.57	1250	180d
		G1-00-52-W	1.57	400	0.22	0.42	0.00	0.97	0.47	0.31	23	50	16.57	1867	180d
		G1-05-52-W	5.74	1380	0.22	0.42	0.00	0.97	0.47	0.31	23	50	16.57	1750	180d
		G1-10-52-W	9.91	2360	0.22	0.42	0.00	0.97	0.47	0.31	23	50	16.57	1627	180d
		G1-15-52-W	14.08	3340	0.22	0.41	0.00	0.97	0.47	0.31	23	50	16.57	1386	180d
		G1-00-54-W	1.57	400	0.23	0.43	0.00	0.97	0.46	0.31	23	50	16.57	1920	180d

		G1-05-54-W	5.74	1380	0.22	0.43	0.00	0.97	0.47	0.31	23	50	16.57	1786	180d
		G1-10-54-W	9.91	2360	0.22	0.42	0.00	0.97	0.47	0.31	23	50	16.57	1653	180d
		G1-15-54-W	14.08	3340	0.22	0.42	0.00	0.97	0.47	0.31	23	50	16.57	1386	180d
		G2-00-50-W	1.57	400	0.22	0.42	0.00	0.97	0.47	0.31	23	50	16.57	1600	180d
		G2-05-50-W	5.74	1380	0.22	0.42	0.00	0.97	0.47	0.31	23	50	16.57	1546	180d
		G2-10-50-W	9.91	2360	0.22	0.42	0.00	0.97	0.47	0.31	23	50	16.57	1440	180d

		G2-15-50-W	14.08	3340	0.22	0.41	0.00	0.97	0.47	0.31	23	50	16.57	1466	180d
		G2-00-52-W	1.57	400	0.23	0.43	0.00	0.97	0.46	0.31	23	50	16.57	1653	180d
		G2-05-52-W	5.74	1380	0.22	0.43	0.00	0.97	0.47	0.31	23	50	16.57	1600	180d
		G2-10-52-W	9.91	2360	0.22	0.42	0.00	0.97	0.47	0.31	23	50	16.57	1600	180d
		G2-15-52-W	14.08	3340	0.22	0.42	0.00	0.97	0.47	0.31	23	50	16.57	1573	180d
		G2-00-54-W	1.57	400	0.23	0.44	0.00	0.97	0.46	0.31	23	50	16.57	1840	180d

		G2-05-54-W	5.74	1380	0.23	0.43	0.00	0.97	0.46	0.31	23	50	16.57	1750	180d
		G2-10-54-W	9.91	2360	0.23	0.43	0.00	0.97	0.46	0.31	23	50	16.57	1669	180d
		G2-15-54-W	14.08	3340	0.22	0.43	0.00	0.97	0.47	0.31	23	50	16.57	1626	180d
		G1-00-50-P	1.57	400	0.22	0.42	0.00	0.97	0.47	0.31	23	50	16.57	1893	180d
		G1-05-50-P	5.74	1380	0.22	0.41	0.00	0.97	0.47	0.31	23	50	16.57	1813	180d
		G1-10-50-P	9.91	2360	0.22	0.41	0.00	0.97	0.47	0.31	23	50	16.57	1706	180d

		G1-15-50-P	14.08	3340	0.22	0.41	0.00	0.97	0.47	0.31	23	50	16.57	1467	180d
		G1-00-52-P	1.57	400	0.22	0.42	0.00	0.97	0.47	0.31	23	50	16.57	2080	180d
		G1-05-52-P	5.74	1380	0.22	0.42	0.00	0.97	0.47	0.31	23	50	16.57	1973	180d
		G1-10-52-P	9.91	2360	0.22	0.42	0.00	0.97	0.47	0.31	23	50	16.57	1750	180d
		G1-15-52-P	14.08	3340	0.22	0.41	0.00	0.97	0.47	0.31	23	50	16.57	1493	180d
		G1-00-54-P	1.57	400	0.23	0.43	0.00	0.97	0.46	0.31	23	50	16.57	2240	180d

		G1-05-54-P	5.74	1380	0.22	0.43	0.00	0.97	0.47	0.31	23	50	16.57	2053	180d
		G1-10-54-P	9.91	2360	0.22	0.42	0.00	0.97	0.47	0.31	23	50	16.57	1786	180d
		G1-15-54-P	14.08	3340	0.22	0.42	0.00	0.97	0.47	0.31	23	50	16.57	1520	180d
		G2-00-50-P	1.57	400	0.22	0.42	0.00	0.97	0.47	0.31	23	50	16.57	1786	180d
		G2-05-50-P	5.74	1380	0.22	0.42	0.00	0.97	0.47	0.31	23	50	16.57	1760	180d
		G2-10-50-P	9.91	2360	0.22	0.42	0.00	0.97	0.47	0.31	23	50	16.57	1733	180d

		G2-15-50-P	14.08	3340	0.22	0.41	0.00	0.97	0.47	0.31	23	50	16.57	1626	180d
		G2-00-52-P	1.57	400	0.23	0.43	0.00	0.97	0.46	0.31	23	50	16.57	2000	180d
		G2-05-52-P	5.74	1380	0.22	0.43	0.00	0.97	0.47	0.31	23	50	16.57	1867	180d
		G2-10-52-P	9.91	2360	0.22	0.42	0.00	0.97	0.47	0.31	23	50	16.57	1813	180d
		G2-15-52-P	14.08	3340	0.22	0.42	0.00	0.97	0.47	0.31	23	50	16.57	1733	180d
		G2-00-54-P	1.57	400	0.23	0.44	0.00	0.97	0.46	0.31	23	50	16.57	2080	180d

		G2-05-54-P	5.74	1380	0.23	0.43	0.00	0.97	0.46	0.31	23	50	16.57	1973	180d
		G2-10-54-P	9.91	2360	0.23	0.43	0.00	0.97	0.46	0.31	23	50	16.57	1893	180d
		G2-15-54-P	14.08	3340	0.22	0.43	0.00	0.97	0.47	0.31	23	50	16.57	1813	180d
2022	Ou et al.	44F0S0	1.79	425	0.24	0.38	2.46	1.00	0.29	0.47	20	60	22.79	1207	360d
		47F0S0	1.79	425	0.25	0.39	2.31	1.00	0.29	0.47	20	60	22.79	1320	360d
		50F0S0	1.79	425	0.25	0.40	2.18	1.00	0.28	0.46	20	60	22.79	1698	360d

		47F25S0	1.73	424	0.25	0.39	2.31	1.00	0.29	0.47	20	60	22.79	1169	360d
		47F0S5	11.39	1404	0.25	0.39	2.31	1.00	0.29	0.47	20	60	22.79	1094	360d
		47F0S10	20.98	2383	0.25	0.39	2.31	1.00	0.29	0.47	20	60	22.79	1018	360d

Acknowledgement

First and foremost, I would like to show my deepest thanks to my doctoral course supervisor, Prof. Kiyofumi Kurumisawa, for his support, guidance, patience, kindness and knowledge during my study and life in Hokkaido University. It is a great treasure for me to be Prof. Kurumisawa's student and get his greatest help in my research work.

I would like to express my thanks to Prof. Tsutomu Sato and Prof. Masaji Kato, the Professor and Assistant Professor in our Laboratory, for their valuable support and professional instructions on my academic life and experimental work.

I also would like to thank English Engineering Education Program (e3) to provide such a great opportunity for me to study in Hokkaido University. Moreover, e3 family gives me a chance to meet other international friends.

Great thanks go to the Hokkaido University DX Doctoral Fellowship (JPMJSP2119). DX scholarship provides me with the help and support in my doctoral course, so that I can put all my focus on my study and research work.

I also appreciate the help I received from my groupmates and friends Zhai, Lang, Sun, Hanaoka, Muragami, Kondo, Kudo, Nakashima and Yamashina.

Last but not least, please let me express my sincerest thankfulness to my parents who always encourage me and offer me the continuous support in my whole life.

List of Publications

All the publications derived from the research work in the doctoral course are listed below:

(1) Y.K. Kong, K. Kurumisawa, Application of machine learning in predicting workability for alkali-activated materials, Case Stud. Constr. Mater. 18 (2023) e02173. https://doi.org/10.1016/j.cscm.2023.e02173.

(2) Y.K. Kong, K. Kurumisawa, Fresh properties and characteristic testing methods for alkali-activated materials: A review, J. Build. Eng. 75 (2023) 106830. https://doi.org/10.1016/j.jobe.2023.106830.

(3) Y.K. Kong, M. Kato, K. Kurumisawa, Recent advances in x-ray computed tomography for alkali-activated materials: A review, J. Adv. Concr. Technol. 21 (2023) 573-595. https://doi.org/10.3151/jact.21.573.

(4) S.H. Chu, K. Kurumisawa, Y.K. Kong, Physically explicable mathematical model for strength prediction of uhpfrc, Eng. Struct. 275 (2023) 115191. https://doi.org/10.1016/j.engstruct.2022.115191.

(5) Y.K. Kong, K. Kurumisawa, S.H. Chu, Infilled cementitious composites (icc) – a comparative life cycle assessment with uhpc, J. Clean. Prod. (2022) 134051. https://doi.org/10.1016/j.jclepro.2022.134051.

(6) Y.K. Kong, S. Ruan, K. Kurumisawa, Recycling of calcined carbonated cement pastes as cementitious materials: Proposed CCUS technology for calcium

looping, J. Environ. Chem. Eng. (2022) 108247. https://doi.org/10.1016/j.jece.2022.108247.

(7) Y.K. Kong, K. Kurumisawa, Prediction of the drying shrinkage of alkali-activated materials using artificial neural networks, Case Stud. Constr. Mater. 17 (2022) e01166. https://doi.org/10.1016/j.cscm.2022.e01166.

(8) Y.K. Kong, Y. Song, Y. Weng, K. Kurumisawa, D. Yan, X. Zhou, S. Wang, S. Ruan, Influences of CO_2-cured cement powders on hydration of cement paste, Greenhouse Gases: Sci. Technol. (2022) https://doi.org/10.1002/ghg.2141.

(9) Y.K. Kong, Y. Song, K. Kurumisawa, T. Wang, D. Yan, Q. Zeng, X. Zhou, S. Ruan, Use of hydrated cement pastes (HCP) as a CO_2 sponge, J. CO2 Util. 55 (2022) 101804. https://doi.org/10.1016/j.jcou.2021.101804.

(10) Y.K. Kong, S.H. Chu, Modeling the drying shrinkage of cement paste prepared with wastewater, J. Mater. Civ. Eng. 34 (6) (2022) 04022104. http://doi.org/10.1061/(ASCE)MT.1943-5533.0004249.

(11) S.H. Chu, Y.K. Kong, Mathematical model for strength of alkali-activated materials, J. Build. Eng. 44 (2021) 103189. https://doi.org/10.1016/j.jobe.2021.103189.

Apart from the above published papers, the author also holds several manuscripts that are under review or working, which are listed below:

(1) Y.K. Kong, K. Kurumisawa, Prediction model for compressive strength and drying shrinkage of alkali-activated materials: Evaluation of XGBoost and LightGBM, Comput. Concr. (2023) under review.

(2) Y.K. Kong, K. Kurumisawa, Characterization of microstructure development of alkali-activated slag paste during fresh stage, (2023) under working.